

**UNSTEADY DIFFUSER FLOW IN AN AEROENGINE CENTRIFUGAL  
COMPRESSOR**

by

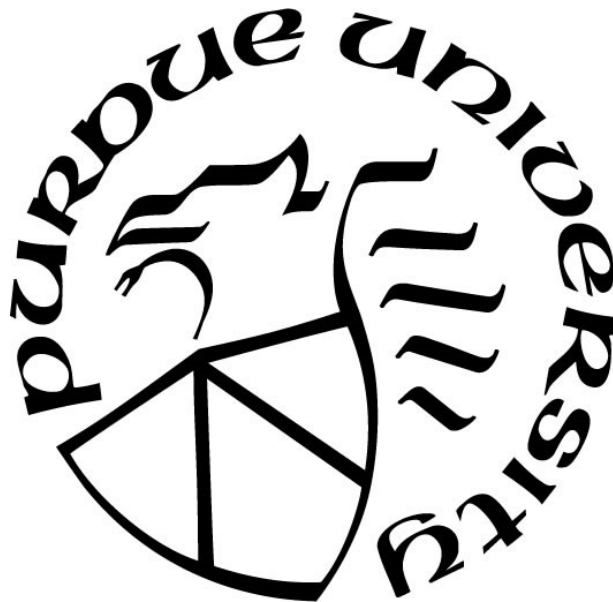
**William James Gooding**

**A Dissertation**

*Submitted to the Faculty of Purdue University*

*In Partial Fulfillment of the Requirements for the degree of*

**Doctor of Philosophy**



School of Mechanical Engineering

West Lafayette, Indiana

May 2020

**THE PURDUE UNIVERSITY GRADUATE SCHOOL  
STATEMENT OF COMMITTEE APPROVAL**

**Dr. Nicole Key, Chair**

School of Mechanical Engineering

**Dr. Carson Slabaugh**

Department of Aeronautics and Astronautics

**Dr. Guillermo Paniagua**

School of Mechanical Engineering

**Dr. Terrence Meyer**

School of Mechanical Engineering

**Approved by:**

Dr. Nicole Key

*To all my family, friends, and teachers over the years*

## ACKNOWLEDGMENTS

I am endlessly thankful to the many people who have supported this work over the years. First, I am extremely grateful for the mentorship, encouragement, and push from my advisor, Nicole Key. Her leadership and guidance has shaped and grown me professionally and intellectually. This work was funded primarily by Rolls-Royce, and I appreciate the technical support of various members of the Rolls-Royce team including Steve Mazur, Mark Gritton, Dave Sayre, and Mark Whitlock. The technical guidance of John Fabian, Fangyuan Lou, Cliff Weissman of Dantec Dynamics, Bill Holmes and Laith Zori of ANSYS, and my committee (Carson Slabaugh, Guillermo Paniagua, and Terrence Meyer) also is gratefully acknowledged. Additionally, the assistance provided by the entire staff at Zucrow Laboratories was critical to the success of this work, especially the technical skills and feedback from Rob McGuire.

The students and friends of the Purdue Compressor Lab with whom I have worked over the years have undoubtedly contributed in a significant way to this work. The CSTAR students—Jeanne Methel, Ruben Adkins-Rieck, and Matt Meier—have endured hundreds of hours of testing, conversations, and troubleshooting through the course of this project. Additionally, thank you for the friendship and help over the years to Amelia, Cameron, Doug, James, Nick, Trey, Ben, Raz, Nitya, Matt, Will, Andrew, Evan, Yu Ning, Yujun, Grant, Andy, Reid, and Natalie.

My mom and dad, my siblings, my grandparents, my in-laws, and Ruby have all been an invaluable support network and source of love and encouragement throughout my life. I love you all. Finally, I am thankful to my lovely wife, Hannah. Your support, encouragement, and love throughout this season—as girlfriend, fiancée, and wife—have carried me through the tough times.

# TABLE OF CONTENTS

LIST OF TABLES .....	8
LIST OF FIGURES .....	9
LIST OF SYMBOLS .....	14
LIST OF ABBREVIATIONS.....	15
ABSTRACT.....	17
1. INTRODUCTION.....	19
1.1 Motivation.....	19
1.2 Centrifugal Compressors .....	21
1.3 Impeller Aerodynamics.....	23
1.3.1 Jet/Wake Model.....	24
1.3.2 Tip Leakage Flow .....	27
1.3.3 Impeller Pressure Rise .....	28
1.4 Diffuser Aerodynamics.....	28
1.4.1 Vaned Diffuser Performance .....	29
1.4.2 Impeller-Diffuser Interaction.....	30
1.4.3 Diffuser Inlet Aerodynamics .....	31
1.4.4 Incidence Effects .....	33
1.4.5 Unsteady Effects.....	33
1.4.6 Diffuser Passage Aerodynamics .....	34
1.5 Measurement Techniques .....	35
1.5.1 Conventional Techniques .....	35
1.5.2 Non-Intrusive Techniques .....	37
1.6 Laser Doppler Velocimetry.....	39
1.6.1 LDV Theory.....	39
1.6.2 LDV Uncertainty and Statistics .....	43
1.6.3 Seeding for LDV.....	44
1.6.4 Applications on Centrifugal Compressors.....	46
1.7 Computational Fluid Dynamics .....	47
1.7.1 Turbulence Modeling.....	48

1.7.2	Stage Simplifications and Treatment of Unsteadiness .....	50
1.7.3	CFD Use in Design.....	52
1.8	Research Objective .....	52
2.	RESEARCH METHODOLOGY .....	54
2.1	CSTAR Facility Infrastructure.....	54
2.2	CSTAR Baseline Compressor Stage.....	56
2.2.1	Steady Flow Instrumentation.....	57
2.2.2	Tip Clearance Measurements .....	58
2.2.3	Modifications to Allow LDV.....	59
2.2.4	Baseline Performance Data.....	60
2.3	LDV System.....	63
2.3.1	Traverse and Seed Systems .....	65
2.3.2	LDV Post-Processing.....	67
2.3.3	Relevant System Parameters.....	75
2.4	Numerical Approach.....	77
2.4.1	Grid Independence Study .....	80
3.	LASER DOPPLER VELOCIMETRY RESULTS AND DISCUSSION.....	82
3.1	Overview of Obtained Data .....	82
3.2	Velocity Vector Field at Constant Span.....	85
3.2.1	Unsteady Vector Field at Constant Span.....	91
3.3	Impeller Jet and Wake Progression in the Diffuser Inlet Region .....	103
3.4	Development of Cross-Passage Flow Profiles.....	109
3.5	Unsteady Development of the Passage Vortex.....	120
3.6	Reynolds Stress Measurements.....	128
4.	COMPUTATIONAL RESULTS AND DISCUSSION .....	141
4.1	Impact of Turbulence Model on Flow Development.....	143
4.1.1	On the Computational Cost and Convergence Behavior.....	146
4.2	Effect of Other Modelling Decisions on Flow Development.....	147
4.2.1	Effect of Modelling Inclusions on Overall Performance Predictions.....	152
4.2.2	Modelling Recommendation for Steady-State Computations .....	158
4.3	Accuracy of the Frozen Rotor Approach in Resolving Unsteady Effects .....	160

4.4 Unsteady Results.....	165
5. COMPARISON BETWEEN NUMERICAL AND LDV RESULTS.....	179
5.1 Development of Flow Through the Vaneless Space.....	180
5.2 Propagation of Flow Through the Diffuser Passage.....	186
6. SUMMARY AND CONCLUSIONS.....	198
6.1 Observations Regarding the Research Objectives.....	198
6.2 Recommendations for Future Study.....	203
REFERENCES.....	204
APPENDIX A: MAXWELL'S EQUATIONS.....	215
APPENDIX B: ADDITIONAL REYNOLDS STRESS DATA.....	216
VITA.....	224
PUBLICATIONS.....	225

## LIST OF TABLES

Table 2.1: Mixture modeling process validation results.....	73
Table 2.2: LDV system parameters .....	77
Table 2.3: Optical transformation angles.....	77
Table 4.1: Computational cost summary for various turbulence models .....	146

## LIST OF FIGURES

Figure 1.1 : Centrifugal compressor .....	22
Figure 1.2 : Example compressor map .....	23
Figure 1.3: Jet/wake model (adapted from [12]) .....	25
Figure 1.4: Velocity deficit regions at impeller exit (in red) .....	26
Figure 1.5: Tip leakage flow .....	27
Figure 1.6: Diffuser station and region nomenclature .....	30
Figure 1.7: Fringe model.....	40
Figure 1.8: Measurement volume .....	42
Figure 2.1: CSTAR test facility .....	54
Figure 2.2 : CSTAR stage slice view .....	57
Figure 2.3: Instrumentation locations .....	58
Figure 2.4: Shroud comparison.....	60
Figure 2.5: Window frame assembly exploded view.....	61
Figure 2.6: Baseline and LDV performance map comparison .....	61
Figure 2.7: Baseline and LDV tip clearance comparison at design point.....	62
Figure 2.8: Diffuser throat (left) and exit (right) static pressure comparison at design point .....	63
Figure 2.9: Diffuser exit total pressure contour comparison at design point.....	63
Figure 2.10: Traverse system alignment tool.....	65
Figure 2.11: Particle size distribution and cut-off frequencies .....	67
Figure 2.12: Ensemble averaging procedure .....	68
Figure 2.13: Examples of noise in LDV results.....	70
Figure 2.14: Mixture modeling process .....	72
Figure 2.15: Noise removal example results.....	74
Figure 2.16 : Example results in Cartesian coordinate system .....	75
Figure 2.17: Measurement directions and coordinate system.....	76
Figure 2.18: Surface temperature profile through stage .....	80
Figure 2.19: Grid independence study results.....	81

Figure 3.1: LDV acquisition map for the standard points (A), refined points (B), and Reynolds stress points (C).....	83
Figure 3.2: Passage-to-passage variation in velocity magnitude at $R/R_2 = 1.0125$ , 50% span ....	84
Figure 3.3: Time-averaged streamwise velocity normalized by the impeller tip speed at 30% (A), 50% (B), 70% (C), and 95% (D) span .....	86
Figure 3.4: Time-averaged pitchwise velocity normalized by the impeller tip speed at 30% (A), 50% (B), 70% (C), and 95% (D) span .....	89
Figure 3.5: Time-averaged axial velocity at 30% (A), 50% (B), 70% (C), and 95% (D) span ....	90
Figure 3.6: Unsteady streamwise velocity contours at 30% span for a $t/t_{BP}$ of 0.00 (A), 0.25 (B), 0.50 (C, lower right), and 0.75 (D, lower left).....	92
Figure 3.7: Unsteady pitchwise velocity contours at 30% span for a $t/t_{BP}$ of 0.00 (A), 0.25 (B), 0.50 (C, lower right), and 0.75 (D, lower left).....	93
Figure 3.8: Unsteady axial velocity contours at 30% span for a $t/t_{BP}$ of 0.00 (A), 0.25 (B), 0.50 (C, lower right), and 0.75 (D, lower left).....	94
Figure 3.9: Unsteady streamwise velocity contours at 50% span for a $t/t_{BP}$ of 0.00 (A), 0.25 (B), 0.50 (C, lower right), and 0.75 (D, lower left).....	96
Figure 3.10: Unsteady pitchwise velocity contours at 50% span for a $t/t_{BP}$ of 0.00 (A), 0.25 (B), 0.50 (C, lower right), and 0.75 (D, lower left).....	97
Figure 3.11: Unsteady axial velocity contours at 50% span for a $t/t_{BP}$ of 0.00 (A), 0.25 (B), 0.50 (C, lower right), and 0.75 (D, lower left).....	98
Figure 3.12: Unsteady streamwise velocity contours at 95% span for a $t/t_{BP}$ of 0.00 (A), 0.25 (B), 0.50 (C, lower right), and 0.75 (D, lower left).....	100
Figure 3.13: Unsteady pitchwise velocity contours at 95% span for a $t/t_{BP}$ of 0.00 (A), 0.25 (B), 0.50 (C, lower right), and 0.75 (D, lower left).....	101
Figure 3.14: Unsteady axial velocity contours at 95% span for a $t/t_{BP}$ of 0.00 (A), 0.25 (B), 0.50 (C, lower right), and 0.75 (D, lower left).....	102
Figure 3.15: Point location for jet/wake analysis.....	103
Figure 3.16: Radial velocity distribution at a radius ratio of 1.0125 (Point 37).....	104
Figure 3.17: Radial velocity distribution at a radius ratio of 1.05 (Point 8).....	106
Figure 3.18: Radial velocity distribution at a radius ratio of 1.08 (Point 27).....	107
Figure 3.19: Radial velocity distribution within the semi-vaneless space (Point 116).....	108
Figure 3.20: Radial velocity distribution at the exit of the semi-vaneless space (or the entrance to the diffuser passage, Point 124).....	109
Figure 3.21: Cross passage planes geometric details.....	110

Figure 3.22: Unsteady velocity field at a radius ratio of 1.05.....	111
Figure 3.23: Unsteady velocity field at a radius ratio of 1.08.....	113
Figure 3.24: Unsteady velocity field at the USTM A plane (-5% passage progression).....	114
Figure 3.25: Unsteady velocity field at the throat (0% passage progression) .....	115
Figure 3.26: Unsteady velocity field at the DSTM B plane (10% downstream from the throat).....	117
Figure 3.27: Unsteady velocity field at the DSTM D plane (20% downstream from the throat).....	118
Figure 3.28: Unsteady velocity field at the DSTM G plane (40% downstream from the throat).....	119
Figure 3.29: Time-averaged absolute flow angle at 50% span.....	120
Figure 3.30: Deviation of each velocity component ( $U_i$ ) from the instantaneous planar mean value ( $\bar{U}$ ) during wake propagation.....	122
Figure 3.31: Deviation of each velocity component ( $U_i$ ) from the instantaneous planar mean value ( $\bar{U}$ ) during jet propagation .....	125
Figure 3.32: Unsteady nature of vortex development.....	127
Figure 3.33: Reynolds stress components at $R/R_2 = 1.05$ (Point 6).....	130
Figure 3.34: Reynolds stress components at $R/R_2 = 1.05$ (Point 10).....	131
Figure 3.35: Reynolds stress components at $R/R_2 = 1.08$ , adjacent to the vane LE (Point 26).....	132
Figure 3.36: Reynolds stress components at $R/R_2 = 1.08$ , at mid-passage (Point 29).....	133
Figure 3.37: Reynolds stress components within the semi-vaneless space, at mid-passage (Point 116).....	134
Figure 3.38: Reynolds stress components at the throat, near the suction surface (Point 30).....	135
Figure 3.39: Reynolds stress components at the throat at mid-passage (Point 34).....	136
Figure 3.40: Reynolds stress components at the throat, near the pressure surface (Point 32).....	137
Figure 3.41: Unsteady turbulence intensity upstream of the diffuser passage .....	139
Figure 3.42: Unsteady turbulence intensity within the passage.....	140
Figure 4.1: Diffuser exit total pressure contours measured experimentally (A) and as predicted by various turbulence models (B-I) .....	143
Figure 4.2: Total pressure contours at 15% span through the diffuser passage for each turbulence closure model.....	145
Figure 4.3: Diffuser exit total pressure with the SST turbulence model and various additional modelling features.....	148
Figure 4.4: Total pressure contours at 15% span with the SST turbulence model and various additional modelling features.....	148

Figure 4.5: Diffuser exit total pressure contours with the high-fidelity configuration .....	150
Figure 4.6: Total pressure contours at 15% span with the high-fidelity configuration .....	151
Figure 4.7: Overall performance predictions for the various modelling combinations for TPR (A) and isentropic efficiency (B).....	154
Figure 4.8: Diffuser exit total pressure contours for high-loading (left column) and near choke (right column) conditions for experimental data (A-B), SST (C-F), and BSL-EARSM (G-J) ..	157
Figure 4.9: Performance difference from experimental values .....	159
Figure 4.10: Frozen rotor variations in TPR (A) and Efficiency (B) with the high-fidelity configuration .....	161
Figure 4.11: Time-averaged diffuser exit total pressure contours experimentally (A), with the SST model (B-C), and with the BSL-EARSM model (D-E).....	162
Figure 4.12: Diffuser exit total pressure with the SST turbulence model for various instances in the blade-pass period for frozen rotor (left) and unsteady (right) simulations .....	163
Figure 4.13: Diffuser exit total pressure with the BSL-EARSM turbulence model for various instances in the blade-pass period for frozen rotor (left) and unsteady (right) simulations .....	164
Figure 4.14: Time-averaged static pressure progression through the diffuser passage .....	166
Figure 4.15: Time-averaged Mach number progression through the diffuser passage.....	168
Figure 4.16: Time-averaged total pressure progression through the diffuser passage .....	170
Figure 4.17: Static pressure variation through the diffuser passage .....	172
Figure 4.18: Total pressure variation through the diffuser passage.....	173
Figure 4.19: Unsteady total pressure field at the diffuser throat.....	175
Figure 4.20: Spanwise profiles of total pressure at the diffuser throat at various pitchwise positions and instances in the blade-pass period .....	177
Figure 5.1: Key geometric locations for CFD-LDV comparison .....	179
Figure 5.2: Radial velocity contour at a radius ratio of 1.0125 (Point 37) for Experimental data (top) and SST (middle) and BSL-EARSM (bottom) turbulence models.....	180
Figure 5.3: Axial velocity contour at a radius ratio of 1.0125 (Point 37) for Experimental data (top) and SST (middle) and BSL-EARSM (bottom) turbulence models .....	181
Figure 5.4: Unsteady turbulent kinetic energy, $k$ , at a radius ratio of 1.0125 (Point 43).....	182
Figure 5.5: Radial velocity contour at a radius ratio of 1.05 (Point 8) for Experimental data (top) and SST (middle) and BSL-EARSM (bottom) turbulence models .....	183
Figure 5.6: Unsteady turbulent kinetic energy, $k$ , at a radius ratio of 1.05 (Point 10).....	183
Figure 5.7: Inlet incidence field at a radius ratio of 1.08 (Point 27).....	184

Figure 5.8: Unsteady turbulent kinetic energy, $k$ , at a radius ratio of 1.08 (Point 26).....	185
Figure 5.9: Streamwise velocity at the Leading Edge plane.....	187
Figure 5.10: Axial velocity at the Leading Edge plane .....	187
Figure 5.11: Streamwise velocity at the throat .....	188
Figure 5.12: Axial velocity at the throat .....	189
Figure 5.13: Unsteady turbulent kinetic energy, $k$ , at the throat, pressure side (Point 32).....	190
Figure 5.14: Unsteady turbulent kinetic energy, $k$ , at the throat, mid-passage (Point 34).....	191
Figure 5.15: Unsteady turbulent kinetic energy, $k$ , at the throat, suction side (Point 30).....	192
Figure 5.16: Streamwise velocity 10% downstream from the throat (DSTM B) .....	193
Figure 5.17: Streamwise velocity 40% downstream from the throat (DSTM G).....	194
Figure 5.18: Time-averaged turbulent kinetic energy progression downstream of the throat....	196

## LIST OF SYMBOLS

<u>Roman</u>	<u>Description</u>	<u>Greek</u>	<u>Description</u>
$A$	Area	$\alpha$	Absolute flow angle
$B$	Blockage factor	$\alpha$	Beta Distribution parameter
$C_p$	Static pressure recovery coefficient	$\beta$	Relative flow angle
$d$	Diameter	$\beta$	Beta Distribution parameter
$d_f$	Focused beam diameter	$\Delta$	Difference
$f$	Focal length	$\delta_i$	Measurement volume dimension
$f$	Frequency	$\varepsilon$	Diffuser effectiveness
$f_c$	Cut-off frequency	$\eta$	Efficiency
$f_d$	Observed Doppler frequency	$\theta$	Angle
$f_s$	Applied shift frequency	$\lambda$	Wavelength
$i$	Incidence	$\mu$	Dynamic viscosity
$I$	Turbulence Intensity	$\rho$	Density
$k$	Turbulent kinetic energy	$\tau_0$	Characteristic time scale
K	Diffuser loss parameter	$\tau_{ij}$	Reynolds stress tensor
LDA <sub><math>i</math></sub>	Velocity measurement channel $i$	$\omega$	Angular velocity
$\dot{m}$	Mass-flow rate		
$N$	Rotational speed		
$N_f$	Number of fringes in measurement volume	<u>Subscripts</u>	<u>Description</u>
$P$	Pressure	$0$	Stagnation (total) quantity
$R$	Radius	$1$	Impeller inlet
$R_c$	Streamline curvature radius	$2$	Impeller exit
$Re_{ij}$	Reynolds stress tensor	$3$	Diffuser leading edge
Ro	Rossby number	$4$	Diffuser throat
$s$	Slip velocity proportion	$5$	Diffuser trailing edge
$S_{ij}$	Strain-rate tensor	$j$	Jet quantity
$t$	Time	$P$	Pitchwise (velocity)
$T$	Temperature	$R$	Radial (velocity)
$t_{BP}$	Blade-pass period	$S$	Streamwise (velocity)
$t_i$	Transit time measurement	$s$	Static Quantity
$U$	Velocity of the rotating frame (wheel speed)	$x,y,z$	Cartesian axes' directions
$u_i$	A particular velocity sample	$w$	Wake quantity
$U_i$	$i$ component of velocity vector	$\theta$	Tangential (velocity)
$U_2$	Impeller tip velocity	$\overline{(\ )}$	Mean quantity
$V$	Stationary frame velocity (absolute velocity)	$(\ )'$	Fluctuating component
$v_{\perp}$	Perpendicular Velocity		
$W$	Relative frame velocity		
$x_i$	Cartesian coordinate $i$		

## LIST OF ABBREVIATIONS

<i>ASME</i>	American Society of Mechanical Engineers
<i>BSA</i>	Burst Spectrum Analyzer
<i>CDF</i>	Cumulative Distribution Function
<i>CFD</i>	Computational Fluid Dynamics
<i>CSTAR</i>	Centrifugal Stage for Aerodynamics Research
<i>DEHS</i>	Di-Ethyl-Hexyl-Sebacate
<i>EARSM</i>	Explicit Algebraic Reynolds stress model
<i>FB</i>	Full Blade
<i>HPC</i>	High Pressure Compressor
<i>HX</i>	Heat Transfer
<i>L2F</i>	Laser-2-Focus velocimetry
<i>LDA</i>	Laser Doppler Anemometry
<i>LDV</i>	Laser Doppler Velocimetry
<i>LE</i>	Leading Edge (of a blade or vane)
<i>LSCC</i>	Low-Speed Centrifugal Compressor
<i>MP</i>	Mid-Passage
<i>NASA</i>	National Aeronautics and Space Administration
<i>OPR</i>	Once-Per-Revolution
<i>PDF</i>	Probability Density Function
<i>PIV</i>	Particle Image Velocimetry
<i>PS</i>	Pressure Side (of a blade or vane)
<i>RANS</i>	Reynolds Averaged Navier Stokes
<i>RS</i>	Reynolds Stress (turbulence model)

<i>RTD</i>	Resistance Temperature Detector
<i>SB</i>	Splitter Blade
<i>SS</i>	Suction Side (of a blade or vane)
<i>SST</i>	Shear-Stress Transport
<i>TE</i>	Trailing Edge (of a blade or vane)
<i>TPR</i>	Total Pressure Ratio

## ABSTRACT

Rising fuel costs and growing environmental concerns have forced gas turbine engine manufacturers to place high value on reducing fuel burn. This trend has pushed compressor technology into new design spaces that are not represented by historical experience. Specifically, centrifugal compressor diffusers are trending toward higher pressure recovery and smaller diameters. The internal fluid dynamics in these new flow regimes are not well understood and additional study is necessary. This work outlines detailed experimental and numerical observations of the flow field through a vaned diffuser for aeroengine applications.

The experimental data consist of extensive Laser Doppler Velocimetry measurements of the unsteady velocity field from the impeller trailing edge through the majority of the diffuser passage. These data were obtained non-intrusively and yielded all three components of the velocity vector field at approximately 2,000 geometric points. The correlation between fluctuations in the three velocity components were also observed at several key locations to determine the components of the local Reynolds stress tensor.

These data indicated a jet/wake profile at the impeller exit represented by a consistent velocity deficit region from hub to shroud adjacent to the suction surface of the passage. This region was more prevalent adjacent to the splitter blade. The unsteady fluctuations due to the propagation of the jet and wake through the diffuser passage persist to 40% downstream of the throat. A complex secondary flow field was also observed with large axial velocities and a passage-spanning vortex developing through the diffuser passage. The velocity data and total-pressure data indicated a region of flow separation developing along the pressure surface of the vane near the hub due to the unsteady propagation of the jet and wake flow through the diffuser. Although this region was stable in time, its development arose due to unsteady aspects of the flow. Finally, the strong interconnection between the jet and wake flow, unsteady fluctuations, secondary velocities, incidence, and flow separation was demonstrated.

Computationally, a “best-practice” methodology for the modelling of a centrifugal compressor was developed by a systematic analysis of various turbulence models and many modelling features. The SST and BSL-EARSM turbulence models with the inclusion of fillets, surface roughness, and

non-adiabatic walls was determined to yield the best representation of the detailed flow development through the diffuser in steady (mixing-plane) simulations. The accurate modelling of fillets was determined to significantly impact the prediction of flow separation with the SST turbulence closure model. Additionally, the frozen rotor approach was shown to not accurately approximate the influence of unsteady effects on the flow development.

Unsteady simulations were also compared to the detailed experimental data through the diffuser. The BSL-EARSM turbulence model best matched the experimentally observed flow field due to the SST model's prediction of flow separation in the shroud-pressure side corner of the passage. In general, lower levels of axial velocity were predicted numerically that resulted in less spanwise mixing between the endwall and freestream flows. Additionally, the turbulent kinetic energy levels in the computational results showed little streamwise variation through the vaneless and semi-vaneless space. The large variation observed experimentally indicated that the production and dissipation of turbulent kinetic energy through this region was not accurately predicted in the two turbulence models implemented for the unsteady simulations.

# 1. INTRODUCTION

## 1.1 Motivation

Growing concerns regarding environmental change and rising fuel costs have forced gas-turbine engine manufacturers to place unprecedented value on reducing fuel burn. One method of achieving this goal is to increase the propulsive efficiency by increasing the bypass ratio of the engine by either increasing the fan outer diameter or decreasing the engine core size. The fan outer diameter is limited by several factors. For large aircraft, the primary restrictions are the space available for current under-wing engine mounting schema, losses arising from increased tip speeds, and noise considerations. For smaller aircraft, the contribution of the engine nacelle to overall aircraft drag leads to a limit beyond which the additional nacelle drag offsets the gains in efficiency of a larger fan diameter.

The alternative is to reduce the engine core size. The limit that arises in terms of so-called “small-core engines” occurs due to practical manufacturing and operability constraints surrounding tip clearance and blade profile tolerances. Regarding tip clearance, manufacturing and assembly tolerances on the blades and casing do not scale proportionally with blade size. As such, the rear block of a typical axial-compressor series, where the blades are the shortest, has a higher-than-optimum tip-clearance-to-blade-height ratio. This creates an increase in the losses associated with endwall flows and leads to a deterioration of overall stage efficiency and a reduction in stall margin [1]. Identical performance decrements occur due to the operability need of maintaining positive clearance during speed transients, through which the clearance can change by 2% of the blade height [2]. This necessitates a higher-than-optimum steady-state clearance to maintain engine operability and safety. In terms of blade profile tolerances, the primary consequence of reducing engine core size and, consequently, blade height in an axial compressor arises due to the aerodynamic sensitivity of axial-compressor performance to blade shape. With manufacturing limits, the fidelity of a prescribed aerodynamic blade shape decreases with blade size. Reference [3] shows that state-of-the-art machine profile tolerance bands can allow a 6% variation in profile thickness and a  $\pm 1^\circ$  change in inlet blade angle on a blade with a one inch chord length. These large uncertainties can prove detrimental to overall compressor performance and produce a lower limit on standard axial-compressor core size. An alternative approach to reducing fuel

consumption in an aeroengine is to increase the thermal efficiency of the engine cycle. This is achieved by increasing the pressure ratio through the core compressor series. The density of the air delivered to the rear compressor stages increases which, again, necessitates smaller blades in the rear compressor stages. Therefore, this alternative approach to reducing fuel consumption, through the thermodynamic cycle rather than the bypass ratio, leads to the same issue.

Because of these additional losses that arise in the rear stages of axial compressors in small-core engines, an attractive option is to use a low specific-speed centrifugal compressor. The typical advantages of axial compressors—high flow capacity and efficiency—are weakened in the rear block and the benefits of a centrifugal compressor—higher pressure rise and lower sensitivity to geometric precision [2, 3]—make them a competitive alternative. The higher pressure rise obtainable through a single centrifugal stage allows the replacement of several rear axial stages with a single centrifugal stage. The overall engine part count, weight, and length can all be reduced, resulting in a system-level benefit compared to incorporating several axial stages. The lower sensitivity to geometric precision, both regarding aerodynamic profiles and tip clearance losses, can allow the efficiency of a centrifugal stage to equal or surpass that of the axial stages it would replace in this flow regime. Altogether, these factors present a centrifugal stage as an attractive alternative to axial stages in the rear block of modern jet engine compressor series.

It is not as straightforward as simply removing several axial stages and installing a centrifugal stage. The practical difficulty, and the reason additional research is necessary, is the atypical flow regime in which a centrifugal compressor must perform for this application. The High-Pressure Compressor (HPC) consists of the rear stages of a compressor series and is typically driven by a single shaft. The centrifugal compressor must, therefore, match the upstream axial compressor's rotational speed and mass-flow rate. This forces the centrifugal compressor to rotate at a speed which is slower than optimum for the required mass-flow capacity. Historically, centrifugal compressor design has relied upon scaling of previous design data and simple correlations [4, 5]. These methods are unreliable when extrapolation is required beyond existing experience and data. The application of centrifugal compressors to replace axial stages in an aeroengine HPC falls well outside traditional experience and requires significant experimental investment before the benefits can be fully realized. Detailed datasets, leveraged to better understand the internal flow physics,

calibrate computational models, and inform design correlations, are crucial to obtain higher propulsive efficiency and push centrifugal compressor technology into new design spaces.

## 1.2 Centrifugal Compressors

Radial-flow turbomachinery has a rich history since the first demonstration of a crude radial pump by Denis Papin in 1688 [6]. For propulsion applications, the first two turbojet engines, developed independently in pre-WWII England and Germany, both relied upon centrifugal compressors. This occurred due to the largely trial-and-error progress that had been made in centrifugal compressor technology and the relative infancy of axial compressor technology. Post-WWII demand for larger and longer-range aircraft shifted the focus to the axial compressor, which was more easily broken down into constituent parts to be analyzed separately. For example, an axial designer could run stationary cascade tests on a wide range of blade designs to choose the optimum configuration. For a centrifugal compressor designer, full-scale testing is often necessary to glean meaningful data as there is strong interaction between the components. This fact allowed the axial compressor to develop more quickly and to overtake the centrifugal compressor in terms of overall efficiency, becoming the dominant technology implemented in propulsive devices.

As analytic tools and experimental methods improved, the internal flow mechanisms of centrifugal compressors were greatly elucidated. Efficiency values rose at approximately  $2/3^{\text{rds}}$  of a point per year from the 1960s to the 1980s due to a more informed control of rotor blade loading [7]. More recently, the majority of applications that utilize centrifugal compressors are found in industrial applications: fluid compression and movement. Across all sectors, pumps account for an estimated 10% of global electricity consumption and even small efficiency increases can have significant effects [8]. In the aerospace sector, centrifugal turbomachinery is implemented in turboshaft and turboprop engines where the high pressure ratio obtained in a single centrifugal stage is leveraged to allow a compact and light engine.

A centrifugal compressor stage consists of a bladed, rotating impeller followed by a stationary radial diffuser which may be a simple radial passage (a vaneless diffuser) or contain guide vanes which act to more completely recover the kinetic energy present at the impeller exit. A cutaway diagram of an experimental compressor stage is presented in Figure 1.1. The inlet region of the impeller blading, known as the inducer, draws air into the stage by reducing the local static

pressure. The rotation of the impeller is used to impart work into the flow, resulting in a rise in both static pressure and kinetic energy. The diffuser then acts to recover the kinetic energy in the flow leaving the impeller into usable static pressure [5].

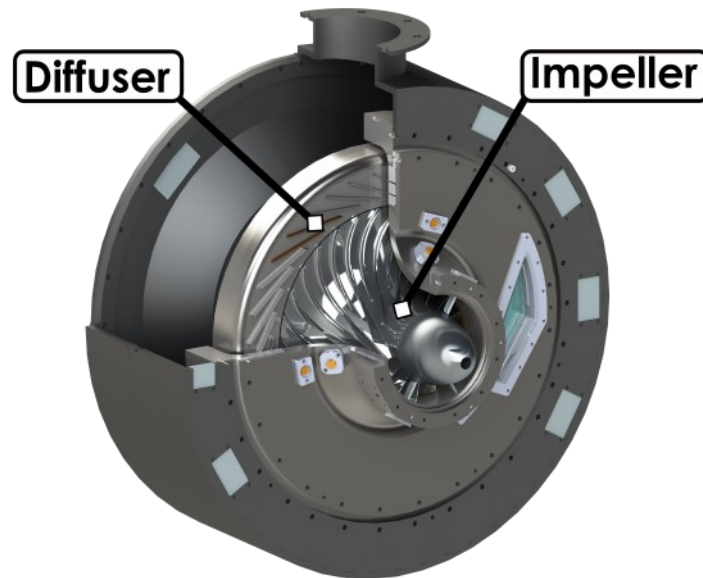


Figure 1.1 : Centrifugal compressor

General performance of a centrifugal compressor is typically summarized using a combination of rotational speed,  $N$ , total pressure ratio (TPR), mass-flow rate ( $\dot{m}$ ), and efficiency ( $\eta$ ). The TPR of a machine depends primarily (although not exclusively) on the outlet diameter of the stage and the rotational speed while the mass-flow rate depends primarily on the inlet area and rotational speed [2]. Performance data for a given compressor stage are typically presented on “maps.” Multiple operating lines of mass-flow and either TPR or efficiency are plotted for constant rotational speeds to show the stable operating range of a certain design, as illustrated in the example given in Figure 1.2. The operating range of a centrifugal compressor is limited by two fluid dynamic phenomena. Toward higher mass-flow rates, the operation is limited by the choking of the flow through the stage. At this point, a further decrease in the back pressure on the stage results in the TPR and efficiency decreasing sharply with no appreciable increase in mass-flow rate. Toward lower mass-flow rates, the operation is limiting by stall or surge. Steady stall occurs due to either boundary layer separation or a saddle point in the flow field. This separation can arise from highly loaded blade channels (passage separation), excessive leading edge incidence (leading edge separation), or other, less common causes [5]. Regardless of the cause, a maximum

pressure ratio is obtained after which a further reduction in mass-flow rate produces a sudden change in the compressor flow pattern which can manifest itself in one of three distinct patterns. Progressive stall is characterized by a manageable and slow roll-off in TPR and efficiency (see Figure 1.2, mark A). Abrupt stall is characterized by a sudden decrease in both TPR and mass-flow (see Figure 1.2, mark B). These stall behaviors occur due to rotating stall cells redistributing mass-flow into annular regions of high and low mass-flux [2]. The aerodynamics surrounding centrifugal compressor stall are extraordinarily complex and a more detailed description can be found in [9]. While the terms surge and stall are often used interchangeably, surge refers to a *system wide* oscillation in mass-flow as the compressor progresses in and out of a stalled state (see Figure 1.2, mark C). In extreme situations, surge can involve complete reversal of flow through the compressor [2, 5, 9]. Both abrupt stall and surge can result in catastrophic engine failure if they occur in a full engine and must be avoided.

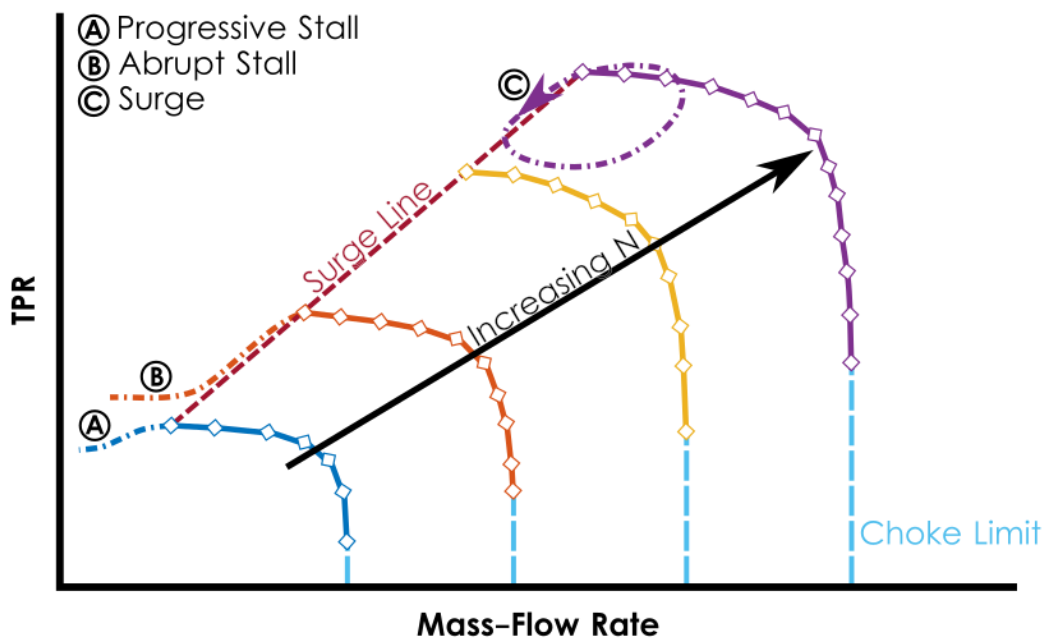


Figure 1.2 : Example compressor map

### 1.3 Impeller Aerodynamics

The flow through the impeller of a centrifugal compressor develops due to the complex interaction of Coriolis forces, curvature effects, boundary layer growth, regions of flow separation, and tip clearance effects [10]. The prediction of flow development through the impeller is critical for

three reasons: it determines the amount of work that is done on the flow, it sets up the flow that the diffuser must be able to handle effectively, and it contributes its own losses and inefficiencies [11]. While impeller geometries can vary greatly, those used in aerospace applications are typically highly loaded, unshrouded (a tip clearance gap exists between the blades and the casing), with axial inlet flow, and backswept trailing edges. Blades that begin partway through the impeller meridional passage, known as splitters, are often used to minimize blockage at the inducer while maximizing flow guidance at the outlet.

### 1.3.1 Jet/Wake Model

The typical assumption of the exit flow from impellers is that of the jet/wake model. Hypothesized by Dean and Senoo in 1960 [12] and supported by circumstantial evidence from flow visualization in water [13] and simplified component studies [11, 14], this behavior was first directly measured by Eckardt [15, 16]. The model first proposed is depicted schematically in Figure 1.3. Although simplified, this was the first attempt to account for the non-uniformity of the impeller exit flow in predicting compressor performance. The assumption is that the impeller exit flow is split into two distinct regions, known as the jet and the wake, which are assumed to have identical relative flow angles ( $\beta$ ) and have a constant, although distinct, relative frame velocity across each region. The jet lies adjacent to the pressure side of the impeller blade and consists of high momentum (in the relative frame) flow while the wake lies adjacent to the suction side of the impeller blade and consists of low-momentum flow. These terms describe *relative* frame quantities. In the *absolute* frame the “jet” actually has lower momentum than the “wake.” This is depicted by the velocity triangle in Figure 1.3, where subscripts  $w$  and  $j$  refer to wake and jet flow quantities, respectively, and  $U_2$ ,  $V$ , and  $W$  refer to the tip speed of the impeller, stationary frame velocities, and relative frame velocities, respectively. Although this model was a significant step toward improved understanding and modeling of centrifugal compressor flow, it did not attempt to describe the source of the jet/wake profile nor is it completely accurate. The first experimental measurement of the jet/wake’s existence and origin was obtained using Laser-2-Focus Velocimetry (L2F) by Eckardt in 1975 [15, 16]. These measurements showed the existence of a region of low relative velocity at the exit of the impeller focused near the suction surface of the impeller passage. The primary difference between these results and the original theory was that the wake region was focused near the shroud, rather than across the entire passage. Jet/wake behavior was determined

to arise from flow separation of the suction surface boundary layer adjacent to the shroud due to effects of streamline curvature and system rotation.

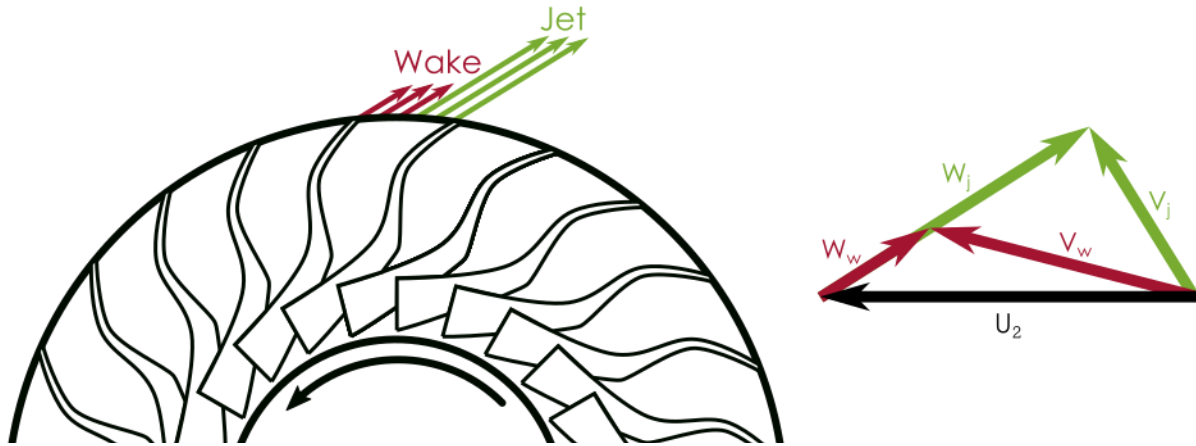


Figure 1.3: Jet/wake model (adapted from [12])

Later studies on a more modern impeller design by Krain [10] showed conflicting results. Krain's results showed a velocity deficit region near the shroud spread across much of the passage, not focused along the suction side of the blade. In fact, a wide range of velocity profiles have been experimentally measured including the distinct jet/wake in the shroud-suction side corner [15–21], a linear cross-passage gradient [22, 23], and a nearly uniform profile with a slight deficit near the shroud [10, 24, 25]. Accurately predicting the nature of the impeller exit flow remains an open area of research, although some insight and approximate guidelines exist.

Boundary layers begin growing along each solid surface at the inducer. Initially, the core flow tends to follow the contour of the blade quite well [5] before Coriolis forces, streamline curvature, and tip clearance effects cause deviations from the ideal potential flow solution. Coriolis effects occur due to the system rotation, influencing the boundary layer development and separation on the hub and blade surfaces (and the shroud surface for a shrouded impeller). Additional acceleration occurs, which has the same effect as an external pressure gradient [26, p. 651]. Along the suction (trailing) surface of the blade, this results in the transport of momentum into the boundary layer [11] and suppression of the turbulence level therein [2, 27]. Compared to the boundary layer along the pressure (leading) surface of the blade, the result is a thicker boundary layer that is more prone to separate. The streamline curvature effect on the flow development is

analogous to flow through a curved pipe. Low momentum flow migrates toward the convex surface [28] (referenced in [29]) due to the centrifugal force acting on flow particles [26, p. 589, 29] and the turbulence levels are suppressed. These factors combine to form a low momentum and low turbulence intensity boundary layer along the convex surface which is more likely to remain laminar [30] and, consequently, more prone to separate. This holds through the impeller and causes the shroud, which is convex, to be more susceptible to boundary layer separation than the hub [2, 5].

The general conclusion is that the rotation (Coriolis) and curvature effects interact with the aerodynamic blade loading to determine the flow development and profile at the exit [2, 10, 31]. A rough prediction can be gleaned using the Rossby number,  $Ro$ , which gives the ratio of inertial to Coriolis forces acting on the flow and is defined as:

$$Ro = \frac{W}{\omega R_c}. \quad (1)$$

$W$  is the relative velocity magnitude,  $\omega$  is the angular velocity of the impeller, and  $R_c$  is the local streamline curvature in the relative frame. A large Rossby number indicates that the curvature effects dominate over the Coriolis effects of system rotation. As such, for an impeller with a large Rossby number, the separated region would be focused more on the curved shroud and less shifted toward the suction surface. Although a thorough analysis of existing data has not been carried out, it seems logical that the distinct jet/wake in the shroud-suction side corner would develop for impellers with small Rossby numbers (less than one), a more linear cross-passage gradient for impellers with Rossby numbers around unity, and full-passage shroud deficits for impellers with large Rossby numbers. A cartoon of these possibilities is depicted in Figure 1.4, where the relative velocity deficit region is noted in red for different relative Rossby numbers.

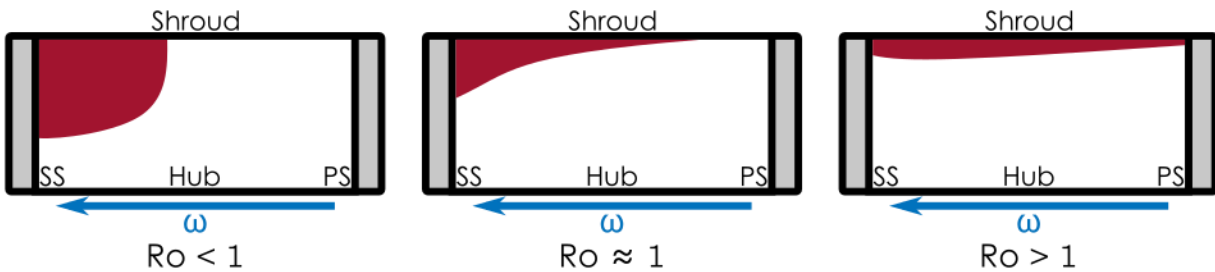


Figure 1.4: Velocity deficit regions at impeller exit (in red)

### 1.3.2 Tip Leakage Flow

Impellers can be manufactured with an integral shroud to completely enclose the rotating passage. However, in most aeroengine applications this is not possible due to manufacturing limitations and stress considerations. In unshrouded impellers, the presence of tip leakage flow acts as a further complication to the secondary and primary flow development through the impeller. The necessary gap between the rotating impeller blades and the stationary shroud allows flow to pass over the tips of the blades between adjacent passages. This flow tends to “roll-up” over the tip of the blade, driven from pressure side to suction side by the pressure difference, as illustrated in Figure 1.5. Historically, tip leakage flow has been treated only in terms of its overall contribution to loss through the impeller and the concomitant reduction in stage efficiency [2]. Senoo and Ishida [32], building upon [3], predicted roughly a 1% loss in efficiency per 4% increase in the tip-clearance-to-blade-height-ratio. Despite the relatively narrow gap, as much as 12% of the total mass-flow through the machine leaks through the clearance gap [33]. This leakage impacts the overall flow development through the impeller passage. The leakage flow, with lower meridional momentum than the primary flow, adds to the wake development in the shroud/suction side corner [15, 22] and follows a cross-passage trajectory from suction surface toward the adjacent pressure surface [34]. Additional flow is entrained into the tip leakage vortex as it traverses the passage until it impacts the adjacent blade. At this point the flow can either pass over that blade, continuing on a cross-passage trajectory in the adjacent passage, or form a low momentum region along the pressure surface of the blade as depicted in Figure 1.5 [22, 35, 36]. The blockage induced by the tip flow also acts to accelerate the primary flow in order to maintain the mass-flow rate through the machine [36].

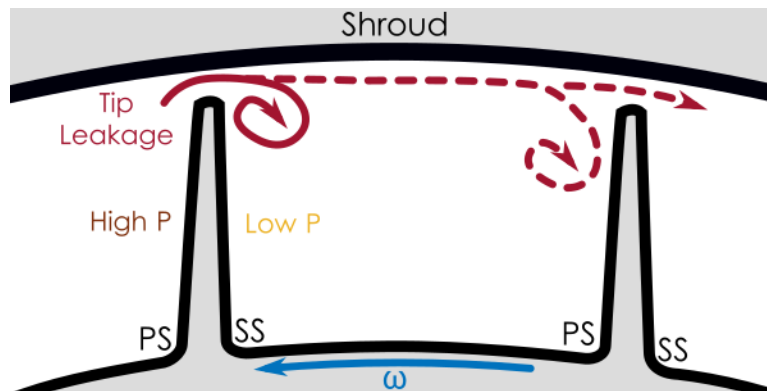


Figure 1.5: Tip leakage flow

### 1.3.3 Impeller Pressure Rise

Despite the significant secondary flows occurring within the passage, impeller efficiencies greater than 90% are often obtained [2, 5, 10]. This is achievable due to the dual means by which an impeller imparts work to the flow. The first is identical to the rotor of an axial compressor, occurring due to diffusion in the relative frame as the relative flow velocity magnitude is exchanged for static pressure rise [37, 38]. The second is due to the centrifugal effect. As the flow is brought to a larger radius the absolute kinetic energy of the flow is increased by the rotation of the reference frame. This kinetic energy must then be diffused and recovered into static pressure by the diffuser. One of the main benefits of a centrifugal compressor is that this second means of pressure rise through the impeller occurs “for free,” in an aerodynamic sense. It depends only upon the impeller blade speeds at inlet and outlet and is unrelated to the fluid mechanics of the machine. Contrarily, the relative frame diffusion is susceptible to aerodynamic losses and irreversibilities that occur due to the processes mentioned previously [2, 5, 37]. The centrifugal effect can be responsible for up to 50% of the work input by the impeller [2, 5, 33] allowing extremely efficient impellers to be designed. However, this shifts the aerodynamic difficulties to the diffuser.

### 1.4 Diffuser Aerodynamics

The role of the diffuser is to convert the high kinetic energy leaving the impeller into static pressure as completely and effectively as possible. This process is complicated by the nature of the impeller exit flow, which is typically inclined at large angles from radial, highly unsteady, and non-uniform. There are two types of diffusers. Vaneless diffusers consist of a simple annular passage surrounding the impeller. Vaned diffusers include aerodynamic blades, or vanes, which act to guide the flow as it leaves the impeller. These are more common in aeroengine applications due to their ability to obtain a higher pressure ratio while maintaining low frontal area [2, 5, 37, 39]. Static pressure rise is achieved through two avenues stemming from the conservation of mass and the conservation of angular momentum. First, an increase in the flow area necessitates a reduction in the mean flow velocity by the continuity equation. Second, increasing the mean flow path radius,  $R$ , reduces the tangential velocity,  $V_\theta$ , by the conservation of angular momentum:

$$R V_{\theta} = \text{Constant} . \quad (2)$$

Vaned diffusers act by imposing an aerodynamic torque on the flow to actively reduce the angular momentum of the flow and recover additional pressure [37, 39, 40]. The aerodynamics of vaneless diffusers will not be covered in depth as vaned diffusers are the topic of this study. Performance of vaneless diffusers is primarily driven by the passage height and the radius ratio utilized. Most have a slight pinch, or reduction in flow passage height, immediately downstream of the impeller tip which provides a radial acceleration to the flow necessary for stability. The conservation of mass and angular momentum equations can be solved, assuming incompressibility, to yield a constant-flow-angle, logarithmic-spiral flow-trajectory through the vaneless diffuser. Density variations with pressure and temperature cause the flow angle to increase with radius forcing the flow to follow a tighter spiral through the diffuser [5]. The dominant loss contributor through a vaneless diffuser is viscous stress due to the long flow path taken by the fluid [2]. Historically, designs have relied upon a modeled bulk friction factor to account for all loss through the vaneless diffuser; however, more advanced designs account for the non-uniformity of the impeller exit flow [12] and sudden expansion of the impeller discharge [41]. Even more thorough analyses utilize an interactive core-boundary layer computation method as described in [42].

#### 1.4.1 Vaned Diffuser Performance

Vaned diffuser performance is less understood due to the added complications of vanes and the wide variety of vane geometries and possible design choices. Because no work is done through the diffuser, “efficiency” is an ill-defined term to describe diffuser performance. Typically, four alternative rating parameters are used to evaluate diffuser performance. The static-pressure-recovery coefficient,  $C_p$ , is used to evaluate the obtained static pressure rise between two stations normalized by the available dynamic head [2]. The diffuser effectiveness,  $\varepsilon$ , is defined as the ratio of the achieved  $C_p$  through the diffuser to the ideal  $C_p$  that would be obtained for isentropic flow through the same area ratio [43]. The loss parameter,  $K$ , is the total pressure loss through the diffuser normalized by the available dynamic head at the inlet [5]. Finally, the blockage factor,  $B$ , is defined as one minus the ratio of the effective area of the flow to the geometric area of the passage.  $A_{\text{effective}}$  is defined as the area that would pass an identical mass-flow rate with constant velocity and density equal to the average quantities for the core flow (similar to a displacement

thickness but applied in two dimensions ) [40]. The formulas for these performance parameters are given by:

$$C_p = \frac{P_5 - P_2}{P_{02} - P_2}, \quad (3)$$

$$\varepsilon = \frac{C_p}{C_{p,ideal}}, \quad (4)$$

$$K = \frac{P_{05} - P_{02}}{P_{02} - P_2}, \quad (5)$$

$$\text{and } B = 1 - \frac{A_{\text{effective}}}{A_{\text{geometric}}}. \quad (6)$$

Equations (3)–(6) can be defined between any two stations. Of particular note are the parameters defined for the whole diffuser (i.e. between stations three and five, as written in the Equations) and defined from the impeller exit to the diffuser throat (see Figure 1.6 for station numbering). The majority of designs rely upon correlations relating these performance metrics to non-dimensional geometric design parameters. These correlations are limited in their applicability due to the obfuscating effect of the diffuser-impeller interaction and the large potential design space for diffuser vane shapes.

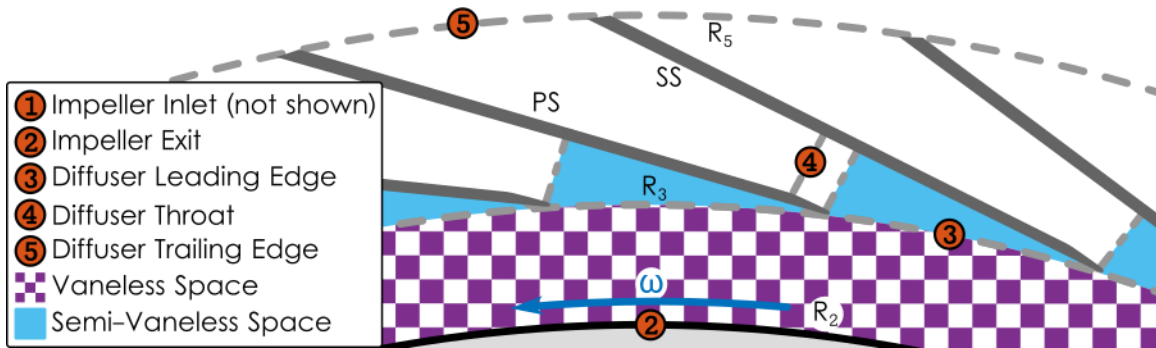


Figure 1.6: Diffuser station and region nomenclature

### 1.4.2 Impeller-Diffuser Interaction

The performance of the impeller and the diffuser are interconnected due to the extension of the diffuser potential field into the impeller. In the rotating frame of reference, the impeller blade tips pass through an unsteady potential field causing a shift in the flow distribution and blade loading

[44, 45]. This coupling can cause significant differences in the impeller flow field to occur as far upstream as the inducer [37]. While the potential field of the diffuser affects the impeller, the converse does not significantly occur. The biggest impact of the impeller on the diffuser performance occurs due to the non-uniformity of the impeller exit flow, discussed previously [11].

### 1.4.3 Diffuser Inlet Aerodynamics

The inlet region to the diffuser consists of the area between the diffuser throat (station 4) and the impeller exit (which is sometimes referred to as the diffuser inlet, station 2) and is divided into two separate sectors: the vaneless space and semi-vaneless space (purple-hatched and teal in Figure 1.6, respectively). The vaneless space is the annular region between the trailing edge of the impeller blades (at radius  $R_2$ ) and the leading edge of the diffuser vanes (at radius  $R_3$ ). The semi-vaneless space consists of the region where the flow is guided by the suction side of a vane but has not yet passed the pressure side leading edge of the adjacent vane. Together these sectors form the inlet region of the diffuser and yield the three most important parameters defining the diffuser performance. Perhaps the most critical is the value of the blockage computed at the diffuser throat—the point of minimum channel cross sectional area. The overall  $C_p$  is closely correlated with the throat blockage, as is the choking mass-flow rate of the machine. Excessive growth of throat blockage due to boundary layer growth and separation bubbles often limits the efficiency and range of an entire machine [2, 31, 37, 40, 46, 47]. The static pressure recovery from the impeller exit to the diffuser throat,  $C_{p,24}$ , is also critical in that it impacts both the blockage at the throat and the stability limit of the stage. Correlations have been developed between the diffusion upstream of the throat (as measured by  $C_{p,24}$ , a design choice) and the throat blockage to predict diffuser performance [5]. Intuitively, the blockage at the throat increases with the diffusion achieved up to the throat. Excessive diffusion upstream of the throat results in excessive blockage at the throat and a reduction in the operating range of the machine [2]. Several studies have concluded that the primary cause of stall in a vaned diffuser is the breakdown of flow in the semi-vaneless space [40, 48–50] typically caused by either excessive diffusion upstream of the throat or off-design incidence. Incidence,  $i$ , is the angle between the flow direction and the vane set angle, the third important design parameter. Diffuser vanes are typically designed around a single, time-averaged optimum value of  $i$  depending upon the vane shape, radial extent of the vaneless space, and the impeller exit flow asymmetry [51]. Proper incidence is key in obtaining a well-matched

impeller-diffuser pair, ensuring a wide operating range, and achieving high stage efficiency [52]. The aerodynamic root of this importance is the large losses and drastic increase in blockage that occurs due to flow separation around the vane leading edge at high positive or negative incidences [24]. Further specifics of incidence effects are discussed in Section 1.4.4.

The vaneless space is a necessary inclusion to reduce the diffuser-impeller interactions, provide diffusion upstream of the vane leading edges, partially dissipate the jet/wake non-uniformities, and reduce the aeromechanic forcing of the diffuser vanes on the impeller blade trailing edges [31, 37, 40]. Compared to the vaned portion, the vaneless space offers efficient, albeit slow, diffusion of the flow. The radial extent of the vaneless space can vary greatly, from 103% to 130% of the impeller tip radius. The optimum radial gap typically falls between 105% and 115%, although results vary [47, 50]. Too large a gap results in excessive boundary layer growth upstream of the throat and flow recirculation back into the impeller [2, 47]. Too small a gap causes performance to deteriorate due to the non-uniform flow impacting the leading edge of the diffuser vane and potential aeromechanics issues [5, 37].

The semi-vaneless space flow is dominated by unsteady effects and viscous boundary layer growth along the hub, shroud, and suction surface of the vane. Limited diffusion is achieved along the front portion of the suction surface due to the non-uniform pattern of the impeller exit flow [31, 51]. Together, the vaneless and semi-vaneless space are the most critical factors in the overall diffuser performance. In one low-speed study, overall stage efficiency was measured at 86%. The entire impeller was determined to be responsible for 4% of the overall reduction in efficiency while 9% was attributed to only the inlet region of the diffuser [53].

The high loss through this region arises from several contributing factors. Surface friction losses are large as boundary layers on the hub and shroud grow rapidly in the strong adverse pressure gradient [37, 51]. Simultaneously, shear flow in the semi-vaneless space from suction side to pressure side gets “rolled up” by the pressure side leading edge to form a large passage vortex [20, 21, 54]. The final contributor to losses in the semi-vaneless space is the vane incidence.

#### **1.4.4 Incidence Effects**

As mentioned, improper incidence on the vane causes a major deterioration of overall stage performance including reducing the diffuser effectiveness and static pressure recovery [55]. Experimental and numerical investigations into the importance of the incidence angle have been published in many places. The overall performance of the stage has been observed to shift by 5% [56] and 8% [55] with small changes in vane setting angle and, consequently, incidence angle. The difficulty in properly designing for incidence arises due to the complex nature of the impeller discharge flow and the development of that flow through the vaneless space. The reduced radial velocity component in the boundary layer along the hub and shroud results in hub-to-shroud gradients in incidence as large as  $20^\circ$  in the time-averaged flow field [41]. In the unsteady sense, flow angle pulsations as high as  $17^\circ$  (at one geometric point) were observed by Krain as far downstream as the diffuser throat [19]. These incidence swings can form large passage vortices and induce large blockages in the passage [18, 20, 54, 57]. The unsteady change in incidence that occurs due to the difference in absolute flow angle between the jet and the wake can also cause a dynamic boundary layer separation alternating on each side of the vane immediately downstream of the leading edge [24]. Finally, the non-uniform incidence shifts the loading on the leading edge of the vane which can, in some instances, prove advantageous [1, 58].

#### **1.4.5 Unsteady Effects**

Many conflicting conclusions have been proposed regarding the relative importance of unsteady effects on diffuser aerodynamic performance. Early studies on simplified models of compressor flow [59, 60] and on a low-speed rig [44] concluded that the jet and wake mixed out quickly and had little effect on overall performance. Today, as designs are pushed to higher efficiencies and pressure ratios, this conclusion may no longer be valid. More recent experimental and numerical studies have concluded that the unsteady effects have a small effect on overall stage performance and a large effect on the detailed flow structure through the diffuser. Peeters and Sleiman [61] showed significantly more diffusion occurring through the diffuser passage in an unsteady (as compared to a steady) simulation. Robinson et al. [62] numerically showed an increase in efficiency with a smaller radial gap that was only detected in unsteady simulations. Similar conclusions were reached in [1, 18, 63], showing different flow structures observed in unsteady

simulations that were missed by steady simulations and discussing the design implications. Experimentally, Justen et al. [64] showed that the unsteadiness of the impeller discharge flow did not decay through the diffuser and influenced the time-dependent pressure rise through the passage. Intuitively, unsteady effects are more critical at lower radial gaps where the jet and wake have had less time to agglomerate. A possible reason for the relatively good agreement between steady simulations and experimental data—suggesting that unsteady effects are unimportant—was given by Bourgeois et al. [65]. They suggested that the positive effect of averaging the unsteady flow at the impeller-diffuser interface counteracts the negative effect of computational techniques being too diffusive and overpredicting boundary layer thickness. More details on numerical techniques will be discussed in Section 1.7. Based on this recent evidence, it appears that unsteady effects may be critical in pushing centrifugal compressor design to higher efficiencies and meeting more aggressive performance demands.

#### **1.4.6 Diffuser Passage Aerodynamics**

Downstream of the diffuser throat, the flow structure is primarily driven by the area progression of the passage. The presence of the vanes acts to isolate individual passages and limit the influence of adjacent passages. Although the flow is still unsteady and contains complex secondary flows and regions of flow separation, it is more straightforward than the flow in the inlet region [2, 31]. Precise vane contouring has, historically, been determined to have only secondary importance concerning overall performance which has been observed to be primarily driven by the diffuser throat area and the area ratio of the passage [31]. The large area ratios through the diffuser often result in regions of flow separation developing on the vane surfaces. The flow typically reattaches and, along with the low aspect ratio (diffuser height divided by the vane chord length), this means that the flow turning achieved through the passage does not deteriorate. Therefore, unlike an axial compressor, performance does not decline catastrophically despite the presence of potentially large regions of flow separation [1, 2]. Boundary layer growth continues to contribute to the overall skin friction losses through the diffuser along the hub, shroud, and vane surfaces until there is no distinct core and boundary layer regions (similar to fully developed pipe flow). The final contributor to the overall loss is a potential dump loss at the trailing edge of thick vanes. This occurs due to irreversibilities that arise as the flow from adjacent passages fills the area behind the vanes. Although it is typically concluded that the majority of loss in the diffuser arises through the inlet

region, recent studies [66] have demonstrated the possibility of effecting efficiency gains through a carefully designed area progression through the vane passage.

## **1.5 Measurement Techniques**

The rapid progress of gas turbine engine technology over the past several decades has occurred due to a tandem investment in modeling and experimental development. Experimental studies were relied upon almost exclusively in early design efforts as the complexities of the flow fields inherent to centrifugal compressors were far beyond contemporary computational resources. Tests were conducted with the dual purpose of gaining insight on the flow physics and iterating designs toward higher efficiency, higher pressure ratios, and greater reliability. Modern advances in computing technology have greatly increased the reliance upon numerical methods in design; however, experimental efforts are crucial for validating and improving models—especially in flow regimes where numerical models are known to fall short—and ensuring design goals are met in actuality. American Society of Mechanical Engineers (ASME) and other organizations have put together standards and guides for proper test facility procedures [67–70].

### **1.5.1 Conventional Techniques**

The majority of data are obtained through what are known as conventional techniques. There is no firm definition, but techniques termed “conventional” include low-tech methods of measuring thermodynamic properties, typically by the physical insertion of a probe into the flow. Steady (time-averaged) pressure and temperature measurements are the most common, while more advanced techniques yield time-resolved pressure or flow velocity results.

Steady measurements of static pressure are predominantly obtained through wall “taps.” This consists of a hole perpendicular to the boundary of a flow path that is connected to a pressure transducer through closed tubing. Nearly every experiment uses static taps to observe pressure gradients along solid surfaces. Considerable errors and invalid conclusions can result if a tap is placed in a region of strong fluctuations [71] or if the tap itself is not formed correctly [72]. Total pressure measurements are obtained by inserting a tube surrounded by a cylindrical Kiel into the flow and orienting it opposite the predicted flow direction. Also known as a shrouded Pitot tube, these are relatively insensitive to incoming flow angle, a necessity for highly skewed

turbomachinery flows. Multiple taps can be arranged with different orientations in a single “multi-hole” probe to deduce flow angle from measured pressure differences between the different orientations [71]. The static temperature of a flow is not readily measured due to the unavoidable recovery of kinetic energy into thermal energy as flow is brought to rest on the surface of any stationary probe. Total temperature is measured using either a thermocouple or Resistance Temperature Detector (RTD) embedded in a vented Kiel. RTDs have the advantage of a simpler calibration and greater accuracy, however, are generally larger, more expensive, and less adaptable at high temperatures than thermocouples. Primarily due to the size advantage, thermocouples are most often used in turbomachinery applications. In practice, the indicated temperature does not perfectly correspond to the actual stagnation temperature of the flow due to the non-adiabatic and incomplete process of decelerating the flow at the probe head. Probes must be calibrated to determine the recovery factor for a range of Mach and Reynolds numbers to ensure accurate determination of the true stagnation temperature of the flow [71, 73].

The most common fast-response measurement techniques are hot-wire anemometry and semiconductor unsteady pressure transducers. Hot-wire anemometry measures the local flow velocity in a certain direction by maintaining a thin-wire sensor at a constant temperature. A feedback loop controls the voltage applied to the sensor to balance the convective heat transfer between the sensor and the flow. The heat transfer is proportional to the local velocity and, with proper calibration, the applied voltage can be monitored to yield the flow velocity. Multiple wires can be used to yield additional components of the velocity vector field. Hot-wire sensors require extensive calibration to account for the wide variety of Mach numbers, Reynolds numbers, and turbulence intensities which all can vary significantly through typical turbomachinery flow fields. Additionally, the small diameter sensor wire with low thermal inertia, required for a high-frequency response, leads to exceedingly fragile probes which have been known to break in the hostile, unsteady flow environment within centrifugal compressors [71, 74]. Semiconductor pressure transducers contain a miniature Wheatstone bridge formed directly on a silicon diaphragm. Pressure forces flex the diaphragm and elongate two of the resistor elements, causing a predictable change in overall sensor resistance related to the magnitude of the applied pressure. This allows extremely small sensors with high-frequency response to be manufactured [71]. They may be installed either flush with solid surfaces or in Kiel rakes in the same manner as standard pressure taps.

Conventional techniques have several significant disadvantages in turbomachinery applications. Measurements embedded in walls are influenced by boundary layers and can also lead to erroneous conclusions when unexpected gradients in properties exist between the core flow and the wall. With conventional techniques, any observation of the flow field away from walls is necessarily intrusive. Centrifugal compressors are generally characterized by small hydraulic diameters and high levels of unsteadiness. Blockage induced by intrusive probes is typically on the same order as the area of the flow passage (especially at the diffuser throat, a key location of interest for determining compressor performance) and forces one to question the validity of such measurements [71, 75]. In some cases, the reduction in flow area due to intrusive probes has led to performance instabilities during testing [58]. These factors limit the ability of conventional techniques to yield a deeper understanding of the internal flow physics that govern centrifugal compressor performance and necessitate advances in alternative, non-intrusive, techniques. Eckardt describes the necessity of non-intrusive studies for turbomachinery development as summarized below:

- 1) The greatest advancements in turbomachinery performance may be expected by a design procedure which is largely determined by a detailed physical understanding of the internal flow phenomena at real operating conditions
- 2) Dynamic, non-intrusive measuring techniques with high-frequency resolution, reliable design, and high measurement sensitivities have to be applied for adequate understanding of the complex flow field in high-speed turbomachinery
- 3) Conventional, time averaging techniques are unsuitable to fulfill these special demands
- 4) Accomplished progress in the field of non-intrusive measuring techniques will accelerate the development of improved computational models and push the performance of advanced turbomachinery further toward its ultimate gains [71].

### **1.5.2 Non-Intrusive Techniques**

Non-intrusive techniques rely on optical, electrical, chemical, or acoustic phenomena to observe thermodynamic or physical properties without physical insertion of a probe into the flow field. No measurement technique is entirely non-intrusive [76]. The term “non-intrusive” should truly be “minimally-intrusive” as there is no physical intrusion of a probe into the flow field. The most widely utilized approaches include optical and electrical techniques. For most optical techniques, the focus of this study, microscopic seed particles are introduced into the flow upstream of the test

section which are assumed to follow the local flow velocity. Methods have been developed to observe hot-running tip clearances [77] and two-dimensional temperatures [78], but the most important developments have been in non-intrusive velocity measurements, of which three key techniques exist: PIV, L2F, and LDV.

Particle Image Velocimetry (PIV) involves high-frequency imaging of laser pulses passed through the flow. Seed particles are added to the flow, illuminated by the pulses, and correlations are used to pair particles in subsequent images. The velocity is deduced from the known time between images and the distance moved by each particle yielding a planar “picture” of the two-dimensional velocity field. More advanced techniques can yield all three components of the velocity vector or even velocity data over a three-dimensional region [79]. Recent advances in pulsed laser and high-speed camera technology have allowed PIV to be utilized with temporal resolution adequate for high-speed centrifugal compressor research [80, 81]. The main difficulties with PIV arise due to the high seed density required and the necessity of two axes of optical access.

Another group of optical techniques for velocity measurements are known as transit-time (or time-of-flight) anemometers. The most common, Laser-2-Focus (L2F) involves two highly-focused and parallel laser beams introduced into the flow, which act as timing gates. Particles that pass through both beams (of a known separation distance) trigger a “start” and “stop” timer which yields the velocity of the particle. The pair of beams is then rotated to yield velocity measurements in different directions. Recent advances have allowed the in-plane component of the velocity to be measured as well utilizing a hybrid L2F-LDV system [82]. L2F has been the most widely utilized technique in turbomachinery applications, including the first observation of the jet/wake flow development in an impeller [16]; however, it has many drawbacks. Since perpendicular components are measured in series, temporal fluctuations of velocity vectors cannot be observed. L2F measurements are also more sensitive to the misalignment effects of measurements through curved windows. Furthermore, since signals are only generated by particles passing through both beams, the overall data rate is much lower for L2F than other methods. Finally, L2F is known to have difficulties in regions of high turbulence intensities because the probability of two different particles generating the “start” and “stop” signals increases [23].

## 1.6 Laser Doppler Velocimetry

Laser Doppler Velocimetry (LDV<sup>1</sup>) was first developed by Yeh and Cummins in 1964 [83] to provide a quantitative alternative to dye injection studies of flow velocity and structure. The fundamental principle of LDV is the Doppler Effect, the frequency shift that occurs due to relative motion between a signal source and observer [84]. For electromagnetic waves, as opposed to sound waves, this frequency shift is exceedingly small and can only feasibly be detected using heterodyne techniques. The main advantage of LDV over PIV is the relative ease of obtaining the third velocity component and the reduced need for optical access. The main advantage of LDV over L2F is the high data rate, ability to obtain multiple velocity components simultaneously, and ability to take measurements closer to solid surfaces [23, 85].

### 1.6.1 LDV Theory

LDV relies upon the measurement of the elapsed time for scattering centers, typically artificially introduced particles, to pass through a known distance in space. The Doppler Effect, defined by:

$$f_{\text{receiver}} = f_{\text{beam}} + \frac{v_{\perp}}{\lambda}, \quad (7)$$

relates the frequency observed by a stationary receiver,  $f_{\text{receiver}}$ , to the original frequency of the incident light,  $f_{\text{beam}}$ , the perpendicular (relative to the beam) velocity of the particle,  $v_{\perp}$ , and the wavelength of the incident beam,  $\lambda$ . The Doppler shift (the second term) is typically less than 100 MHz. This is virtually impossible to directly observe relative to the frequency of laser light, which is on the order of  $10^8$  MHz [86]. This limitation is overcome through the use of heterodyne systems using two coherent beams. The superposition of the electromagnetic fields of the incident beams forms a measurement volume at their intersection with a known, albeit complex, spectral intensity distribution. Particles passing through this intersection region scatter light in accordance with Lorenz-Mie or Rayleigh scattering theory (depending upon the size of the particle). Scattered light falls upon a photodetector receiver and provides an image of the intensity distribution through the measurement volume. The frequency of this scattered light is dependent only upon the incident light frequency, the angle between the incident beams, and the velocity of the particle [86]. A

---

<sup>1</sup> Some texts use the term Laser Doppler *Anemometry* (LDA) in lieu of LDV. Anemometry refers to velocimetry specifically applied to gaseous flows and the terms are typically used interchangeably

more intuitive, although less physically rigorous, explanation that yields the same result is through the so-called “fringe” model, Figure 1.7.

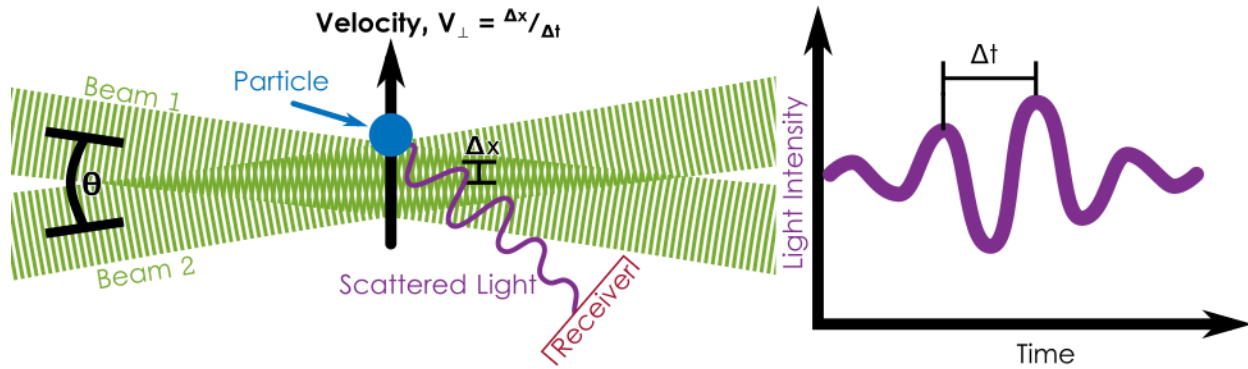


Figure 1.7: Fringe model

Two coherent beams having planar wave fronts (as would be found at the waist region of Gaussian beams, see APPENDIX A) intersect at an angle  $\theta$ . This yields an interference pattern of “light” and “dark” strips (known as “fringes”) through which particles pass scattering alternating bands of high and low intensity light corresponding to the fringes. The fringe spacing, defined by:

$$\Delta x = \frac{\lambda}{2 \sin(\theta/2)}, \quad (8)$$

and the Doppler frequency (the inverse of the time difference,  $\Delta t$ , between detected peaks),  $f_d$ , yields the velocity of the particle perpendicular to the beams’ bisector in terms of easily measured quantities:

$$v_{\perp} = \frac{\Delta x}{\Delta t} = f_d \frac{\lambda}{2 \sin(\theta/2)}. \quad (9)$$

This model is only *strictly* accurate for small particles with diameters significantly smaller than the wavelength of the incident light, which can be assumed to exactly sample the local intensity of the interference pattern. However, it provides a convenient visualization for understanding the LDV principle even for larger particles [86].

As depicted above, the system would not be able to differentiate between positive and negative velocities. This ambiguity is resolved using an acousto-optic modulator (such as a Bragg cell) to induce a small frequency shift in one of the incident beams. The result is a linear variation in the

phase of the scattered signal causing a stationary particle to scatter a cosine intensity variation. Spatially, this can be interpreted as a moving fringe pattern and the velocity can be calculated via:

$$v_{\perp} = (f_d - f_s) \frac{\lambda}{2 \sin(\theta/2)}, \quad (10)$$

a modification of Equation (9), where  $f_s$  is the applied frequency shift. The measurement volume for a single component system (consisting of a pair of beams) forms from the overlap of the two beam waists (in a well-aligned system). The resulting intensity distribution is continuous, but the standard definition of the measurement volume boundary is the surface at which the intensity has decayed by a factor of  $e^{-2}$ . An ellipsoidal measurement volume is formed with characteristic diameters as illustrated in Figure 1.8. The diameter in the direction bisecting the two beams,  $\delta_z$ , is significantly longer than the other characteristic diameters. The other diameter in the plane of propagation,  $\delta_x$ , and the perpendicular diameter,  $\delta_y$ , are of the same order and are given by:

$$\delta_x = \frac{d_f}{\cos(\theta/2)}, \quad (11)$$

$$\delta_y = d_f, \quad (12)$$

$$\text{and } \delta_z = \frac{d_f}{\sin(\theta/2)}, \quad (13)$$

where  $d_f$  is the waist diameter of each focused beam (see APPENDIX A). Combining this result with Equation (8) allows the computation of the number of fringes present within the measurement volume in the direction of the measured velocity:

$$N_f = \frac{\delta_x}{\Delta x} = \frac{2d_f}{\lambda} \tan(\theta/2). \quad (14)$$

The accuracy of the velocity measurements increases with number of fringes since, in essence, more samples of the Doppler frequency are obtained. However, greater spatial resolution is obtained with a smaller measurement volume which trends toward a measurement volume with fewer fringes. A balance must be found between these conflicting demands while also accounting for signal processing limits, lasing power capabilities, and other system and flow parameters.

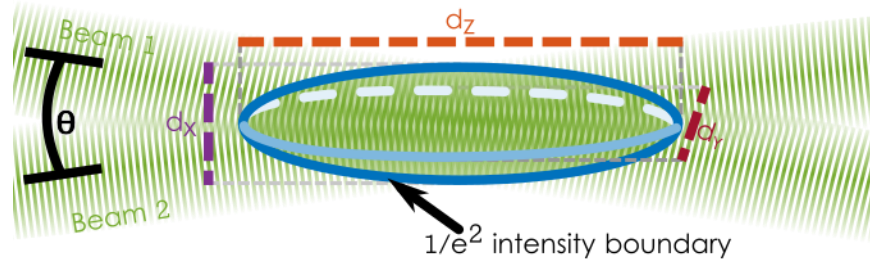


Figure 1.8: Measurement volume

To maintain the Doppler frequency within reasonable bandwidth limits, the angle  $\theta$  is typically small. This results in the length of the measurement volume in the direction of beam propagation being significantly longer than the other characteristic lengths (that is,  $\delta_z$  is markedly larger than  $\delta_x$  and  $\delta_y$ ). In turbomachinery applications, this elongated axis is typically aligned with the spanwise direction. The result is poor spatial resolution, especially in machines with small blade heights. This issue can be mitigated by operating in coincident mode or by implementing off-axis collection. For multi-component systems, the signal processor only accepts bursts which have produced valid signals in all collected components for coincident collection. This reduces the measurement volume to the region of overlap between the ellipsoidal measurement volumes formed for each measurement component. Off-axis collection utilizes a receiver that is not aligned with the beams themselves. This reduces the measurement volume to the overlap region between the field of view of the receiver and the original ellipsoidal intersection region formed by the beams. For representative values, either of these approaches can reduce  $\delta_z$  by half, effectively doubling the spatial resolution in that direction [87].

Multiple components of the velocity field are obtained using multiple pairs of beams of different wavelengths crossing at a single point. For a three-component system, the measurement volume is formed as the overlap region between the three ellipsoids (see above) arising from each beam pair. Since direct observation of each Cartesian velocity coordinate is rarely possible due to optical access restrictions, measurements are obtained in a skew coordinate system and a vector transformation is used to deduce the Cartesian velocity components.

## 1.6.2 LDV Uncertainty and Statistics

The signal that is sampled in an LDV system arises due to light scattered from finite particles in the flow. An accurate determination of the particle velocity depends upon resolution of the frequency of this signal. The frequency determination is a complicated result of several signal processing techniques which are described in [84, 86, 88, 89]. Exact processes and errors arising in each step will not be addressed here, only a bulk uncertainty in the frequency determination will be utilized in this study. The differences between the statistics surrounding LDV data and typical experimental data lie in the random nature of the sampling. Samples are not obtained at a fixed rate with equal time steps between subsequent samples. Instead, samples are obtained through the random arrival of particles in the measurement volume with an average arrival rate. The most significant result is the elimination of the standard Nyquist upper bound of frequency resolution. Relevant conclusions regarding frequency resolution are determined by the interarrival time, the time between subsequent signals which follows an exponential distribution, rather than the mean data rate. Since the time between valid signals is randomly distributed, signals that arrive close together can provide information about flow fluctuations at frequencies significantly higher than would be possible for traditional, fixed-rate sampling. There is no equivalent to the sampling theorem or the Nyquist frequency, and it is possible to achieve unbiased and alias-free estimates at frequencies significantly higher than the mean particle arrival rate [86].

The nature of the sampling induces a bias in results which must be accounted for. The rate of particles passing through the measurement volume is governed by the *volumetric* flux of fluid. Assuming a uniform distribution of particles upstream of the test region, the sample rate of the velocity will, therefore, be proportional to the velocity itself. The result is that higher velocities are more likely to be sampled than lower velocities. This is accounted for using transit-time weighted averaging. The time taken for the particle to transit the measurement volume will be inversely proportional to the velocity of the particle, and it has been proven, [90], that using this as a weighting factor yields an unbiased estimator for mean flow velocities:

$$\bar{u} = \frac{\sum u_i t_i}{\sum t_i}. \quad (15)$$

The overbar denotes a mean quantity,  $u_i$  and  $t_i$  denote individual measurements of a velocity and transit time, and the summation is over all observations at a particular location and, if the data are

ensemble averaged, at a particular instance in the relevant period. The same weighting method is utilized for estimators of the second moment and for joint moments between the velocity components [86].

Uncertainty in the velocity and moment estimates arises from physical characteristics of the system, signal processing, flow properties, and random noise. The primary sources of system-related error occur due to misalignment. If the beam waists do not coincide with the measurement volume, then the wave fronts will not be planar, causing non-constant fringe spacing. This results in a changing Doppler frequency through the measurement volume and errors in the velocity estimates [86]. Errors are also propagated through the transformation matrix if the angles between the skew (measurement) coordinate system and the Cartesian (laboratory) coordinate system are not accurately measured. Additionally, a greater uncertainty in the third component typically arises due to a limitation in measuring parallel to its axis in typical applications [91]. Curved windows used for optical access can act as a second lens and change the fringe spacing, again, introducing error if not properly accounted for [89]. An improper choice of seed particle can also introduce error, as will be discussed subsequently. Signal processing can introduce errors related to the temporal discretization and precise determination of the Doppler frequency from a validated signal. Additionally, the flow itself can add complications. The measurement volume is generally regarded as small enough to assume a constant velocity throughout; however, this does not always hold. Similarly, the finite transit time of particles yields some ambiguity in the Doppler resolution due to turbulent and temporal fluctuations of the local velocity [88]. These sources combine with random noise from unwanted reflections or stray light to give an overall estimation of the accuracy of a particular LDV system in a particular application.

### **1.6.3 Seeding for LDV**

LDV systems measure the motion of seed particles which are, in most cases, artificially added to the flow. The primary aspects of seeding that must be considered are the size of the particles introduced, the choice of seed material, and the method of introduction into the flow. Seed can either be of a solid or liquid form. Solid seeds are produced by atomization of a suspension or from powders while liquid aerosols can be generated utilizing atomization or condensation. Atomization can be achieved in various ways [92, 93] however the impact-jet atomizer is the most

common. The seed fluid is drawn from a reservoir into a high-speed air jet which quickly forms a polydisperse aerosol. This is then passed over a spherical impactor which is used to remove larger droplets from the air stream. The mean droplet size can vary greatly and is dependent upon the atomizing airflow rate, the impactor design, and the liquid used [86]. The size distribution of the particles in the aerosol is crucial to accurately resolving flow velocities. It can be derived that for liquid or solid seeds in gaseous flows (where the density of the seed is much larger than that of the flow), a characteristic frequency response exists for particles that is dependent upon the material and the particle size. The inertia of the particles acts as a low-pass filter in terms of responding to velocity fluctuations in the flow [86, 92]. This cutoff frequency,  $f_c$ , for a particle to follow changes in the flow velocity with a particular slip,  $s$  (defined as the relative difference between the particle and the true flow velocity), is given in terms of the characteristic timescale of the particle,  $\tau_0$ , by:

$$\tau_0 = \left( \frac{\rho_p d_p^2}{18\mu_f} \right) \quad (16)$$

$$\text{and } f_c = \frac{1}{\tau_0} \frac{1}{2\pi} \sqrt{\frac{1}{(1-s)^2} - 1}. \quad (17)$$

Here  $\rho_p$ ,  $d_p$ , and  $\mu_f$  are the particle density, particle diameter, and dynamic viscosity of the fluid [86]. Smaller particles can respond to higher frequency fluctuations, however, scatter less light than larger particles and, thus, are more difficult to detect. Specifically, Equations (16) and (17) indicate that the frequency response of seed particles is proportional to the inverse of the diameter squared. However, Rayleigh Scattering theory shows that the amplitude of the scattered signal decreases with the sixth power of diameter for small particles. Therefore, particles must be generated with a narrow size distribution that are small enough to follow the highest frequency fluctuations expected in the flow and no smaller to yield the highest possible signal quality. Lower density seed particles are advantageous as they can follow higher frequency velocity changes without sacrificing signal quality. Finally, when choosing a seed substance, one must consider droplet survival for adequate time at the test temperatures (without evaporating or condensing), substance toxicity (especially for tests which exhaust to the environment), and the ease and cost of obtaining the substance.

The final consideration is the introduction of the seed into the flow. The seed particles must be given adequate time to accelerate to the local flow velocity. The slip decreases exponentially with time (from injection) and a residence of  $6.9\tau_0$  is required to achieve 0.1% slip due to acceleration. It is also desired to locally seed individual streamtubes rather than to globally seed the full volumetric flow passing through the test article. This extends test time by minimizing condensation on windows (which, over time, will block optical access) while maintaining adequate seed concentration in the measurement volume [86]. An actuation device must be utilized to maneuver the seed injection point to achieve this goal.

#### **1.6.4 Applications on Centrifugal Compressors**

Various studies have been conducted over the years using LDV to determine the flow field within a centrifugal compressor stage. Adler and Levy in 1979 [25] utilized a one-component system to determine the distribution of radial velocity through a shrouded, radial, pump-style impeller with a rotating shroud-side window operating at low speed. Separated flow at the inlet, due to a small radius of curvature along the shroud, may have skewed their results; however, the impeller exit flow was uniform. Fagan and Fleeter in 1989 [23, 94] conducted an extensive characterization of one-component measurements through an un-shrouded impeller operating at low-speed using a Plexiglas shroud for optical access. They showed a velocity deficit region develop along the shroud that did not migrate to the suction surface of the blade. Significant studies have also been conducted at NASA on the Low-Speed Centrifugal Compressor (LSCC) in 1993 [95] and the so-called CC3 compressor in 1997 [22]. The LSCC study resolved the ensemble averaged three-component flow field by two serial measurements of two-component velocities conducted at different probe angles. These independent two-component results were then ensemble averaged and combined to yield the full three-component flow field. This represented the first resolution of the three-component flow field through the impeller and showed a significant spanwise secondary flow that was not predicted by computations. The study conducted on the CC3 compressor produced the first LDV data from a high-speed centrifugal compressor. Two components of the velocity field were resolved through three repeated one-component measurements with the probe rotated at different angles. These data showed a linear velocity gradient at the impeller exit, similar to the L2F results of Krain [10]. They also showed a rapid decay of this non-uniformity through the vaneless diffuser.

Cattanei et al. [24] and Stahlecker et al. [20, 21, 96] obtained the first high-speed compressor LDV data with a modern, vaned diffuser. Cattanei et al., with a two-component system, focused on the unsteady boundary layer development along the diffuser vane surfaces and the results were discussed previously. Stahlecker et al. obtained three-component results using a blending of duplicated two-component results similar to the LSCC study mentioned above. They showed the development of a large passage vortex through the vaned diffuser. Through the semi-vaneless space, a strong shear flow near the shroud developed from suction to pressure side. This flow impacted the leading edge of the adjacent pressure side and was driven down the vane from shroud to hub, forming the passage vortex. Data revealed that this structure was temporally stationary. More recent high-speed, two-component studies have been conducted through the impeller [45, 97, 98] and a pipe diffuser [65]. The general conclusion is that computational methods are too dissipative [98], do not match with experimental results of flow development through the diffuser [65], and are still lacking experimental datasets for validation and refinement [45, 65, 97, 98]. It is important to note the lack of true three-component, simultaneous velocity data for resolution of the unsteady flow field and Reynolds stress development through the diffuser.

## **1.7 Computational Fluid Dynamics**

Historical prediction tools utilized in design relied upon two-dimensional boundary layer models combined with inviscid analyses to develop and numerically optimize a design. These methods then shifted the performance predictions using models to account for additional loss from aspects not included in the flow model [37]. Much progress was made; however, developing a complete theoretical model was deemed a “rather dim” possibility [37]. Attention was then turned to three-dimensional, viscous-flow computations to predict the flow development through a centrifugal compressor from fundamental flow equations rather than theoretical correlations. One of the first successful computations is described in Moore and Moore [99]. They developed a three-dimensional parabolic method to solve the governing equations in the rotating reference frame of the impeller on a non-orthogonal grid. Their simulation utilized only 1000 grid points; omitted compressibility, unsteadiness, tip leakage, and stationary shroud effects; and did not include the diffuser. Despite the great simplifications, the results were relatively accurate in predicting the development of the wake through the impeller and proved a great step forward for numerical technology regarding centrifugal compressors.

Advances in computing and storage capabilities over the past several decades have enabled Computational Fluid Dynamics (CFD) to become a major design tool. While more advanced techniques (Large Eddy Simulation and Direct Numerical Simulation) have emerged recently, the typical method in turbomachinery is through the Reynolds Averaged Navier-Stokes (RANS) equations. The RANS equations represent a modification to the standard Navier-Stokes equations for turbulent flow as given, using Einstein tensor notation, by:

$$\rho \frac{\partial U_i}{\partial t} + \rho U_j \frac{\partial U_i}{\partial x_j} = -\frac{\partial P}{\partial x_i} + \frac{\partial}{\partial x_j} \left( 2\mu S_{ji} - \overline{\rho u'_j u'_i} \right). \quad (18)$$

$U_i$  represents a component of the velocity vector,  $x_i$  represents a component of the position vector,  $\rho$  is the local density,  $P$  is the local pressure,  $\mu$  is the dynamic viscosity, and  $S_{ij}$  is the strain-rate tensor. The final term,  $\overline{\rho u'_j u'_i}$ , is the Reynolds stress tensor and is sometimes denoted  $\tau_{ij}$ . The Reynolds stress tensor is a symmetric tensor with six independent components each of which represents the average correlation between fluctuations in two velocity components [100]. Together with the continuity equation, this yields a system of four equations (continuity and three components of momentum) with a total of ten unknowns. This is the so-called “closure problem” and the general solution is to develop turbulence models relating the Reynolds stress tensor to the fundamental flow properties [100].

### 1.7.1 Turbulence Modeling

The most basic solution to the closure problem is using algebraic models or “zero-equation” models. These models apply the Boussinesq eddy-viscosity approximation—that the Reynolds stress tensor is proportional to the mean strain-rate tensor [101]. The constant of proportionality, known as the eddy-viscosity, depends upon local flow properties and that dependence forms the model. These models include the mixing-length model of Prandtl [102], the Cebeci-Smith model [103], and the Baldwin-Lomax model [104]. Modifications of the latter two models are still utilized due to their simple and computationally cheap nature. These models only work well in flows for which the model parameters have been finely tuned and extrapolation is not advised. Both work adequately for incompressible turbulent boundary layers under moderate pressure gradients without significant boundary layer separation. Algebraic models are inherently

incomplete as they provide no information regarding the length scale of the turbulence and should be used cautiously for complex flows [100].

The next generation of turbulence closure models, one- and two-equation models, still rely on the Boussinesq approximation, but are based upon differential (rather than algebraic) equations for the turbulent kinetic energy,  $k$ , and its relation to the Reynolds stress tensor. Two-equation models and modern one-equation models solve the completeness problem of algebraic models by providing information regarding the length scale of the turbulence as well. The most common one-equation models are the Baldwin-Barth and the Spalart-Allmaras models which are used primarily for external flows [100]. Two-equation models are more difficult to converge numerically than algebraic models but have been purported to be significantly more accurate and form the workhorse of modern CFD including (among myriad others) the well-known  $k$ - $\epsilon$  [105],  $k$ - $\omega$  [100], and Shear-Stress Transport (SST) models [106]. The specific formulation of each will not be addressed; however, in general, the  $k$ - $\epsilon$  model has difficulties near walls, the  $k$ - $\omega$  model performs well near walls but is sensitive to freestream conditions, and the SST model attempts to blend the two. The SST model acts as the  $k$ - $\omega$  model near solid walls and blends to the  $k$ - $\epsilon$  model in the freestream in order to reduce the  $k$ - $\omega$ 's sensitivity to freestream conditions. Additionally, the SST model includes a shear-stress limiter to constrain the over-prediction of eddy-viscosity in sharp velocity gradients [106, 107]. The most recent modification to the  $k$ - $\omega$  by Wilcox helps to address the freestream dependency through the introduction of a cross-diffusion term and a stress-limiter [108].

These models mispredict flows with strong streamline curvature and system rotation [100]. In these applications, linear models fail due to turbulence anisotropy which cannot be accurately modeled under the standard Boussinesq approximation [109]. This is a major shortcoming in centrifugal compressor applications which are dominated by these characteristics. Much work has been done specific to turbomachinery to develop modifications to these models with improved performance under these conditions [110, 111]. However, these approaches are often completed in an “*ad hoc*” manner in matching a specific set of experimental data rather than from first principles [112].

An alternative is an approach in which the prediction of turbulence anisotropy developing from streamline curvature and system rotation arises from the underlying model. The most direct approach is by modeling each component of the Reynolds stress tensor by the application of transport equations [109]. Full Reynolds stress models shift the modeling burden to higher order correlations that are more physically realistic. However, current Reynolds stress models produce extremely stiff systems that pose numerical challenges in obtaining converged solutions in complex flows [113]. An alternative is to replace the Boussinesq approximation using Explicit Algebraic Reynolds Stress Models (EARSM) to relate the Reynolds stress components and the mean velocity gradient field [112]. These models add anisotropy to the constitutive relations in an explicit manner to produce a compromise, maintaining the numerical robustness of models relying upon the Boussinesq approximation while adding the ability to accurately predict the flow effects of system rotation and streamline curvature [109, 112].

### **1.7.2 Stage Simplifications and Treatment of Unsteadiness**

The unsteady simulation of a full-annulus centrifugal compressor is far beyond the computational resources available in the design phase. As such, simplifications are made to reduce the computational load and allow results to be obtained in a reasonable and useful time period. The first assumption, used in nearly every simulation, is that of perfect rotational symmetry. Each identical blade passage is assumed to have identical flow distributions. This assumption allows the simulation to be run on only a single passage (or a small number of passages), rather than the full annulus, and can reduce the computational load by an order of magnitude. Another simplification that is commonly used is to neglect complex geometric features such as blade fillets or backface cavities. This allows a simpler and smaller (in terms of node count) grid to be utilized and can improve the rate of convergence [114]. Similarly, walls are often treated as smooth and adiabatic to simplify the modeled physics and reduce computational cost of simulations. However, these simplifications have an impact on the prediction of flow development through the centrifugal compressor. Walls are not truly adiabatic nor smooth nor are corners perfectly perpendicular, and these physical drivers can have dramatic impact on the predicted flow profile [113].

A major difficulty arises in connecting the rotating impeller domain to the stationary diffuser domain. Early methods used a simple circumferential average which is not physically realistic.

The most common modern method is the “mixing plane” approach [115], a process which conserves mass, energy, and momentum while allowing circumferential variation to exist along the interface plane. This allows the pressure field from the diffuser to influence the impeller within the confines of a steady simulation. Another option is the “frozen rotor” approach which fixes the impeller in a particular orientation relative to the diffuser. In this approach, local flow conditions are directly transmitted from the impeller exit domain to the diffuser inlet domain. Simulations are typically conducted at a range of angular offsets between the impeller and diffuser domains to produce an estimation of the flow field at various instances through the blade passing period of the impeller [116].

The final, and most computationally expensive, option is to run an unsteady interaction model. Various transformation methods exist to allow unsteady computations on reduced models of the stage and account for pitch differences between the impeller and diffuser. The simplest, Profile Transformation, simply stretches or compresses the impeller exit domain to match the pitchwise extent of the diffuser inlet domain. This allows stages to be run with any pitch ratio; however, detailed flow features may be inaccurate due to imposing phase-shifted periodicity on all boundaries [117]. The Time Transformation method adds a time delay to the interface plane and inclines the stationary domain in time (in the solver) to allow for phase differences without physical scaling or shifting of the domains. The drawback is that excessive pitch ratios can cause numerical instabilities to occur [117, 118]. A third method is the Phase Transformation (or Phase-Lag) approach of Erdos and Alzner [119]. The flow parameters are stored on the periodic boundaries for an entire additional period to cover the interface plane regardless of the current relative orientation. This approach does not suffer from the scaling issues of the Profile Transformation method nor the stability issues of the Time Transformation method, however, it is extremely memory intensive. A modification of this technique that solves this memory issue is the Fourier Transformation method of He [120]. Instead of storing flow parameters, Fourier coefficients of the flow profiles at the interface plane are stored. This allows the interface data to be reconstructed across the circumference while avoiding the memory intensive storage of the complete flow data.

### **1.7.3 CFD Use in Design**

CFD is a crucial tool for centrifugal compressor design and will only become more critical as computational capabilities advance and resources become more widely available. As designs are pushed outside of historical experience and are iterated upon more rapidly, CFD is often the only information forming the basis for major design decisions. This can pose an issue as typical CFD turbulence models are calibrated to canonical cases such as the flat plate, two-dimensional steps, and simple jets. Use of these turbulence models in scenarios for which they are not well-calibrated is advised only with extreme caution [100]. Additionally, computational speed is of high importance to designers who must be able to rapidly iterate through many design choices to produce an optimized final product. This often results in neglecting physical drivers—such as surface roughness, heat transfer, and fillets—as mentioned previously. Further experimental data are needed to specifically calibrate turbulence models to centrifugal compressors. Additionally, a systematic approach to key modeling choices must be conducted to determine how simplifications impact internal flow profiles and flow development and which drivers are critical to the accurate prediction of flow physics. These steps are necessary if fine details of the flow are to be reliably leveraged to increase design efficiency.

## **1.8 Research Objective**

This introduction informs the objective of, and the need for, this proposed study. Centrifugal compressor technology is progressing into novel design spaces, and the twofold demand of rising fuel costs and environmental concerns make even small performance gains extremely valuable when the ubiquity of centrifugal compressors and pumps is considered. To achieve these gains, additional experimental data are required to improve understanding of the complex internal flow phenomena and improve existing computational turbulence models and methodology. This study will realize that goal by obtaining the first unsteady, three-dimensional, and simultaneous three-component data of the flow field in a modern aeroengine centrifugal compressor vaned diffuser using non-intrusive measurement techniques. It will also provide the first non-intrusive measurement of Reynolds stress development in the entry region of the vaned diffuser. These data will be invaluable for gaining additional insight into the flow structure and to validate and improve

current computational models, especially in the diffuser entry region where models are known to fall short.

More specifically, this study will address the following topics relating to advancing understanding of vaned diffuser aerodynamics and validating computational models:

*Vaned diffuser aerodynamics:*

1. Determine the details and rate of mixing between the jet and wake through the diffuser
2. Resolve the three-dimensional development of secondary flows through the inlet region of the diffuser passage
3. Experimentally determine the location and temporal nature of regions of flow separation within the diffuser passage
4. Understand the extent of unsteady fluctuations in the streamwise direction and variations in unsteadiness levels across the span
5. Acquire the unsteady and spanwise variation of incidence at the vane leading edge
6. Study the relationship and interconnectedness of topics 1-5

*Validating Computational Models*

1. Compare the experimental and predicted diffusion and dissipation of the jet and wake through the diffuser passage
2. Resolve turbulent kinetic energy levels at several planes through the diffuser inlet region to compare to predictions developed from various turbulence models
3. Study the predicted location and extent of regions of flow separation within the diffuser
4. Investigate the importance of information lost across a mixing-plane interface and the downstream effects in terms of flow field predictions
5. For each of the previous, determine the accuracy of various turbulence closure methods and make suggestions regarding best-practice modeling decisions for centrifugal compressors and areas where turbulence models must be further developed and tailored for this specific application

## 2. RESEARCH METHODOLOGY

The experimental work supporting this project was conducted using the Purdue Compressor Lab Centrifugal Stage for Aerodynamic Research (CSTAR) facility. The facility has been operational since 2015 and was developed to study a centrifugal compressor stage for implementation as the rear stage of an axial-centrifugal compressor series. It is designed to accept test articles at engine-representative size and rotational speed and allow rapid component changes for detailed aerodynamic evaluation of design changes.

### 2.1 CSTAR Facility Infrastructure

The CSTAR facility infrastructure includes the support systems necessary for high-speed compressor testing. The systems included are the inlet and exhaust ducting; the drive system; the lubrication and cooling oil circuit; and the data acquisition system. The primary components of these systems are illustrated in Figure 2.1 (excluding the data acquisition system).

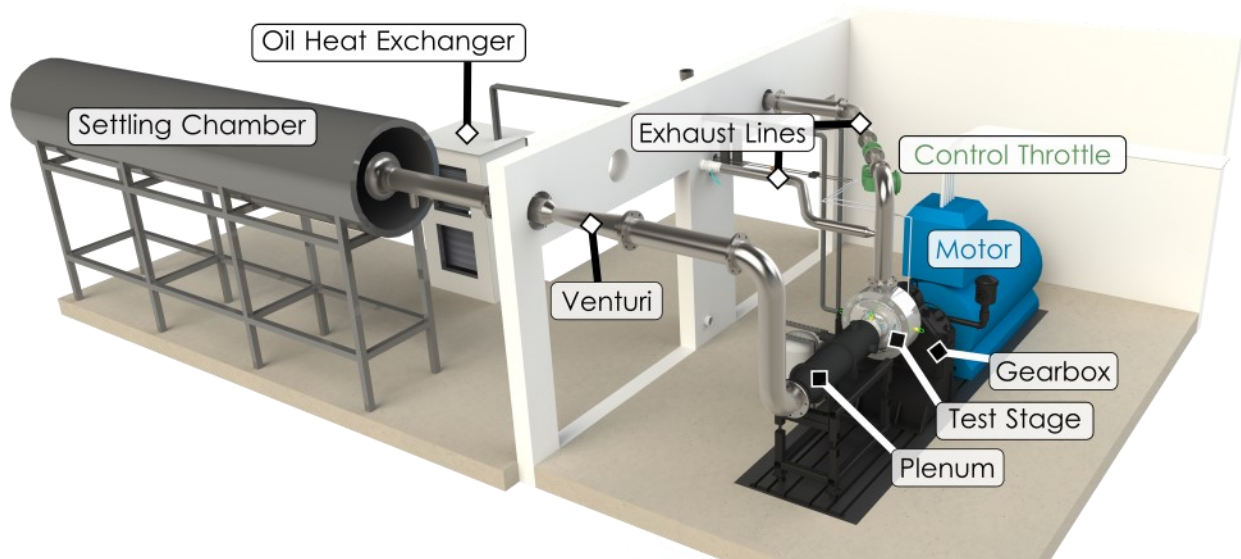


Figure 2.1: CSTAR test facility

The inlet air system is designed to supply well-conditioned atmospheric air to the compressor test stage. A settling chamber that is twenty feet in length and three feet in diameter fitted with a perforated-steel inlet screen acts to mitigate the effects of unsteady ambient conditions. The air is

drawn from this large volume and passes through a seven-micron filter to remove particles and debris from the flow. A bellmouth smoothly transitions the flow to the eight-inch ducting diameter of the ASME standard long-form venturi, where the mass-flow rate is measured. Five pipe diameters upstream of the venturi a pitot probe and flush mounted hygrometer measure the total temperature, total pressure, static pressure, and relative humidity of the ingested air. Two ninety-degree bends align the airflow with the compressor stage. Downstream of these bends is the inlet plenum, designed to provide a final stage of conditioning to the flow. First, a perforated flow spreader acts to break up the formation of a central jet while increasing the ducting diameter of the flow. Two rows of honeycomb screen then act to further homogenize the flow. The uniformity of the inlet total temperature and total pressure profiles is verified using rakes spanning the plenum diameter. Finally, a bellmouth provides a smooth transition to the compressor inlet diameter while avoiding the ingestion of the plenum wall boundary layer.

The air leaving the compressor stage passes into a large-volume collector before exhausting vertically. The exhaust stream is split into two paths. The primary path goes through a pneumatically actuated vee-ball valve control throttle which is used to backpressure the compressor while testing. The secondary path passes through a manual control valve which is adjusted prior to testing to set the control range of the pneumatic valve.

The drive system consists of a 1,400 HP AC electric motor controlled by a variable-frequency drive system. The motor can provide a maximum speed of 1,792 RPM and the drive controls the motor output speed to within 0.01% of the full speed range. A 30.46:1 speed-increasing gearbox is used to allow tests at engine-representative speeds. The maximum rated speed of the high-speed shaft is 54,000 RPM; however, current testing operates at a maximum speed of 22,500 RPM.

The driveline consists of the gearbox high-speed shaft and the compressor drive shaft, to which the impeller is fixed. The gearbox shaft is supported by two tilting-pad journal bearings and is mated to the compressor shaft using a spline interface. The compressor shaft is supported by a precision rolling element bearing, to maintain radial positioning of the shaft, and a precision ball bearing which bears the axial load from the impeller. The ball bearing is mounted within a squeeze-film damper to suppress shaft motion while passing through resonant speeds.

A dedicated oil lubrication system allows safe high-speed operation of the drive system. Oil is supplied to all four high-speed bearings for cooling and lubrication. Additional oil is supplied to the spline interface between the gearbox and compressor shafts, as well as the squeeze-film damper. Flow is driven using a gear pump fixed to a 7.5 HP electric motor. The speed of this pump is adjusted to provide stipulated flowrates and pressure levels to all system components. The temperature of the oil is maintained using two automated heat exchangers which cool the oil using atmospheric air. The proportion of oil that passes through the heat exchanger loop can be adjusted during testing to maintain a stable oil temperature through a variety of testing and ambient conditions.

Finally, the data acquisition systems allow for observation of important flow quantities. Two Scanivalve rack-mounted enclosures (DSAENCL4000) with DSA3016 digital sensor arrays and three Scanivalve DSA3217 pressure scanning units are used for the majority of pressure measurements with an accuracy of 0.05% full scale. Two Mensor Digital Pressure Transducers are used to measure the absolute reference pressure and the pitot total pressure to within 0.005 PSI. Finally, Rosemount 3051C pressure transducers are used to precisely measure the pressure levels through various venturi flow meters. Temperature measurements are taken using an Agilent 34980A Multifunction Switch/Measure mainframe capable of a multitude of measurement types. Multiple 34921T connector blocks with dedicated cold-junction reference terminals allow thermocouple measurements to be made with system uncertainty contributions of only 0.9 °F. Various other systems are used to actively measure tip clearance, rotational speed, and relative humidity. Further details regarding the test facility, acquisition system, rotordynamic behavior, and test procedures can be found in [121, 122].

## **2.2 CSTAR Baseline Compressor Stage**

The baseline CSTAR compressor stage operates at a design corrected speed of 22,500 RPM. The backswept impeller has 15 full blades and 15 splitter blades beginning at 34% of the impeller meridional passage. The tip clearance of the unshrouded impeller is adjusted using axial shims during assembly. The channel diffuser consists of 35 thin wedge vanes with chamfered leading edges beginning at a radius ratio of 1.08. Downstream of the diffuser, the deswirl component consists of a simple, annular, ninety-degree turn-to-axial from which the flow exits into the large

volume collector. A cutaway diagram of the CSTAR stage is given in Figure 2.2, depicting the stage from the inlet bellmouth through the collector. A special shroud was designed and the original diffuser modified for optical access. Two windows can be inserted, one over the impeller (partially observable in Figure 2.2) and the other over the diffuser (not in Figure 2.2), to allow optical access to nearly 85% of the flow passage through the impeller and diffuser. Additional details regarding the optical access and window configuration are discussed below and the design process is detailed in [123]. Bleed air passing over the impeller tip and behind the impeller exits the compressor through two independently throttled and instrumented bleed lines to cool the impeller backside and reduce disk friction losses.

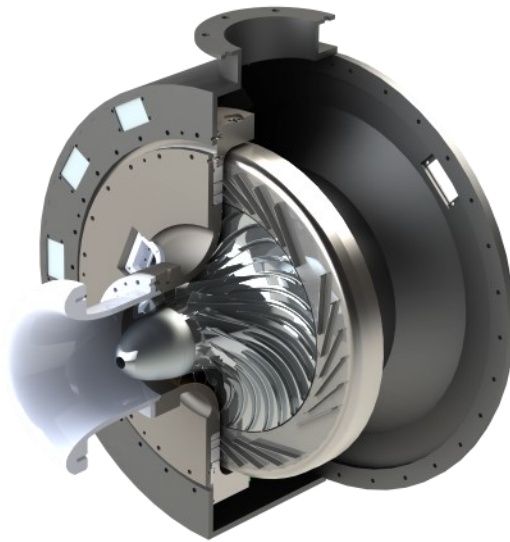


Figure 2.2 : CSTAR stage slice view

### 2.2.1 Steady Flow Instrumentation

The CSTAR stage is heavily instrumented to allow detailed studies of the aerodynamics through the individual components. Rakes measure either total pressure or total temperature across the span of the flow passage at the impeller inlet, diffuser inlet, diffuser exit, and the exit of the deswirl component. These measurements are used to compute total pressure and total temperatures ratios through the components and to evaluate overall performance. The impeller inlet has two, five-element total temperature and total pressure rakes distributed evenly around the circumference to define the stage inlet properties. The diffuser inlet has two, four-element total pressure and two,

three-element total temperature rakes embedded in the leading edges of four diffuser vanes—one rake per vane. The diffuser exit has eight, four-element total pressure rakes. The total of eight is composed of two rakes at each of four pitchwise positions to form a two-dimensional array of total pressure data across the diffuser passage. These rakes are distributed around the circumference of the diffuser exit to prevent excessive blockage impacting the flow through any one passage. Finally, the exit of the deswirl component has six, four-element total pressure rakes and four, four-element total temperature rakes, distributed evenly around the circumference, to complete the performance measurements of the stage.

The original shroud, without optical access windows, contains 23 static pressure taps through the impeller meridional passage. The diffuser contains two sets of three static pressure taps at both the throat and the trailing edge of the vane. All of these taps are located on the shroud side of the passage. Additionally, the deswirl duct has three static pressure taps on both the hub and shroud walls located through the turn to axial. Finally, two sets of three static pressure taps show the radial progression of pressure through the backface cavity. The location of all instrumentation is depicted in Figure 2.3.

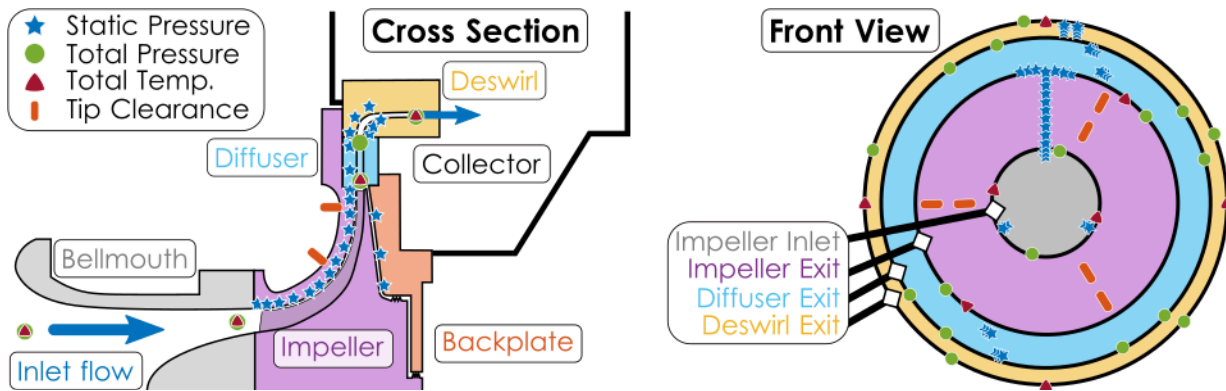


Figure 2.3: Instrumentation locations

### 2.2.2 Tip Clearance Measurements

The hot-running tip clearance of a centrifugal impeller is critical both in terms of performance impact and safe operation. With increasing speed, centrifugal forces, acting to lift up the thin impeller blades, and thermal growth, due to the increased impeller work input at higher speeds, both act to decrease the clearance. The precise change in clearance from the “cold,” as-assembled,

geometry to the “hot” geometry at design conditions can be significant and difficult to predict. For example, for the CSTAR geometry, the “cold-to-hot” clearance change has been observed to be nearly 2% of the impeller trailing edge blade height. Tests at various tip clearance configurations have yielded a reduction of approximately 1.25% in total pressure and 0.5% in stage efficiency for every 1% increase in tip clearance. Additionally, the extremely small gap between the rotating impeller and the stationary shroud poses an issue from an operational perspective in terms of avoiding catastrophic damage to the facility. Both factors necessitate the ability to monitor the hot-running tip clearance levels during tests. From a performance perspective, this ensures that performance data are comparable between test days and configurations. From a health perspective, this ensures that tests can be aborted, and the tip clearance corrected, if the actual clearance shrinkage is larger than was predicted.

This is achieved, in the CSTAR facility, using six capacitance-based probes mounted in the shroud. They are located at three circumferential locations and two meridional locations, at the knee and the exducer of the impeller blades. The CapaciSense system consists of a probe, an oscillator, and a demodulator. The oscillator drives the probe circuit with a fixed frequency signal. The passage of impeller blades past the probe head induces a change in the capacitance of the probe proportional to the spatial gap between the metallic blade and the probe head. This capacitance change modulates the frequency of the probe circuit which is then converted into a voltage by the demodulator. Prior to the installation of the shroud, each probe-oscillator-demodulator group is mounted a known distance from the impeller blades. The probe is then actuated away from the blades by a controlled amount and the resulting voltage signal is observed to develop a calibration curve connecting the voltage and the tip clearance. This calibration procedure allows the hot-running tip clearances to be monitored in real time, for both performance and health considerations. The system has a frequency response of 10 MHz and a resolution of approximately 0.001”.

### **2.2.3 Modifications to Allow LDV**

The baseline configuration needed several modifications to allow optical access and permit the LDV study. The first aspect of this process was included in the initial commissioning of the rig and resulted in a narrow plenum being selected to not impede motion of the LDV probe and positioning equipment in front of the test stage. More significantly, the shroud and diffuser needed

modification to allow the installation of windows into the casing walls. The detailed mechanical design and selection procedure are described in [123] and the result was the two-window design, illustrated in Figure 2.4. A new shroud was manufactured which allowed the installation of two window assemblies: one over the impeller blades and one from the impeller tip through the majority of the diffuser passage. Each window assembly consists of a stainless-steel frame, a fused silica window, and multiple window clamps, which act to further secure the window in the frame. An exploded view of the assembly for the diffuser window is presented in Figure 2.5. Silicone sealant is applied around the periphery of the window and acts to securely fix the window and prevent leakage. A gasket is mounted under the flange of the diffuser window frame to prevent leakage and an O-ring is included around the impeller window frame to seal against the complex shroud surface. A plug was also manufactured to fit the impeller window slot to preclude damage to the impeller window while testing was being conducted through the diffuser for this study. The windows were all manufactured from fused silica due to its excellent transmission of visible light and high strength (relative to other glasses). Borosilicate glass was also considered for its similar properties. A future experimental technique may necessitate the superior transmission of fused silica over the near ultraviolet range and, consequently, fused silica was used despite its higher cost and worse machinability properties.



Figure 2.4: Shroud comparison

#### 2.2.4 Baseline Performance Data

Any modification to a centrifugal compressor flow path can have significant impacts on the observed performance of the machine. To ensure that performance between the baseline geometry and the modified geometry with optical access were comparable, speedlines were acquired at the

design rotational speed for both configurations. The TPR and efficiency performance comparison of the stage is given in Figure 2.6. The performance of the two configurations is nearly indistinguishable. The slight differences—slightly higher choking mass-flow and lower total pressure ratio and efficiency of the LDV configuration—are attributable to small differences between the tip clearances attained in the two configurations. The average clearance at design for both configurations is plotted in Figure 2.7. The global mean clearance of the two configurations is identical; however, the difference in the clearance profile is likely the cause of the small differences in performance.



Figure 2.5: Window frame assembly exploded view

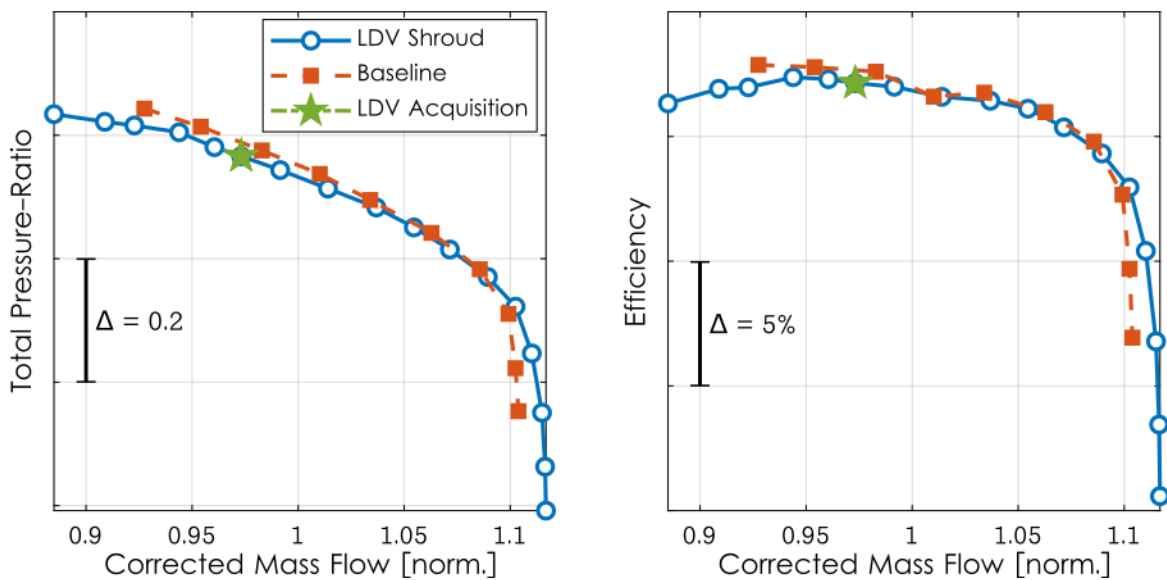


Figure 2.6: Baseline and LDV performance map comparison

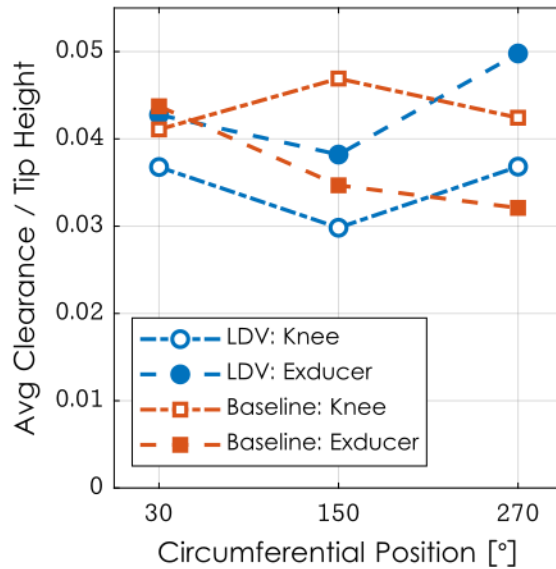


Figure 2.7: Baseline and LDV tip clearance comparison at design point

To show the agreement between the two configurations and further illustrate the fact that the shroud modifications and installation of the LDV windows did not measurably alter the diffuser flow field, the detailed static pressure measurements through the diffuser and the total pressure contours at the diffuser exit are presented in Figure 2.8 and Figure 2.9. The throat static pressure taps show the expected higher static pressure closer to the pressure side of the diffuser vane. The data at the throat from the two configurations show the same profile and similar levels, with the LDV shroud showing greater uniformity between the two circumferential data locations. By the diffuser exit, the two profiles are largely identical between the two configurations. Again, this supports the conclusion that optical access was obtained with little disturbance of the flow field. Finally, the two-dimensional contours of total pressure obtained at the exit of the diffuser vane passage are given in Figure 2.9. The two contours are remarkably similar both in general shape—a core of higher total pressure flow surrounded by lower total pressure flow closer to the endwalls—and in magnitude when normalized by the inlet total pressure. Altogether, these data have illustrated that the Baseline and LDV configurations show identical performance, even in fine details of the flow structure, and thus the modifications have not compromised the integrity of the flow field.

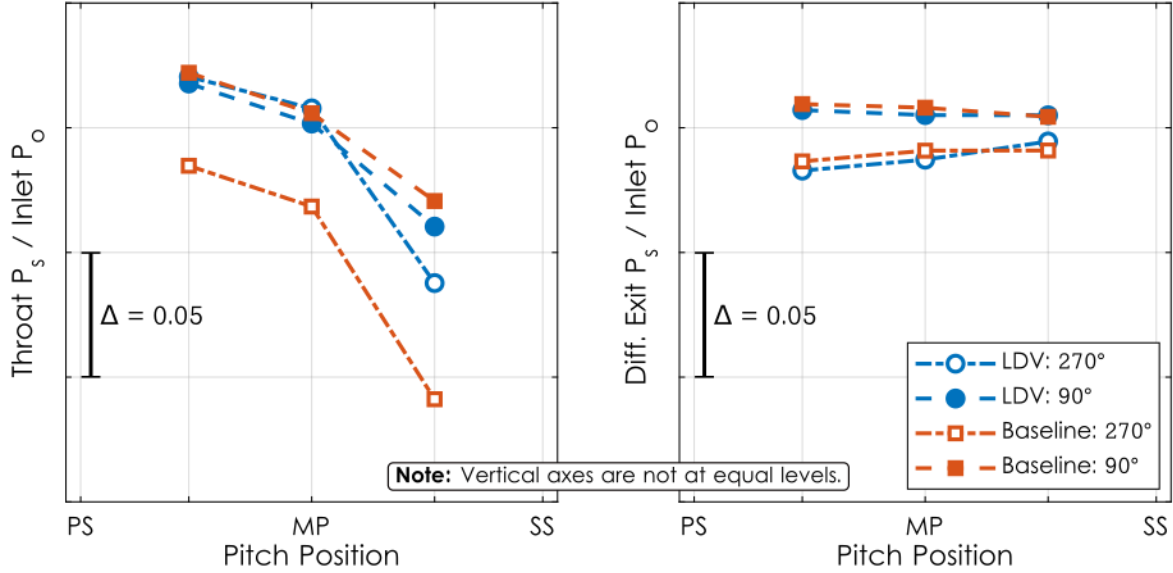


Figure 2.8: Diffuser throat (left) and exit (right) static pressure comparison at design point

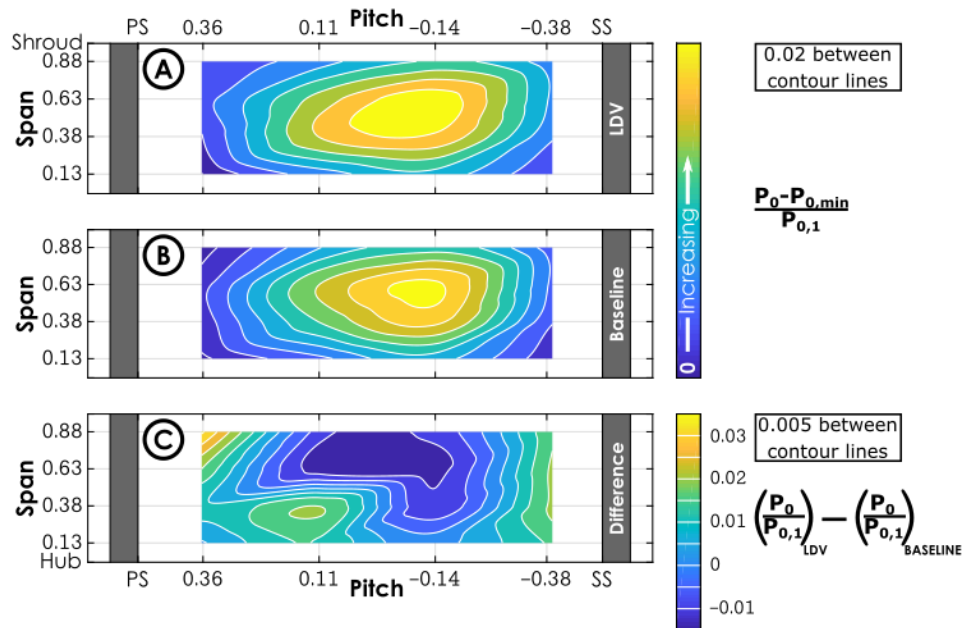


Figure 2.9: Diffuser exit total pressure contour comparison at design point

### 2.3 LDV System

The LDV system utilized for this study is a commercially available three-component system from Dantec Dynamics. The major components of the measurement system include the laser head, the optical transmitter, two probe heads, and the Burst Spectrum Analyzer (BSA). An in-situ designed seed traverse system and a TSI model 9306 six-jet atomizer are used to introduce seed particles

into the flow. A 5.0-Watt Argon-Ion laser head from Coherent Inc. produces the initial laser beam. The internal optics of the optical transmitter then split the beam and select its three primary bands: 514.5 nm (green), 488.0 nm (blue), and 476.5 nm (violet). Each of these three beams, corresponding to each of the three measured velocity components, is then split into two distinct beam paths. One beam of each color pair is passed through a Bragg cell to produce a constant frequency shift of 40 MHz and allow the resolution of negative velocities. Each of these six beams is then output to an optical fiber using an adjustable coupler. Each junction is adjusted in focus and axial and angular alignment until the output power from the fiber is maximized. The beams pass through that fiber and out the head of one of the two probes. The green and blue beam pairs (four total beams) pass through the so-called “2D” probe while the violet pair passes through the “1D” probe. Each probe contains internal optics and a front focusing lens which focuses the beams to a single point. The probes also act as receivers. The scattered light from the measurement volume passes back through the probes’ front lenses, through an optical fiber, to photodetectors mounted in the BSA unit. The BSA unit contains the internal photodetectors and signal conditioners necessary for accurate LDV measurements. The model F80 BSA allows sampling up to 180 MHz with a bandwidth of 120 MHz, allowing measurement of supersonic velocities with large turbulence levels, with appropriate optical configuration. Further details on the BSA operation principles can be found in [124].

To ensure velocities in all three components are measured at the same geometric point in space, an alignment procedure must be completed between the 2D and the 1D probe. First, the 2D probe is mounted in a support arm that can be rotated to move the focal point of the lens. A 50  $\mu\text{m}$  diameter pinhole is placed into position and actuated until all four beams from the 2D probe pass through it. The 1D probe, mounted in a support arm with rotating, tilting, and axial-translation capabilities, is then fixed to the same support structure as the 2D probe and the pinhole. The 1D probe is adjusted, keeping the pinhole at a fixed location, until the two violet beams also pass through the pinhole. This procedure ensures that all three beam pairs sample the velocity field at the same geometric point in space.

### 2.3.1 Traverse and Seed Systems

A three-axis traverse mechanism is used to traverse the measurement volume through the region in question. The traverse has a range of 24 inches and a resolution of 0.00025 inches. The traverse controller is integrated into the Dantec LDV software package for data collection. The alignment of the traverse system to the test compressor coordinate system is critical for accurate measurements. Misalignment causes errors in applying the vector transformation from the LDV skew coordinate system to the laboratory Cartesian system and any geometric differences between the expected and actual measurement locations impede accurate observations of the flow field. To prevent this, a tool was designed to allow the precise alignment between the two coordinate systems. This tool, presented in Figure 2.10, consists of a tight-tolerance machined surface to closely match the contour of the diffuser vane leading edge. Three 0.0040” diameter holes—one labelled “Tool Zero Point” and two forming the “Vertical Axis Reference” in Figure 2.10—were micro-drilled through the piece, and their locations relative to each other and the vane leading edge contour were inspected after machining

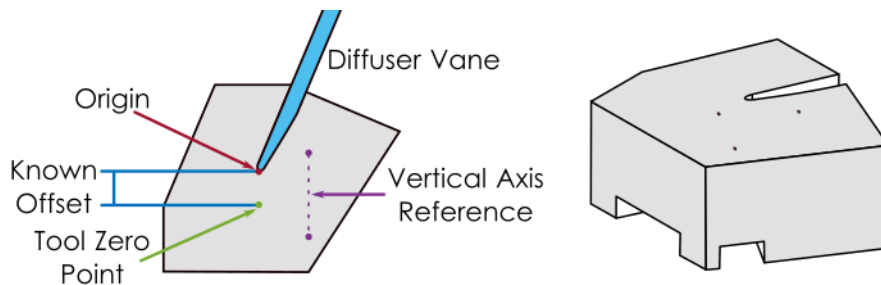


Figure 2.10: Traverse system alignment tool

After the probes are aligned following the procedure detailed previously, the measurement volume is moved to the top of the Vertical Axis Reference pair of holes. The traverse system is translated vertically, and the alignment of the traverse system adjusted until the two Vertical Axis Reference holes align with the vertical motion of the traverse. A similar procedure is followed for the horizontal axis alignment using the Vertical Axis Reference holes and the Tool Zero Point. The orthogonality of the traverse system construction is relied upon to verify the third axis's alignment. The zero point of the measurement coordinate system is defined as the leading edge of a particular diffuser vane. The traverse system is zeroed by first manipulating the measurement volume to align with the Tool Zero Point, and then applying the known offset between the vane leading edge and the Tool Zero Point. The estimated uncertainties in the measurement location—accounting

for the measured tool dimensions, the repeatability of the traverse system, and the dimensions of the measurement volume—are estimated to be approximately 0.0025” in the horizontal and vertical directions and 0.0065” in the third, spanwise, direction. The larger uncertainty in the spanwise direction is due to the elongated nature of the measurement volume ellipsoid in that direction. The uncertainty in the alignment between the traverse and diffuser axes is estimated to be approximately 1°.

An aerosol of Di-Ethyl-Hexyl-Sebacate (DEHS), generated by a TSI 9306 Six-Jet Atomizer, is used as the seed for this study. DEHS was selected due to its small particle size, long aerosol lifetime, low toxicity, and lack of residue upon evaporation. The combination of pressure supplied to the atomizer and the seed material selection, resulted in the distribution of particles presented in Figure 2.11. The corresponding cut-off response frequencies for 1% and 5% slip (see Equation (17)) are also included. For this seed schema, 95% of the particles are expected to follow fluctuations of 25 kHz, with less than 1% slip, or 57 kHz with less than 5% slip. The blade passing frequency is 11.25 kHz, and consequently, these particles are expected to adequately follow the flow. This figure also elicits a significant hurdle in obtaining LDV measurements in turbomachinery. Extremely small particles are required, less than 1  $\mu\text{m}$  in diameter, to adequately respond to the high characteristic frequencies of turbomachinery flows. However, these small particles are both difficult to detect, due to their small scattering amplitudes, and are prone to evaporate prior to measurement, due to their low thermal mass and the often high ambient temperatures.

The seed is introduced into the flow using an actuated mechanism delivering the aerosol to a single 0.5-inch diameter streamtube in the plenum, eight inches upstream of the impeller inlet. The injection point was shifted around the plenum until the data rate was maximized. This method of localized seeding offers a significant advantage over typical global seeding approaches. Localized seeding allows the overall amount of seed injected into the compressor to be minimized—maximizing test duration (by postponing the inevitable condensation of seed on the optical access windows)—while maintaining adequate seed levels in the measurement volume.

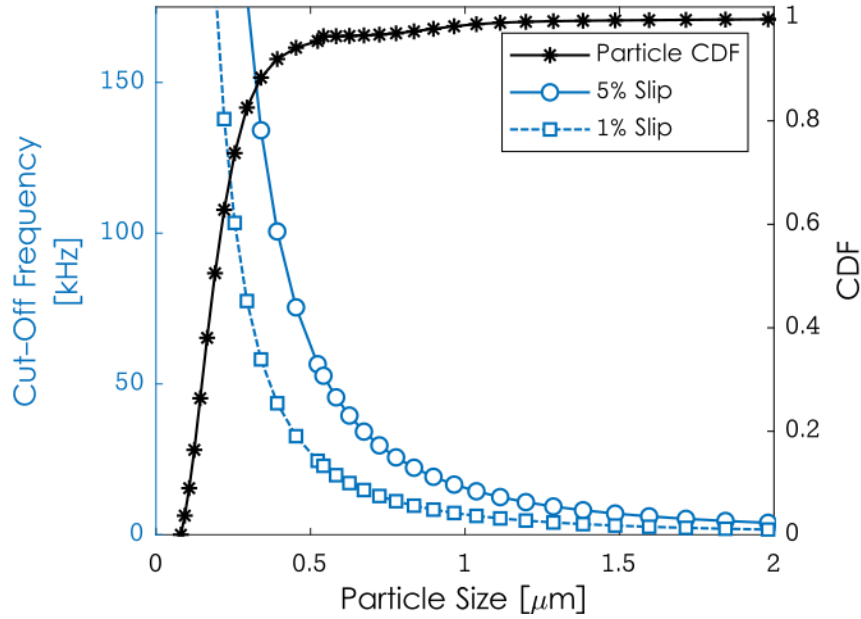


Figure 2.11: Particle size distribution and cut-off frequencies

Seed must be introduced far enough upstream to allow particles to accelerate to the local flow velocity. For particles much denser than the flow medium, the relaxation time for a particle to adjust to the local flow velocity becomes the characteristic timescale of the particle,  $\tau_0$ , as given in Equation (16). A particle injected at zero velocity (the worst-case scenario) will accelerate to within 1% of the flow velocity within an elapsed time of  $6.9\tau_0$  [86]. Streamlines in a steady CFD simulation were utilized to show an elapsed time of  $37\tau_0$  from injection to the forward-most measurement location, indicating sufficient particle adjustment time exists so as to not adversely impact the results.

### 2.3.2 LDV Post-Processing

In non-coincident mode, each acquired data point consists of more than 10,000 individual velocity measurements, each tagged with an instantaneous impeller position, in each of the three components. In coincident mode, each point consists of more than 5,000 three-component velocity vectors, each vector being tagged with a single instantaneous impeller position. The difference is subtle, and in both cases, significant data reduction is necessary to allow a succinct presentation of the data.

The first step in data reduction is the ensemble averaging of the data into a single impeller revolution, followed by a second ensemble average into a mean passage representation. This relies upon the assumption that subsequent revolutions of the impeller can be considered identical replications of each other, and, for the mean passage, that all individual passages are identical. During acquisition, a once-per-revolution (OPR) signal is acquired, indicating the beginning of each impeller revolution. The signal processing conducted during data acquisition tags each validated Doppler burst with the instantaneous angular position of the impeller, as indicated in Figure 2.12, Step A. The instantaneous position represents the angle between the leading edge of the impeller Blade 1 and the OPR sensor location at the moment at which the velocity sample is obtained. This information is then used to compute an ensemble-averaged revolution where the velocity samples from every revolution are overlaid, Step B. At this point, data are analyzed to justify the assumption that each full-blade-splitter-blade dual passage is identical. A second ensemble average can then be utilized to produce a single “representative passage,” knowing the angular spacing of the impeller blades. This is illustrated in Steps C and D of Figure 2.12.

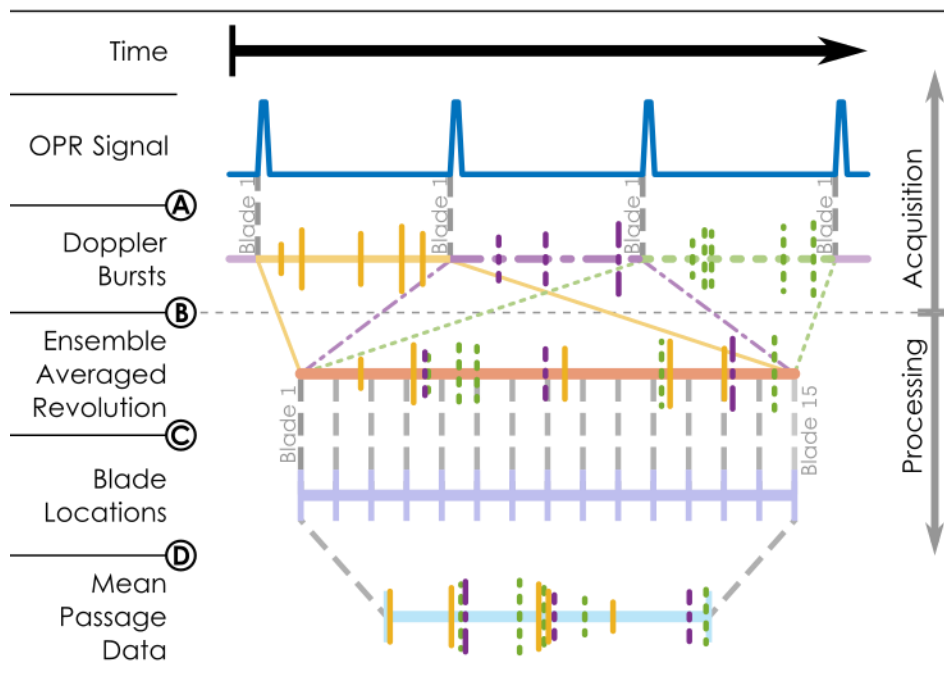


Figure 2.12: Ensemble averaging procedure

The CSTAR impeller contains 15 full and 15 splitter blades, resulting in a  $24^\circ$  spacing between adjacent full blades, with a splitter in between them. All of the data analysis is done on the mean passage representation, with the results assumed to repeat every  $24^\circ$  of impeller rotation. Data are

separated into bins of width  $1^\circ$  and averaged together to yield 24 discrete time steps within one full blade passing event. Time-averaged results are then computed as the arithmetic mean of the averaged data from these 24 time steps. This arithmetic averaging of the data from each time step helps to reduce the skewing results of lower seed density being present within the impeller wake, or within regions of separated or lower-momentum flow that would impact measurements if each sample were weighted equally. The transit-time weighting method, given in Equation (15) on Page 43, is utilized to reduce bias generated by the higher volume-flux associated with higher velocities.

During the initial experimental work, noise was observed, with narrow bandwidth, in all three velocity components. The noise was present at a constant signal frequency between the three channels and two primary central frequencies were observed. The first, with a Doppler frequency equal to the Bragg cell shift frequency (corresponding to 0 ft/s), arose from strong reflections passing through the measurement volume. These reflections produced a measurement of the velocity of the surface from which light was reflecting. An example of this noise is depicted in Figure 2.13A, presenting a histogram of one-component velocity samples at a single geometric location and relative impeller position. The second, centered at a Doppler frequency of approximately 132 MHz, is depicted in Figure 2.13B and Figure 2.13C. The different fringe spacing arising from the different wavelengths used for each component (see Equation (8), Page 40) causes the corresponding velocity signal to have slightly different values for each channel. This noise corresponds to resonance within the primary laser cavity. The first longitudinal mode of the cavity is formed with nodes at either end of the cavity, an anti-node at the center, and a frequency inversely proportional to the length of the cavity. The shape of the mode is identical to that formed by a vibrating string pinned at both ends. This so-called “beat” frequency can be detected in the measurement volume at points where the true signal is weak and is occasionally interpreted as a valid velocity signal.

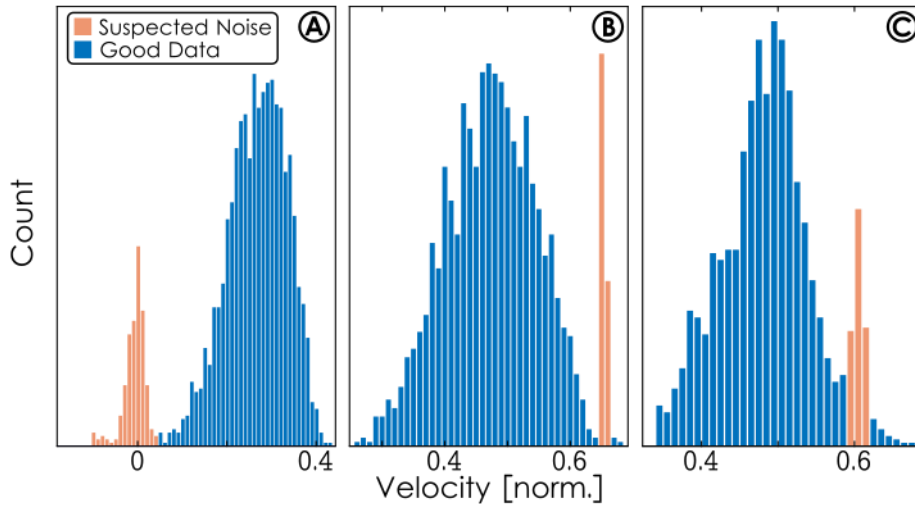


Figure 2.13: Examples of noise in LDV results

In many measurement locations, the noise sources could be removed by adjusting the velocity band accepted by the software. However, flow field velocities overlap with the noise bands' spectral locations and that method would reject true velocity measurements in some locations. For these cases, a post-processing method was developed to aid in isolating and rejecting erroneous measurements, without removing true velocity information.

Identifying and removing the noise manually is a simple process. As evident in Figure 2.13, the noise signals were often dramatic and easily distinguished from the true velocity data that typically follow an approximately normal distribution. Suspect samples could easily be marked and removed after a quick visual inspection of the histograms. However, the test campaign will consist of approximately 2,000 geometric data points, at which three components of velocity will be obtained at 24 time increments. This will produce 144,000 individual histograms that will require manual inspection and processing. This is not a viable way of handling such a large amount of data; an automated method is required.

Drawing from a sabermetrics example that applied statistical mixture modeling to sort data drawn from two populations, without knowing a priori which sample arose from which population [125], an "Expectation-Maximization" iterative technique was developed. The first step is to split the data into two groups. If a distinct mode is detected around one of the two noise centers, the band of data surrounding that mode is placed in one group and the remaining data in the second. In

cases where no clear noise mode is detected, then the samples are split randomly. A maximum-likelihood method is then used to fit a continuous beta distribution to each of the two groups, the “Maximization” step. The continuous beta distribution was chosen as it is simple, being described by only two parameters, yet still allows for skew, which may be present in the data. With random group assignments the two distributions are, initially, nearly identical. However, due to the discrete number of velocity samples, there must always be a marginal difference in the proportion of noisy data, if any, in each group. The result is a slightly higher probability that invalid measurements are in one of the groups rather than the other. The mixture modeling method exploits this marginal difference to divide the data. If the groups were assigned based on a detected mode, the two distributions are already significantly different.

Using the two distributions, two probabilities are calculated for each data point. The first, corresponding to Group A, is the value of the probability density function (PDF) fit to Group A, multiplied by Group A’s prior probability. The prior probability is a concept from Bayesian statistics. In this case, it is simply equal to the number of data points placed in Group A on the previous iteration divided by the total number of data points. This calculated probability can be described as the probability that each data point was produced by the PDF fit to Group A, weighted by the probability that it was previously placed into Group A. The second calculated probability is the analogous value computed for Group B. These two probabilities are computed for the data points in both groups and then compared. For each data point, ignoring the group that the data point was placed into previously, if the probability corresponding to Group A is greater, then the data point is placed into Group A for the next iteration. Otherwise, it is placed into Group B. This forms the final portion of the “Expectation” step of the procedure—placing each data point into the more likely group. This procedure can be summarized in simple terms. Probabilities are computed quantifying the likelihood that a data point arose from the beta distributions fit to either Group A or Group B and that point is placed into the more likely group for the next iteration.

This process continues—iteratively fitting beta distributions to each group and reassigning data to groups—until no data points are reassigned to a different group between iterations. In cases where no noise is present, the result is that all data points are shifted into a single group and the method detects, accurately, that no noise is present in the original data. In cases where the converged solution still contains two groups, a criterion is applied to determine which values can be discarded

with high confidence. First, the group containing the suspect data is determined by comparing the mean of each group to the known noise centers. Then, the probability that each data point arose from the distribution corresponding to the noise is computed applying Bayes’ Theorem:

$$P(U_i \in \text{noise}) = \frac{\text{Beta}(U_i; \alpha_{\text{noise}}, \beta_{\text{noise}})}{\text{Beta}(U_i; \alpha_{\text{noise}}, \beta_{\text{noise}}) + \text{Beta}(U_i; \alpha_{\text{real}}, \beta_{\text{real}})} \quad (19)$$

where  $U_i$  represents a single velocity sample, and “Beta( $U_i, \alpha, \beta$ )” refers to the PDF of the beta distribution evaluated with parameters  $\alpha$  and  $\beta$ , evaluated at  $U_i$ . These parameters are the values that were fit to each group in the final, converged grouping of the data. If this probability, essentially the probability that a sample is considered noise, is greater than a cut-off value (0.95 in this study) then the data point is labelled “noise” and removed from further analysis. The entire process is outlined graphically in Figure 2.14.

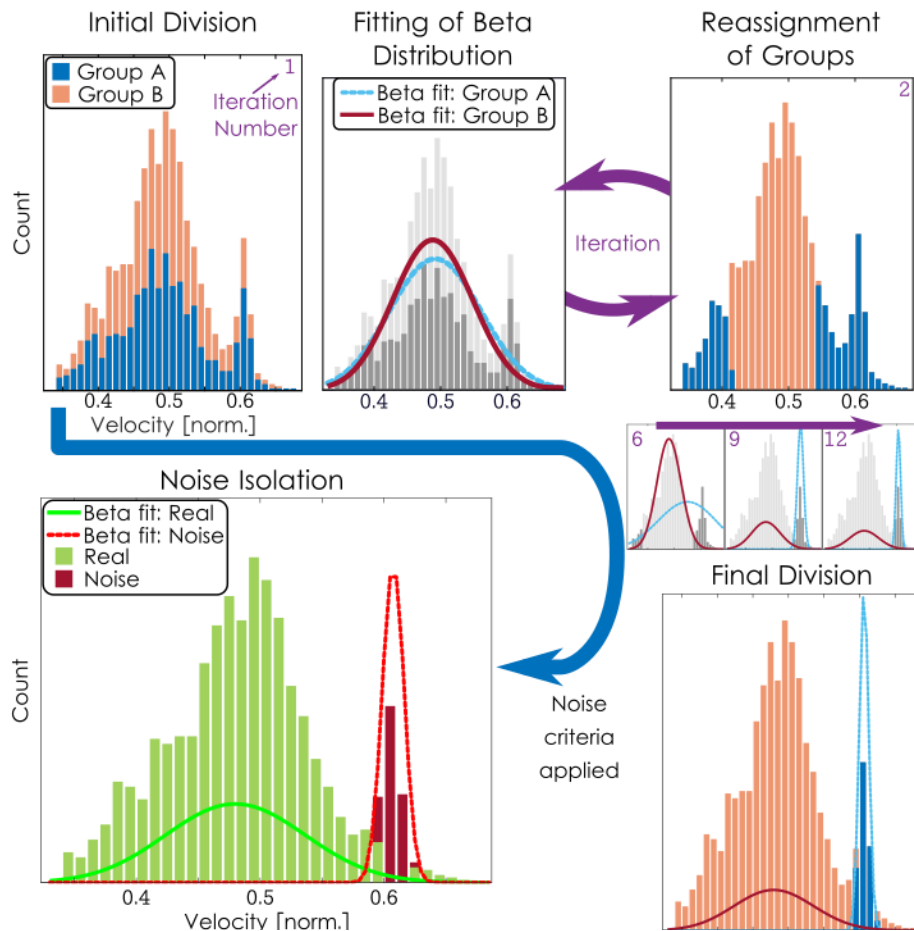


Figure 2.14: Mixture modeling process

The process was evaluated and validated, using a portion of the data, to ensure the algorithm functions as expected. Certain checks are permanently built into the post-processing code. Images of certain histograms showing the data labelled “noise” are selectively saved for manual inspection; examples are given in Figure 2.15. Every case that meets at least one of three criteria is saved for further inspection: if more than 5% of the original data are labelled “noise;” if the “noise” mean differs from the expected noise centers; or if the noise removal causes the data mean to shift by more than 10 ft/s. These “marked” outputs allow the user to manually verify that true data samples are not rejected and that any shifts produced by the algorithm exclusively arise from noise removal. For initial validation, a random additional 1% of the final histograms were also saved to further evaluate the algorithm’s performance. These two output reasons, “marked” and “random,” were chosen to evaluate the Type II and Type I error rates of the algorithm. The type II error, a “false-negative,” corresponds to the percent of randomly outputted results (for which the algorithm deems no noise is present) in which noise, in fact, is present. The Type I error corresponds to the percent of “marked” results in which the noise determination is incorrect. The manual inspection of the output from the initial algorithm run (processing 57,168 individual histograms) is summarized in Table 2.1. Computing a 99% confidence interval on the true rate of Type II error yielded an upper bound of 1.3%. A similar confidence interval for the true rate of Type I error, the proportion that are incorrectly filtered, yields an upper bound of only 2.7%. This supports the high accuracy of the developed algorithm; however, manual inspection of the “marked” results is advised due to the significant consequences of Type I error (incorrectly removing true samples). The primary goals of the post-processing method have been achieved: it correctly removes data; it rarely misses noise that is present; and it reduces the number of manual inspections required by 95% (from 57,168 to 2,394) when the “random” output method is not used.

Table 2.1: Mixture modeling process validation results

<b>Output Reason</b>	<b>Total Number</b>	<b>Number Incorrect</b>	<b>Percent Incorrect</b>
<b>Marked</b>	2,394	45	1.88%
<b>Random</b>	570	1	0.17%

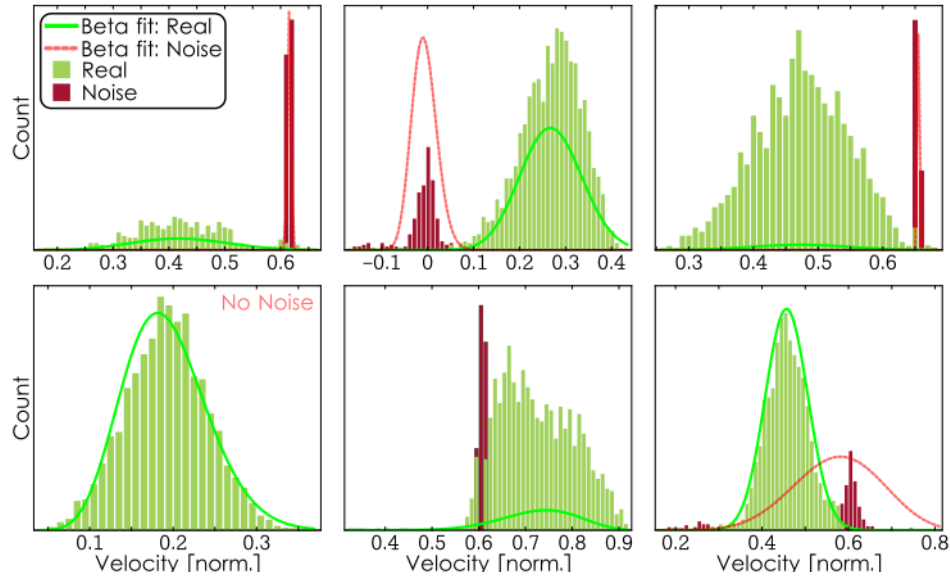


Figure 2.15: Noise removal example results

The filtered results are then transformed from the skew coordinate system of the LDV system into the Cartesian, laboratory coordinate system applying Equation (20) (Page 76). An example of the results in the Cartesian coordinate system, showcasing the success of the mixture-modeling noise removal algorithm, are given in Figure 2.16. This figure presents the axial velocity measured at 85% span through the diffuser entry region at a single relative impeller-diffuser position. The raw data are on the left, and the results after the mixture-model filter is applied are on the right. A band of axial velocity toward the shroud adjacent to a band of velocity toward the hub is discernable in the filtered result, but not the unfiltered result. These bands are indicative of the jet/wake flow at the impeller exit and support the benefit obtained through the noise removal algorithm. Results will be presented and discussed subsequently; this figure is only presented as an example of the performance of the mixture-modeling algorithm and transformation to Cartesian coordinates.

Vector data are also analyzed in the stream-pitch-span passage coordinate system. The streamwise direction, with the positive sense being in the bulk flow direction, is defined in the vaneless space as tangent to the logarithmic spiral aligning with the vane leading edge. Within the passage, the streamwise direction is defined as parallel to the passage centerline. The pitchwise direction is defined as perpendicular to the local streamwise direction, in the plane of the diffuser, with the

positive sense being toward the pressure side of the vane. Mid-passage (MP) is assigned as 0% pitch with the pressure and suction surfaces (PS and SS) corresponding to +50% and -50% pitch respectively. The spanwise direction, to maintain a right-handed coordinate system, is then defined as out of the plane of the diffuser, with the positive sense being from the hub toward the shroud. It is important to note that in the passage frame the direction of the positive spanwise coordinate is opposite of the positive  $z$ -axis in the Cartesian coordinate. For that reason, the labels “toward shroud” or “toward hub” will always be included in presentations of the spanwise velocity to avoid ambiguity.

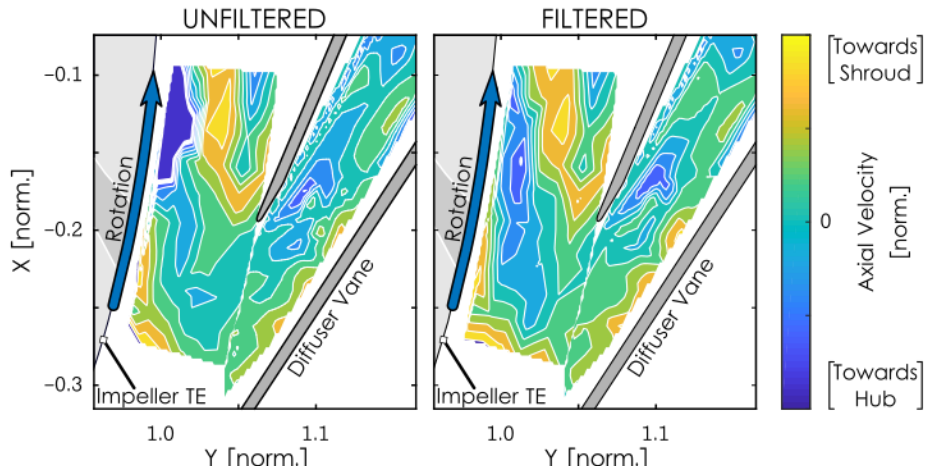


Figure 2.16 : Example results in Cartesian coordinate system

### 2.3.3 Relevant System Parameters

Detailed information regarding the optical setup of the system, as implemented in this study, are presented in Table 2.2 and Table 2.3. Table 2.2 details the relevant system settings and optical parameters utilized in the study. The maximum velocity in LDA<sub>1</sub> and LDA<sub>3</sub> were not quite large enough to fully resolve the highest velocities observed in the vaneless space. The only means of correcting this would be to switch to a 500 mm focal length lens which would, unacceptably, increase the measurement volume size by a factor of nearly ten. Various geometric orientations of the probes are required to obtain data in the hub corners of the pressure and suction surfaces of the vane. Mirrors are used to pass the beams into the flow field from different directions, and the three geometric configurations are described in Table 2.3. In this table,  $\theta_1$  is the angle in the horizontal plane between the measurement direction of the second velocity channel, LDA<sub>2</sub>, and the central axis of the impeller. The angle  $\theta_2$  is defined in the vertical plane between the 1D probe

measurement direction, channel, LDA<sub>3</sub>, and the vertical axis. The first channel, LDA<sub>1</sub> directly measures the vertical component of velocity,  $V_x$ , in all configurations. These angles and the relationship between the measurement directions and analysis coordinate system are given in Figure 2.17. Vector projection and the mathematics of basis transformation yields the transformation matrix for converting velocities measured in the skew coordinate system of the LDV probes to the Cartesian coordinate system:

$$\begin{pmatrix} V_x \\ V_y \\ V_z \end{pmatrix} = \frac{1}{\sin(\theta_2) \cos(\theta_1)} \begin{pmatrix} \sin(\theta_2) \cos(\theta_1) & 0 & 0 \\ \sin(\theta_1) \cos(\theta_2) & \sin(\theta_2) & -\sin(\theta_1) \\ -\cos(\theta_2) \cos(\theta_1) & 0 & \cos(\theta_1) \end{pmatrix} \begin{pmatrix} \text{LDA}_1 \\ \text{LDA}_2 \\ \text{LDA}_3 \end{pmatrix}. \quad (20)$$

The coordinate system utilized in the analysis was chosen to align with the coordinate system of previous computational results. The origin lies at the center of rotation of the impeller. The  $x$ -axis is vertical, with the positive direction oriented upwards. The  $y$ -axis is horizontal, with the positive direction oriented to the right when viewing the compressor from the front. The  $z$ -axis, to maintain a proper right-handed coordinate system, is along the axis of the impeller with the positive direction oriented from the front to the rear of the compressor, the direction of the inlet air flow. This means that a positive  $V_z$ , in the diffuser passage, is a velocity from shroud to hub, which is counterintuitive to some.

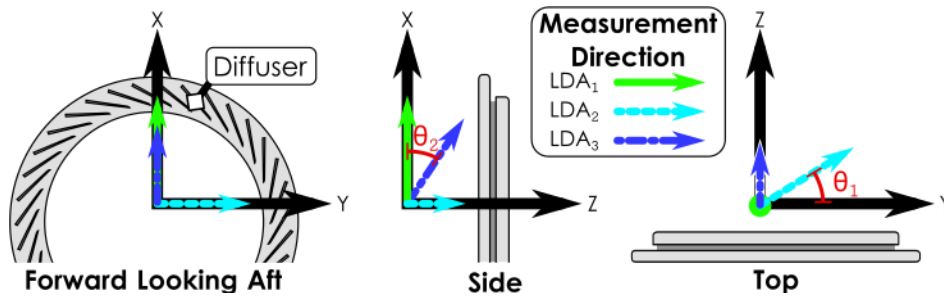


Figure 2.17: Measurement directions and coordinate system

Table 2.2: LDV system parameters

	LDA <sub>1</sub>	LDA <sub>2</sub>	LDA <sub>3</sub>
<b>Wavelength (nm)</b>	514.5	488.0	476.5
<b>Beam Diameter (mm)</b>	2.20	2.20	2.20
<b>Beam Spacing (mm)</b>	38.94	38.54	38.44
<b>Focal Length (mm)</b>	159.8	159.8	159.4
<b>Beam Angle (°)</b>	13.89	13.75	13.75
$\delta_x$ (mm)	0.0479	0.0455	0.0443
$\delta_y$ (mm)	0.0476	0.0451	0.0440
$\delta_z$ (mm)	0.3934	0.3770	0.3672
<b>Fringe Spacing (<math>\mu\text{m}</math>)</b>	2.13	2.04	1.99
<b>Number of Fringes</b>	22	22	22
<b>Maximum Velocity (ft/s)</b>	977	936	914
<b>Minimum Velocity (ft/s)</b>	-279	-267	-261

Table 2.3: Optical transformation angles

	Configuration 1	Configuration 2	Configuration 3
$\theta_1$ (°)	17.23	-20.20	22.24
$\theta_2$ (°)	30.69	30.00	-21.30

## 2.4 Numerical Approach

Numerical simulations were utilized to complement the experimental work in this study. The experimental data obtained form the primary focus of this work; however, CFD yielded a tremendous amount of data regarding the flow field. By pairing rigorous CFD with extensive experimental data, a deeper understanding of flow phenomena was developed. This included the ability to trace the origin of particular flow features upstream in the flow field. The experimental data were also used to help improve CFD methodology for simulating the flow within a centrifugal compressor.

All computations were performed utilizing the commercial ANSYS CFX code Version 19.1. It is a RANS pressure-based solver operating on an element-based finite volume method with a

nonlinear advection scheme. ANSYS TurboGrid was used to generate the solution grid in both the impeller and the diffuser domains and a structured topology of hexahedra elements in O, C, and H blocks was implemented. The solver itself was unstructured, despite the structured grid, and fully implicit, utilizing LU decomposition. Total temperature and total pressure values were prescribed at the inlet plane and either a mass-flow or static pressure exit boundary condition was prescribed depending on the simulated operating condition of the compressor. Static pressure boundary conditions were required as the stage approached the choking condition because of the slope of the performance characteristic.

Steady simulations were primarily conducted using a mixing-plane interface between the impeller and diffuser domains. This method allows for flow in both directions across the interface and circumferentially averages the unsteady flow leaving the impeller in such a way as to conserve mass, momentum, and energy [115]. Some simulations were conducted with a frozen rotor interface. The angular offset between the impeller and diffuser domains was varied between  $0^\circ$  and  $24^\circ$  (one full impeller blade pitch) to produce a first-order treatment of unsteady behavior and allow comparison to the unsteady simulations. The unsteady simulations utilized the Time Transformation method to account for the unequal pitch ratios between the impeller and diffuser. The Profile Transformation method led to erroneous conclusions due to the artificially forced periodicity in the flow features while the Fourier Transformation method presented convergence issues. The transient solution was advanced in time using a fully implicit, second order, backward Euler scheme. For convergence in the transient solution the exit duct of the compressor stage was extended with an extremely coarse grid as a so-called “sponge” layer. This was done to prevent the transient pressure information from reflecting off the exit boundary and interacting with the compressor flow field. Reflections were occurring and causing solutions to diverge during initial attempts to conduct the unsteady simulation. This addition contained inviscid and adiabatic walls, and results were still probed at the same locations as the original grid, in order that the solution would not be altered by the addition. Although this addition was necessary, it did slow convergence as more time steps were required for information to propagate from the inlet plane to the exit plane and back.

Scalable wall functions were implemented adjacent to smooth walls to overcome problems that could arise from near-wall meshing. A sand-grain roughness height [26] was applied to rough

walls in which the roughness was modeled via a downward shift in the near-wall logarithmic velocity profile. Where accessible, the average surface roughness was measured on the experimental hardware. Historically, various approaches have been applied to convert from average roughness to an effective sand-grain roughness for numerical implementation. A simple multiplier is typically applied to the average roughness to yield the effective sand-grain roughness [126]. An average of the multipliers given in relevant studies [127–129] was taken yielding a factor of 8.4 that was used for this study.

Isothermal walls were applied numerically to the shroud side of the flow path to model heat transfer effects. Because the heat flux was not easily measured experimentally, temperature measurements at thirteen locations in the meridional direction were obtained experimentally and applied as an isothermal condition numerically. These measurements were obtained on the outer wall of the shroud, however, the relatively thin walls, low heat flux, and high thermal conductivity of the shroud material (stainless steel) resulted in a negligible difference between the inner and outer wall temperatures. This assumption was verified using the computed heat flux and radial conduction equations to calculate a “corrected” inner wall temperature which showed no significant difference from the prescribed temperature. The measured temperatures followed a piece-wise linear relationship with radius through the stage as illustrated in Figure 2.18. For this illustration, the inlet total temperature measured value was prescribed an artificial radius of 0. In the inlet domain the wall temperature increased only slightly due to conduction from the downstream components. Through the impeller, the temperature increased linearly with radius to a nearly constant value through the diffuser and downstream components. Figure 2.18 displays both the measurements and the three linear fits that were constructed to apply these relations to the numerical grid for a single operating point. The linear fits were shifted slightly to maintain continuity at the interfaces between the three regions and new fits were constructed based on the experimental measurements for each operating point computed numerically.

Simulations were conducted using the  $k$ - $\omega$ ,  $k$ - $\epsilon$ , and SST two-equation turbulence models. The Spalart-Allmaras one-equation model, two EARSM models (based off the  $k$ - $\omega$  and  $k$ - $\epsilon$  models), and two full Reynolds stress models were also implemented to determine which best predicted the flow development through the stage. Finally, simulations were conducted with and without fillets to determine their impact on flow development.

The solution domain began far enough upstream of the impeller leading edge, so the inlet flow is assumed to be purely axial. The exit domain, except in the transient case mentioned previously, ended at the exit of the deswirl component. The collector and the impeller backface cavity were not included in these simulations.

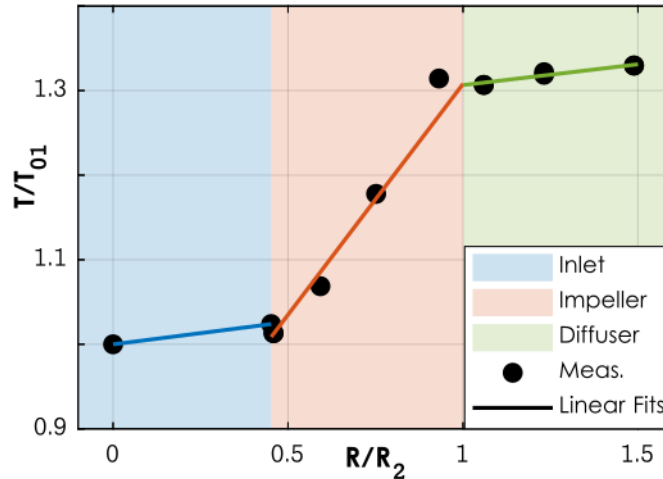


Figure 2.18: Surface temperature profile through stage

#### 2.4.1 Grid Independence Study

A grid independence study was conducted with grids containing from 430,000 to 39,000,000 (39M) total nodes through the impeller and diffuser domains. The impeller domain consisted of 1/15<sup>th</sup> of the impeller wheel, representing one full-blade- and one splitter-blade-passage while the diffuser domain consisted of two diffuser passages. This combination was selected to maintain the domain pitch ratio within the stability limits required for implementing the Time Transformation method. The grid independence study results are presented in Figure 2.19 in terms of predicted stage isentropic efficiency. Below 13M nodes, the isentropic efficiency increased significantly with grid refinement. The efficiency increased by 0.14% between 13M and 21M, 0.04% between 21M and 31M, and 0.01% between 31M and 39M. Many would conclude that the 21M node or even the 13M node case were sufficient based on these results. However, the 31M node case was selected for all further analysis for several reasons. This grid independence study was conducted only for a single combination of modeling parameters (SST turbulence, with smooth walls, no heat transfer, and no fillets). Therefore, the denser grid was selected to ensure that the grid would remain adequate even with these modeling choices. Secondly, the denser

grid was selected to more fully capture details of the flow development, even if they did not effect a discernible shift in the stage performance. The resulting grid consisted of 16.1M nodes in the impeller domain and 7.4M in each of the two diffuser passages with a  $y^+$  maintained below 10 along all solid surfaces. The impeller domain contains approximately 90 spanwise nodes, 85 pitchwise nodes within each passage, and 31 spanwise nodes within the tip gap. The diffuser contained approximately 120 spanwise nodes and 110 pitchwise nodes within each passage.

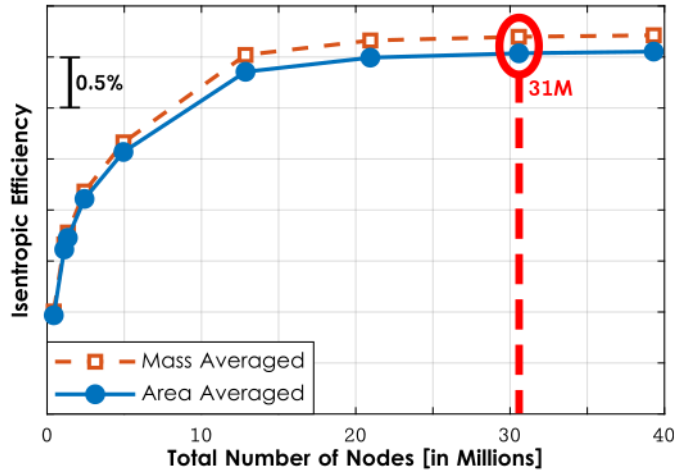


Figure 2.19: Grid independence study results

### 3. LASER DOPPLER VELOCIMETRY RESULTS AND DISCUSSION

#### 3.1 Overview of Obtained Data

A detailed, systematic grid of LDV measurements was obtained at the compressor design point to characterize the unsteady flow field through the vaned diffuser. This was composed of three phases. The first phase consisted of a dense grid through the entire diffuser from the impeller exit through approximately 70% of the diffuser passage (the limit of optical access) that included six spanwise positions: 15%, 30%, 50%, 70%, 85%, and 95%. Data acquisition was also attempted at 5% span; however, the signal quality was too low to yield any meaningful results. The goal of this phase was to provide an overall characterization of the unsteady flow development through the diffuser. Data points were located at eight constant-radius arcs between the impeller tip and the diffuser leading edge spanning 1.2 diffuser pitches (approximately equivalent to the angular spacing between adjacent impeller blades). In the semi-vaneless space, 34 points were placed to show the adjustment of the flow to the presence of the vanes. Within the passage, nine pitchwise points at thirteen streamwise planes were attempted to show the development of the flow to the throat and through the remainder of the passage. Additional points were placed between these cross-passage planes in the region surrounding the throat and further downstream in the passage (where the full passage width was not optically accessible). The total number of distinct points in the first phase was 290 (at each of which six spanwise positions were attempted). The location of these points is indicated by the circles in Figure 3.1A. The shading of each circles represents the number of spanwise positions at which data were acquired. In general, all points were successfully acquired except points at 30% span in configurations that required mirrors (typically adjacent to the vane surfaces) and at some points closest to the impeller where optical access was not possible, as indicated in Figure 3.1A.

The second phase of data acquisition aimed to increase spanwise resolution and better resolve hub-to-shroud gradients at several key measurement planes. Thus, data at seven additional (thirteen total) spanwise positions were obtained at radius ratios of 1.0125 (near the impeller tip), 1.05 (in the vaneless space), and 1.08 (at the vane leading edge), as well as at the throat, just upstream and downstream of the throat, and at approximately 20% and 40% diffuser passage (downstream of the throat). The location of these planes is indicated in Figure 3.1B where the shading of each

circle indicates the number of spans at which data were acquired. The additional spanwise positions were at 10%, 20%, 40%, 60%, 80%, 90%, and 97.5%. Data acquisition was also attempted at 2.5% span; however, the signal quality was too low to yield meaningful results. Most points were successfully acquired, except points at 20% span in configurations that required mirrors and at some points at a radius ratio of 1.0125, as indicated in Figure 3.1B.

The final phase of data acquisition focused on obtaining, for the first time, the full Reynolds stress tensor at several locations through the flow field. These points are distributed as follows: three in the vaneless space, two at the diffuser leading edge radius, one in the semi-vaneless space, three at the throat, and three downstream of the throat as noted in Figure 3.1C. At these points, a significantly longer data acquisition time was utilized to obtain coincident data. This allowed the determination of the local Reynolds stress information at each point as the correlations between fluctuations in all three velocity components were directly measured. Due to the higher signal requirements of coincident collection, data were only acquired at and above 40% span at all points with the exception of Point 43 (see Figure 3.1C for Point ID information) and Point 10. Data were only acquired at and above 85% span at Point 43 (at a radius ratio of 1.0125), due to reflections from the impeller blades, and at and above 50% at Point 10, as indicated in Figure 3.1C.

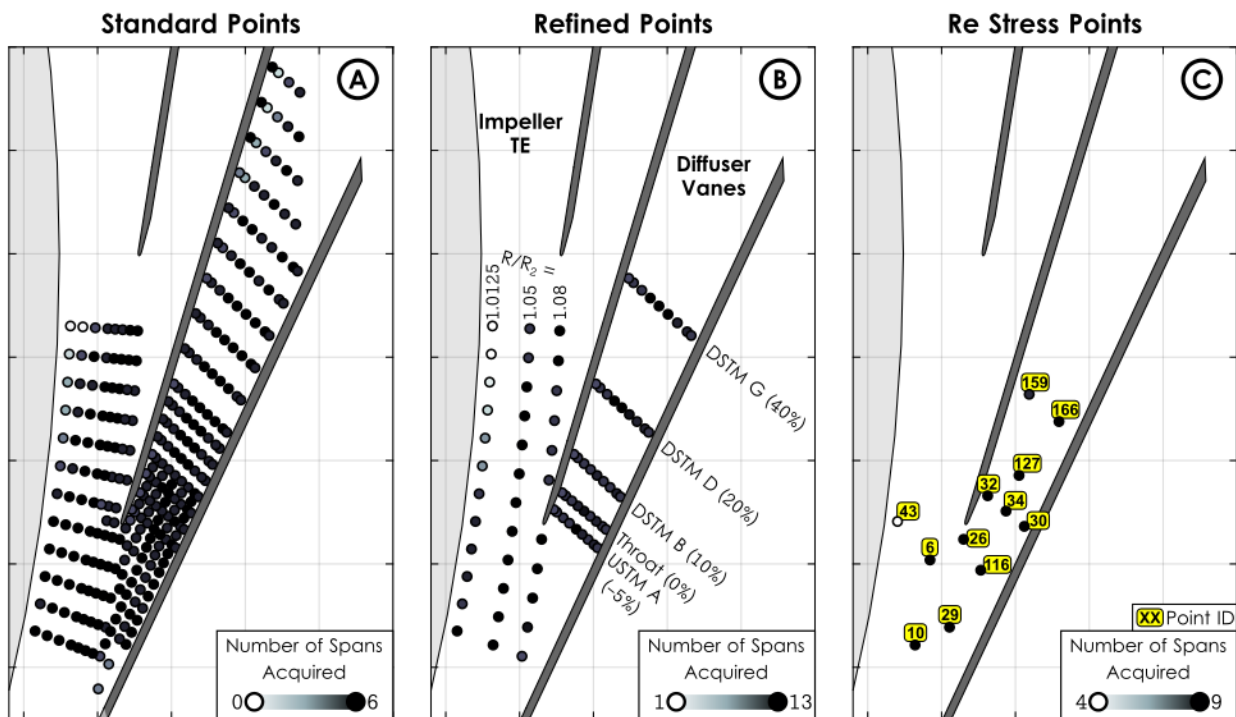


Figure 3.1: LDV acquisition map for the standard points (A), refined points (B), and Reynolds stress points (C)

All data were acquired at the compressor design point. The acquisition time at each point varied depending upon the achieved data rate with longer acquisition times needed in regions of separated flow or areas where the signal-to-noise ratio was reduced. Data rates were typically between 700 Hz and 1.5 kHz and data were acquired for 60 seconds. In some regions, data rates dropped to approximately 100 to 200 Hz and acquisition times were extended as long as 150 seconds to ensure sufficient data were collected. Coincident points were acquired for 5 to 7 minutes with data rates falling between 50 and 150 Hz. In total, data were collected at 2,036 geometric points (including the 102 coincident points).

As mentioned in Section 2.3.2, all data analysis was based on a mean passage representation. To justify this assumption, the velocity magnitude data at a radius ratio of 1.0125 at 50% span is portrayed for all fifteen dual passages (splitter blade and full blade) in Figure 3.2. The ordinate is the velocity magnitude normalized by the impeller tip speed ( $U_2$ ) and the abscissa is time ( $t$ ) normalized by the full blade passing period ( $t_{BP}$ ). The approximate instances representing the passage of a splitter blade (SB) and full blade (FB) are indicated by the corresponding vertical lines. The average difference between the minimum and maximum values from all fifteen passages at a single instance in the blade-pass period is less than 2.5%. This value is partially inflated by the sharp gradients measured immediately behind each blade and these data indicate sufficient justification for the use of the mean passage representation.

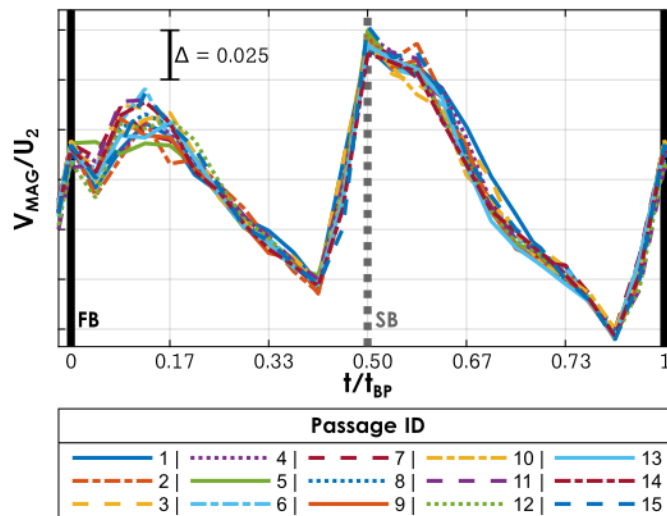


Figure 3.2: Passage-to-passage variation in velocity magnitude at  $R/R_2 = 1.0125$ , 50% span

The detailed nature of the acquired dataset in both space and time require a multi-faceted approach to fully analyze and illustrate important features of the flow field. First, the data will be visualized at constant span “slices” of the diffuser passage in Section 3.2 to present a general overview of the flow field. Section 3.3 will then focus on the development of the impeller jet and wake through the diffuser inlet region. The nature of the flow progression through the full passage will then be visualized on cross-passage planes in Section 3.4. Section 3.5 will then combine the observations from the previous sections in detailing the unsteady formation of a passage spanning vortex. Finally, Section 3.6 will focus on the details of the obtained Reynolds Stress measurements.

### **3.2 Velocity Vector Field at Constant Span**

The time-averaged results for the three velocity components are presented in Figure 3.3 (streamwise velocity), Figure 3.4 (pitchwise velocity), and Figure 3.5 (axial velocity). The streamwise velocity,  $V_S$ , and the pitchwise velocity,  $V_P$ , are normalized by the impeller tip speed,  $U_2$ , and the axial velocity,  $V_z$ , is presented in ft/s. For each component, data are presented at 30% span (A), 50% span (B), 70% span (C), and 95% span (D). In the vaneless space, the streamwise velocity data (Figure 3.3) illustrate the potential field influence of the diffuser vanes on the time-averaged flow deceleration upstream of the passage. The flow, in general, decelerates with increasing radius due to the increase in flow area. Near the leading edge of the diffuser vanes, a region of flow with lower streamwise velocity (relative to other locations at the same radius) exists at all spans. This region represents the potential field of the diffuser vanes as the flow adjusts to the downstream presence of the vanes. The potential field extends to the smallest radius (the closest to the impeller trailing edge) at 30% span and this extent decreases with increasing span. A comparison of corresponding contour levels between the four spanwise positions shows that the potential field extends to an approximate radius ratio of 1.025 at 30% span, 1.0375 at 50% span, and 1.05 at 70% and 95% span. These details of the potential field are important for several reasons. First, as designs trend toward smaller radial gaps between the impeller and diffuser, there is an increased risk of aeromechanic and aerodynamic interaction between the components. The diffuser’s potential field extending into the rotating impeller domain can cause unacceptable aeromechanic response at the impeller trailing edge and can influence the stall and surge behavior of the stage. Additionally, the spanwise trend indicates that hub- or shroud-based static pressure measurements may overestimate or underestimate (respectively) the extent of this potential field.

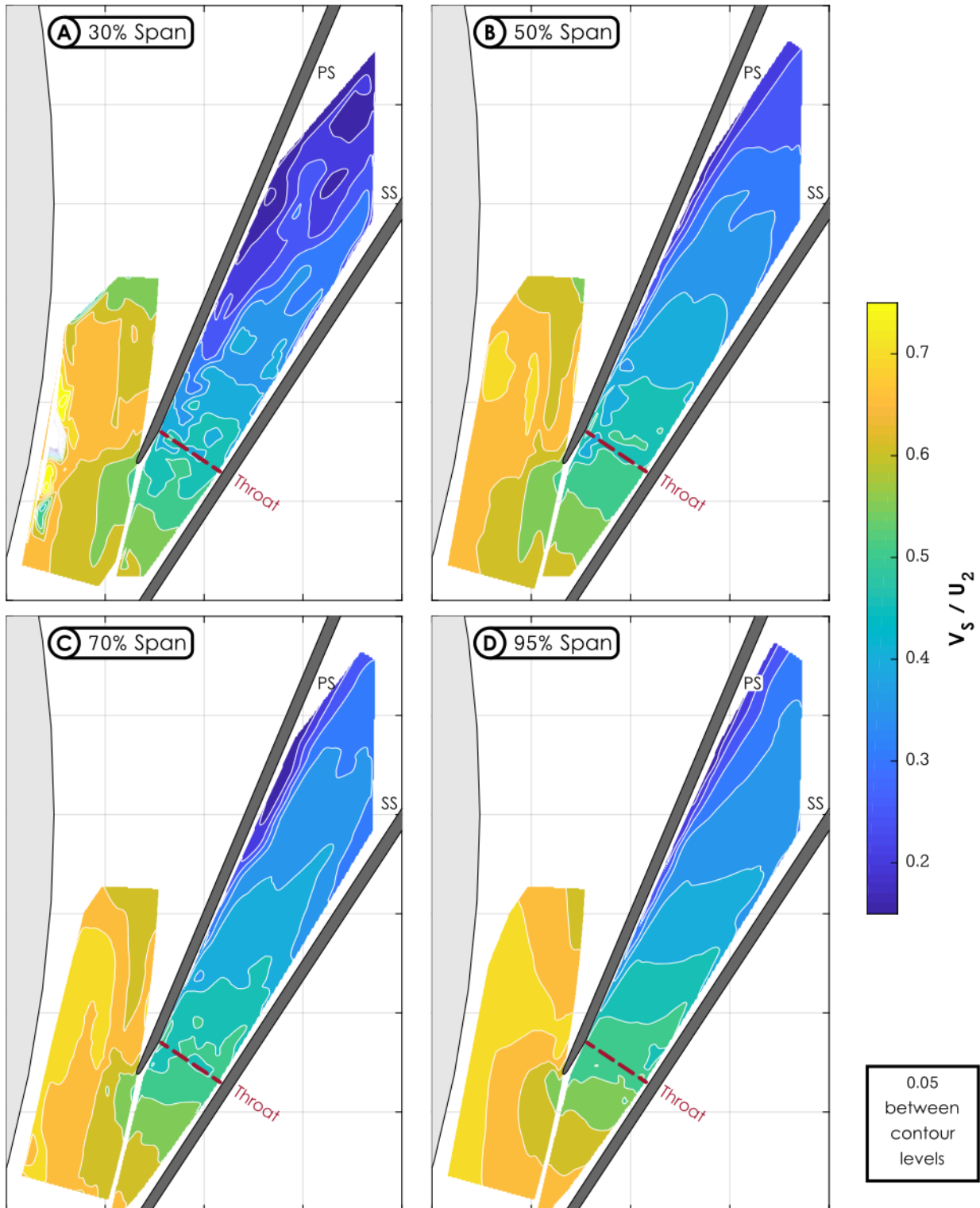


Figure 3.3: Time-averaged streamwise velocity normalized by the impeller tip speed at 30% (A), 50% (B), 70% (C), and 95% (D) span

Proceeding downstream, the semi-vaneless space and the near-throat regions indicate relatively uniform deceleration (in the streamwise direction) of the flow with little cross-passage gradient in the streamwise velocity. In other words, the lines of constant streamwise velocity are roughly perpendicular to the vanes. This represents an effective diffusion process as the diffusion “load” is evenly distributed across the full passage width. However, downstream of the throat, a low streamwise velocity region develops along the pressure surface of the vane. At 30% span, this region of low streamwise velocity grows out from the pressure surface of the vane, beginning just downstream of the throat until it fills most of the passage width at the downstream limit of the measurements. At the higher spanwise positions the cross-passage gradient in streamwise velocity develops more slowly and less dramatically, with a much smaller region of low streamwise velocity developing along the pressure surface of the vane. These data suggest flow separation occurring along the pressure surface of the vane near the hub. The blockage induced by this region of flow separation induces an acceleration along the suction surface of the vane and results in the observed profiles of streamwise velocity.

The pitchwise velocity (Figure 3.4) illustrates the adjustment of the flow leaving the impeller associated with the presence of the vanes. The vane acts as a divider of the flow in that a streakline must pass into one of the two passages bordering the vane. Just upstream of the leading edge at all spans, a region of more positive pitchwise velocity is observed. This represents the flow diverting to pass on the counterclockwise side of the vane rather than into the passage in which data were obtained. This is observed at all spanwise positions; however, the region has a smaller circumferential extent at 95% span, implying more radial flow adjacent to the endwall. Fundamentally, this is the result of surface friction acting on the flow. In the vaneless space, the flow field is characterized by flow that is nearly tangential (typically between 70 and 90 degrees from radial). Considering this flow from a two-dimensional perspective, this indicates that the tangential velocity component is significantly larger than the radial velocity component. Since frictional forces are proportional to the square of the velocity, the frictional force acting in the tangential direction is larger than the force acting in the radial direction. The result is a larger deceleration of the tangential velocity and a turning of the flow toward radial. Within the passage, the pitchwise velocity profile is relatively chaotic (in that no distinct profile is apparent) through the throat. Downstream of the throat, a region of high velocity toward the PS is present for a narrow pitchwise extent along the pressure surface of the vane. This region extends across a larger

portion of the pitch at 30% span but extends for a larger streamwise distance at 50% and 70% span. The remainder of the passage is characterized by a slight cross-passage gradient (increasing toward the PS) and relatively little change in the streamwise direction.

The axial velocity data (Figure 3.5) in the vaneless space show a region of large axial velocity toward the shroud between a radius ratio of 1.025 and 1.065, extending for about half of the circumferential extent of the dataset and centered (circumferentially) in line with the vane leading edge. This is present at 30%, 50%, and 70% span, although the precise shape and location is shifted slightly. From a radius ratio of approximately 1.065 to the vane leading edge radius (at a radius ratio of 1.08) the axial velocity is predominantly toward the hub at all spans; however, the 50%, and 70% span data are near zero. At all spans, a small lobe of strong axial velocity toward the shroud is present on the counterclockwise edge of the leading edge. Within the passage, the axial velocity indicates a large motion toward the hub along the pressure surface of the passage at all spans. This motion is least prevalent at 95% span. Additionally, the magnitude of the axial velocity component does not decrease in the streamwise direction downstream of the throat.

Together, the three components of the time-averaged velocity vector field suggest a description of the flow development that can be succinctly summarized. The potential field of a diffuser vane extends far into the vaneless space and acts to divide the incoming flow between the adjacent passages. The flow entering the passage in which data were acquired develops a relatively uniform cross-passage gradient in streamwise velocity approaching the throat, indicating effective diffusion occurring in the semi-vaneless space. However, beginning just downstream of the throat, a region of low streamwise velocity flow develops and grows, beginning along the pressure surface of the vane near the hub surface, indicative of flow separation. With the development of this region of low streamwise velocity, the pitchwise velocity develops a consistent low-level pitchwise motion toward the PS. Adjacent to the pressure surface immediately downstream of the throat, a significant pitchwise velocity toward the PS and a strong axial velocity toward the hub are observed. This is indicative of a bulk vortical motion with a counterclockwise sense (about the streamwise direction), which will be discussed in more detail in Section 3.5.

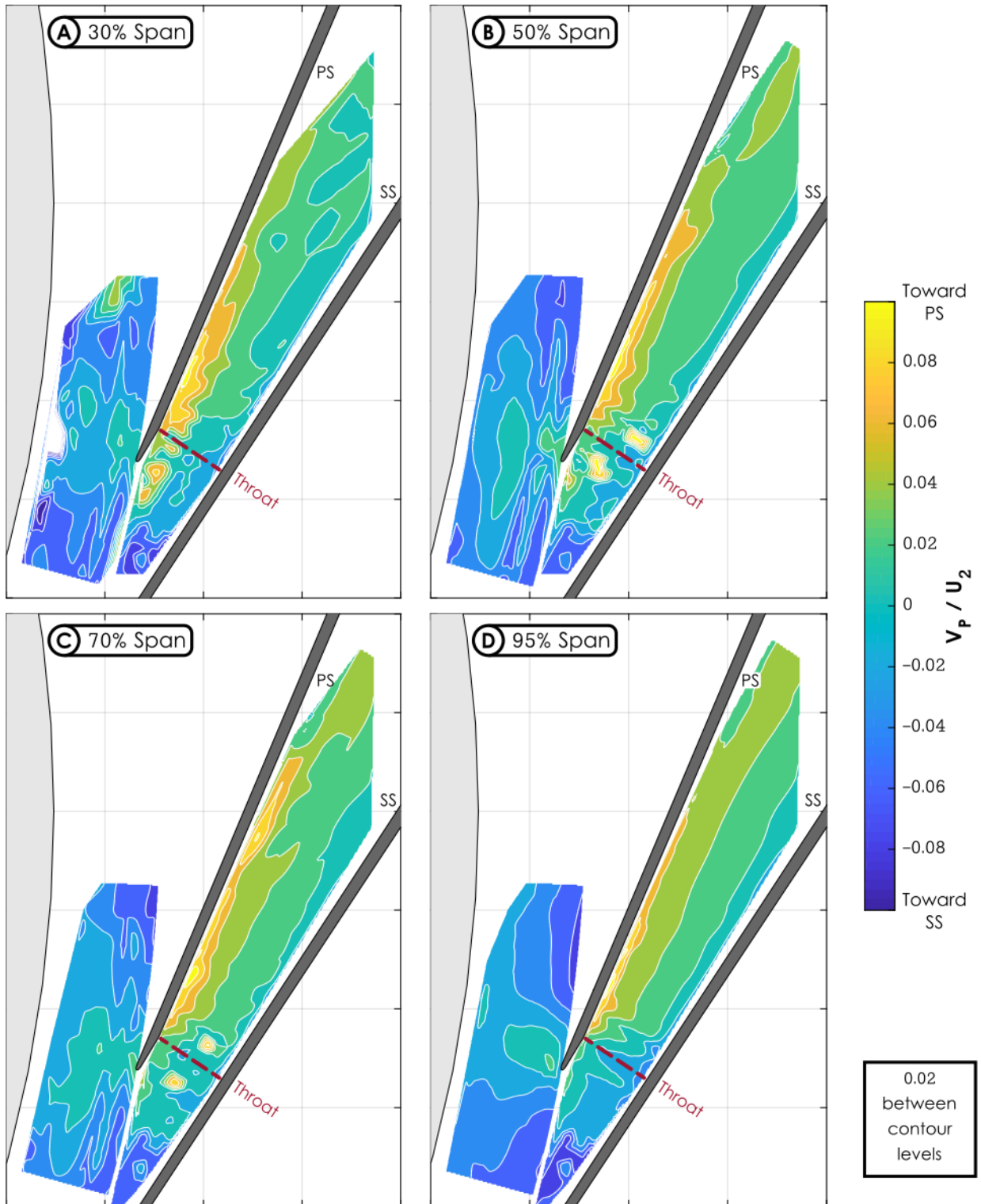


Figure 3.4: Time-averaged pitchwise velocity normalized by the impeller tip speed at 30% (A), 50% (B), 70% (C), and 95% (D) span

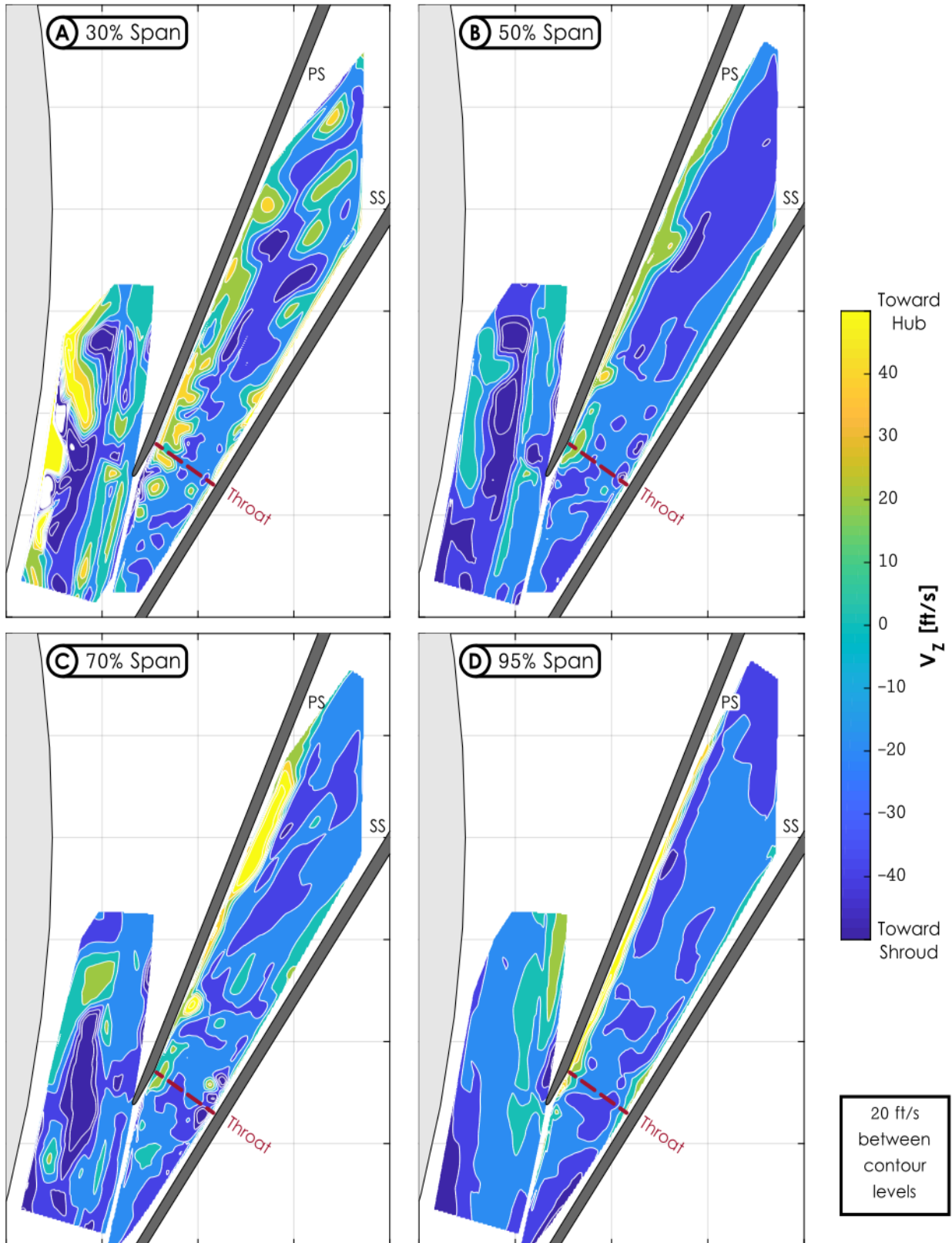


Figure 3.5: Time-averaged axial velocity at 30% (A), 50% (B), 70% (C), and 95% (D) span

### 3.2.1 Unsteady Vector Field at Constant Span

These observations have been made regarding the time-averaged development of the velocity vector field. The unsteady nature of the flow development is presented in the following figures. The streamwise velocity data at 30% span are presented in Figure 3.6, the pitchwise velocity in Figure 3.7, and the axial velocity in Figure 3.8. Each contour is presented at a single instance in time, equally distributed through the impeller blade-pass period. The contours proceed forward in time in the clockwise direction around each figure. The instances corresponding to  $t/t_{BP} = 0.25$  and  $0.75$  correspond to when the wake flow trailing the main blade and the splitter blade, respectively, impact the leading edge of the vane. The wake flow propagation is indicated by an arc of more positive pitchwise velocity through the vaneless space and the semi-vaneless space corresponding to the more tangential flow within the wake. At 30% span, the potential field from the diffuser vane interacts with the propagation of the impeller jet and wake flow and makes the jet/wake pattern more difficult to discern. In the streamwise velocity data, alternating bands of high streamwise velocity (corresponding to the wake) and low streamwise velocity (corresponding to the jet) are present closer to the impeller trailing edge. This pattern interacts with the potential field and is less distinguishable closer to the vane leading edge radius. The *increased* streamwise velocity associated with the wake flow in the vaneless space arises due to the definition of the streamwise direction as tangent to a logarithmic spiral aligning with the vane leading edge. This is analogous to describing “purely streamwise” flow as that with zero incidence through the vaneless space. Typical designs aim for negative average incidence for stability considerations. Consequently, the wake region, with its more tangential flow, tends to higher incidence and a velocity vector that is more aligned with the defined streamwise direction than in the jet region.

Within the passage, the streamwise velocity at 30% span (Figure 3.6) does not indicate clear fluctuation patterns. Higher streamwise velocities persists slightly further downstream at the instances associated with wake impingement ( $t/t_{BP} = 0.25$  and  $0.75$ , Figure 3.6B and D); however, the fluctuations are small downstream of the throat. The exact nature of the unsteady streamwise velocity field is partially obscured by the large velocity scale required to resolve the velocity range through the full diffuser passage as the flow decelerates. Additional details will be discussed in Section 3.4 at cross-passages planes where the streamwise velocity range is smaller and finer details are discernible.

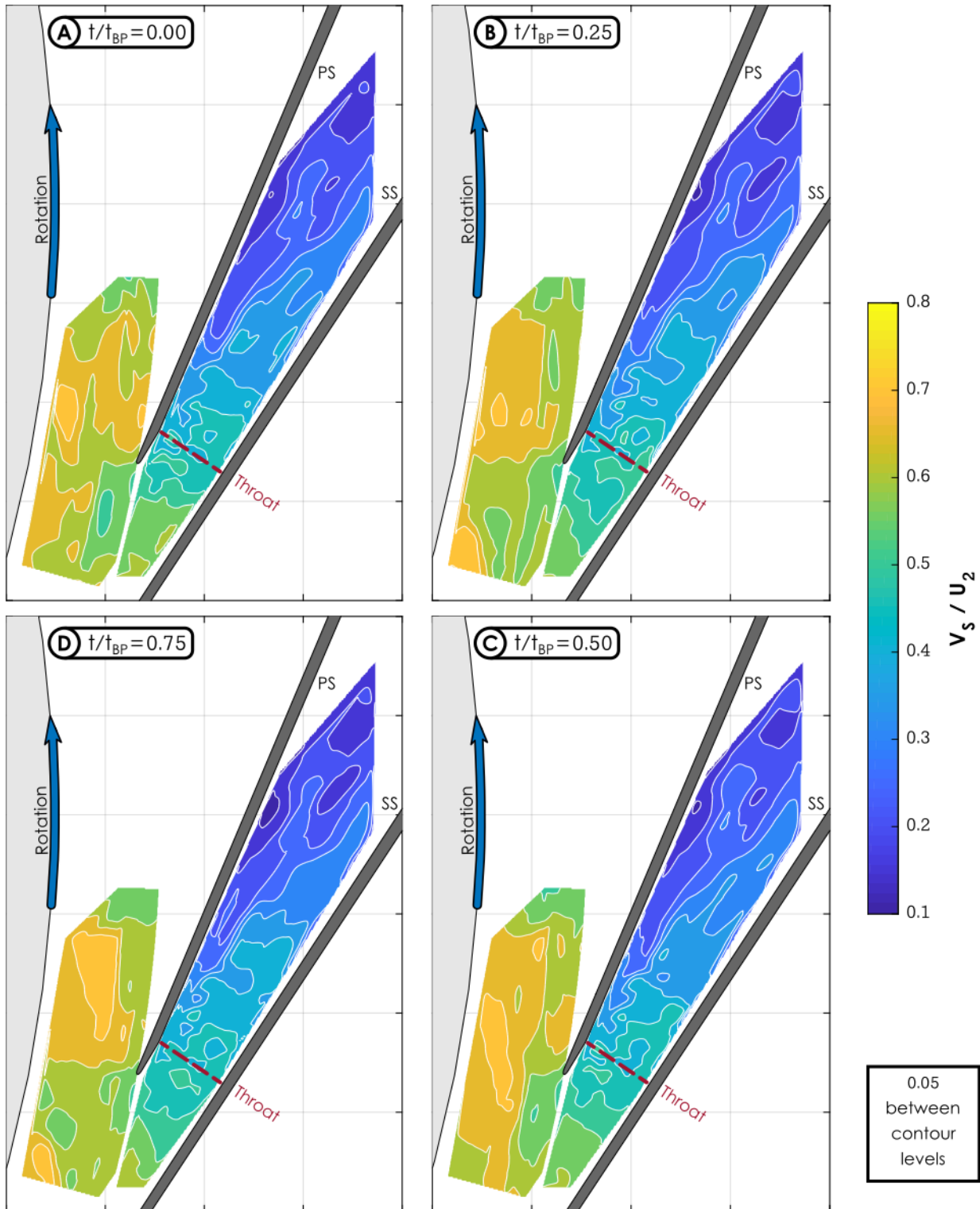


Figure 3.6: Unsteady streamwise velocity contours at 30% span for a  $t/t_{BP}$  of 0.00 (A), 0.25 (B), 0.50 (C, lower right), and 0.75 (D, lower left)

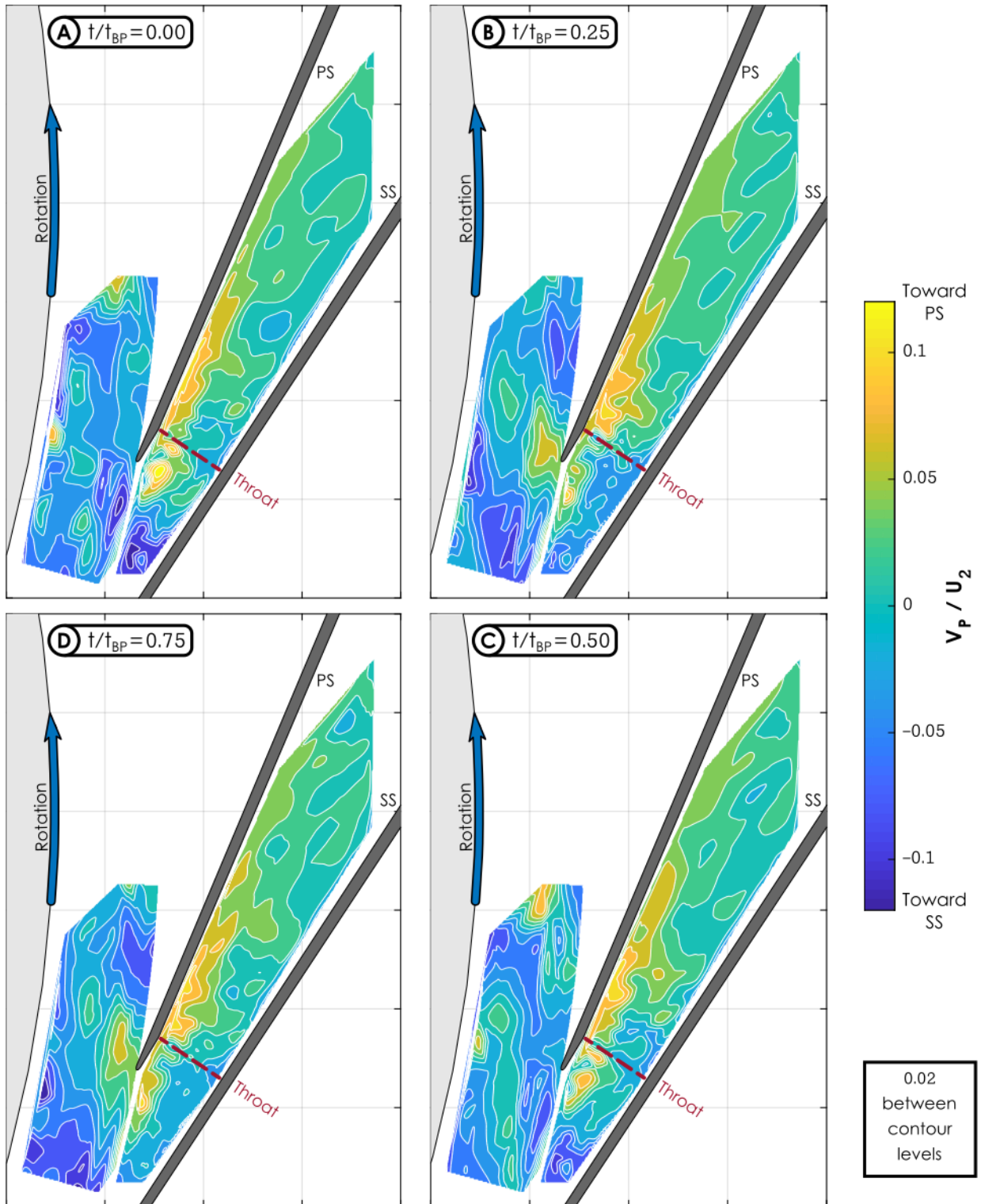


Figure 3.7: Unsteady pitchwise velocity contours at 30% span for a  $t/t_{BP}$  of 0.00 (A), 0.25 (B), 0.50 (C, lower right), and 0.75 (D, lower left)

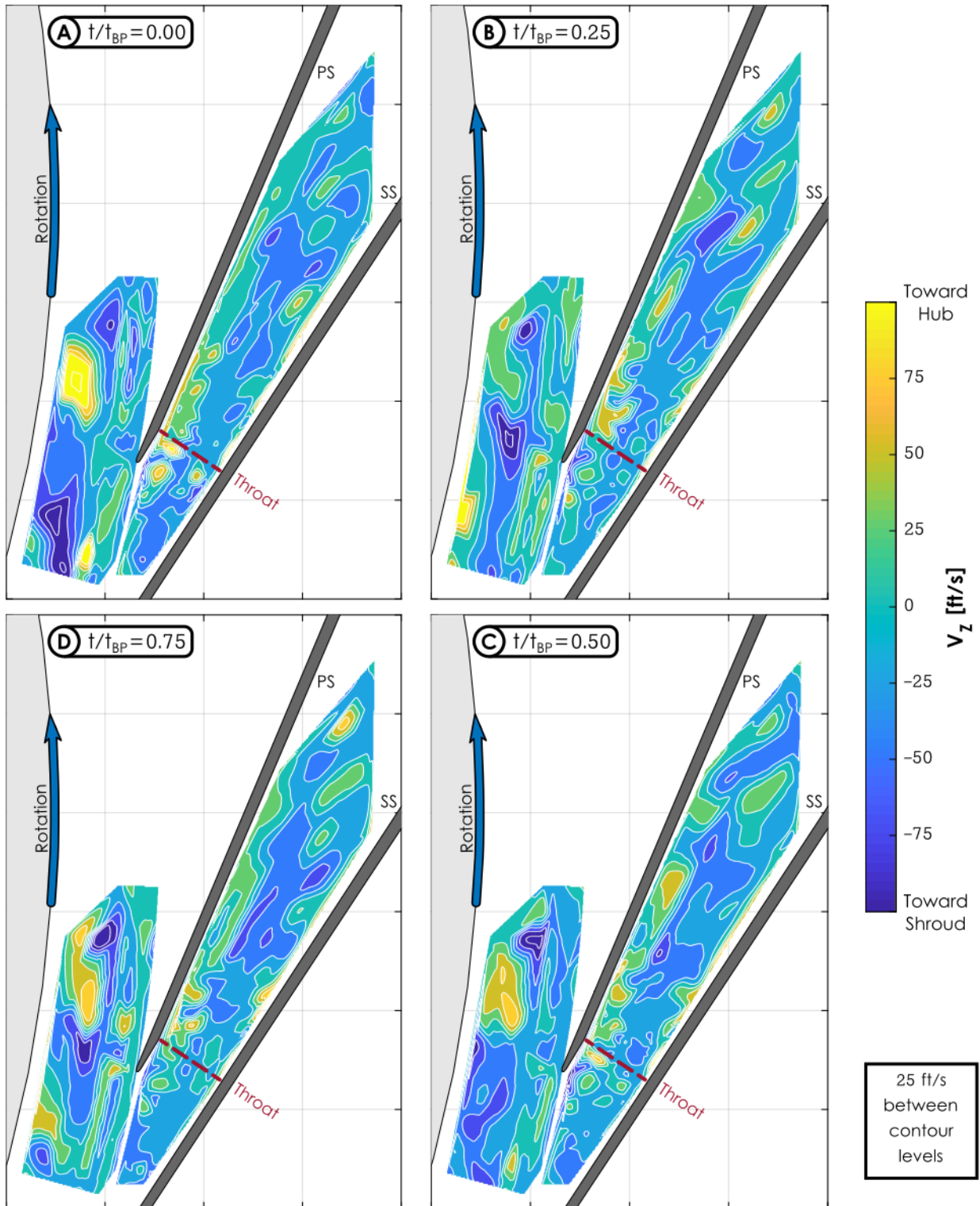


Figure 3.8: Unsteady axial velocity contours at 30% span for a  $t/t_{BP}$  of 0.00 (A), 0.25 (B), 0.50 (C, lower right), and 0.75 (D, lower left)

The pitchwise velocity data within the passage indicate a region of high pitchwise velocity toward the PS present along the pressure surface of the vane, just downstream of the throat, at all instances in time. Additionally, alternating bands of higher pitchwise velocity (associated with the wake flow) are discernible downstream of the throat. The pitchwise velocity within these bands decreases toward the suction side of the passage and the difference between these bands and the surrounding velocity values decreases in the downstream direction. The axial velocity indicates isolated regions of high velocity toward the hub along the suction surface of the vane. These regions propagate downstream, decreasing in peak magnitude while growing spatially.

The data at 50% span indicate similar flow patterns. The streamwise velocity field at 50% span is presented in Figure 3.9. The peak value within the impeller wake flow is larger in magnitude at 50% span than at 30% span; however, the general pattern remains similar. Within the passage, the streamwise velocity at 50% span exhibits less variation across the pitch than the 30% span data. This is due to the large deficit region along the pressure surface of the vane at 30% span that is not present at 50% span. Altogether, with the exception of some variation immediately downstream of the throat, the streamwise velocity data at 50% at all instances within the passage closely resemble the time-averaged result (Figure 3.3B). This indicates that unsteady fluctuations in the streamwise velocity field at 50% span have reduced in magnitude

The pitchwise velocity at 50% span (Figure 3.10) has similar patterns to the 30% span data (Figure 3.7). Specifically, regions of more positive pitchwise velocity are present in the impeller wake flow and these bands persist well into the diffuser passage. Additionally, a temporally stable region of high velocity toward the PS exists adjacent to the pressure side within the passage. This region extends further downstream and the high pitchwise velocity bands are more distinct (especially at  $t/t_{BP} = 0.25$ , Figure 3.10B) at 50% span than at 30% span. The appearance of further streamwise propagation of fluctuations in the pitchwise velocity compared to the streamwise velocity could be due to the velocity scales used for these figures. The streamwise velocity decreases significantly in the streamwise direction due to the diffusion process while the pitchwise velocity does not. This allows a narrower range to be used for the pitchwise velocity possibly leading to fluctuations being more apparent. Specific details at various streamwise locations will be discussed in Section 3.4. The axial velocity data at 50% span (Figure 3.11) show isolated regions of velocity toward the hub that convect downstream, similar to those observed at 30% span.

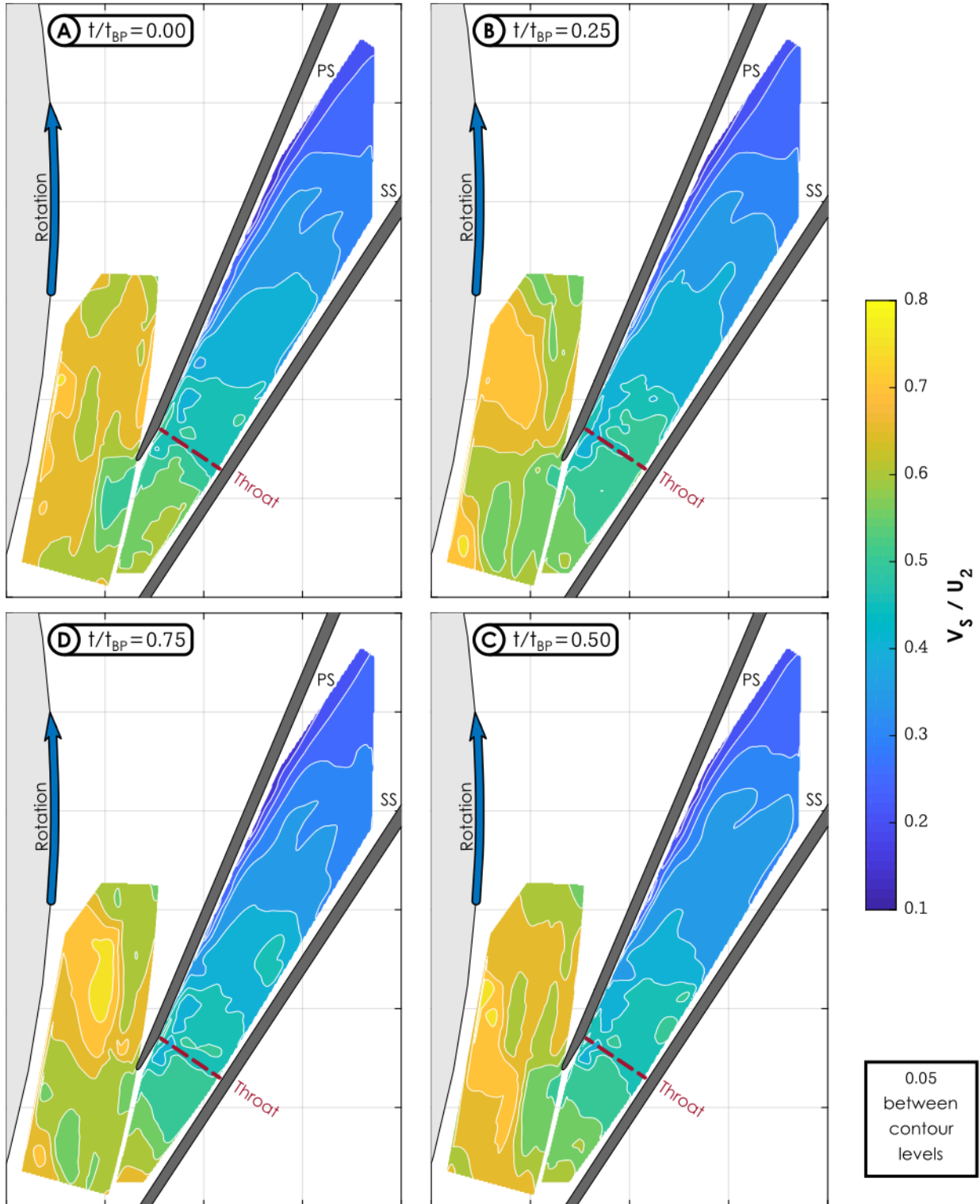


Figure 3.9: Unsteady streamwise velocity contours at 50% span for a  $t/t_{BP}$  of 0.00 (A), 0.25 (B), 0.50 (C, lower right), and 0.75 (D, lower left)

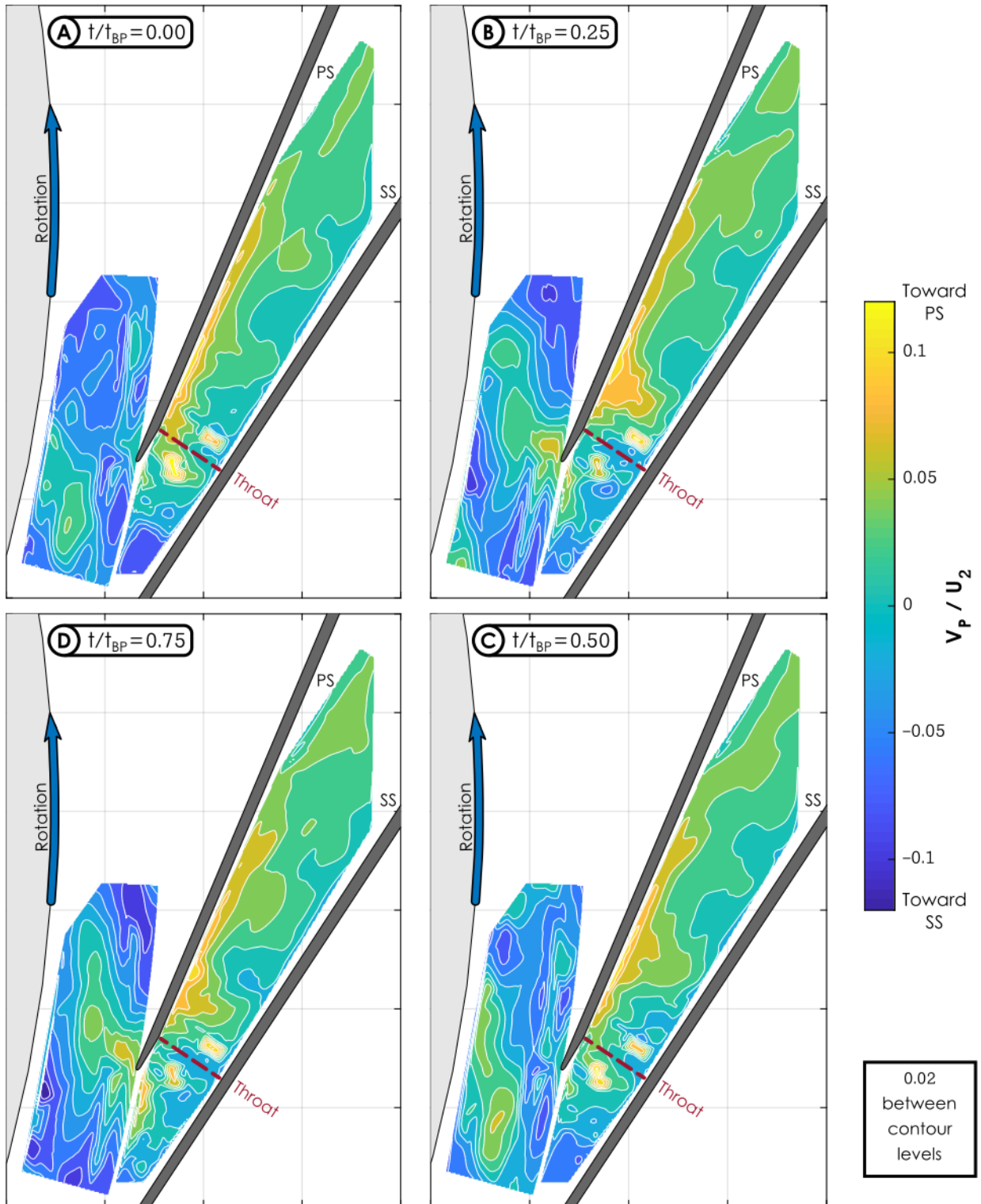


Figure 3.10: Unsteady pitchwise velocity contours at 50% span for a  $t/t_{BP}$  of 0.00 (A), 0.25 (B), 0.50 (C, lower right), and 0.75 (D, lower left)

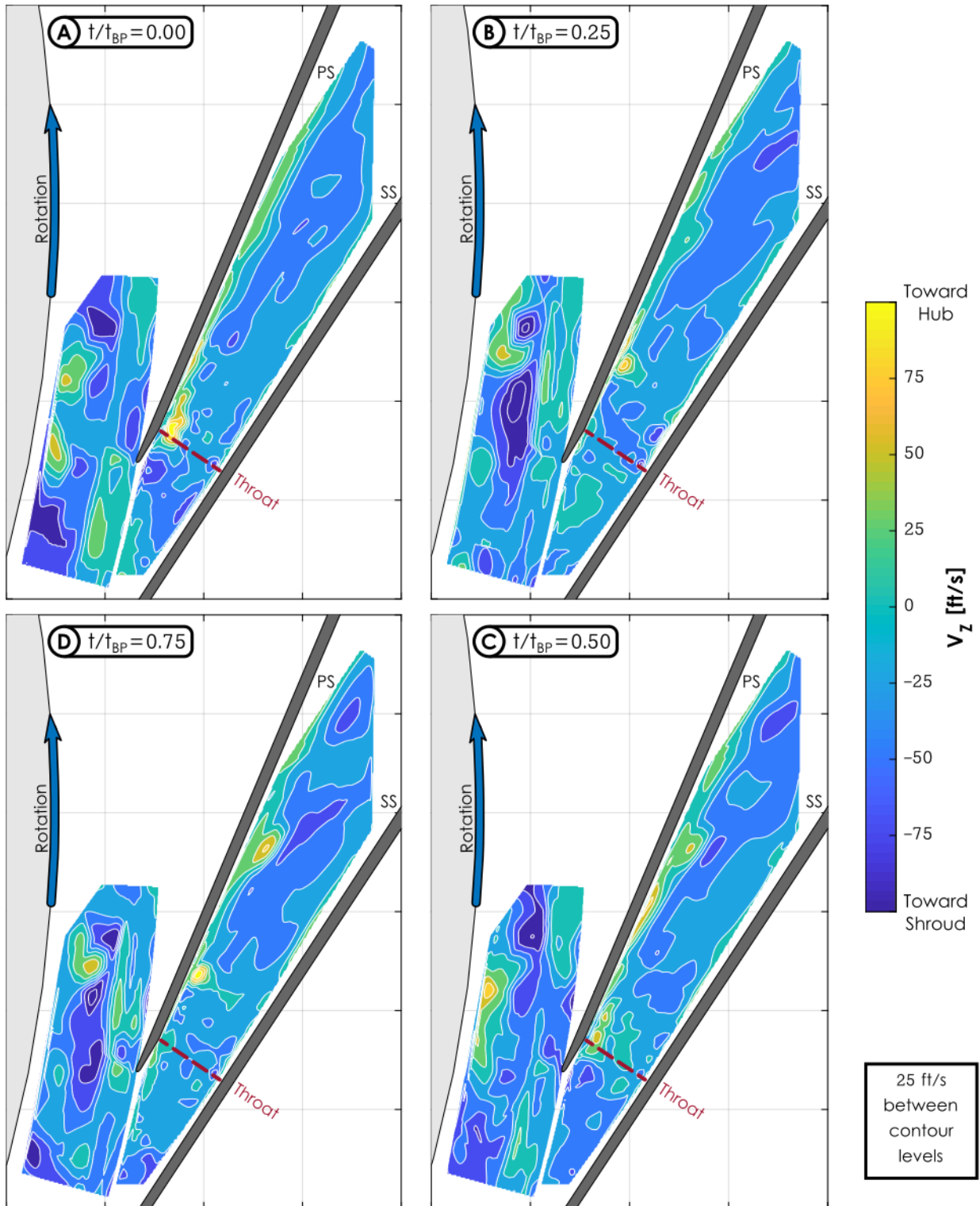


Figure 3.11: Unsteady axial velocity contours at 50% span for a  $t/t_{BP}$  of 0.00 (A), 0.25 (B), 0.50 (C, lower right), and 0.75 (D, lower left)

The unsteady results at 70% span are nearly identical to those at 50% and are omitted from this section. The streamwise velocity data at 95% span are presented in Figure 3.12. Compared to the data at 50% span, the wake flow at the impeller trailing edge has a larger circumferential extent at 95% span, close to the shroud. This is due to the influence of the tip leakage flow on the formation of the wake. The additional losses and reduced guidance associated with the tip leakage vortex tends to increase the wake size in the tip region, as discussed in Section 1.3.1. Closer to the leading edge, the potential effect of the diffuser vanes is again observed. Downstream of the throat, slightly higher streamwise velocities develop along the suction surface of the vane at 95% span. This likely occurs due to the larger (relative to the 50% span data) extent of low streamwise velocity flow along the pressure surface of the vane in the downstream portion of the passage. This region is not as large as that observed at 30% span but does influence the streamwise velocity progression through the passage.

The pitchwise velocity data at 95% span (Figure 3.13) also illustrate several differences from the data at 50% span. First, in the vaneless space, the alternating bands of high and low pitchwise velocity associated with the wake and jet flow, respectively, are more distinct. This occurs due to the reduced potential field effects at 95% span (allowing the jet and wake to propagate to the leading edge with less interference). Additionally, this suggests that the near-shroud flow exhibits not only a larger wake region but also a more dramatic wake flow as the difference in pitchwise velocity between the jet and wake flow is larger at 95% span than at 30% or 50% span. Contrarily, within the passage the pitchwise velocity data have less extreme values. A lower magnitude and smaller region of high pitchwise velocity is measured along the pressure surface of the vane and the cross-passage bands of higher pitchwise velocity are less distinct. This behavior arises due to either additional mixing occurring between the higher spans and the rest of the flow field or the influence of the wall in damping flow fluctuations.

The axial velocity data at 95% span (Figure 3.14) are approximately zero within the passage with the exception of a narrow region along the pressure surface of the vane and a small lobe just downstream of the throat, along the suction surface at  $t/t_{BP} = 0.25$  and  $0.75$ . In the vaneless space, the wake flow is more associated with hub-oriented axial flow than at the other spanwise positions. However, the relative magnitudes of the axial velocity data in the vaneless space are lower than were observed at the lower spans because of the influence of the shroud wall.

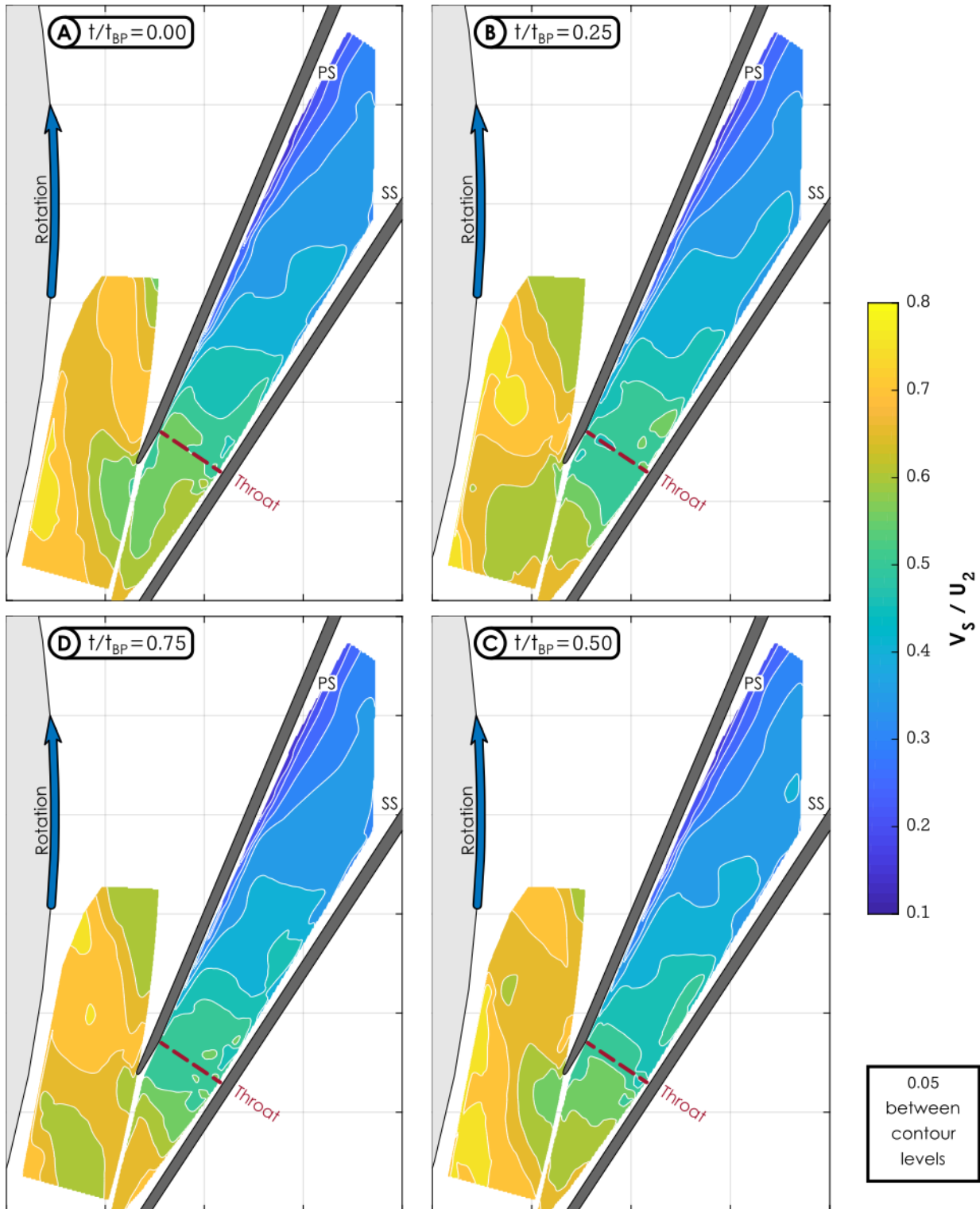


Figure 3.12: Unsteady streamwise velocity contours at 95% span for a  $t/t_{BP}$  of 0.00 (A), 0.25 (B), 0.50 (C, lower right), and 0.75 (D, lower left)

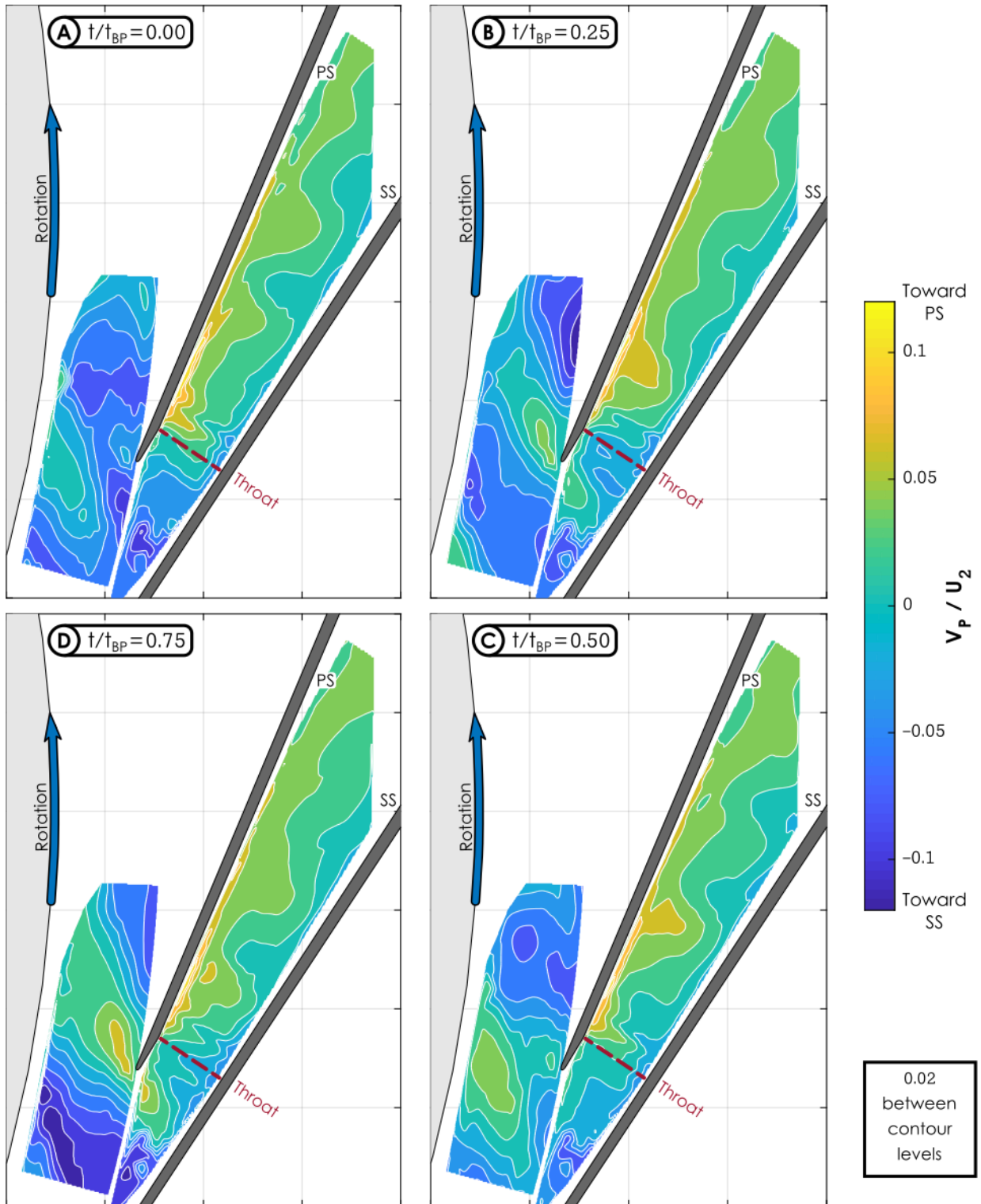


Figure 3.13: Unsteady pitchwise velocity contours at 95% span for a  $t/t_{BP}$  of 0.00 (A), 0.25 (B), 0.50 (C, lower right), and 0.75 (D, lower left)

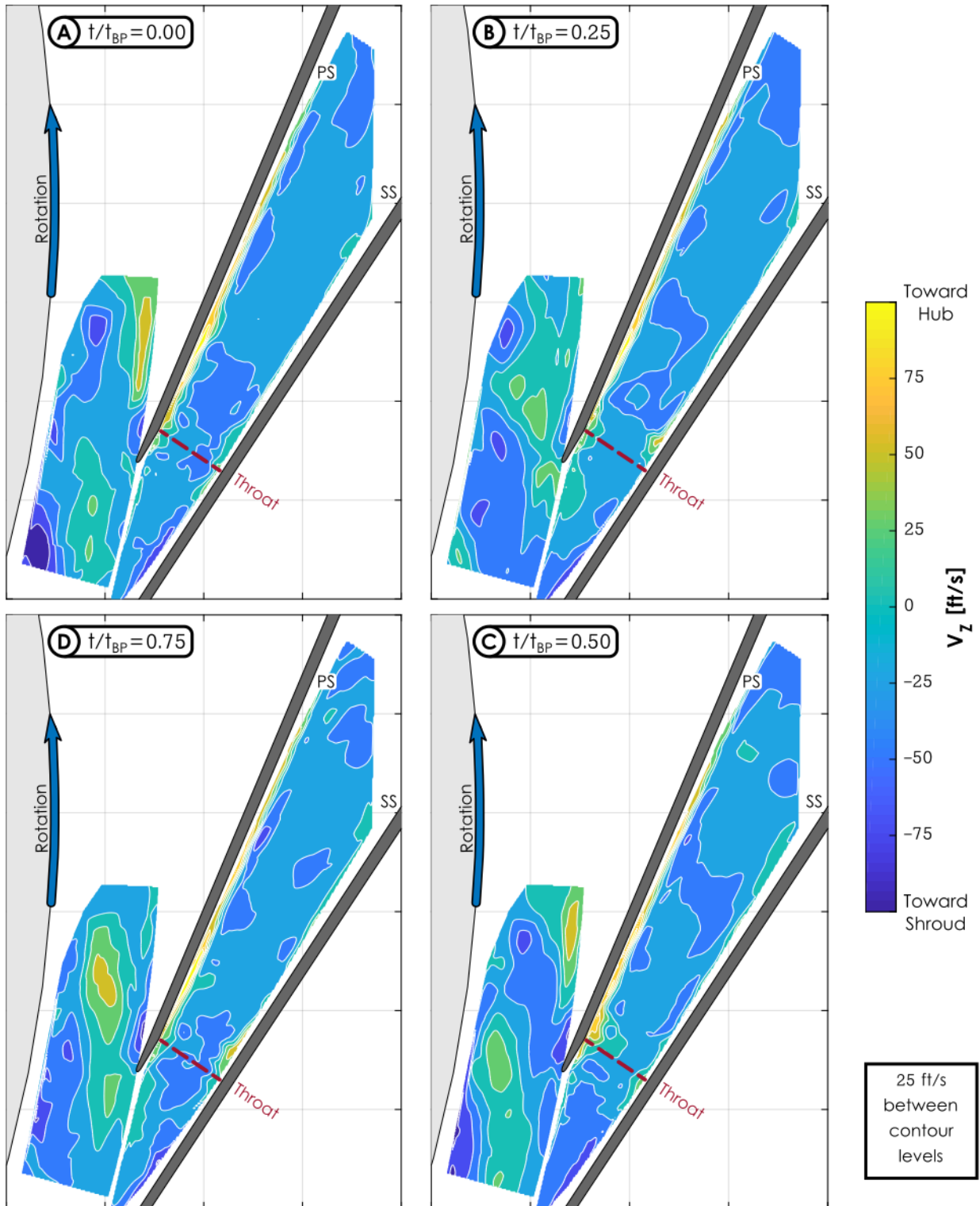


Figure 3.14: Unsteady axial velocity contours at 95% span for a  $t/t_{BP}$  of 0.00 (A), 0.25 (B), 0.50 (C, lower right), and 0.75 (D, lower left)

### 3.3 Impeller Jet and Wake Progression in the Diffuser Inlet Region

Through the vaneless space and into the passage, the previous results highlight the importance of the impeller discharge jet/wake on the diffuser flow development. To further investigate the propagation and potential dissipation of the jet and wake in the diffuser inlet region, data at specific geometric points will be presented in additional detail. The position of the points in question in the vaneless and semi-vaneless space are presented in Figure 3.15. These points are distributed from near the impeller trailing edge, at a radius ratio of 1.0125 (Point 37), to the end of the semi-vaneless space (Point 124).

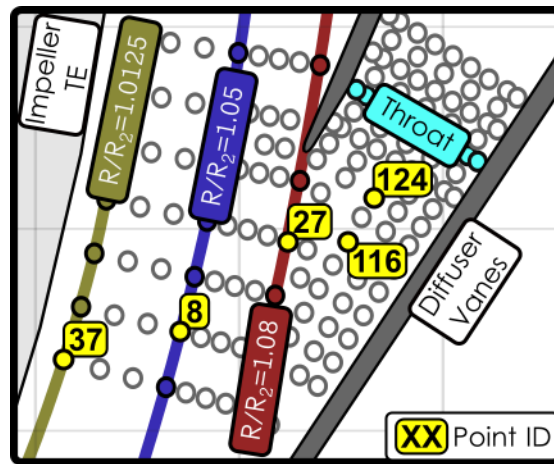


Figure 3.15: Point location for jet/wake analysis

The jet/wake profile at a radius ratio of 1.0125 (Point 37) is presented in Figure 3.16. The radial velocity,  $V_R$ , normalized by  $U_2$ , is presented from 10% to 97.5% span through the full blade-pass period with two visualization techniques. The surface plot presents a three-dimensional view of the jet/wake profile with time on the abscissa, spanwise position on the ordinate, and radial velocity on the applicate. This reflects the visualization style implemented in early studies that experimentally determined the impeller discharge flow characteristic (such as [15, 19]). A deficit in the radial velocity is indicative of the more tangential nature of the wake flow. The same data are also presented in a two-dimensional format using shading to indicate the radial velocity. In this presentation, the abscissa is time, the ordinate is spanwise position (from hub to shroud), and the coloring refers to the radial velocity with *darker* shading indicating *lower* radial velocity. Both methods contain circles indicating the data points used to generate the interpolated visualizations.

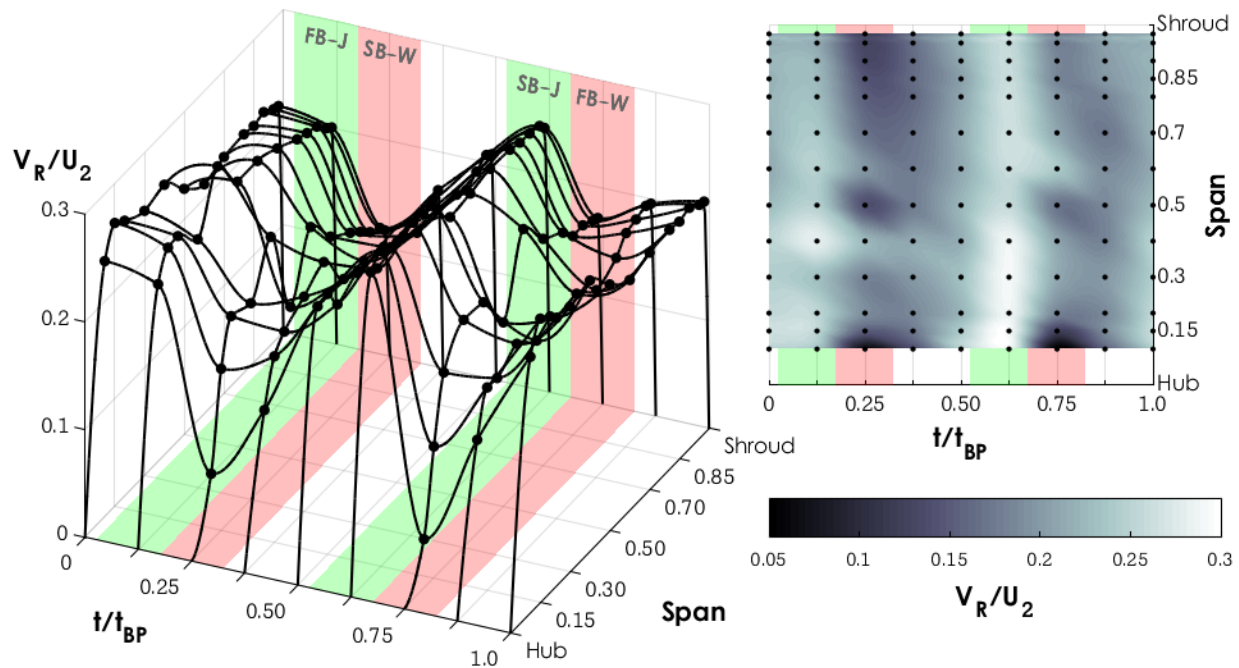


Figure 3.16: Radial velocity distribution at a radius ratio of 1.0125 (Point 37)

Lower radial velocities associated with the impeller wake are present at  $t/t_{BP} = 0.25$  and  $0.75$ . An inspection of the impeller geometry indicates that the wake occurring at  $t/t_{BP} = 0.25$  is the wake that trails the splitter blade while the wake occurring at  $t/t_{BP} = 0.75$  is associated with the full blade. Within the wake regions, a deficit is present across the full span. The deficit is greatest adjacent to the hub and the shroud. Additionally, the wake associated with the splitter blade ( $t/t_{BP} = 0.25$ , labelled SB-W) shows lower radial velocity magnitudes than that associated with the full blade ( $t/t_{BP} = 0.75$ , FB-W). The stronger wake associated with the splitter blade is accompanied by higher peak velocities in the adjacent jet ( $t/t_{BP} = 0.625$ , SB-J). The “adjacent jet” refers to the jet exiting from the same impeller passage as the wake in question. For example, the wake that developed along the suction surface of the splitter blade and the jet that developed along the pressure surface of the full blade exit from the same passage. This greater radial velocity (relative to the other jet flow) occurs due to the deceleration of the wake flow within the impeller passage. Neglecting tip leakage flow, the greater deceleration of the splitter blade wake flow through the impeller passage necessitates a greater acceleration of the adjacent jet flow to conserve mass-flow. The more severe nature of the splitter blade wake flow is contrary to expectation. Krain showed a more severe full blade wake due to the longer flow path and resulting increased boundary layer development [19]. However, the pitchwise location and blade angle of the splitter leading edge

can lead to different behavior developing along either side of the splitter blade [130]. It is likely that positive incidence at the leading edge of the splitter blade leads to a stronger adverse pressure gradient, and more rapid boundary layer growth. Within this design, these factors produce a more significant effect than the increased flow path length along the full blade and produce a more severe wake along the suction surface of the splitter blade.

These profiles do not align well with the profiles measured by Eckardt (a deficit region focused in the shroud-SS corner of the impeller passage [15]) or by Krain (a deficit region across most of the passage but only adjacent to the shroud [19]). In fact, the historical jet/wake description that best aligns with these data is Dean and Senoo's original model that assumes no spanwise variation within the jet and the wake regions [12]. More precisely, the wake region observed at the discharge of this impeller can be described as spanning the full passage height, with greater deficits adjacent to the hub and shroud surfaces (relative to the deficit at mid-passage), and greater deficits trailing the splitter blade (relative to the deficit trailing the full blade). This profile could be influenced by the actual blade wake (the bluff body wake, not the passage wake) as the hub portion of each blade is much thicker than the tip. Additionally, it could be the result of an exceedingly low Rossby number. Looking back to the generic wake shapes (Figure 1.4), if the curvature effects were extremely small relative to the Coriolis effects, the wake profile could reflect the measured profile. The impeller exit has a Rossby number of approximately 0.168, indicating that Coriolis effects are stronger than system curvature effects. However, it is unclear where this Rossby number lies relative to impellers previously studied. If the other impellers exhibited larger Rossby numbers, then this could adequately explain the observed profile. Other factors of the impeller flow development could also impact the wake flow development and a future study obtaining LDV measurements within the impeller is recommended to further elucidate these details.

In addition to the nature of the jet/wake flow at the impeller discharge, the convection and dissipation of that flow profile through the vaneless and semi-vaneless space is of interest. To investigate this, the radial velocity data are presented from a radius ratio of 1.05 to the exit of the semi-vaneless space (at Points 8, 27, 116, and 124, see Figure 3.15 for full details of the measurement locations). Figure 3.17 displays the radial velocity data at in the vaneless space, at a radius ratio of 1.05 (Point 8). These data illustrate a similar wake profile to that present at the impeller discharge indicating that little dissipation has occurred. Quantitatively, at a radius ratio

of 1.0125 (Point 37) the average range of the radial velocity through the full blade passage was 12.5% of  $U_2$ . This indicates that the difference between the radial velocity in the jet and in the wake was  $1/8^{\text{th}}$  of the impeller tip velocity when averaged across the full span. This equates to approximately 60% of the average radial velocity. At a radius ratio of 1.05 (Point 8), this range decreased to 8.3% of  $U_2$  (but still 46% of the average radial velocity). These data suggest that the jet and wake have not significantly dissipated between a radius ratio of 1.0125 and a radius ratio of 1.05. The qualitative shape of the radial velocity profile remains unchanged and the magnitudes of the unsteady fluctuations associated with the jet/wake flow have only slightly decreased in progressing through this portion of the vaneless space.

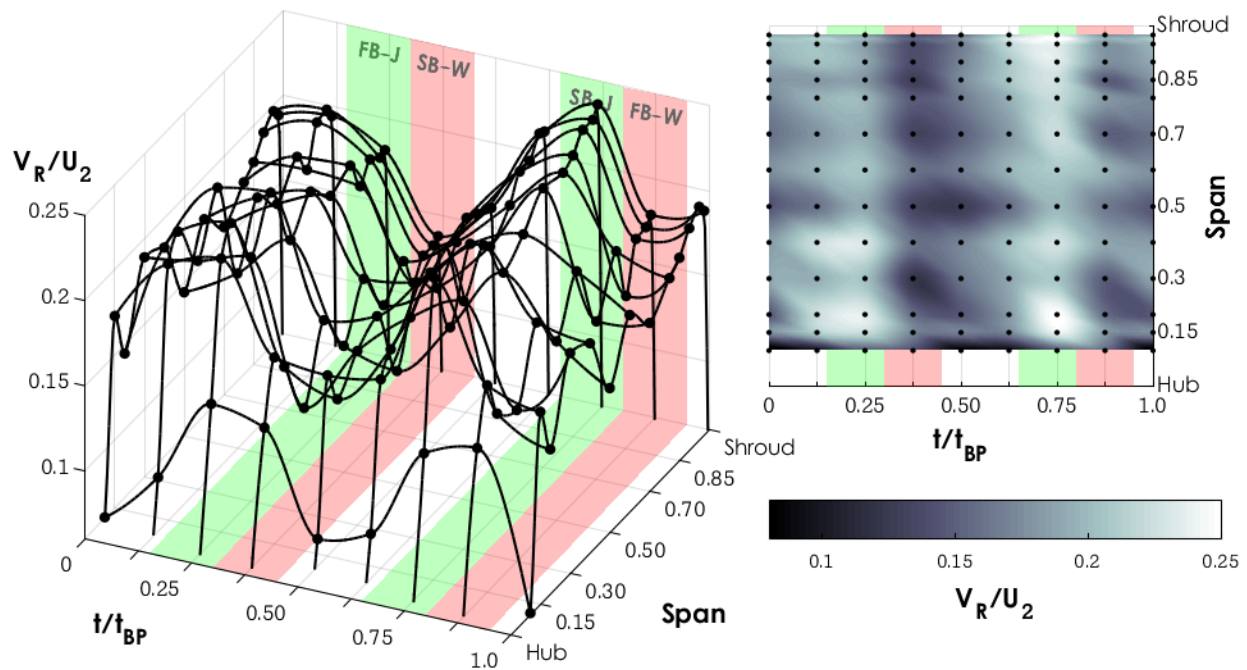


Figure 3.17: Radial velocity distribution at a radius ratio of 1.05 (Point 8)

The data at the end of the vaneless space, at a radius ratio of 1.08 (Point 27) are presented in Figure 3.18. At this location, the wake trailing the splitter blade passes at  $t/t_{BP} = 0.75$ . Several differences have developed in the jet/wake flow profile. First, the wake associated with the full blade (at a  $t/t_{BP}$  of approximately 0.25) has dissipated slightly and shows a reduced radial velocity deficit. However, the wake associated with the splitter blade has not dissipated. Both wake structures have broadened and inclined slightly in time. In other words, the wake adjacent to the shroud convects through this geometric location slightly before (at a smaller  $t/t_{BP}$ ) the wake region adjacent to the hub. Quantitatively, the mean range has decreased slightly more to 7.5% of  $U_2$ . However, the radial velocity tends to decrease with radius and this range relative to the average radial velocity has decreased by only 2%, to 44%. These data support the conclusion that significant unsteady fluctuations are still present at the exit of the vaneless space and do not dissipate upstream of the diffuser leading edge. The jet/wake have dispersed only marginally in terms of both qualitative profiles and quantitative fluctuation levels through the vaneless space. Through the semi-vaneless space, these strong fluctuations remain prevalent and only dissipate slightly as observed within the semi-vaneless space (Point 116, Figure 3.19) and at the exit of the semi-vaneless space or the entrance to the diffuser passage (Point 124, Figure 3.20).

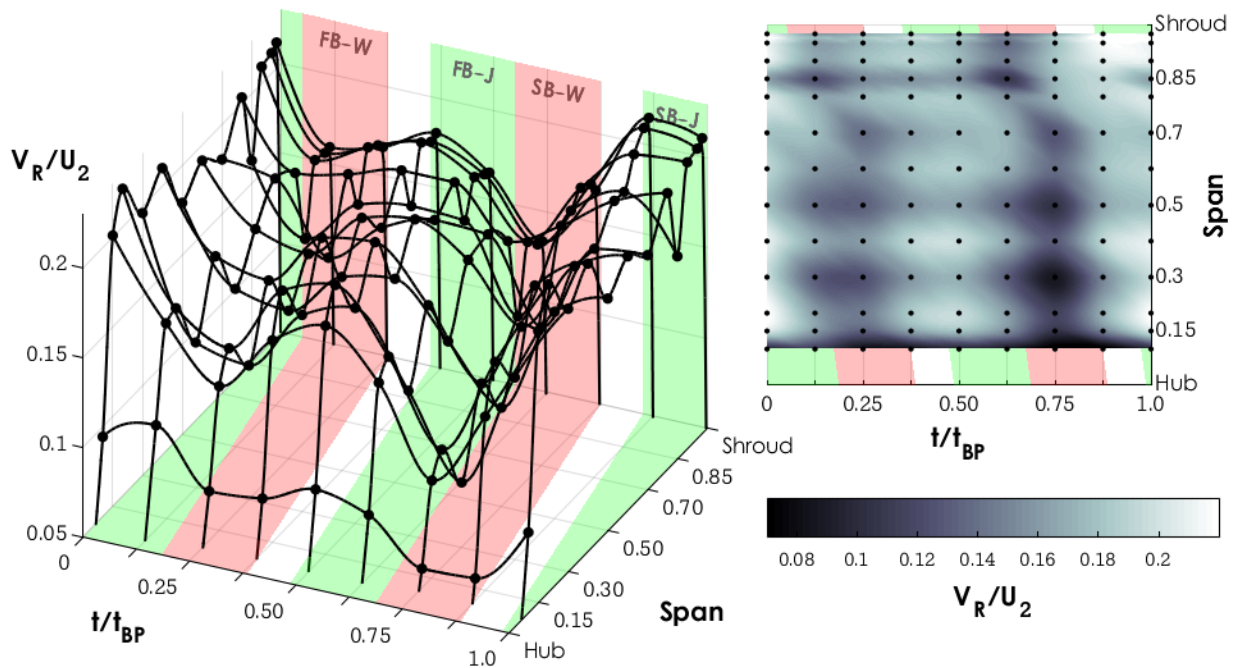


Figure 3.18: Radial velocity distribution at a radius ratio of 1.08 (Point 27)

These data illustrate the persistence of the fluctuations associated with the impeller jet and wake into the diffuser passage. Within the semi-vaneless space (at Point 116, Figure 3.19), the wake profile is still evident in the velocity data although the fluctuation range has decreased further to 5.4% of  $U_2$ . Well within the influence of the vane potential fields, the radial velocity has increased slightly and the fluctuation levels relative to the average radial velocity have decreased to 29%. While this is a significant reduction relative to the previous value of 44%, it is still a large level of unsteadiness that has a significant impact on the flow development through the diffuser passage. Similar levels of unsteadiness (4.9% of  $U_2$  and 27% of the average radial velocity) are observed at the entrance of the diffuser passage (Point 124, Figure 3.20). Additionally, both points illustrate the further temporal inclination of the wake flow (convecting earlier at higher spans) that was described previously. These data lead to several conclusions regarding the dissipation of the impeller jet and wake upstream of the diffuser passage. First, significant unsteady fluctuations corresponding to the impeller jet and wake are still observed at the entrance to the diffuser passage. Second, the adjustment of the flow to the presence of the vane in the “zone of rapid adjustment [31]” (the upstream portion of the semi-vaneless space) is responsible for the majority of the dissipation that does occur.

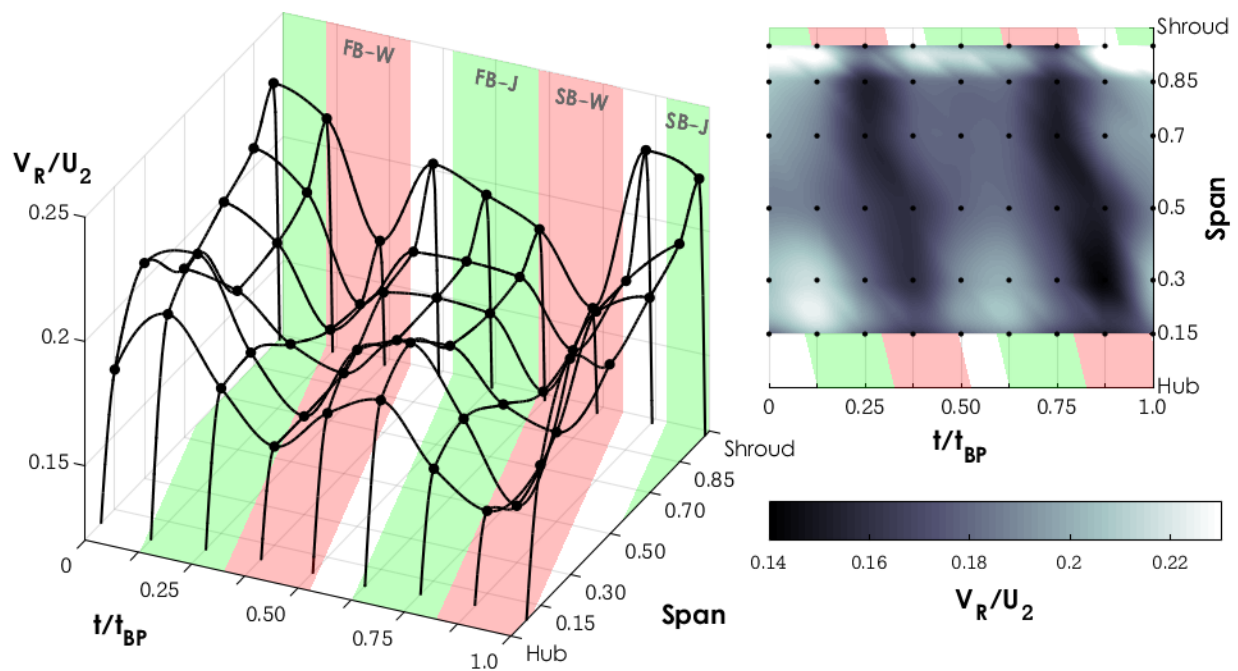


Figure 3.19: Radial velocity distribution within the semi-vaneless space (Point 116)

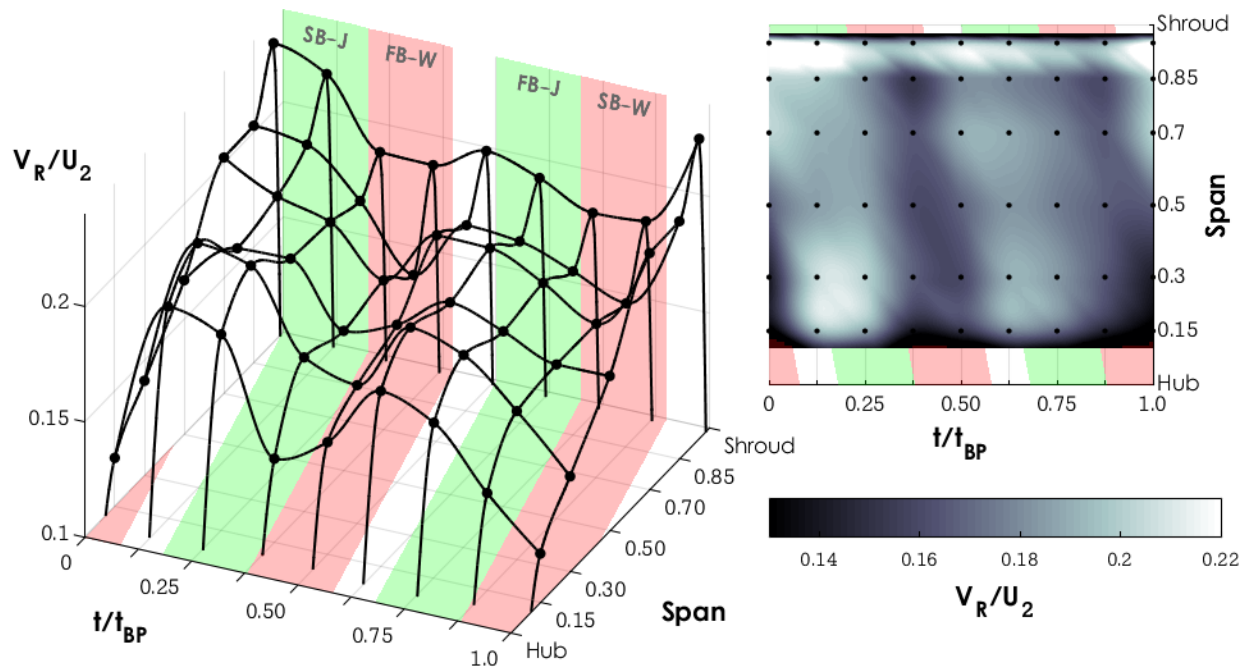


Figure 3.20: Radial velocity distribution at the exit of the semi-vaneless space (or the entrance to the diffuser passage, Point 124)

### 3.4 Development of Cross-Passage Flow Profiles

The unsteady fluctuations through the vaneless space are present in all components of the velocity vector field. This section will focus on the flow development through the diffuser using cross passage planes (at constant streamwise position). The planes highlighted in Figure 3.21 will be probed to describe the spatial evolution of unsteady flow structures through the diffuser passage. The percentage given with each plane within the passage reflects the streamwise position of that plane. A value of 0% corresponds to the throat, 100% corresponds to the trailing edge of the diffuser passage, and negative values refer to locations that are upstream of the throat.

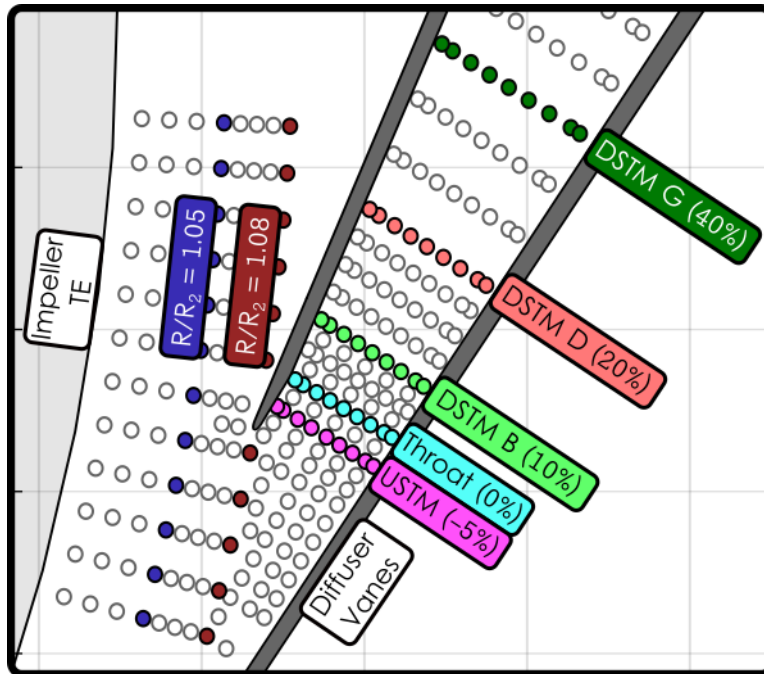


Figure 3.21: Cross passage planes geometric details

The velocity field at a radius ratio of 1.05 is presented in Figure 3.22. The left column contains the streamwise velocity data and the right column presents the axial velocity data. The center column presents the incidence angle. Within the vaneless space, the incidence is a more useful representation of the component of velocity in the pitchwise direction. Within the passage (in subsequent figures) the pitchwise velocity will still be used. The top row contains the time-averaged result and the remaining rows contain the instantaneous data at four equally spaced instances through the full blade passing period. The selected instances will be offset at each plane in order to capture the convection of the impeller jet and wake flow through each plane. The abscissa is the pitchwise direction and the ordinate is the span. The view is oriented in the downstream direction and the direction of impeller rotation is from right to left.

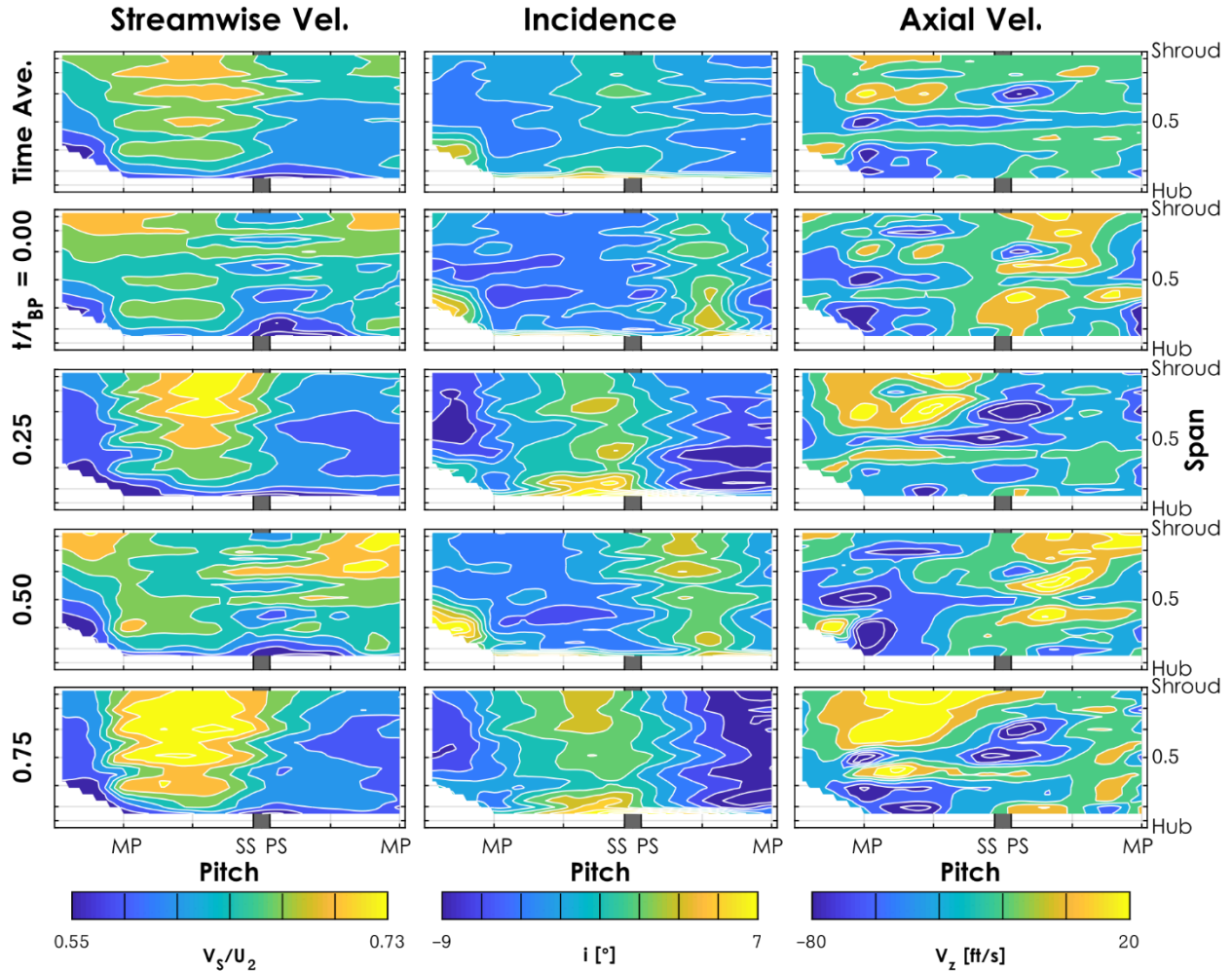


Figure 3.22: Unsteady velocity field at a radius ratio of 1.05

In the unsteady data, the wake flow is indicated by high levels of streamwise velocity and more positive incidence, as discussed previously. The region of high streamwise velocity present at a  $t/t_{BP}$  of 0.25 corresponds to the wake trailing the main blade with the splitter blade wake visible at  $t/t_{BP} = 0.75$ . A region of wake flow is also present at the other time instances due to the circumferential extent of the data. The interaction between the jet/wake and the potential field of the diffuser is indicated by the greater streamwise velocity observed when the wake flow is located to the suction side of the downstream vane (indicated by the grey rectangle) than when the wake flow is elsewhere relative to the vane position. The regions of high streamwise velocity at all instances in time are accompanied by a more positive incidence. While the time-averaged incidence field indicates near-zero or slightly negative incidence across the majority of the plane, the unsteady data reveal periodic regions of high positive incidence (more tangential flow)

associated with the wake flow from the impeller. This could cause a deterioration in the performance and stability of the diffuser. However, these data are obtained from within the vaneless space; the incidence at the leading edge is more important in determining the diffusion characteristics through the diffuser passage. The axial velocity data also suggest flow features correlated with the impeller jet and wake. At all instances, a region of significant positive (toward the hub) axial velocity occurs within the wake flow. At the instances when the wake flow interacts with the potential field to produce the largest magnitudes of streamwise velocity, this region of velocity toward the hub is accompanied by a region of negative (toward the shroud) axial velocity immediately upstream of the vane. These pairs of opposing axial velocity directions are indicative of streamwise vorticity.

The velocity data at a radius ratio of 1.08 (aligned with the vane leading edge) are presented in the same format in Figure 3.23. The streamwise velocity field maintains a relatively constant profile through the blade-pass period. The relative magnitudes of the velocity change, but a region of high streamwise velocity adjacent to the suction side of the leading edge and a region of low streamwise velocity adjacent to the pressure side of the leading edge remain through all time instances. This region is the most pronounced within the wake flow from the splitter blade ( $t/t_{BP} = 0.83$ ). Within the full blade wake flow ( $t/t_{BP} = 0.33$ ) the region of high streamwise velocity is focused toward the shroud. The incidence field contains more significant variations through the blade-pass period both in terms of magnitude and profile. Within the wake flow, a region of high positive incidence is present aligned with the leading edge of the vane. At this radius, the vane forces a division in the incoming flow between the clockwise (negative incidence) and counterclockwise (positive incidence) passages. Qualitatively, this pattern is associated with the wake flow inducing an intermittent “jumping” of the flow into the adjacent passage. This behavior is more pronounced below approximately 70% span. At these instances, small areas appear of negative (toward the shroud) axial velocity in the hub-PS corner of the vane leading edge and of positive (toward the hub) axial velocity in the shroud-PS corner. This region is more pronounced within the splitter blade wake ( $t/t_{BP} = 0.83$ ) and adjacent to the hub.

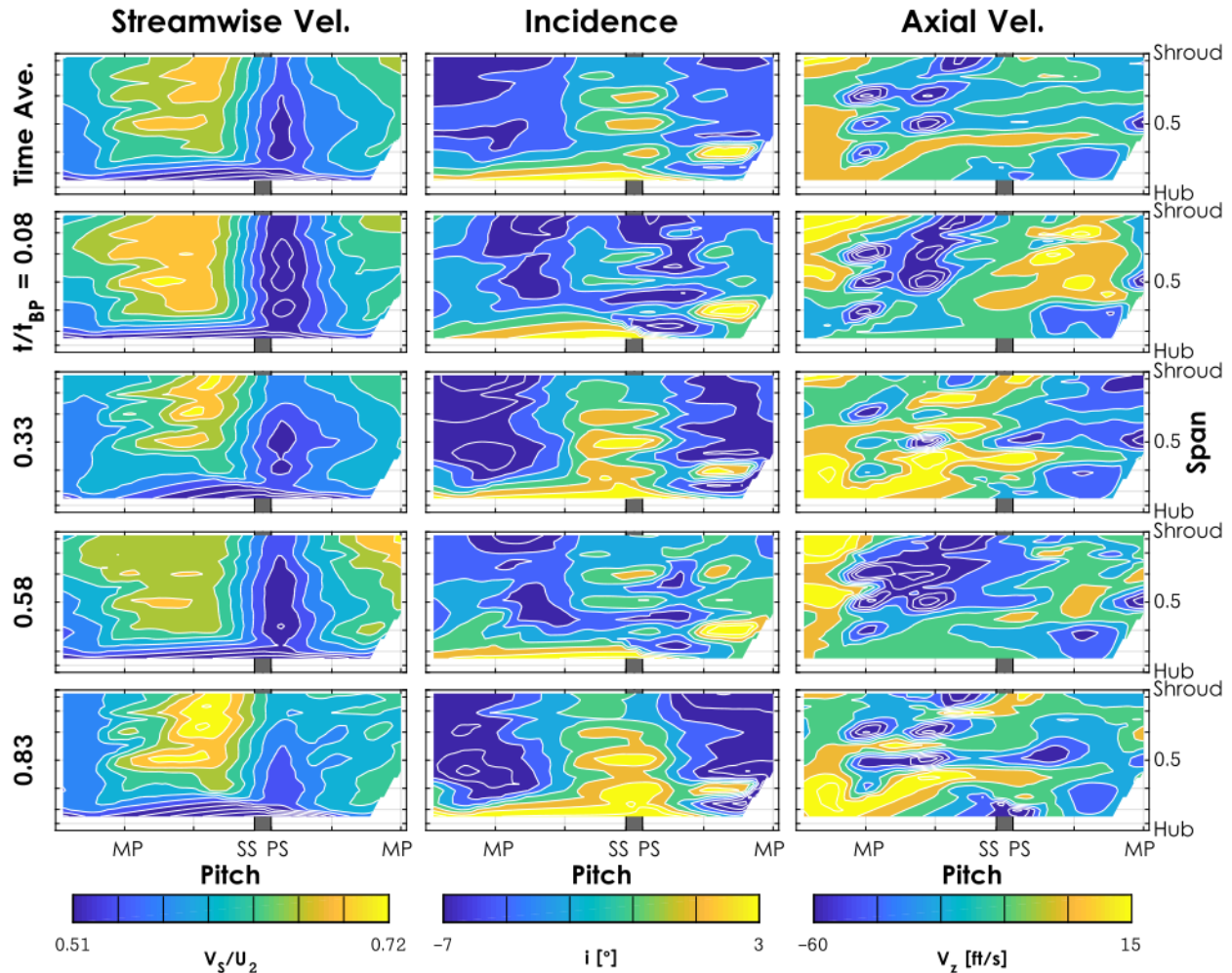


Figure 3.23: Unsteady velocity field at a radius ratio of 1.08

Within the passage, the data at a streamwise progression of -5% (USTM A plane) are presented in Figure 3.24. Relative to the vaneless space, the pitchwise dimension is significantly reduced within the passage. Consequently, the jet and wake flow constitute most of the cross-passage area at the instances in which they convect through the plane in question. This is in contrast to the “bands” of jet and wake flow which could be observed simultaneously within a single plane in the vaneless space. This is apparent in Figure 3.24. The splitter blade wake flow convects through the USTM A plane at  $t/t_{BP} = 0.92$  and the full blade wake flow at  $t/t_{BP} = 0.42$ . The jet adjacent to the splitter blade wake convects through at  $t/t_{BP} = 0.17$  and the corresponding jet for the full blade wake at  $t/t_{BP} = 0.67$ . A sharp divide in the streamwise velocity contour is present during the splitter blade wake flow convection—high streamwise velocity being present above 50% span and low streamwise velocity below 50% span. During the full blade wake convection, this pattern is

present albeit less dramatic with a reduction in the magnitude of the high streamwise velocity near the shroud. Within the jet (especially at  $t/t_{BP} = 0.17$ ), this pattern has rotated by ninety degrees. The high streamwise velocity region is present along the suction surface of the passage with the low streamwise velocity region shifted to the pressure side. The shroud-focused high streamwise velocity during wake convection is accompanied by a strong increase in positive (toward the PS) pitchwise velocity adjacent to the pressure surface of the passage at mid-span. Conversely, the high streamwise velocity region within the jet convection ( $t/t_{BP} = 0.25$ ) accompanies a pitchwise velocity toward the SS. Additionally, the axial velocity data indicate a predominantly positive (toward the hub) motion below 50% span and the opposite above 50% span. A peak in the axial velocity is observed to correspond with the positive pitchwise velocity region during wake convection (predominantly at  $t/t_{BP} = 0.92$ , within the splitter blade wake).

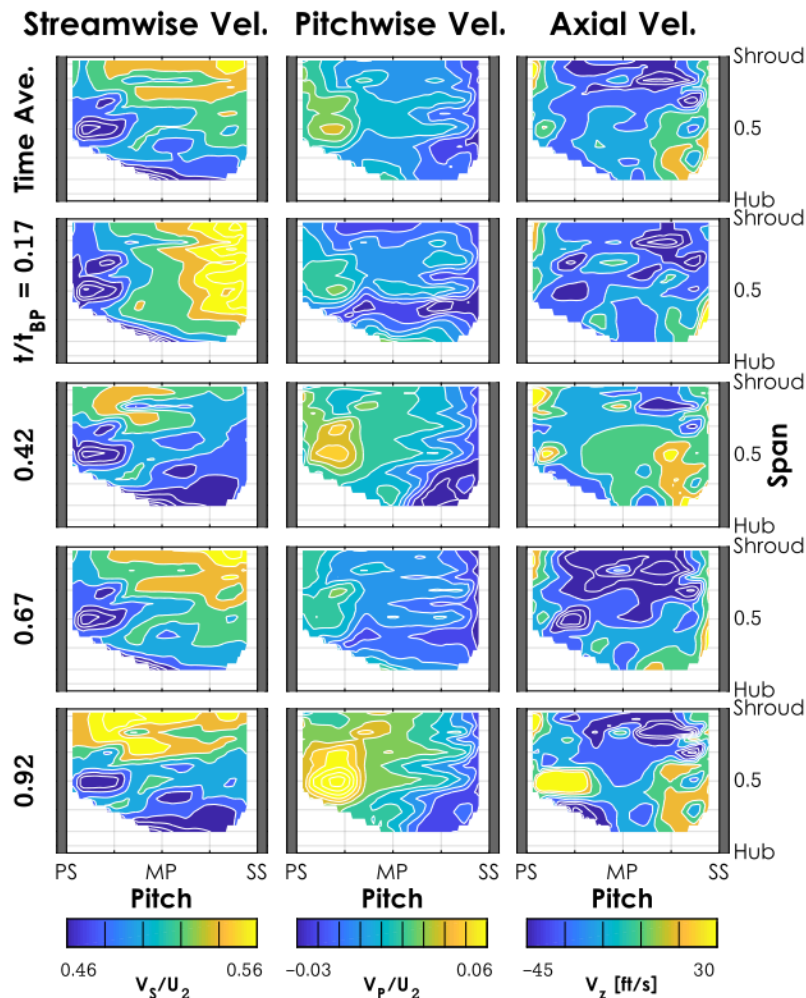


Figure 3.24: Unsteady velocity field at the USTM A plane (-5% passage progression)

The velocity data at the throat (0% streamwise position) are presented in Figure 3.25. The general profile of the jet- and wake-associated streamwise and pitchwise velocity fields are similar to those present at -5% passage (Figure 3.24). The splitter blade wake flow ( $t/t_{BP} = 0.00$ ) contains a large streamwise velocity region along the shroud surface and a positive (toward the PS) pitchwise velocity region along the pressure surface. Compared to the -5% data, the high streamwise velocity region extends to a slightly lower span and the high pitchwise velocity region is distributed across a larger spanwise region. Again, the full blade jet flow illustrates similar profiles that are marginally less distinct. The axial velocity during the splitter blade wake convection indicates a vertical band of velocity toward the hub adjacent to the pressure surface of the vane adjacent to a parallel band of velocity toward the shroud closer to mid-passage. This pattern indicates the presence of streamwise vorticity in the pressure-side half of the passage within the wake flow.

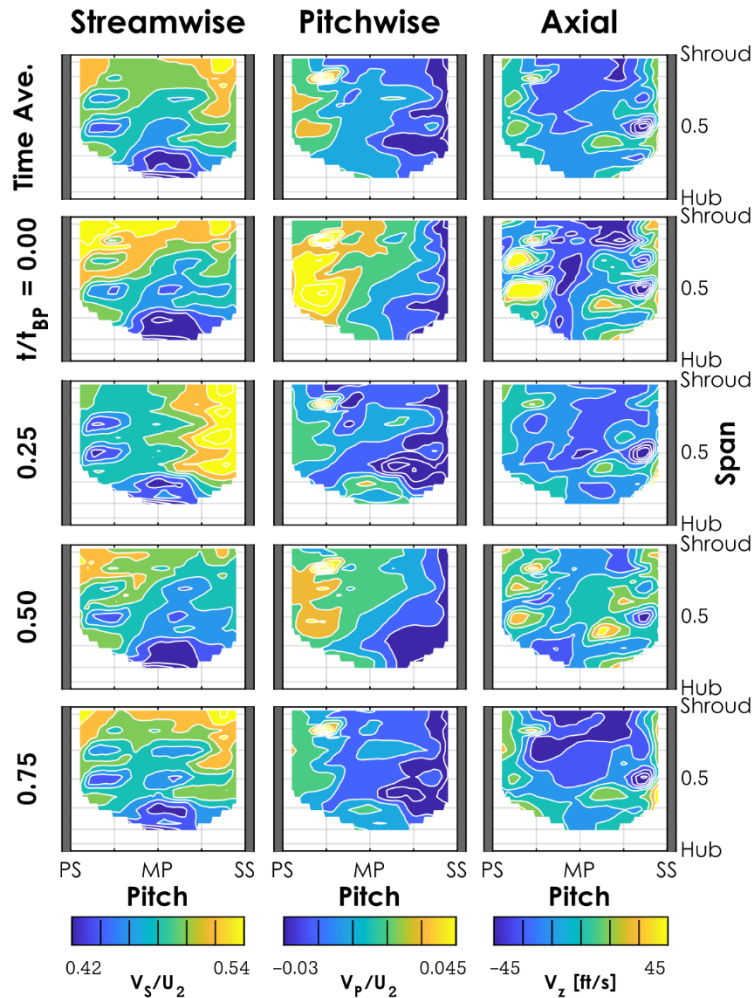


Figure 3.25: Unsteady velocity field at the throat (0% passage progression)

The secondary velocity data at these two planes within the diffuser passage inform a potential explanation for the lack of dissipation or mixing between the impeller jet and wake flow. The pitchwise and axial velocity fields are oriented in such a way as to oppose mixing. Take the throat, for example. At  $t/t_{BP} = 0.00$ , the splitter blade wake flow exhibits a “core” region of high streamwise velocity centered in the shroud-PS corner of the passage. Within this region, the pitchwise velocity is oriented toward the pressure side of the passage. This causes this portion of the wake flow to remain in the shroud-PS corner and not mix with the rest of the flow field. Similarly, within the adjacent jet flow ( $t/t_{BP} = 0.25$ ), the region of high streamwise velocity along the SS of the vane is maintained in that position by the pitchwise velocity toward the SS.

At the DSTM B plane (10% downstream of the throat), the secondary flow profiles begin to assimilate between the jet and wake flow. These data are presented in Figure 3.26. In terms of the pitchwise velocity, all instances present a predominantly cross-passage gradient with higher values along the pressure surface of the vane. A higher value is present in the hub-PS corner during wake-associated time instances ( $t/t_{BP} = 0.13$  and  $0.63$ ); however, the overall profiles are very similar through the entire blade-pass period. This is significantly different from the behavior observed at the throat in which the pitchwise velocity profiles were markedly different within the jet and the wake flows. The streamwise velocity does not indicate the same degree of assimilation. The wake flow still contains a region of high streamwise velocity adjacent to the shroud with the predominant gradient being in the spanwise direction. Within the jet flow, this region is adjacent to the suction surface of the passage with the predominant gradient being in the pitchwise direction. These data indicate that the mixing of the jet and wake flow does not occur isotropically: the secondary velocities profiles within the jet and wake flow begin to emulate each other before the primary (streamwise) velocity. There are two potential explanations for this phenomenon. First, the fluctuations in the secondary velocities could dissipate more quickly due to their lower average magnitudes. Alternatively, this could occur due to the role of the secondary velocities in maintaining the separate jet and wake flow profiles (as discussed previously). This impact on the mixing process could mean that the mixing of the secondary flow velocity profiles is a necessary condition for the agglomeration of the streamwise velocity profiles. In other words, the secondary flow profiles must assimilate before the primary flow profiles can begin to mix to a significant degree.

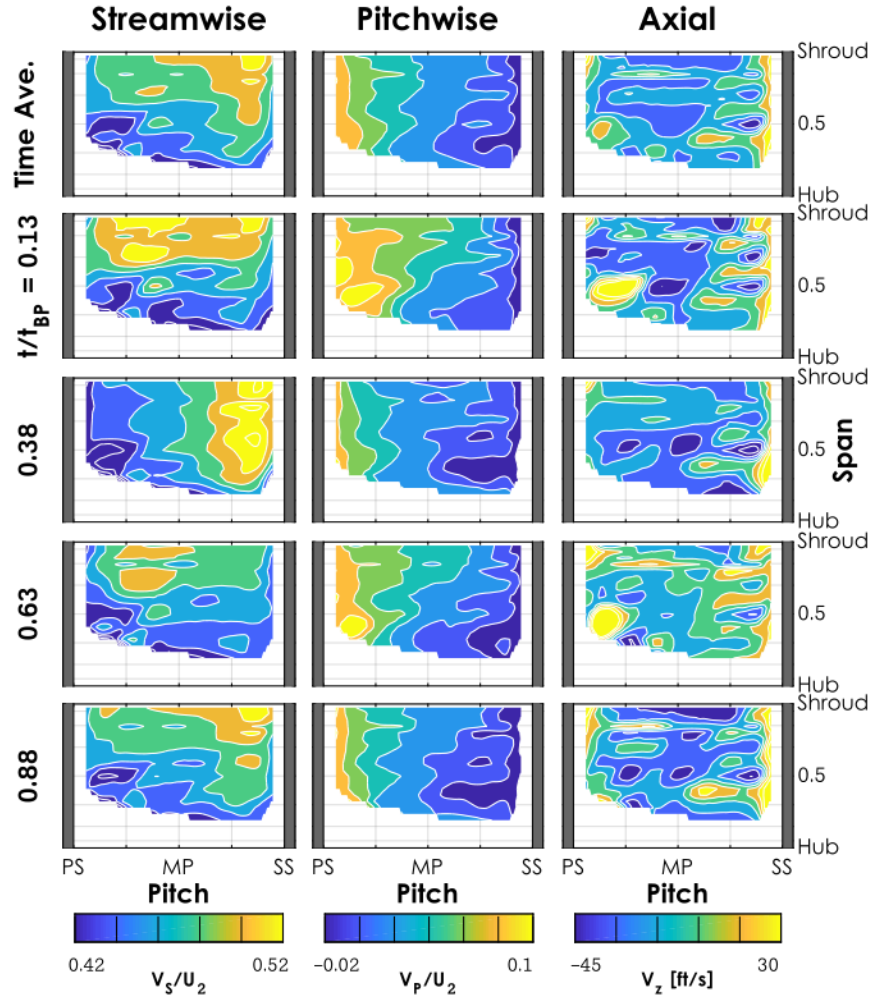


Figure 3.26: Unsteady velocity field at the DSTM B plane (10% downstream from the throat)

This plane also contains the first indication of an increased streamwise velocity deficit region developing in the hub-PS corner of the passage (as was discussed with the constant-span data presented in Section 3.2). This lower streamwise velocity is present in the hub-PS corner of the passage through all instances. Within the wake flow, this region extends across the passage toward mid-passage. Unfortunately, data were not obtained below 30% span along the pressure surface of the passage due to the decreased signal-to-noise ratio accompanying the mirrors necessary for optical access to that corner of the flow path. This prevented a more thorough determination of the shape and origin of this region.

Further downstream, the fluctuations continue to dissipate and the jet and wake flow profiles assimilate in all velocity components. At the DSTM D plane (20% downstream from the throat),

this process is almost complete as the profiles in the streamwise, pitchwise, and axial velocity components remain almost constant through the blade-pass period, Figure 3.27. A small region of increased pitchwise velocity extends out from the pressure surface of the vane within the splitter blade wake flow ( $t/t_{BP} = 0.42$ ) and a small region of increased streamwise velocity extends down along the suction surface of the vane within the adjacent jet flow ( $t/t_{BP} = 0.67$ ). The growth of the low streamwise velocity region along the pressure side of the passage and the hub surface is also apparent at all instances in time. This is indicative of the region of separated flow developing as discussed previously.

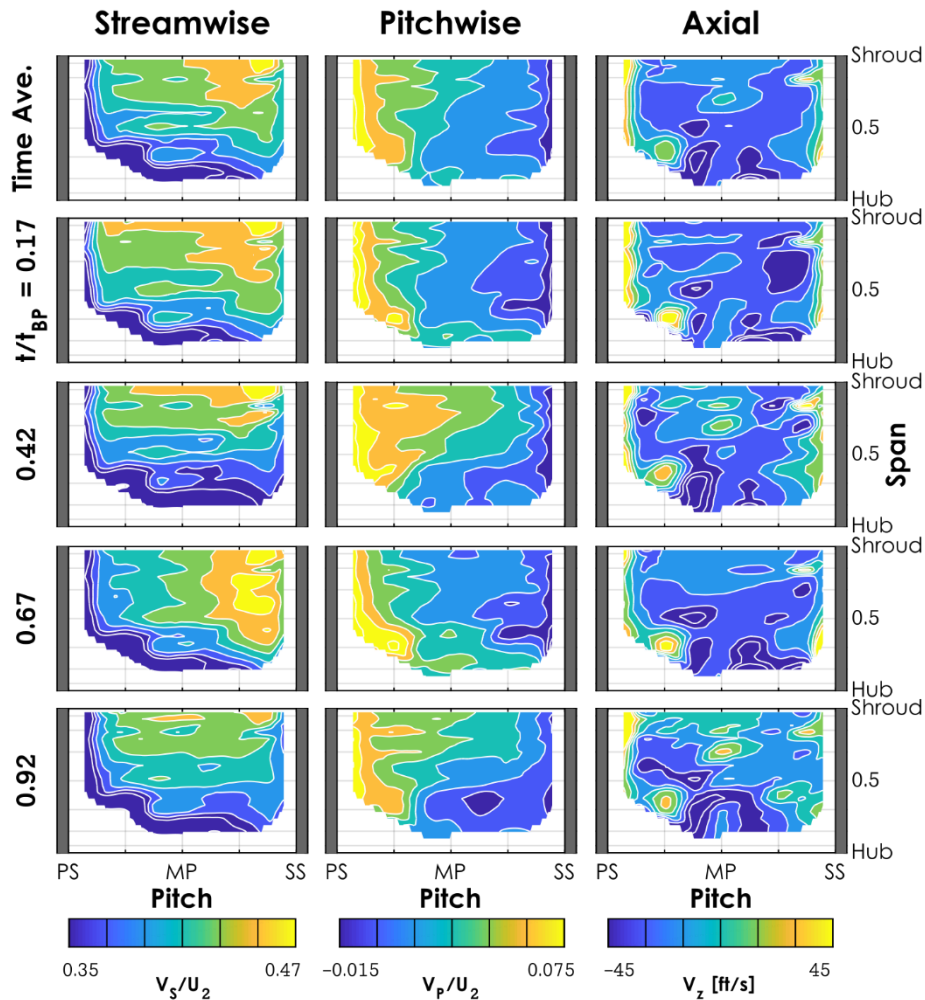


Figure 3.27: Unsteady velocity field at the DSTM D plane (20% downstream from the throat)

The DSTM G plane (40% downstream), the final refined data plane, illustrates the end result of the jet/wake mixing process, Figure 3.28. The cross-passage profiles remain constant through the

entire blade-pass period with only minor fluctuations being present. This steady profile contains a core region of high streamwise velocity in the shroud-SS corner of the passage. From this core region, the streamwise velocity decreases gradually across the majority of the pitch and the span, until a sharp decrease occurs adjacent to the hub and pressure side surfaces. The pitchwise velocity is positive (toward the PS) across the entire passage with a larger magnitude adjacent to the pressure side. This is indicative of the flow not fully turning to follow the vane trajectory and retaining kinetic energy in the tangential velocity component that is not recovered into static pressure. The axial velocity contains a region of strong positive (toward the hub) axial velocity along the pressure surface and a similar but smaller and weaker region along the suction surface. Away from the vane surfaces the axial velocity is predominantly directed toward the shroud (negative) below 50% span and near-zero above 50% span.

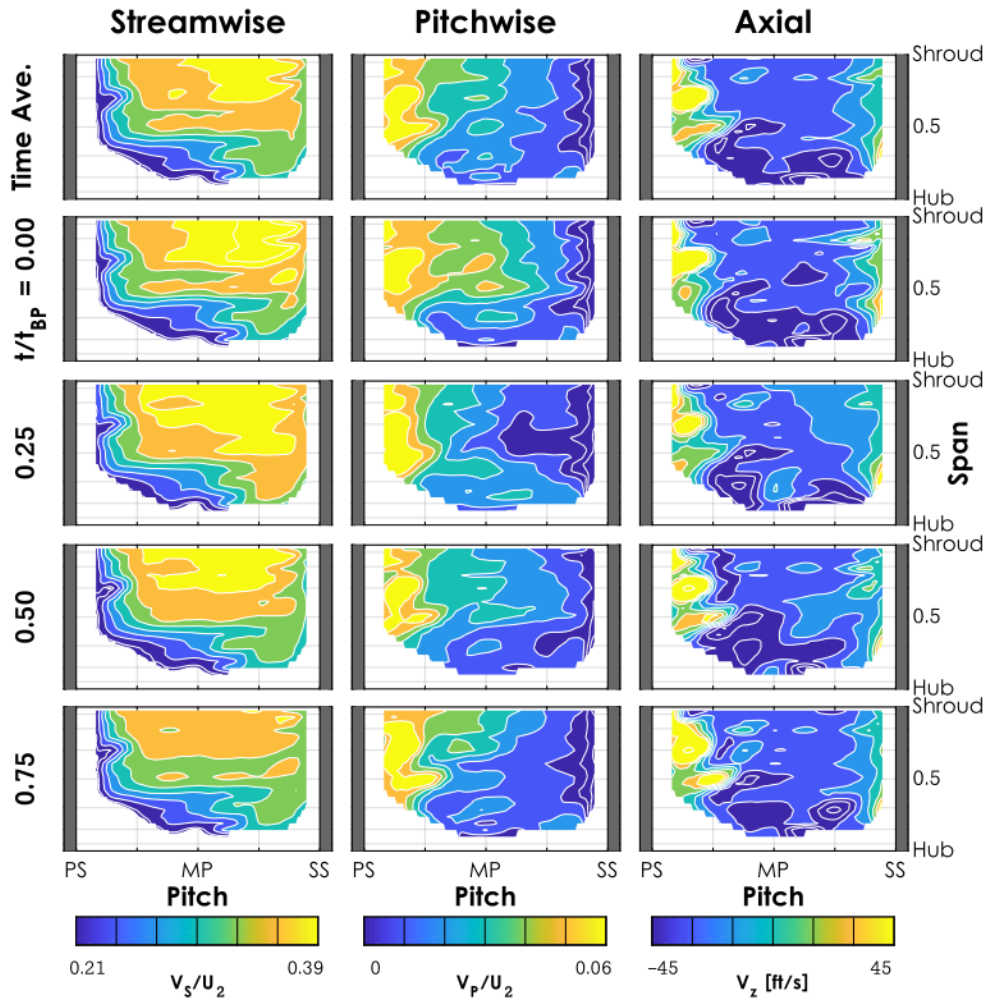


Figure 3.28: Unsteady velocity field at the DSTM G plane (40% downstream from the throat)

### 3.5 Unsteady Development of the Passage Vortex

The region of flow separation within the passage that develops along the pressure surface of the diffuser vane is also evident in the turning of the flow through the passage. The time-averaged absolute flow angle,  $\alpha$ , progression through the passage along constant-pitch lines at 50% span is presented in Figure 3.29. The turning of the flow toward the radial direction (a decrease in the absolute flow angle) occurs due to the diffusion of the tangential flow velocity. An ideal diffuser would result in purely radial flow at the exit as this would represent the conversion of all the tangential kinetic energy from the impeller discharge flow into static pressure. The only remaining kinetic energy in the fluid would be that due to the radial velocity, which is necessary for the convection of mass-flow through the stage. These data indicate that across most of the passage, the vanes effectively turn the flow toward the radial direction. However, adjacent to the pressure side (PS) of the passage, the flow angle does not continue to decrease downstream of the throat. Between the throat and 25% downstream, the flow angle *increases* by nearly  $10^\circ$  at 45% pitch. At 37.5% pitch, the flow angle increases by  $6^\circ$  between the throat and 15% downstream. Boundary layer separation occurring along the pressure side of the passage prevents the flow from adequately following the vane trajectory in the pressure side portion of the passage.

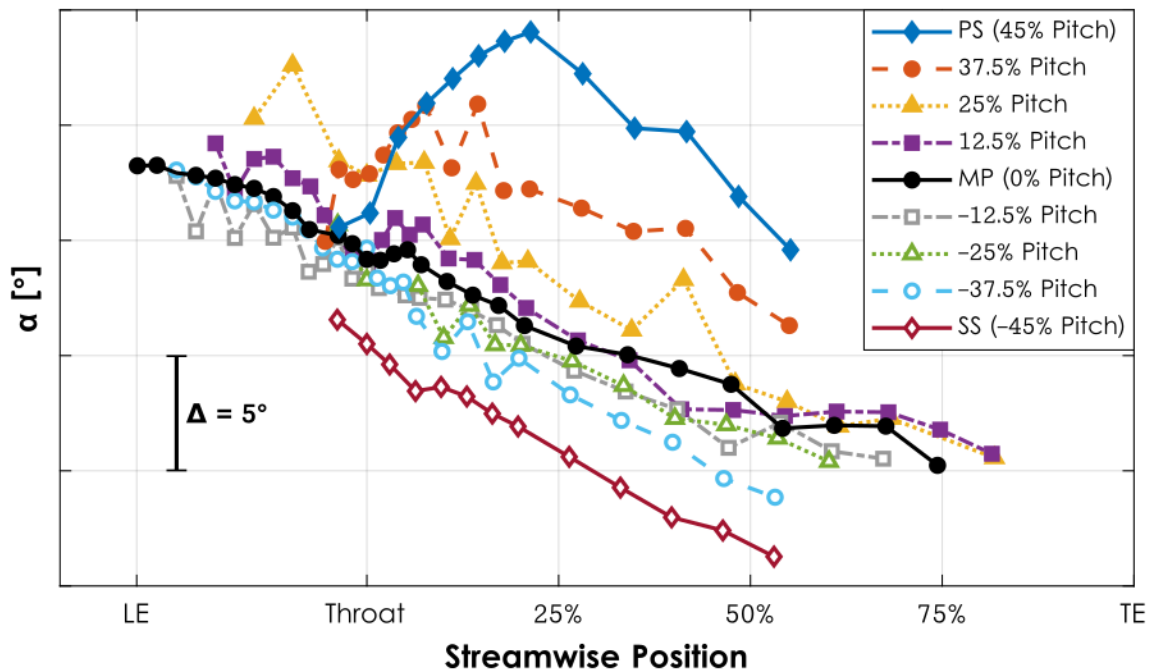


Figure 3.29: Time-averaged absolute flow angle at 50% span

The data consistently indicate a significant flow separation along the pressure surface of the vane. However, the predominantly positive incidence at the leading edge, especially within the wake flow (Figure 3.23), would, intuitively, promote separation along the *suction* surface. This apparent discrepancy is explained by the unsteady development of a passage-spanning vortex.

The convection of the wake flow through the diffuser passage is given in Figure 3.30. The corresponding figure for the convection of the jet flow through the diffuser passage is depicted in Figure 3.31. These figures track the wake (or jet) flow trailing the splitter blade through the diffuser passage. Data are presented at the same refined planes discussed in Section 3.4 at only the instance in time corresponding to the splitter blade wake (or jet) convection through that plane. Instead of the USTM A plane (-5%), data are presented at a cross-passage plane passing just in front of the leading edge of the diffuser vane near the end of the semi-vaneless space. This allows the incidence field just upstream of the leading edge to be included in this presentation. In these two figures, the three velocity components are presented across the rows: streamwise on the top, pitchwise in the middle, and axial on the bottom. Within each plot, the velocity data are presented as the difference between individual measurements,  $U_i$ , and the mean value of that component ( $\bar{U}$ ) across the plane of interest at that instance in time. The planes proceed downstream from left to right. The abscissa is the pitch coordinate with the passage-bounding vanes depicted on either side of the graphs, the pressure surface (PS) on the left and the suction surface (SS) on the right. The ordinate is the span with the hub on the bottom and the shroud on top. The arrows overlaid on the contours represent the secondary flow direction and magnitude at measurement locations.

At the leading edge (LE) plane (the left column of Figure 3.30) the high incidence at the leading edge that was observed in Figure 3.23 is illustrated in both the secondary flow direction and the high pitchwise velocity. The axial velocity data indicate an important companion to the pitchwise velocity field. A lobe of strong negative (toward the shroud) axial velocity occurs adjacent to the hub with an opposing lobe of positive (toward the hub) axial velocity at higher spans. The endwall flow is drawn out toward mid-span to “replace,” so to speak, the flow that passes into the adjacent passage due to the strong pitchwise velocity component. This spanwise gradient in the pitchwise velocity developed during the impact of the wake flow on the vane LE contributes to the production of streamwise vorticity. This begins the formation of a vortex along the pressure surface of the vane in the hub corner.

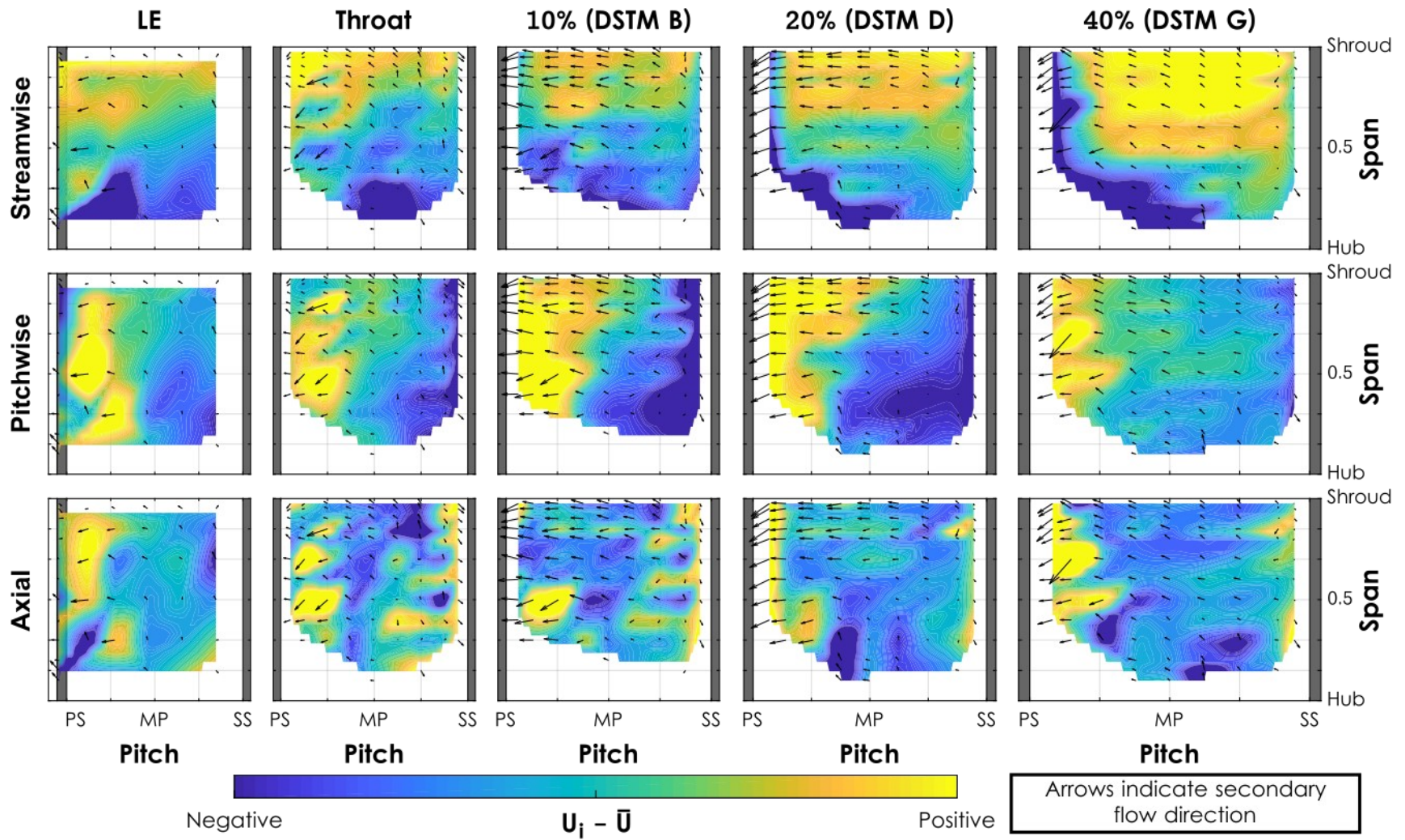


Figure 3.30: Deviation of each velocity component ( $U_i$ ) from the instantaneous planar mean value ( $\bar{U}$ ) during wake propagation

Further downstream, this vortex in the hub-PS corner of the passage is discernible at the throat (second column of Figure 3.30). The counterclockwise vortex now covers nearly the full span and extends out near mid-passage (MP). The extent is evident in the pitchwise velocity and secondary velocity vectors but is most apparent in the adjacent bands of negative (toward the hub) and positive (toward the shroud) axial velocity.

At the 10% downstream plane (DSTM B, the third column of Figure 3.30) the vortex has grown further across the passage with the majority of the secondary flow behavior being in the pitchwise direction, oriented toward the pressure side. The secondary flow vectors indicate a vortex that now extends fully from hub to shroud and from the pressure surface to approximately -25% pitch (halfway between MP and the SS). Immediately adjacent to the pressure surface, a localized band of positive (toward the hub) axial velocity is present but is not a part of this vortex structure. A similar pattern is present at the 20% downstream plane (DSTM D, fourth column of Figure 3.30) with three small differences. First, stronger negative (toward the shroud) axial velocity is apparent adjacent to the hub with a sharp pitchwise gradient appearing between 25% pitch and mid-passage. Second, the deficit in streamwise velocity in the hub-PS corner of the passage is more severe. Third, the secondary flow vectors indicate the vortex structure now fills almost the entire pitch of the passage and the spanwise velocity toward the hub along the suction surface is reduced in magnitude.

Finally, at approximately 40% downstream of the throat (DSTM G, the fifth column of Figure 3.30), the vortical structure is more distinct and extends across the entire passage (with the exception of the narrow region immediately adjacent to the suction surface where an axial velocity toward the hub remains). The bulk motion of this vortex is counterclockwise. A distinct region of high streamwise velocity (the “core” region mentioned previously) is present near the shroud indicating a low-loss region. A summary of this discussion of the unsteady convection of the wake flow through the diffuser passage is presented in the top row of Figure 3.32.

The corresponding data tracking the jet convection through the diffuser passage are presented in Figure 3.31. Comparing the development of the jet and the wake flow evinces the extent to which unsteady structures persist through the diffuser passage. At the LE plane, the jet flow exhibits a consistent increase in the streamwise velocity in the pitchwise direction with a larger magnitude

present along the suction surface. The secondary flow vectors do not present a coherent structure as was present within the wake convection and a pitchwise velocity toward the SS is present immediately in front of the vane. This indicates that the flow at that location is following a trajectory into the passage under consideration rather than across, into the adjacent passage. Similar behavior is observed at the throat (second column of Figure 3.31). There tends to be a slightly higher pitchwise velocity nearer the pressure surface and the hub, however no distinct structure or pattern is present in the secondary flow vectors and the relative magnitudes are low. The streamwise velocity at the throat is high along the suction surface and this region is more distinct than at the LE plane (although this could be due to the denser measurement mesh). Isolated regions of low streamwise velocity are also present adjacent to the pressure surface near ~60% span and along the hub at mid-passage.

A coherent secondary flow pattern does not begin to appear until 10% downstream of the throat (DSTM B, the third column of Figure 3.31). A narrow region adjacent to the suction surface contains a positive (toward the hub) axial velocity. The rest of the passage exhibits a pitchwise velocity toward the PS, growing in magnitude toward the pressure side of the passage. The magnitudes of the axial velocity are slightly larger below 50% span, however the overall levels are low. The high streamwise velocity region adjacent to the suction surface is largely unchanged from the throat, but the isolated regions of low streamwise velocity have merged to form a single region in the hub-PS corner of the passage.

Further downstream (at DSTM D, 20% downstream from the throat, the fourth column of Figure 3.31), the secondary flow structure begins to mirror the structure observed within the wake flow. The bulk motion is consistently toward the shroud and the pressure side of the passage (with the exception of immediately adjacent to the suction surface). The fine details are still different between the wake flow (Figure 3.30) and the jet flow (Figure 3.31). Namely, the jet flow has a stronger axial velocity toward the shroud across the entire passage. Compared to the jet flow at 10% downstream, the high streamwise velocity region at the 20% downstream plane has shifted toward the shroud and has stretched out from the suction surface of the vane toward mid-passage.

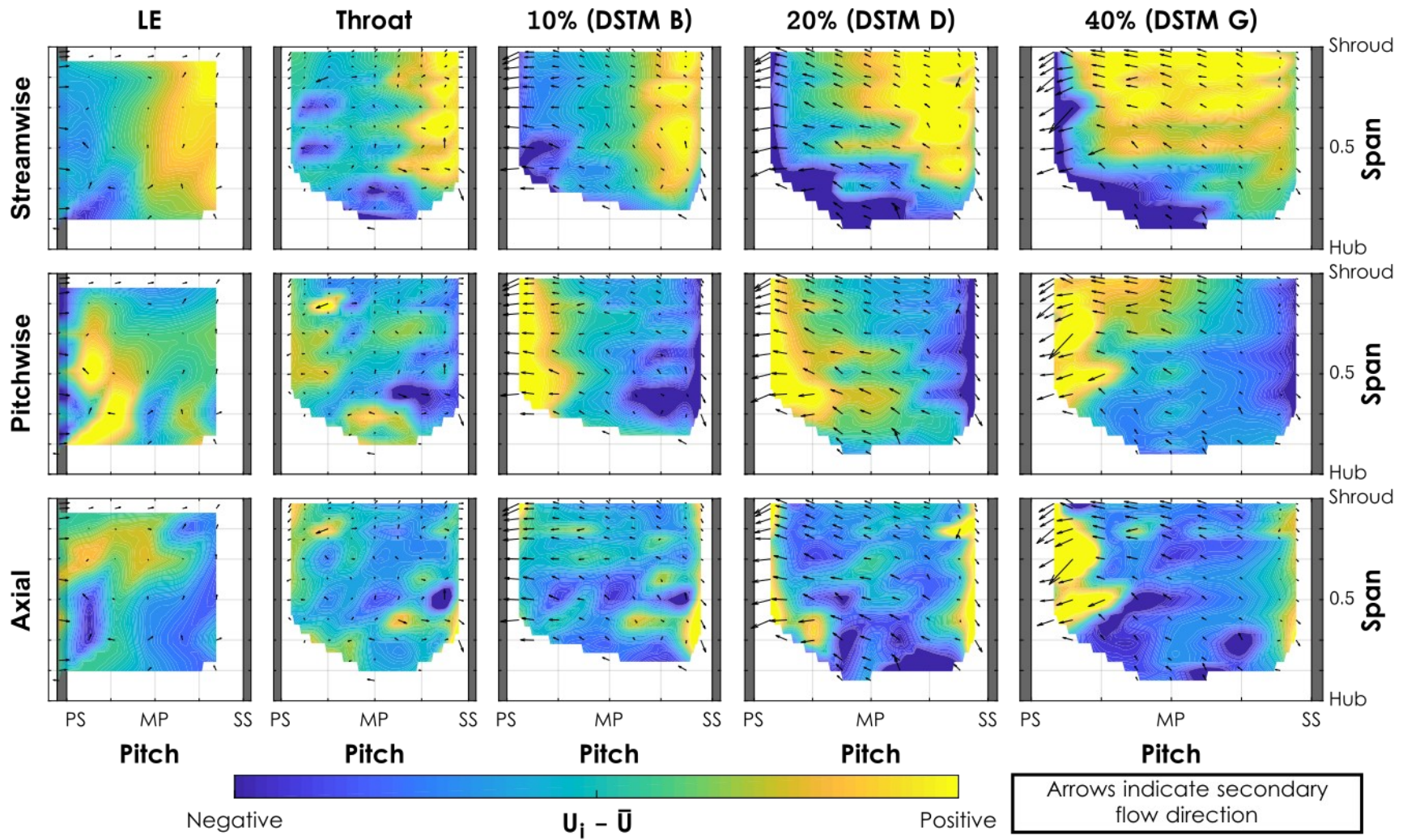


Figure 3.31: Deviation of each velocity component ( $U_i$ ) from the instantaneous planar mean value ( $\bar{U}$ ) during jet propagation

By the final refined plane, 40% downstream of the throat (DSTM G, the fifth column of Figure 3.31) the patterns associated with the jet flow are nearly indistinguishable from the wake flow in terms of both primary and secondary flows. A high streamwise velocity core region is present between 50% span and the shroud and from the suction surface across to approximately 25% pitch (halfway between MP and the PS). Within the wake flow, this core region was first observed at the throat and grew, primarily in terms of magnitude, in propagating downstream; the location remained relatively constant. However, within the jet flow, the core region began further upstream (at the LE plane) but remained adjacent to the suction surface beyond the throat.

A cartoon summarizing the temporal behavior of the formation of this passage-spanning vortex is presented in Figure 3.32. Previous studies have concluded that unsteadiness is effectively dissipated upstream of the throat and has little impact on flow development within the passage. Stahlecker et al. [20] observed a similar passage vortex, but concluded that it was formed upstream of the throat and was steady in time. These results support a different conclusion. Within the diffuser passage, the jet and wake flow still have different streamwise velocities. From a Lagrangian perspective, fluid particles that originally formed the impeller wake will spread forward into the preceding jet flow until the jet and wake flow are indistinguishable. The secondary flow structures interact with this convection process and reduce the rate of mixing between the two regions of flow in the pitchwise and spanwise direction, as described previously. From a Eulerian perspective, the result of this process is a temporal broadening of flow structures associated with the wake flow. This is indicated by the jet flow growing to emulate the wake flow in terms of both primary and secondary flow structures. What is often referred to as “wake dissipation” is perhaps better described as the agglomeration of the jet and wake flow as they merge to form a coherent flow structure. From the data presented, distinct jet and wake flow patterns are evident 10% downstream of the throat. At 20% downstream, the secondary flow pattern within the jet flow is beginning to resemble the wake flow pattern; however, the primary flow patterns are still distinct. It is not until 40% downstream of the throat, much further than often assumed, that the agglomeration process is complete in both the primary and secondary flow structures.

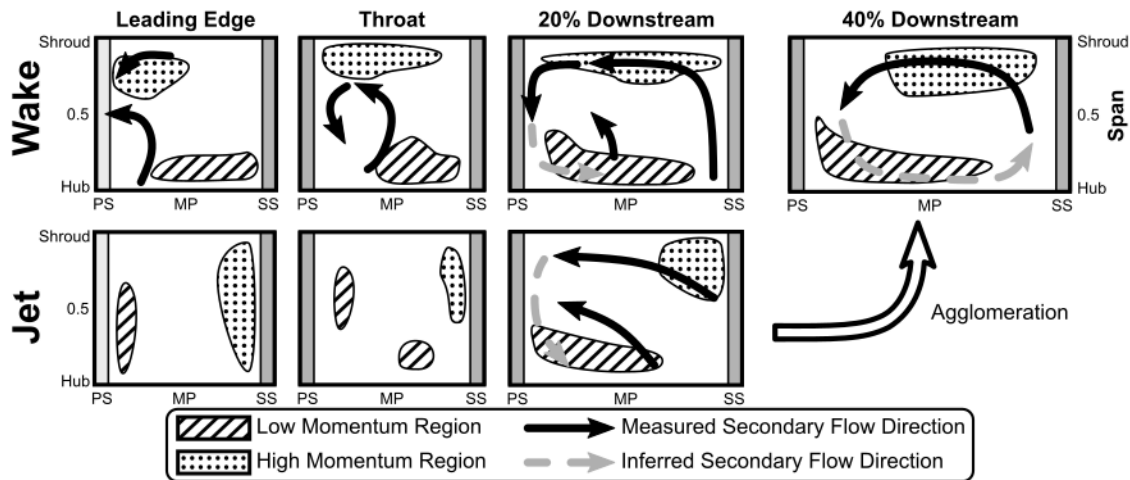


Figure 3.32: Unsteady nature of vortex development

This discussion connects back to the time-averaged flow angle progression through the diffuser presented at the beginning of this section (Figure 3.29). The flow separation along the pressure surface of the vane is not aligned with the high positive incidence present at the vane leading edge (which would promote separation along the suction surface). This apparent discrepancy can be explained by the unsteady vortex development. At the leading edge, the spanwise gradient in incidence (and the pitchwise gradient in axial velocity) induces a streamwise vortex in the hub-PS corner of the passage. Initially, within the “zone of rapid adjustment,” this vortex acts to drive low momentum endwall flow toward mid-span. Within this region, a strong adverse pressure gradient is present as the flow adjusts to the presence of the vanes and this low momentum flow exacerbates the boundary layer that is already separation prone. In approaching the throat, the growing vortex within the wake flow keeps low momentum flow entrained along the pressure surface and prevents higher-momentum core flow from being able to re-energize the boundary layer. This leads to the separation observed along the pressure side of the passage. Once the vortex is fully developed—to span the full passage and be temporally stable—the vortex acts to feed the higher-momentum flow present near the shroud into this region of separated flow. This allows the boundary layer to reattach toward the trailing edge, as indicated by the decrease in the absolute flow angle along the pressure surface beginning at approximately 25% downstream.

The nature of this boundary layer separation is not properly explained by a steady interpretation of the passage vortex. If these structures are assumed to be steady, then the vortex would only act to feed core flow (with high momentum) from the shroud into the hub-PS corner. This would act

to stabilize the boundary layer along the pressure surface of the vane. Combined with the incidence data, this would likely cause the separation to occur on the suction surface of the vane. Only the unsteady development and growth of the passage vortex in the streamwise direction adequately explains the observed steady flow field with separation occurring along the pressure surface of the vane.

### 3.6 Reynolds Stress Measurements

Direct measurement of unsteady fluctuations in the velocity vector field allows the calculation of the full Reynolds stress tensor. Continuing from Equation (18), the elements of the measured Reynolds stress tensor,  $Re_{ij}$ , at an instance in the blade-pass period are calculated via:

$$Re_{ij} = \frac{\tau_{ij}}{\rho} = \overline{u'_i u'_j} = \overline{(u_i - \bar{u}_i)(u_j - \bar{u}_j)}, \quad (21)$$

where the overbar indicates an average. The transit-time weighting method to eliminate bias in the LDV results (see Equation (15) and the discussion in Section 1.6.2) also applies to the computation of Reynolds stress components. Equation (21) then takes the form:

$$Re_{ij} = \overline{(u_i - \bar{u}_i)(u_j - \bar{u}_j)} = \frac{1}{\sum t} \sum [t(u_i - \bar{u}_i)(u_j - \bar{u}_j)]. \quad (22)$$

The summation goes over every observation of the velocity vector at a particular instance in ensemble averaged time,  $t$  is the transit time associated with a particular observation, and  $i$  and  $j$  refer to individual components of the velocity vector (following Einstein tensor notation). The turbulent kinetic energy,  $k$ , and the turbulence intensity,  $I$ , are defined from the Reynolds stress components via:

$$k = \frac{1}{2} Re_{ii} = \frac{1}{2} (Re_{xx} + Re_{yy} + Re_{zz}) \text{ and} \quad (23)$$

$$I = \frac{\sqrt{\frac{2}{3}} k}{|u|} = \frac{\sqrt{\frac{1}{3} (Re_{xx} + Re_{yy} + Re_{zz})}}{\sqrt{u_x^2 + u_y^2 + u_z^2}} = \sqrt{\frac{Re_{xx} + Re_{yy} + Re_{zz}}{3(u_x^2 + u_y^2 + u_z^2)}}. \quad (24)$$

Physically, each Reynolds stress component,  $Re_{ij}$ , describes the role of turbulent fluctuations in convecting other components of momentum. For example,  $Re_{xy}$  represents the turbulent flux of  $x$  momentum in the  $y$  direction. Inspection of Equation (22) shows that the Reynolds stress tensor is symmetric, with only six independent elements. These quantities are computed at each instance in the ensemble-averaged impeller revolution using the same mean passage assumption that has been implemented throughout this work. The uncertainty associated with these measurements differs at each geometric point and at each instance in time due to the stochastic nature of the sampling. Throughout most of the flow field and blade-pass period the uncertainty was maintained below approximately  $\pm 200 \text{ ft}^2/\text{s}^2$ , calculated via the methodology presented in [131]. Within the wake flow the uncertainty increased to a maximum of approximately  $\pm 600 \text{ ft}^2/\text{s}^2$  due to a reduction in the available data rate. The uncertainty levels tended to be closer to the upper-end of these limits adjacent to the shroud and decreased toward mid-span. These values apply generally to every component of the Reynolds stress tensor, except for  $Re_{yz}$  and  $Re_{zz}$ , which had 50% and 100% (double) larger uncertainty levels, respectively. Uncertainties associated with fluctuations in the  $z$ -component of the velocity field were larger due to the inability to directly measure the axial velocity component. Optical access limitations required the axial velocity to be measured at an angle and then projected onto the axial direction, increasing the associated uncertainty. Data were obtained at twelve geometric points between 40% and 97.5% span as detailed in Figure 3.1. The Reynolds stress components at a radius ratio of 1.05 are presented in Figure 3.33 (Point 6) and Figure 3.34 (Point 10). The principal components ( $Re_{ii}$ ) are in the top row, the abscissa is in  $\text{ft}^2/\text{s}^2$ , and the ordinate is the spanwise position. The time-averaged values and the maximum extent (the range) observed through the blade-pass period are presented as well as the instantaneous profile at four time instances.

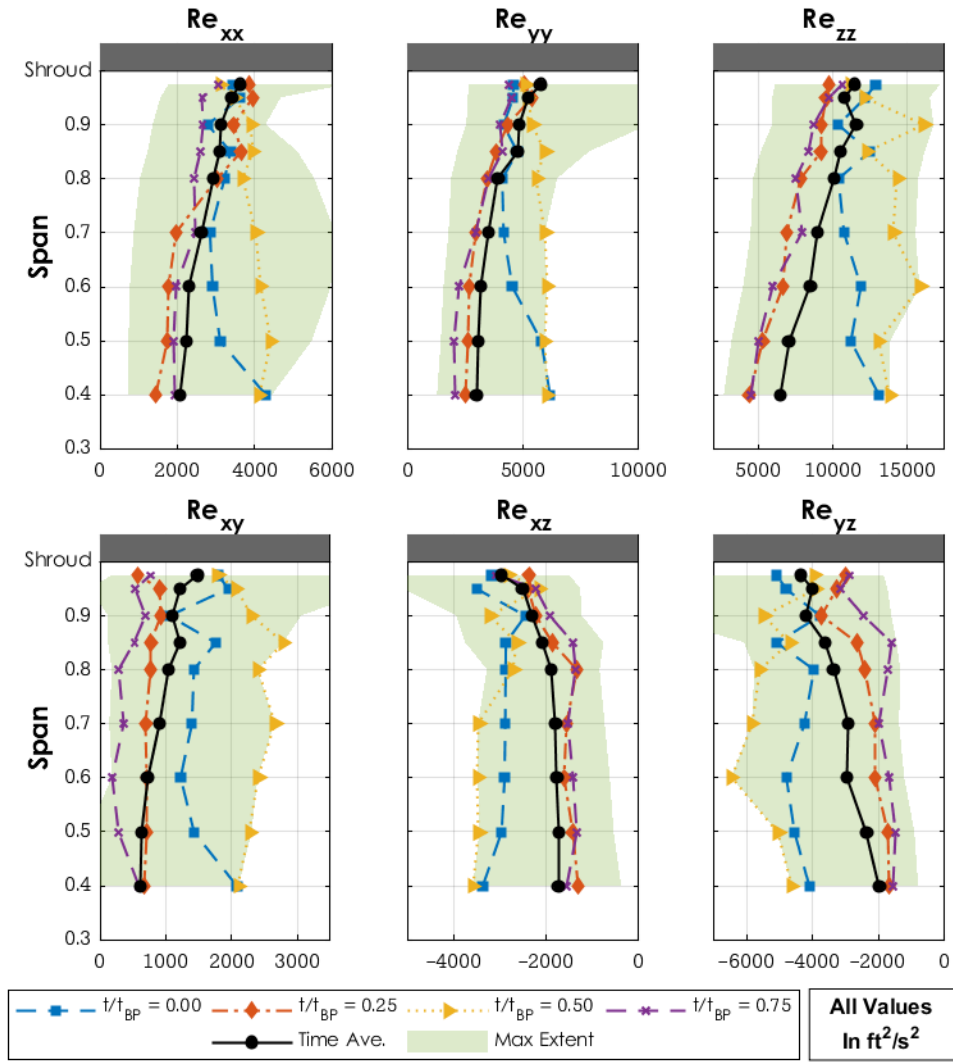


Figure 3.33: Reynolds stress components at  $R/R_2 = 1.05$  (Point 6)

Every component tends to higher absolute values adjacent to the shroud. This could arise due to the shroud-side boundary layer or increased turbulence due to tip leakage flow from the impeller. Additionally, the instantaneous profiles closely resemble the time-averaged profile, only shifted to higher or lower mean values. The range of values observed through the blade-pass period is large relative to the values of each component, indicating the significantly different levels of turbulent fluctuations present within the impeller jet and wake flow. Unsteady traces of Reynolds stress components at particular points will be presented subsequently. The principal components in the  $x$  and  $y$  directions ( $Re_{xx}$  and  $Re_{yy}$ ) are of similar magnitude while  $Re_{zz}$  is significantly larger. Since these two points are located at the same radius ratio, differences in the time-averaged profiles between the two are due to the potential field of the diffuser vane. Point 6 is located within this

potential field while Point 10 is circumferentially aligned with the center of the diffuser passage (see Figure 3.1 for the precise geometric locations). The profiles in the components are largely indistinguishable between the two points except for a minor increase in  $Re_{yy}$  and  $Re_{zz}$  adjacent to the shroud near mid-passage (Point 10) that is not present within the potential field (Point 6).

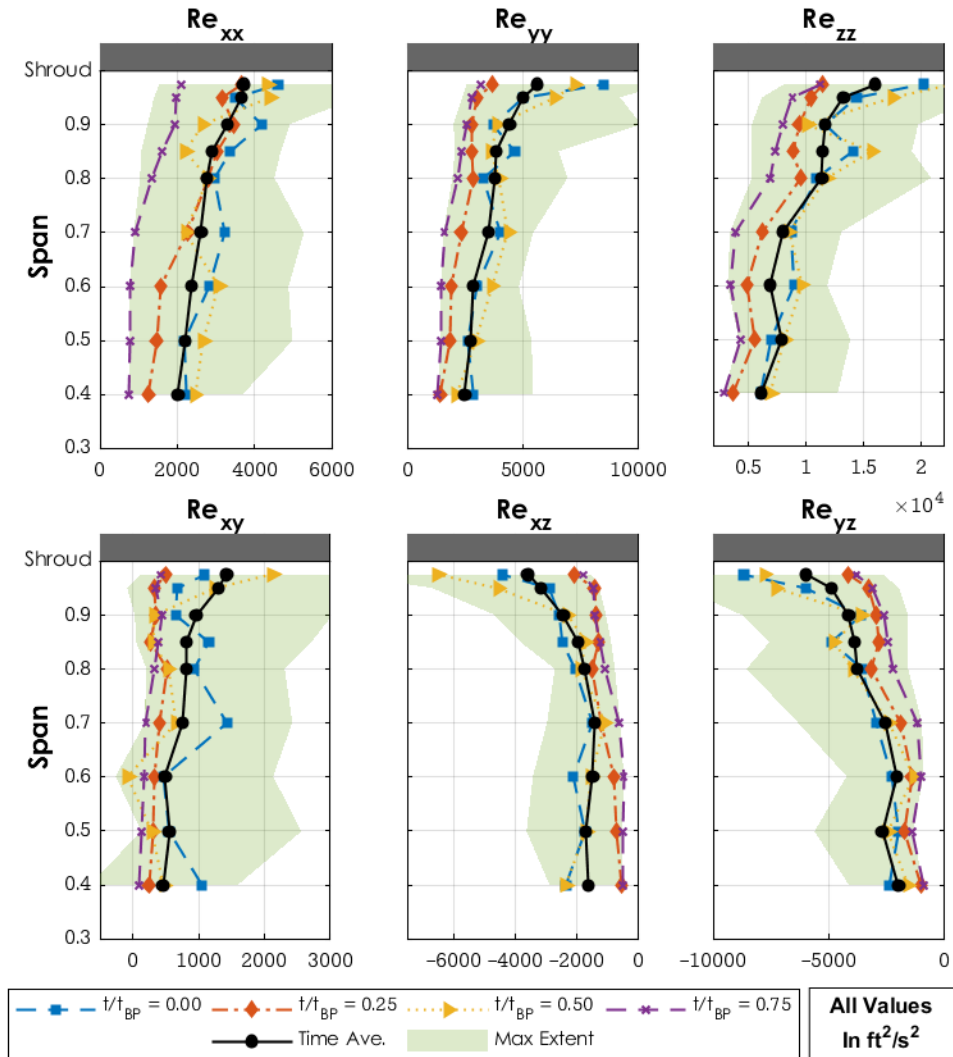


Figure 3.34: Reynolds stress components at  $R/R_2 = 1.05$  (Point 10 )

At the diffuser leading edge radius, the circumferential differences are more pronounced. The data aligned with the leading edge at  $R/R_2 = 1.08$  (Point 26) are presented in Figure 3.35 and the data at mid-passage at  $R/R_2 = 1.08$  (Point 29) are presented in Figure 3.36. Compared to the points within the vaneless space (at a radius ratio of 1.05) the magnitudes of all six components are largely unchanged. This indicates that the Reynolds stress does not dissipate significantly between a

radius ratio of 1.05 and the diffuser leading edge radius. However, the range of values observed at a single spanwise position does decrease in the primary components from a radius ratio of 1.05 (Points 6 and 10, previously presented) and a radius ratio of 1.08, at mid-passage (Point 29). This does not hold in the region adjacent to the vane leading edge (Point 26). At this point, the  $Re_{zz}$  data indicate a large increase in both the time-averaged values and the range of observed values between 70% and 85% span. This is also apparent in the  $Re_{yz}$  component. Additionally, there is greater temporal variation in spanwise profiles of each component adjacent to the leading edge (Point 26) than at mid-passage (Point 29).

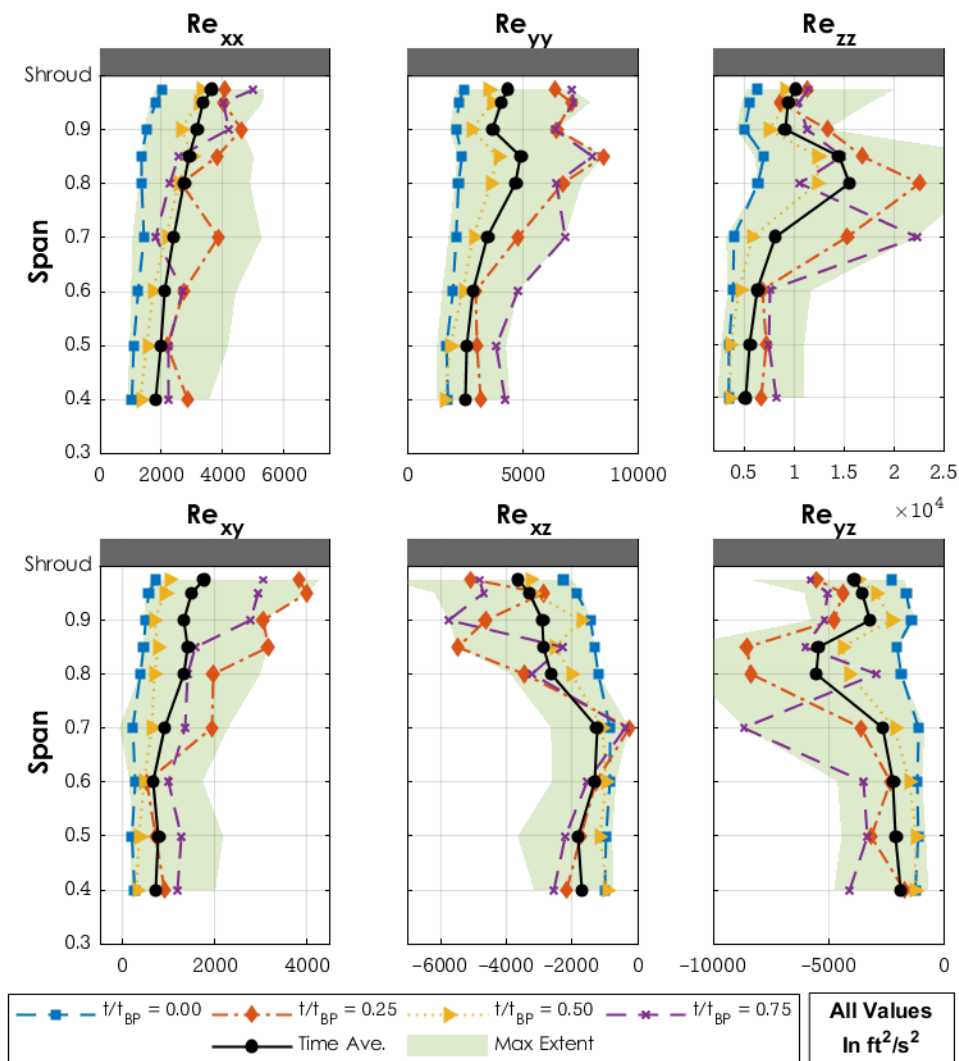


Figure 3.35: Reynolds stress components at  $R/R_2 = 1.08$ , adjacent to the vane LE (Point 26)

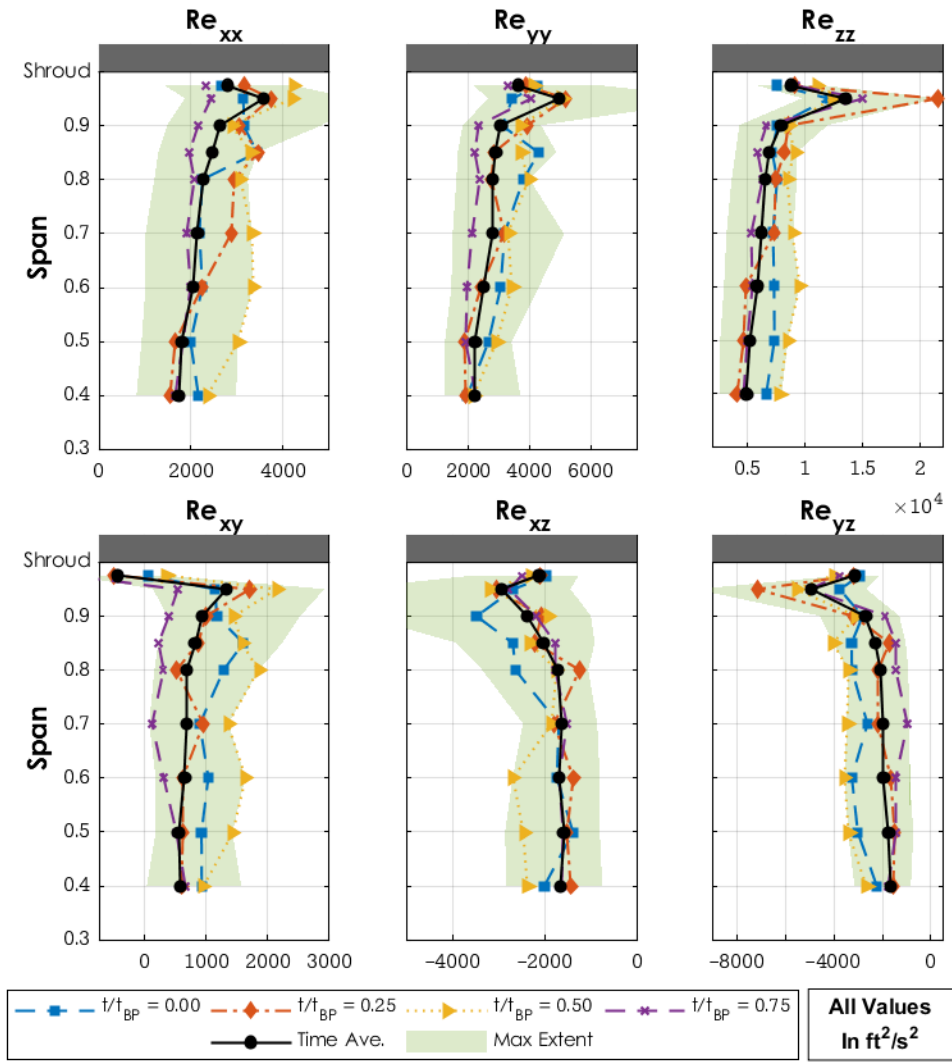


Figure 3.36: Reynolds stress components at  $R/R_2 = 1.08$ , at mid-passage (Point 29)

In the semi-vaneless space at mid-passage (Point 116) larger spanwise gradients are present in many of the components, Figure 3.37. This is most apparent in  $Re_{yy}$ ,  $Re_{zz}$ , and  $Re_{yz}$ . In each of these components, a sharp increase in the magnitude develops above 80% span. The magnitude of each component remains unchanged (relative to the upstream points), except for  $Re_{zz}$  and  $Re_{yz}$ , which indicate larger magnitudes adjacent to the shroud.

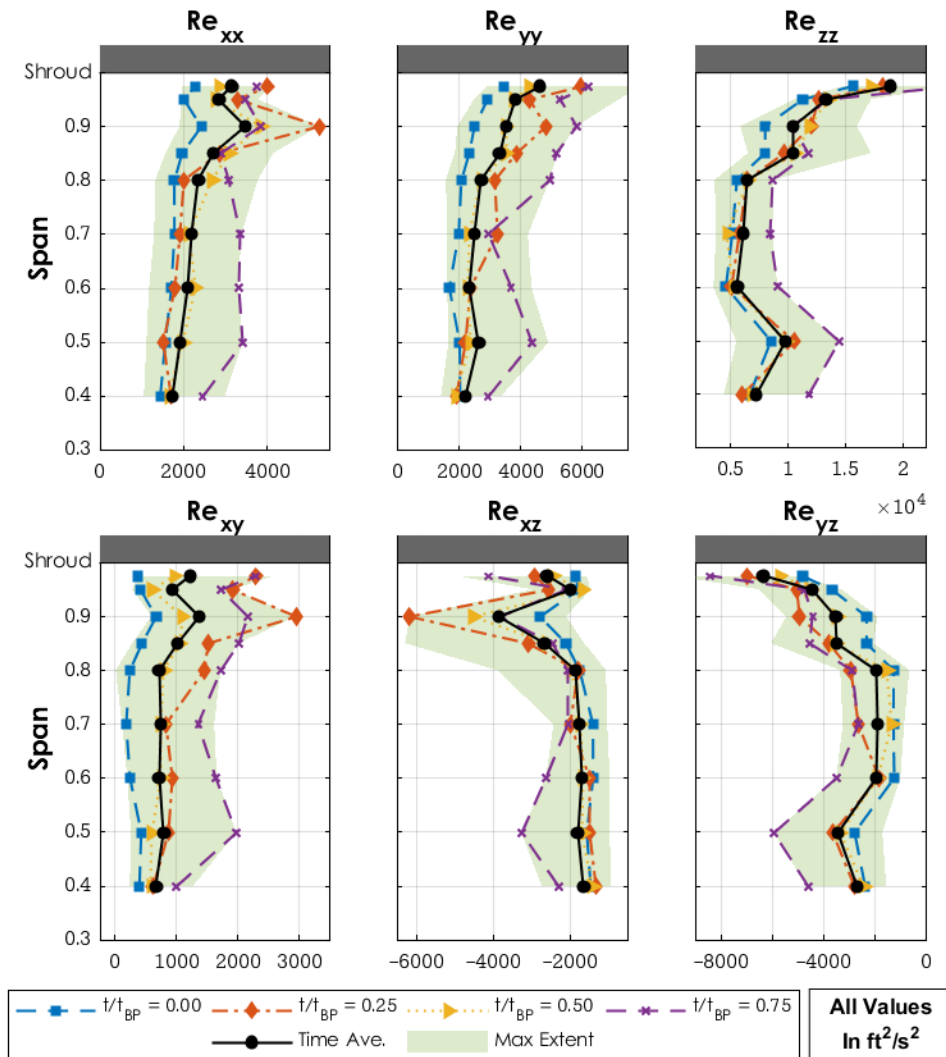


Figure 3.37: Reynolds stress components within the semi-vaneless space, at mid-passage (Point 116)

The Reynolds stress measurements at the throat are presented in Figure 3.38 (Point 30, near-SS), Figure 3.39 (Point 34, at MP), and Figure 3.40 (Point 32, near-PS). The data near the SS indicate the same slight spanwise gradient, with larger magnitudes present adjacent to the shroud, that has

been observed previously. The  $Re_{yy}$ ,  $Re_{xx}$ , and  $Re_{xy}$  components have low time-averaged values ( $Re_{xy}$  is near-zero) with a “max extent” that is biased toward larger magnitudes. This is indicative of short-term but large-amplitude fluctuations in these quantities. The unsteady characteristic will be discussed in more detail subsequently. The mid-passage data indicate larger magnitude values (relative to the near-SS and near-PS data) of all six components. The near-PS data and the near-SS data contain nearly identical time-averaged results in both magnitude and profile. However, the near-PS data contains significantly less variation at lower spans (perhaps due to the reduced velocity magnitude). Additionally, the near-SS and MP data contain a negative  $Re_{xz}$  component while the near-PS data indicate a positive value. This indicates that the correlation between fluctuations in the  $x$ - and  $z$ -velocity components changes sign across the passage.

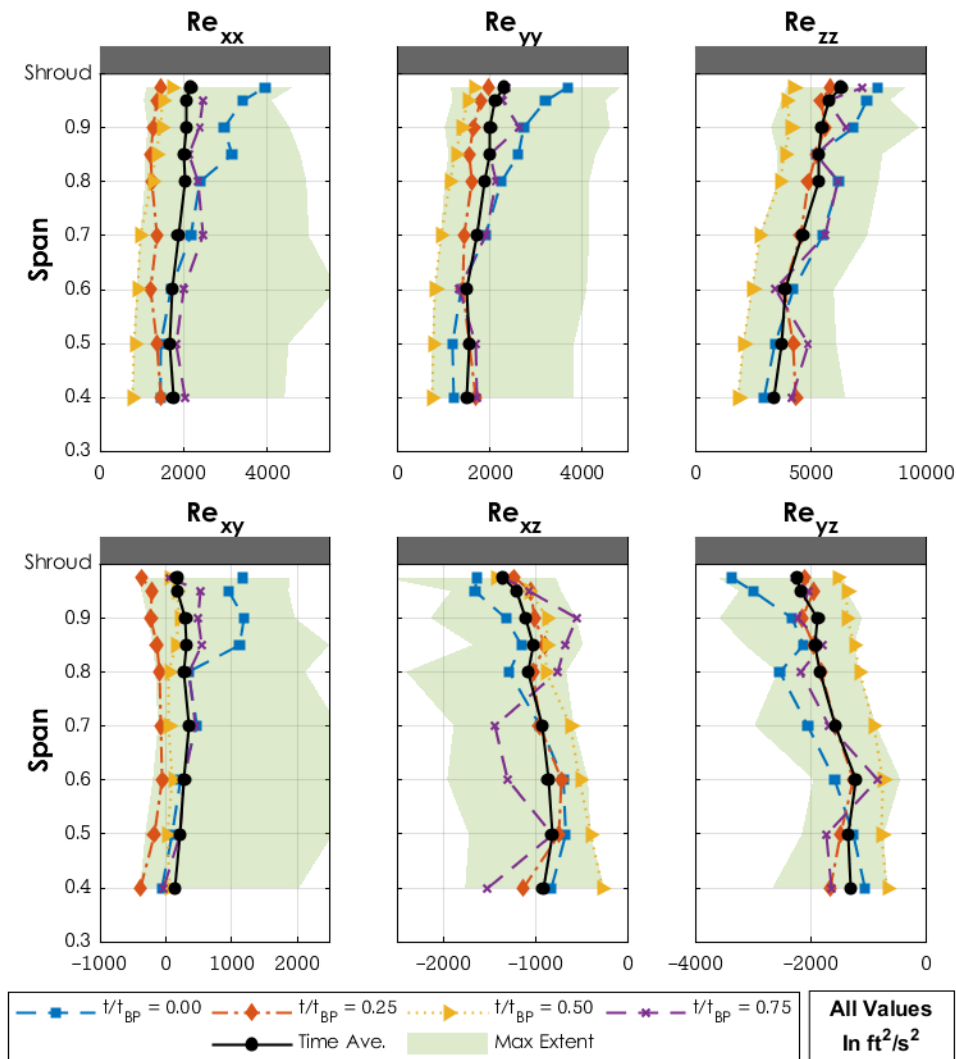


Figure 3.38: Reynolds stress components at the throat, near the suction surface (Point 30)

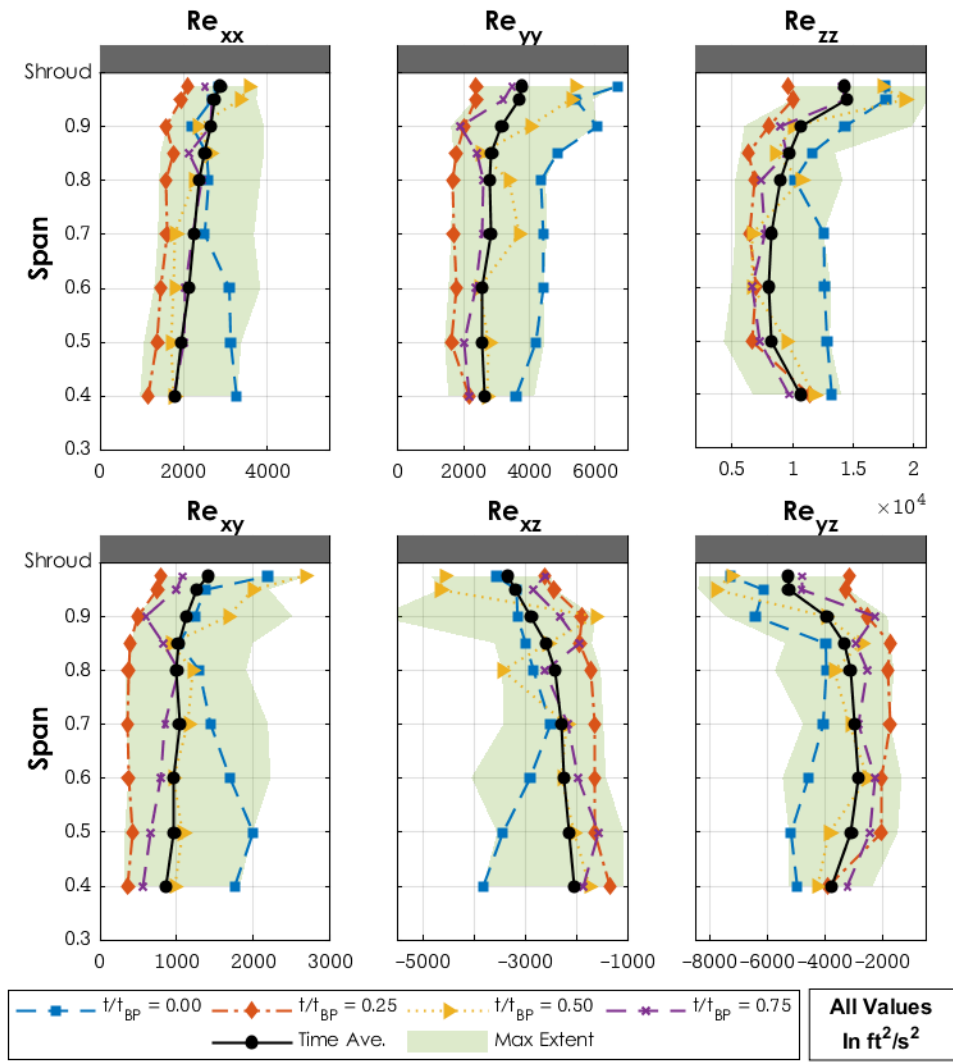


Figure 3.39: Reynolds stress components at the throat at mid-passage (Point 34)

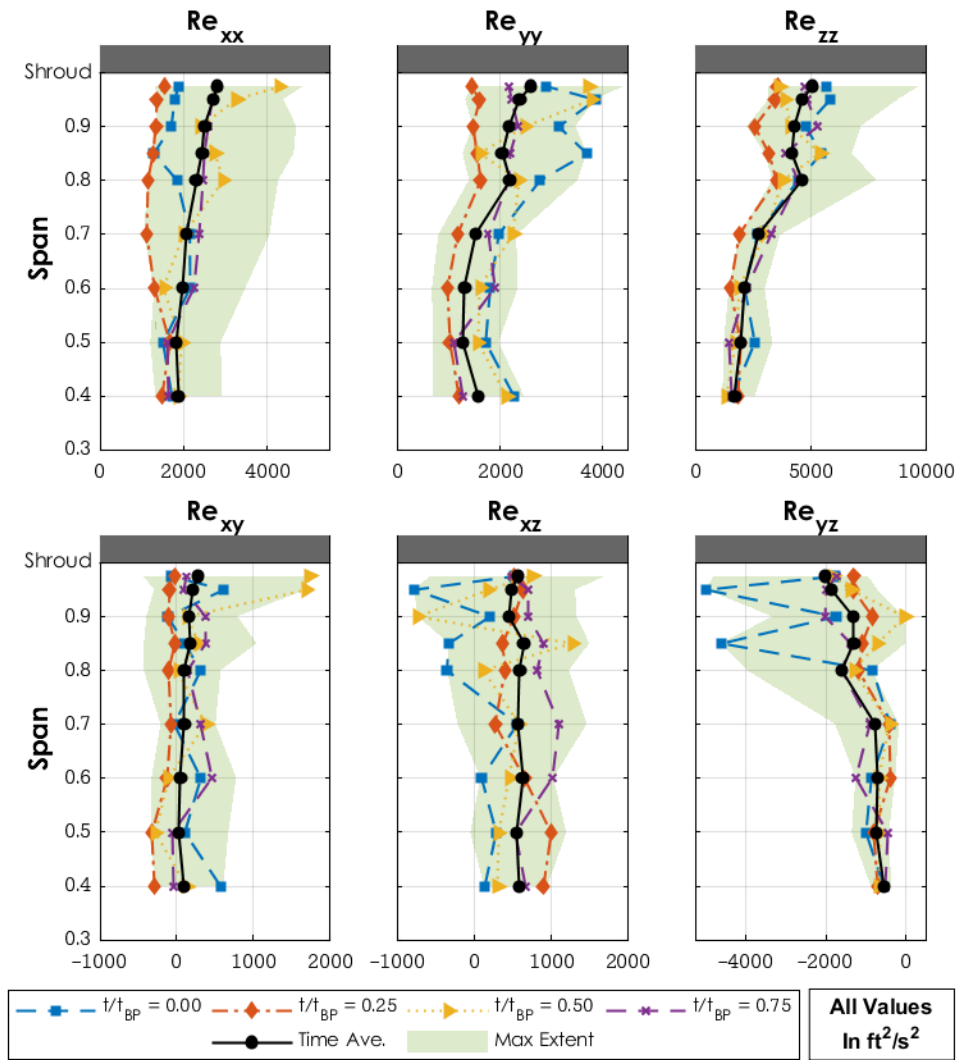


Figure 3.40: Reynolds stress components at the throat, near the pressure surface (Point 32)

The data at the more downstream locations (Points 127, 159, and 166) closely resemble the throat data at the corresponding pitchwise position. These data are included in APPENDIX B. The unsteady properties of the turbulent fluctuations are presented in terms of the turbulence intensity,  $I$ . This quantity typically has more physical meaning to a designer as it directly reflects the energy levels contained within the turbulence, relative to the kinetic energy of the mean flow. The unsteady traces of turbulence intensity through the blade pass-period are presented at the points upstream of the passage in Figure 3.41 and within the passage in Figure 3.42. Data are presented at four spanwise positions (where possible) with the abscissa as time (relative to the blade-pass period) and the ordinate as turbulence intensity.

The data obtained closest to the impeller trailing edge at  $R/R_2 = 1.0125$  (Point 43) and 1.05 (Points 10 and 6) indicate that the turbulence levels are relatively low leaving the impeller. At a radius ratio of 1.0125 (Point 43) levels ranging from 0.06 to a narrow peak of 0.12 are present within the wake flow. At  $R/R_2 = 1.05$  (Points 10 and 6) the peak at 97.5% span (rounded to 98% in the legend) has broadened and the levels have increased slightly to between 0.075 and 0.125. These values continue to increase in approaching the passage at  $R/R_2 = 1.08$ , adjacent to the vane leading edge (Point 26) and within the semi-vaneless space (Point 116). The turbulence spike associated with the wake has decreased in propagating through the vaneless space—the pattern more represents a sine wave rather than a sawtooth wave—although the overall magnitudes have increased by 0.03-0.04. The levels adjacent to the shroud, at higher spanwise positions, are generally higher than the levels closer to mid-span. This could be due to increased turbulence within the impeller tip leakage flow. However, the data just downstream of the impeller trailing edge (Point 43) at 97.5% span does not indicate high values of turbulence. Furthermore, this increased turbulence near the shroud occurs at the vane leading edge (Point 26) but is not as pronounced at the same radius, aligned with the center of the passage (Point 29). This indicates that it is turbulence developed within the shroud-side boundary layer in the strong adverse pressure gradient that develops around the vane leading edge (Point 26) that leads to this increased turbulence intensity. This increased level continues into the semi-vaneless space (Point 116).

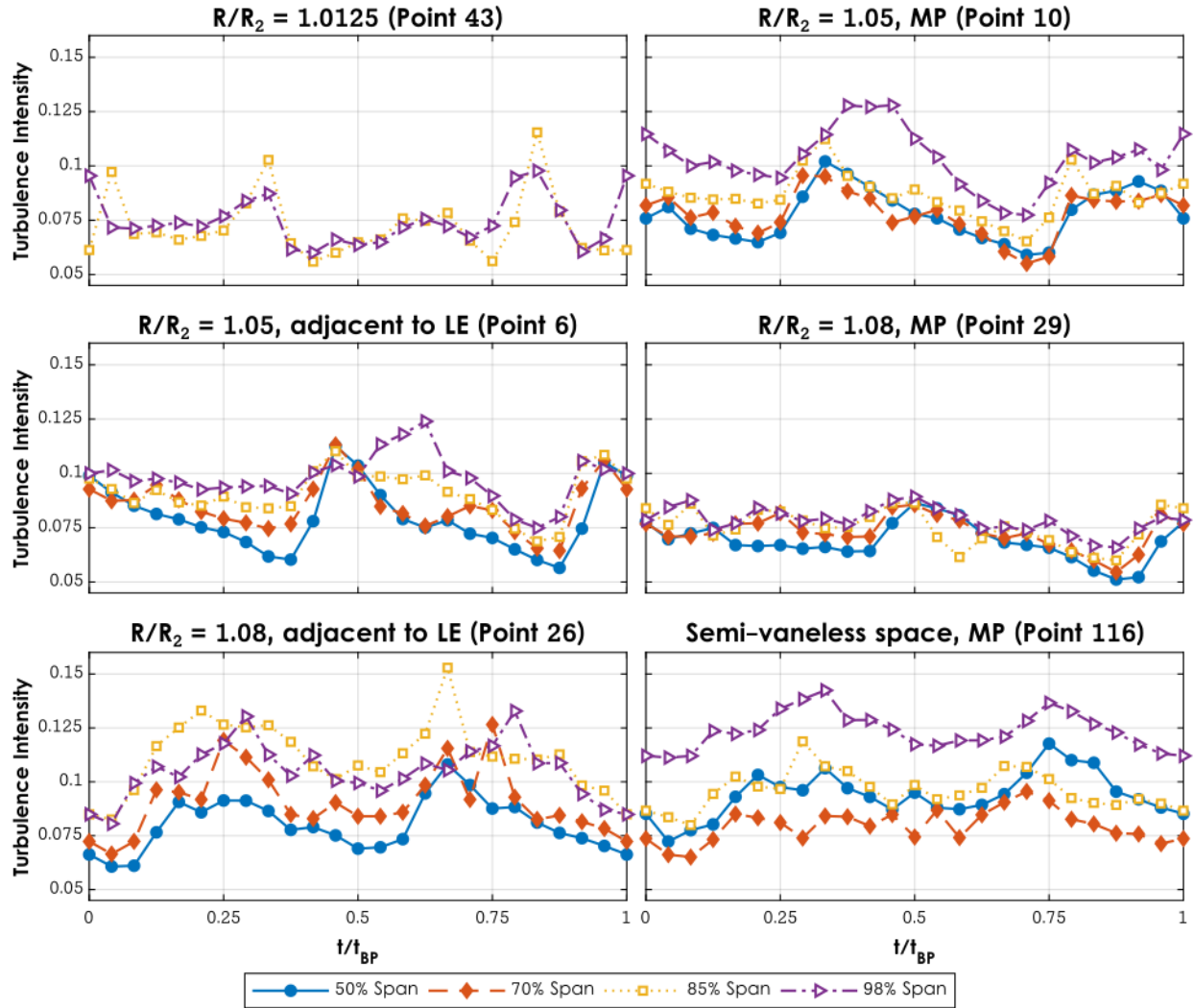


Figure 3.41: Unsteady turbulence intensity upstream of the diffuser passage

Finally, within the passage, the turbulence intensity levels indicate cross passage and streamwise gradients. The left column of Figure 3.42 presents the data obtained at the throat from suction side (Point 30), to mid-passage (Point 34), to the pressure side (Point 32). The right column contains downstream data at the same relative pitch position: from suction side (Point 166), to mid-passage (Point 127), to the pressure side (Point 159). The suction side data contain the lowest turbulence intensity values, and these remain constant in progressing from the throat to 20% downstream (Point 166). At the throat, the mid-passage data (Point 34) indicate the highest levels of turbulence intensity, from 0.075 to 0.14, and these overall levels remain constant to 10% downstream (Point 127). The 97.5% and 85% span turbulence intensity levels do decrease from the throat to 10% downstream (Point 34 to 127), however the 50% and 70% span levels increase. This indicates that

there is spanwise mixing occurring due to either convection or diffusion of turbulence away from the endwalls. Finally, along the pressure surface, low levels of turbulence (0.05-0.10) are present at the throat. This level increases significantly in progressing downstream to 20% downstream (Point 159). These data support the conclusion that separation is occurring along the pressure surface of the vane, as has been discussed extensively, and that the streamwise convection and development of turbulence intensity does not occur uniformly across the pitch of the diffuser. The Reynolds stress values are typically discussed in the context of CFD as their presence in the RANS equations forms the closure problem that turbulence models attempt to address. Consequently, a further discussion of the Reynolds stress data will be present in Chapter 5 in direct comparison with computational results.

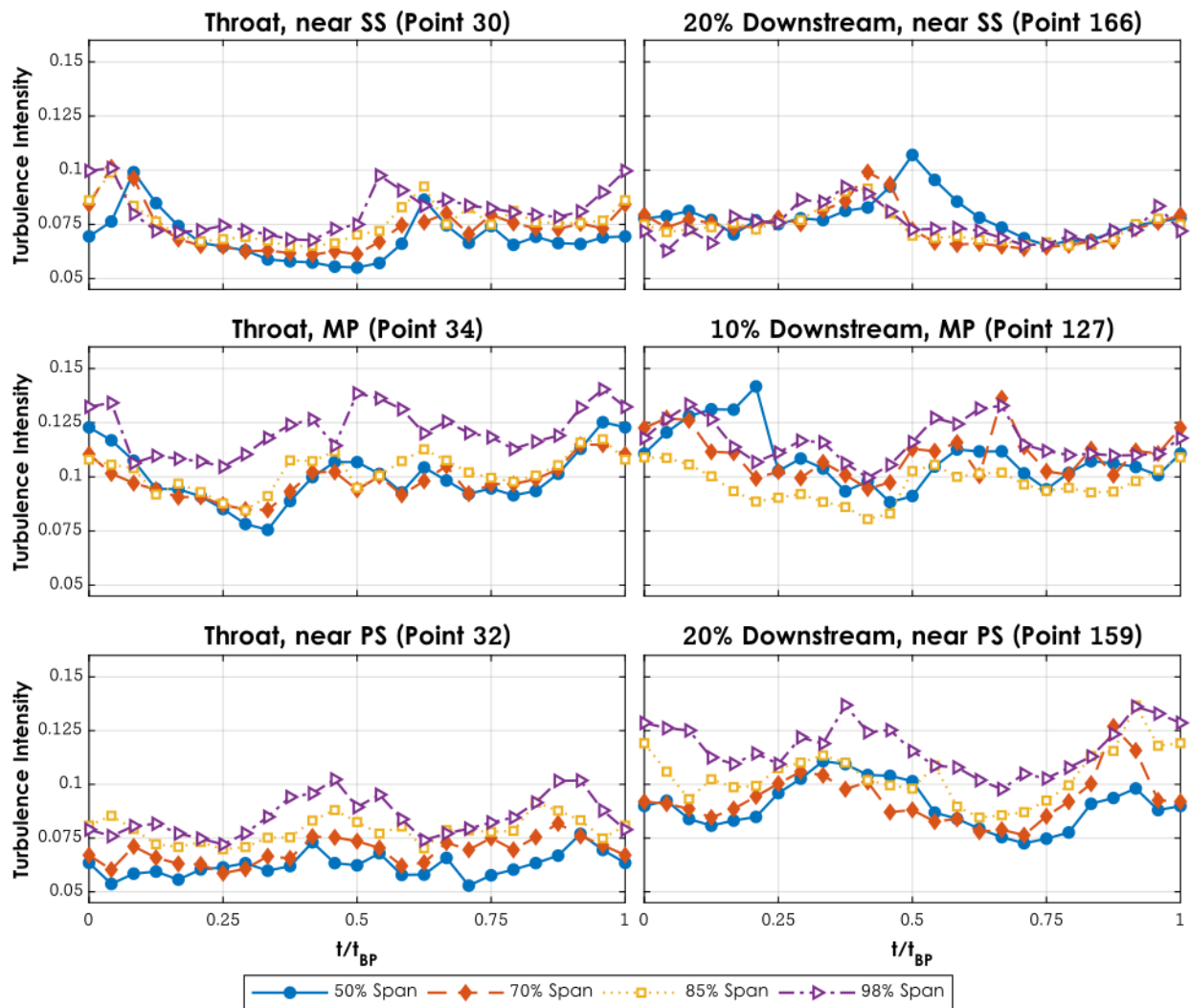


Figure 3.42: Unsteady turbulence intensity within the passage

## 4. COMPUTATIONAL RESULTS AND DISCUSSION

The experimental efforts are complemented with numerical simulations, as described in Section 2.4, to further address the research goals. The twofold purpose of the simulations is to fill in gaps left by the necessarily discrete nature of the experimental study and to evaluate modeling decisions in terms of predicting fine details of the flow field. Numerical simulations inherently provide data at millions of grid points in the flow field. When flow structures and features are noted experimentally, these can be confirmed numerically and then the results can be interrogated to determine upstream sources and downstream development beyond what can be observed experimentally. This chapter focusses on the summary and presentation of the numerical results themselves, while Chapter 5 will compare the unsteady CFD results directly with the LDV measurement data in terms of predicted flow details and Reynolds stress development.

In developing a best-practice methodology for simulating a centrifugal stage, computational results will be compared to experimental measurements. Typically, this analysis and evaluation is conducted using overall performance metrics such as TPR or efficiency. These high-level parameters are the product of many physical processes present in the flow field driving the value to increase or decrease. The resulting values represent the final state of the complicated and chaotic progression of fluid properties through the stage, and there are many distinct combinations of drivers that can produce the same TPR or efficiency value. In other words, there are multiple paths (in terms of flow development) to the same value of overall performance metrics and these high-level parameters yield little information regarding a model's accuracy. This can lead to erroneous conclusions regarding modelling quality. As a theoretical example, consider two turbulence closure models with known flaws. The first is known to *overpredict* viscous losses and *underpredict* the extent of flow separation in adverse pressure gradients. The second is known to *overpredict* viscous losses but accurately predict the extent of flow separation. In a centrifugal stage, the first model would likely better predict the TPR of the stage due to the counteracting effect of those two known flaws. However, the second would better reproduce the actual flow development through the adverse pressure gradient present in the diffuser. In this situation, a traditional analysis would recommend the first model for use in all future studies, which could compromise future design or research conclusions based on the erroneous prediction of flow

development. This example highlights the fundamental limitations of using one-dimensional values to gauge model fidelity.

In this work, high-level parameters are not used to evaluate model fidelity. Instead, the locations in the flow field with the highest fidelity experimental data are used to evaluate predictions of detailed flow structure. The diffuser exit rakes (see Figure 2.3 for details regarding instrumentation location) provide a 4x4 grid of total pressure measurements at the exit of the diffuser passage. This allows a two-dimensional contour of total pressure to be calculated from the experimental data for comparison to computational results. In the numerical results, the flow field is probed at the sixteen locations where experimental data are available to compare the exit profiles. The contours from both experimental and numerical data are then constructed using the same procedure to eliminate errors arising from the increased density of data available in the numerical results. These contours provide information regarding specifics of the flow development through the passage and form a more reliable basis for decisions regarding modelling recommendations in Sections 4.1 and 4.2. For the subsequent figures, the sixteen total pressure measurements at the diffuser exit for each result (experimental and many computational configurations) will be shifted by the minimum total pressure value on that plane, to maintain a consistent color scale between figures, and normalized by the impeller inlet total pressure. The perspective is from the diffuser throat, oriented in the streamwise direction with the pressure side of the passage on the left of the figures and the suction side on the right. The ordinate is the spanwise position, and the vanes bounding the passage are illustrated on either side of each plot.

The uncertainty associated with each total pressure measurement is  $\pm 0.0025$  experimentally and less than  $\pm 0.001$  due to numerical discretization error. In discussing the location of the maximum total pressure in the diffuser exit plane, the sparsity of total pressure measurements leads to some uncertainty. To estimate this uncertainty level, a numerical solution was probed at the sixteen measurement locations and the computed peak total pressure location compared to the “true” maximum total pressure location across the full diffuser exit plane. This process was repeated with the numerical probe locations clocked circumferentially to yield various probe locations relative to the location of the true maximum. This yielded an estimated positional uncertainty of  $\pm 5\%$  in the pitchwise and spanwise directions. Altogether, these uncertainties are not expected to cause a significant impact in the subsequent conclusions regarding modelling performance.

#### 4.1 Impact of Turbulence Model on Flow Development

Eight turbulence models were implemented in solving the flow through the numerical stage described previously in the baseline configuration (no fillets, smooth walls, and walls treated adiabatically). The turbulence models used were the one-equation Spalart Allmaras model; the SST,  $k-\epsilon$ , and BSL ( $k-\omega$ ) two-equation models;  $k-\epsilon$ -EARSM and  $k-\omega$ -EARSM models; and the SSG-RS and BSL-RS Reynolds Stress models. The predicted contours of total pressure at the diffuser exit are presented with the experimental data at the design point in Figure 4.1. The experimental data indicate a core region of high total pressure that decays toward the passage boundaries due to flow separation and viscous losses. This core region is located at -11% pitch and at 54% span. The larger decrement existing in the hub-pressure-side corner of the passage may indicate that more pronounced flow separation occurs on that side of the passage.

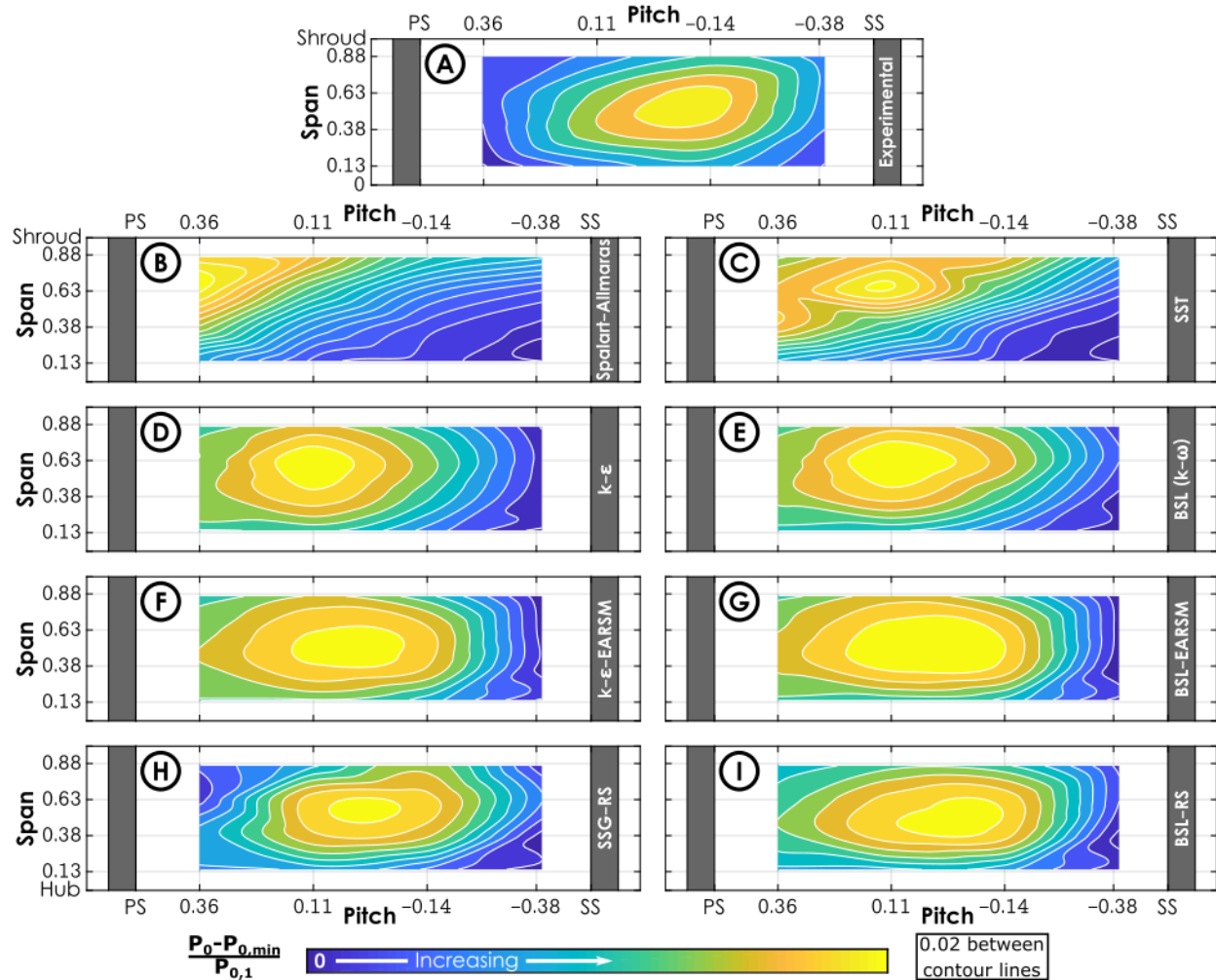


Figure 4.1: Diffuser exit total pressure contours measured experimentally (A) and as predicted by various turbulence models (B-I)

The Spalart-Allmaras model (Figure 4.1B) predicts an unrealistically large region of low total pressure in the hub-suction-side corner of the passage due to a region of flow separation (and the associated total pressure losses) growing from the suction surface of the vane. This flow separation along the vane surfaces is an important driver of diffuser flow development. Contours of total pressure at 15% through the diffuser passage are presented for each of the turbulence models in Figure 4.2 to illustrate this region of flow separation. The result for the Spalart-Allmaras model Figure 4.2A indicates the significant flow separation occurring along the suction surface of the vane which produces the diffuser exit total pressure contour indicated in Figure 4.1B. Comparing this result to the experimental result (Figure 4.1A) leads to the conclusion that the Spalart-Allmaras model is overpredicting the extent of this flow separation.

The SST model (Figure 4.1C and Figure 4.2B) also predicts a significant region of flow separation along the suction surface of the vane, albeit not as large as with the Spalart-Allmaras model. This separation begins just downstream of the diffuser throat and grows across the passage leading to the center of the core region of high total pressure located at +13% pitch and 67% span. The other two-equation models (Figure 4.1D-E) produce more realistic diffuser exit total pressure contours with a clear core region that is located near mid-passage. Both the  $k-\varepsilon$  and BSL ( $k-\omega$ ) models predict the core to be centered at roughly 10% pitch and 60% span. Relative to the SST model, this represents a shift toward the experimentally determined location. Additionally, the qualitative shape of the prediction better matches the experimental data. This supports the conclusion that these models are better representing the true flow development through the passage especially in their prediction of a much smaller region of flow separation along the suction surface of the vane (Figure 4.2C-D). However, these models still predict the core location closer to the pressure surface of the vane and a larger total pressure deficit along the suction surface of the vane (compared to the pressure surface), which does not align with the experimental measurements.

The EARSM models continue to improve on the lower-fidelity models by predicting a core location that is shifted to almost exactly the center of the passage at 1% pitch and 52% span in both EARSM results (Figure 4.1F-G). The data from 15% span (Figure 4.2E-F) indicate that this shift is caused by a slight reduction in the extent of the region of flow separation along the suction surface of the vane compared to the two-equation models. With the RS models, the core location

is predicted at 0% pitch, 57% span (SSG-RS, Figure 4.1H) and at -3% pitch, 50% span (BSL-RS, Figure 4.1I). Both full RS models predict a more balanced prediction of total pressure loss along the horizontal extremes of the passage, as indicated in Figure 4.1H-I and Figure 4.2G-H.

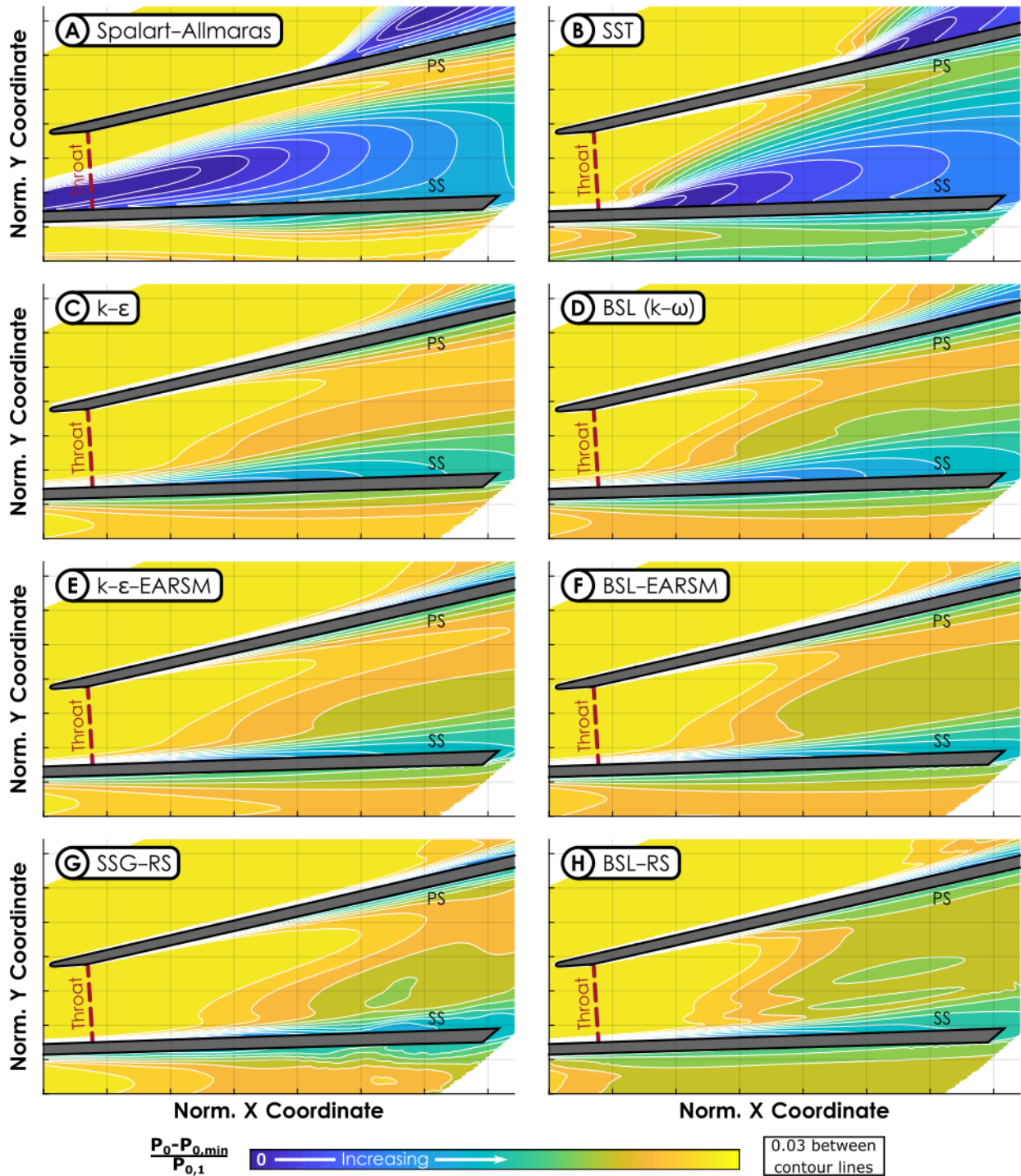


Figure 4.2: Total pressure contours at 15% span through the diffuser passage for each turbulence closure model

#### 4.1.1 On the Computational Cost and Convergence Behavior

These data indicate that the RS models offer slightly improved predictions of the flow structure at the diffuser exit. However, the convergence performance of the RS models was relatively poor due to the numerical stiffness of the systems of equations. Oscillatory behavior in key properties remained in the solution despite significant efforts toward obtaining stable convergence. This contributes additional uncertainty to the results and becomes a more significant problem at off-design conditions. The additional numerical uncertainty and the decreased numerical reliability of obtaining convergence currently limits the usefulness of applying full RS models systematically in both research and design applications.

The computational cost and convergence requirements of the various turbulence models are summarized in Table 4.1. The CPU cost is evaluated as the CPU time required per numerical iteration normalized by the value obtained with the SST turbulence model. The iteration requirement is evaluated as the number of iterations required for convergence normalized by the iteration requirement with the SST turbulence model. This requirement is an approximate evaluation as the true number of iterations required varied with the flow condition, initialization settings, and numerical time stepping parameters. The overall computation cost is then the product of those two values. Based on this information, the EARSM models are not prohibitively expensive computationally and could be implemented in both research and design applications.

Table 4.1: Computational cost summary for various turbulence models

<b>Turbulence Model</b>	<b>CPU Cost per Iteration*</b>	<b>Approx. Iteration Requirement*</b>	<b>Overall Computational Cost*</b>
<i>Spalart-Allmaras</i>	0.87	~1	0.87
<i>SST</i>	1.00	~1	1.00
<i>k-<math>\epsilon</math></i>	0.99	~1	0.99
<i>BSL (k-<math>\omega</math>)</i>	0.92	~1	0.92
<i>k-<math>\epsilon</math>-EARSM</i>	1.03	~3	3.09
<i>BSL-EARSM</i>	1.05	~3	3.15
<i>SSG-RS</i>	1.41	~10	14.1
<i>BSL-RS</i>	1.25	~10	12.5

\*Normalized by the value for the SST turbulence model

## 4.2 Effect of Other Modelling Decisions on Flow Development

In addition to a choice regarding which turbulence closure model to implement, a decision must be made regarding the inclusion of other aspects of the true flow field. Specifically, fillets, heat transfer, and wall roughness are three features of true flow fields which are often neglected in computational models for simplicity and to permit more rapid design iteration. To investigate the impact of these features on the detailed flow development, they were systematically introduced with the most promising turbulence models presented in Section 4.1. The two EARSM models were selected due to their accurate prediction of the diffuser exit flow field in the baseline configuration (no fillets, heat transfer, or wall roughness). Additionally, the SST model was selected for further analysis due to its pervasive use in turbomachinery applications. Fillets were included by a modification of the base coordinate files used in grid generation. Dimensions were obtained from original hardware drawings (and manufacturing inspections where available) and implemented in the mesh while striving to maintain consistent mesh parameters between the original and filleted geometries. Heat transfer was modelled by applying experimental shroud-side temperature measurements as an isothermal boundary condition on the shroud in the numerical model. Surface roughness was modelled by using a scaling factor of 8.4 to convert from measured average roughness values to a sand-grain equivalent roughness implemented numerically. Additional details on the treatment of these features is provided in Section 2.4.

The results with the SST turbulence model with various combinations of modelling features are presented in Figure 4.3 (in terms of diffuser exit total pressure) and Figure 4.4 (in terms of the total pressure at 15% span). The left column of Figure 4.3 presents the absolute results while the right column presents the difference from the baseline configuration result. The diffuser exit contours illustrate a gradual shift in the direction of the experimental measurements of the region of core flow. The inclusion of heat transfer (Figure 4.3A-B and Figure 4.4A) has negligible impact on the total pressure contours. A 1D compressible flow analysis illustrates that heat removal from a subsonic flow should lead to an increase in the total pressure of the flow that is proportional to the local Mach number squared and the rate of heat transfer. The low rates of heat transfer (less than 0.5% of the work input) and the subsonic nature of the flow lead to the negligible impact on the total pressure field at the diffuser exit. However, the heat transfer does have an impact on the calculation of stage efficiency, as will be demonstrated in Section 4.2.1.

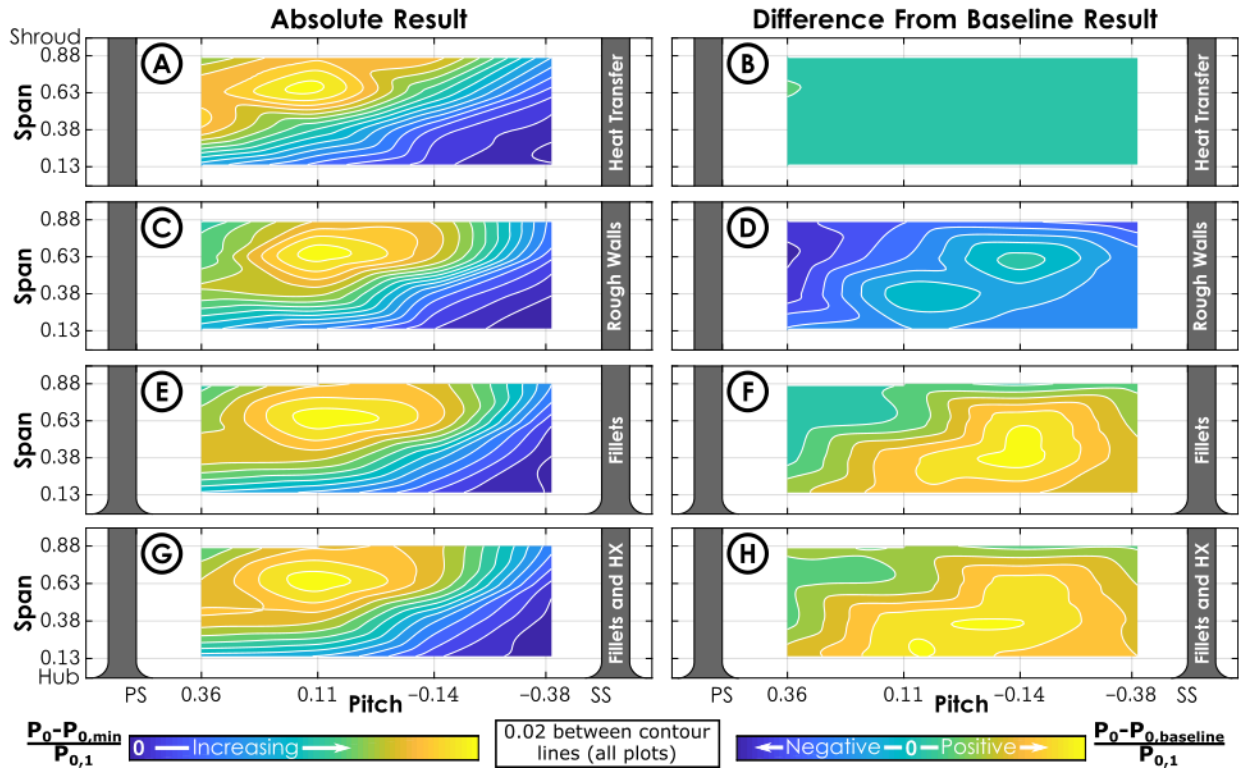


Figure 4.3: Diffuser exit total pressure with the SST turbulence model and various additional modelling features

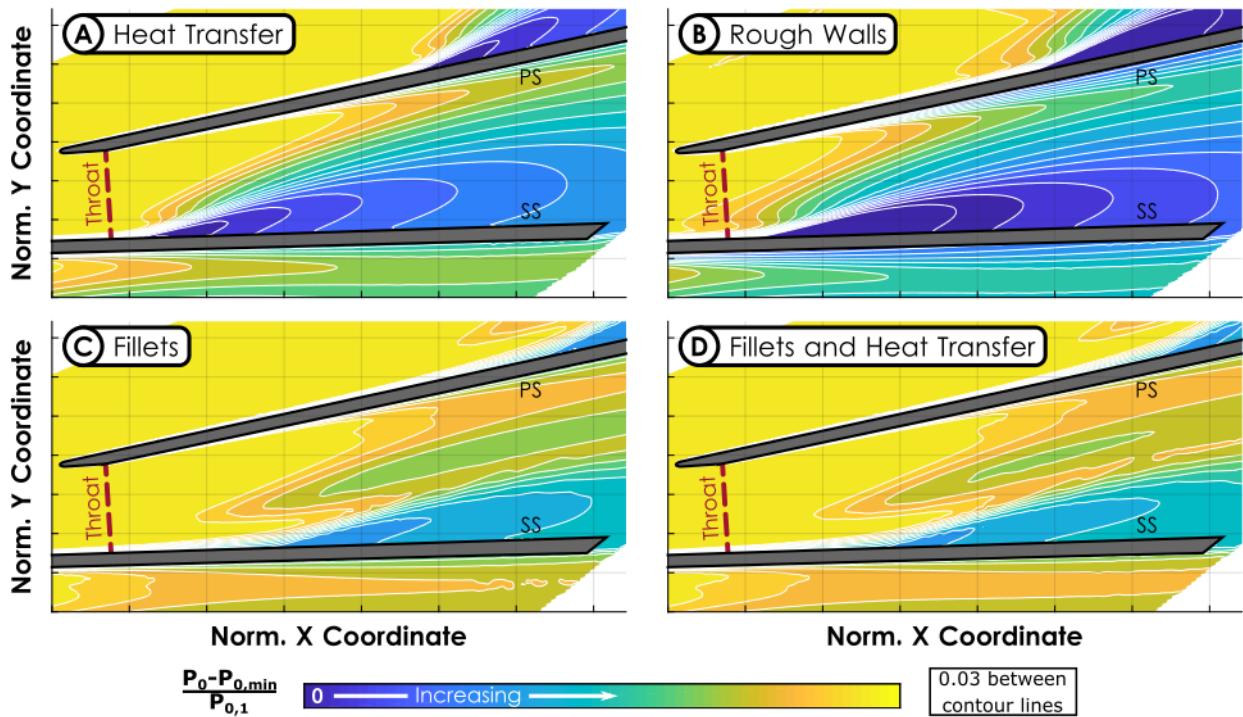


Figure 4.4: Total pressure contours at 15% span with the SST turbulence model and various additional modelling features

The addition of rough walls (Figure 4.3C-D and Figure 4.4B) has a small impact on the diffuser exit contours but a significant effect on the absolute values. As expected, the addition of wall roughness causes a reduction in the predicted total pressure at the diffuser exit due to the additional viscous losses. This reduction is greatest along solid boundaries and decreases to near zero toward the middle of the passage. The effect on the overall profile is to shift the triangle shaped core region predicted in the baseline configuration with the SST turbulence model into an elliptical shape due to the increased losses along the solid walls in the pressure-side-shroud corner of the passage. The inclusion of roughness has a negligible impact on the prediction of flow separation along the suction surface of the vane which leads to the predicted core location falling closer to the pressure side of the passage than observed experimentally.

Of the three features included in this study, the addition of fillets caused the largest shifts in the predicted flow field through the diffuser. In terms of the diffuser exit profiles, the fillets effected an increase in the total pressure across the entire passage with the largest gains present closer to the hub and toward the suction side of the passage (Figure 4.3E-F). This increase in the total pressure at the diffuser exit arises due to a drastic reduction in the extent of flow separation along the suction surface of the vane and, to a lesser extent, along the pressure surface (Figure 4.4C). The region of flow separation along the suction surface of the vane begins further downstream, exhibits a lower total pressure decrement (that is, the total pressure values within the region are closer to the values in the freestream), and occupies a smaller pitchwise portion of the passage in the 15% span plane compared to the baseline configuration. These results highlight a potential flaw in the SST turbulence closure models when unrealistically sharp corners are implemented numerically within a strong adverse pressure gradient. This reduction in the extent of flow separation causes the core region of high total pressure at the diffuser exit to shift slightly more toward the center of the passage (relative to the baseline and the two previous features). Additionally, a simulation was conducted with both fillets and heat transfer (HX) with the results presented in Figure 4.3G-H and Figure 4.4D. These figures illustrate that there is very little interaction between the hub-side fillets and shroud-side heat transfer drivers in the diffuser flow development.

Finally, all three features were included in a model for implementation with the three selected turbulence models: SST,  $k-\varepsilon$ -EARSM, and BSL-EARSM. This configuration is termed the “high-

fidelity” configuration and the results for the prediction of the diffuser exit total pressure are presented in Figure 4.5. The combination of the three features with the SST turbulence model (Figure 4.5A) causes the core region of high total pressure to be shifted closer to mid-passage. Additionally, the total pressure gradient is largely radial, increasing out from the center of the passage, as opposed to the primarily diagonal gradient predicted in the baseline configuration.

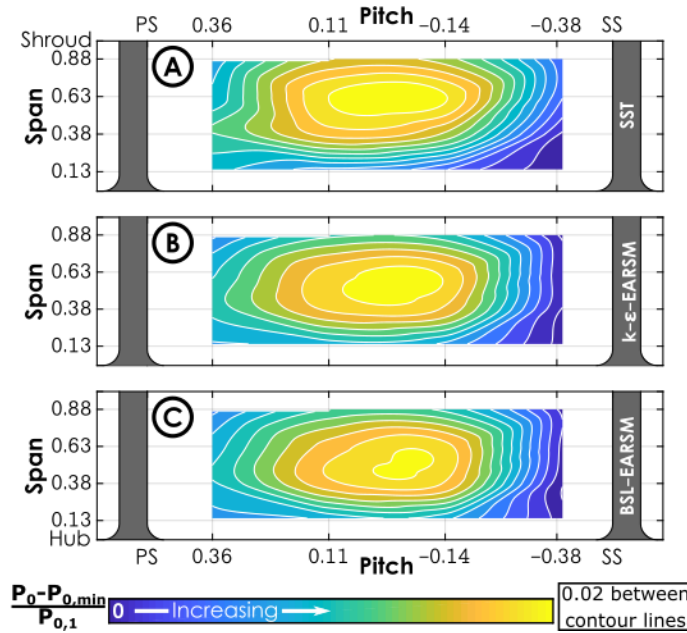


Figure 4.5: Diffuser exit total pressure contours with the high-fidelity configuration

Each EARSM model shows less change between the baseline and the high-fidelity configurations. The location is shifted slightly away from the pressure surface, falling nearly at mid-passage. Additionally, the deficit adjacent to the vane surfaces is more symmetric than in the baseline configuration. However, the SST model showed a much more significant shift due to the high-fidelity modelling features. This arises due to the overprediction of flow separation in the baseline SST result. The total pressure contours at 15% span through the diffuser passage for the high-fidelity configuration are presented in Figure 4.6. The inclusion of fillets in the high-fidelity configuration causes a drastic reduction in the extent of flow separation in the passage with the SST turbulence model as discussed previously. This is the primary driver of the large shift between the predictions of flow development with the SST turbulence model. The wall roughness causes a bulk total pressure decrement over the majority of the passage while the non-adiabatic walls only effects a small shift. In the EARSM models, the baseline configuration represented a more

accurate prediction of the extent of flow separation. Therefore, the addition of fillets did not predict a drastic shift in the flow prediction because there was less “room for improvement,” in a sense. Fillets, with the SST model, could correct the flow prediction to a greater extent because the original prediction was more flawed. However, the SST model still predicts a larger extent of flow separation along the suction surface than the EARSM models even in the high-fidelity configuration.

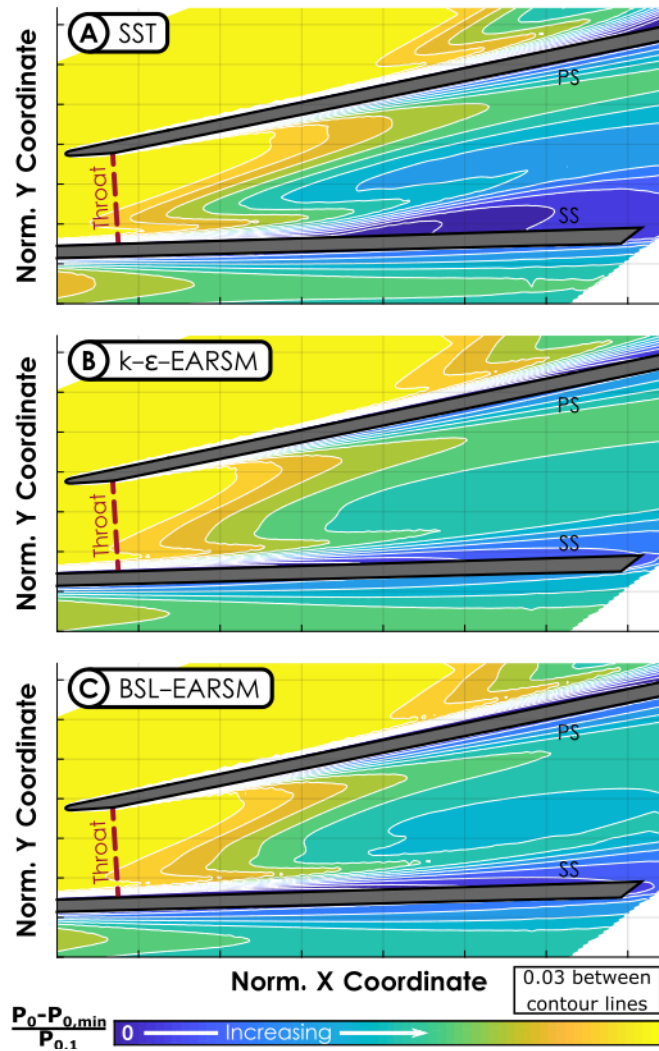


Figure 4.6: Total pressure contours at 15% span with the high-fidelity configuration

These additional modelling inclusions bring the model closer to reality—both in terms of more accurately representing realistic flow physics and more accurately matching experimental measurements. However, none of these simulations predict a core pressure location that is shifted

as close to the suction side of the passage nor a deficit along the pressure surface as large as exhibited in the experimental data. Nevertheless, these results do allow some conclusions to be drawn regarding simulating the flow within the diffuser in a centrifugal stage. The SST model is only recommended when fillets are included in the numerical model due to the drastic overprediction of flow separation within the passage when sharp corners are implemented. The two EARSM models more accurately reproduce the flow field without fillets, and could be utilized in such a scenario where the implementation of fillets would require a large investment in terms of person-hours. However, wherever possible the high-fidelity configuration is recommended due to the negligible increase in computational cost (less than 5% in all cases) and the increased accuracy both in terms of representing the true physical drivers present in the flow field and in matching the experimental measurements at the diffuser exit.

#### **4.2.1 Effect of Modelling Inclusions on Overall Performance Predictions**

The previous analysis was conducted at the design point and focused on fine details of the flow physics. As discussed previously, the matching of absolute values of performance metrics is explicitly not the goal of this work. The computational model does not incorporate every possible source of loss that acts on the experimental compressor. Consequently, adjusting the model to perfectly match absolute values of one-dimensional performance metrics would simply be manipulating the flow drivers that are included numerically to unrealistically account for the neglected aspects of the flow physics. This approach would likely reduce the predictive capability and accuracy of the model for off-design conditions and for novel designs. With that in mind, accurate matching of trends in overall performance metrics predicted by the CFD and demonstrated experimentally can provide another metric of model performance and predictive capability for a wider range of flow conditions.

First, the three selected turbulence models were implemented for two additional operating conditions, one each at a higher and a lower mass-flow rate than the previous simulations. The slope of the numerical predictions in terms of TPR and efficiency were compared to the experimental data, and models that trended well relative to the experimental data were then used to simulate the full speedline at the design operating speed. These results are presented in Figure 4.7. In the initial simulation of two additional operating conditions, the  $k$ - $\varepsilon$ -EARSM turbulence

model with the high-fidelity configuration presented a slightly sharper slope in the TPR trend than the experimental data and the other modelling combinations. For this reason, it was not used to simulate the entire speedline. In this figure, the TPR (Figure 4.7A) and isentropic efficiency (Figure 4.7B) are the ordinates and corrected mass-flow rate is the abscissa. The low mass-flow end of the computational speedlines are not indicative of numerical stall. The experimentally determined compressor surge condition is indicated on the TPR speedline, but no attempt was made to predict the stability limit of the stage computationally due to the inherent uncertainty in determining stall using steady computational methods. The uncertainty in the experimental data is within the symbol size. For data visualization, the line color and style are used to indicate the turbulence model used while the symbol indicates the fidelity of the configuration implemented: open circles for the baseline configuration and filled diamonds for the high-fidelity configuration. The experimental data are indicated by solid filled circles.

The experimental speedlines show a vertical portion indicating the choke limit of the stage at the high-end of the mass-flow-rate range. With decreasing mass-flow rate, the TPR data gradually falls over with a nearly linear trend toward low mass-flow. In terms of efficiency, the data trends with a gradual curve in decreasing the mass-flow rate from the choking condition. Once out of choke, the efficiency remains nearly constant for a wide range of stage mass-flow rate with a small decrease in efficiency at the lowest mass-flow rates recorded.

The SST model (indicated by maroon dotted lines in Figure 4.7) produces a good representation of the experimental trend in TPR versus mass-flow. Relative to the other turbulence models, the SST is unique in that it does not show a significant difference in the TPR prediction between the baseline and the high-fidelity configurations. This occurs due to the opposing effects of the addition of surface roughness and the inclusion of fillets in the numerical configuration. The roughness increases viscous losses along all solid boundaries proportionally to the square of the local flow velocity. This causes a decrease in the TPR through the stage and should also lead to a decrease in the choke-flow capacity of the stage due to increased blockage at the diffuser throat. However, with the SST turbulence model, fillets act to dramatically reduce the size of the region of flow separation within the diffuser passage, as illustrated previously. This tends to increase the choke-flow capacity of the stage (due to reduced blockage in the diffuser passage) and tends to increase the TPR of the stage due to reduced separation losses. Consequently, when both factors

are included in the configuration, they offset each other and lead to comparable TPR and choke-flow capacity predictions between the baseline and high-fidelity configurations.

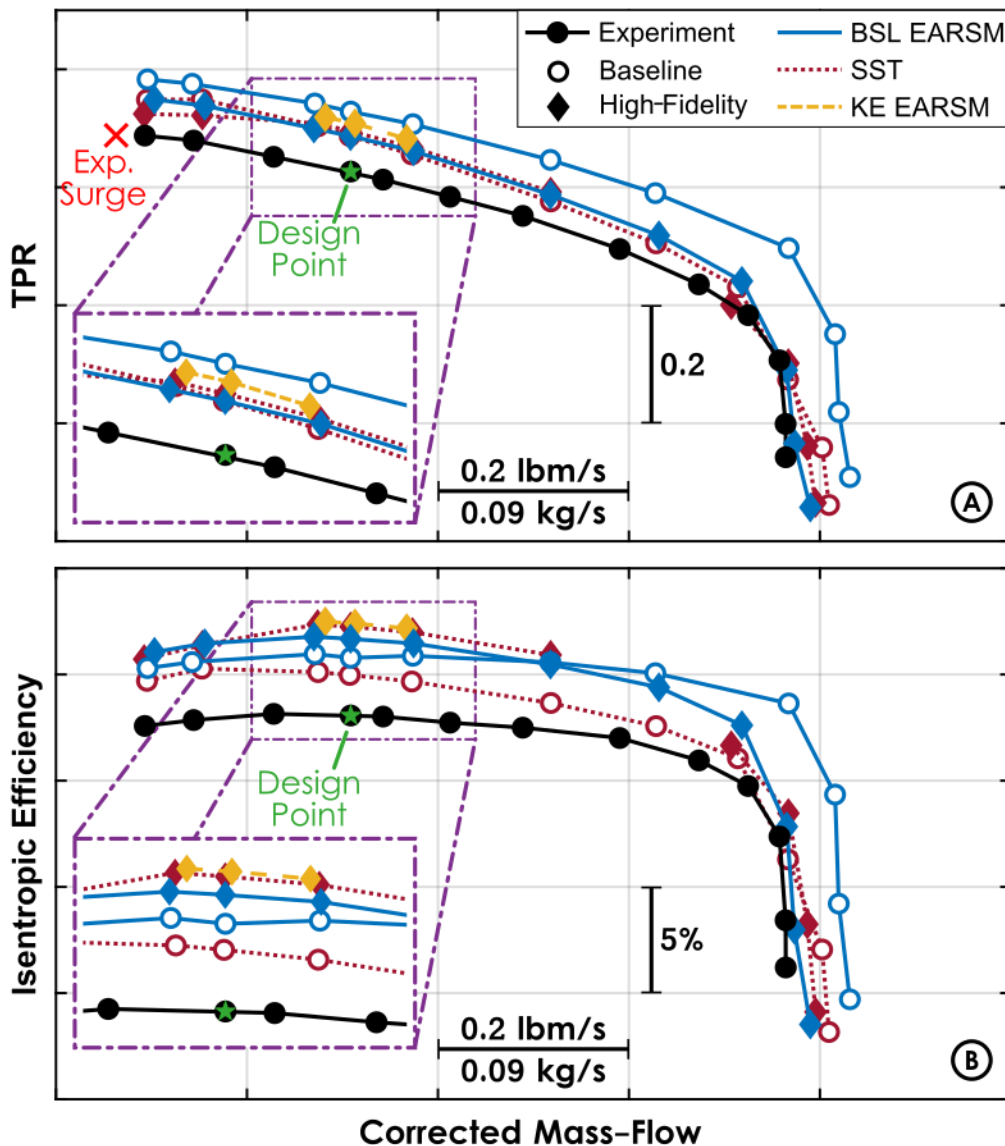


Figure 4.7: Overall performance predictions for the various modelling combinations for TPR (A) and isentropic efficiency (B)

However, the efficiency trend does change between the baseline and the high-fidelity configurations using the SST turbulence model. This occurs due to the influence of the third feature included in the high-fidelity configuration—non-adiabatic walls. While heat transfer does not have a significant impact on the total pressure values present through the diffuser, it does impact the total temperature rise through the compressor stage. At the design point, the overall heat transfer out of the flow path is approximately 0.5% of the overall work input to the flow

through the impeller. For the same TPR, the resulting decrease in the total temperature rise leads to an increase in the calculated stage efficiency. This is only true when temperatures are directly used to compute the stage efficiency as the addition of heat transfer only has a small impact on the aerodynamics of the flow development. If efficiency were computed based on the torque input into the flow, rather than the temperature rise achieved through the stage, the impact of heat transfer would be significantly less. However, the experimental efficiency value is computed based on temperature measurements and, therefore, the computational efficiency was evaluated in the same manner. This result highlights the importance of evaluating parameters in an identical manner when comparing numerical and experimental results, despite the availability of significantly more information in numerical results. If the numerical efficiency were computed using torque a comparison between the efficiency values with and without heat transfer would likely lead to a conclusion that heat transfer was unimportant. However, this conclusion would lead to potentially erroneous inferences when the results are compared to experimental measurements.

The baseline SST model predicts a rise in efficiency with a decrease in mass-flow rate which continues to a maximum value at the second lowest mass-flow rate simulated, decreasing slightly to the lowest mass-flow value. In the high-fidelity configuration, the SST turbulence model predicts an increase in efficiency to a peak at the design point before decreasing significantly toward lower mass-flow rate. In both cases, this trend does not align with the nearly constant value of efficiency measured experimentally outside of choke.

Unlike the SST model, the BSL-EARSM (solid blue lines in Figure 4.7) turbulence model exhibits a discernible shift in both the TPR and efficiency trends and the predicted choking mass-flow between the baseline and high-fidelity configurations. This distinction arises because the baseline BSL-EARSM model does not overpredict the extent of flow separation in the passage, unlike with the SST turbulence model. Therefore, the addition of fillets cannot produce as dramatic of an increase in the predicted TPR because there is no erroneous source of loss to correct. Consequently, the addition of surface roughness, with the resulting decrease in TPR and increase in throat blockage, is not counteracted by any physical driver with the BSL-EARSM turbulence model. Compared to the baseline configuration, the high-fidelity configuration predicts a steeper increase of TPR with decreasing mass-flow rate. The increase in the slope occurs due to the

increased viscous losses. Toward the choking condition, where flow velocities are higher, viscous losses produce a larger total pressure decrement relative to the baseline configuration than at lower mass-flow conditions. The slope is marginally steeper than the experimental results. Reducing the scaling factor used to convert from measured, average roughness to sand-grain roughness would decrease this slope and could produce an exact matching of the experimental slope. However, this is not advisable. As mentioned previously, this adjustment of surface roughness would artificially account for various sources of losses and physical mechanisms that are not included in the model. Further fundamental research connecting measured roughness to sand-grain roughness within the complex aerodynamic environment of centrifugal compressors (adverse pressure gradients, swirling flow, unsteady fluctuations, etc.) is necessary to develop a better scaling factor. With regards to efficiency, the high-fidelity BSL-EARSM model predicts more variation away from choke than the experimental data suggest and the baseline configuration speedline indicates a sharp corner in transitioning out of choke.

To further the analysis at off-design conditions, contours of total pressure at the diffuser exit were computed at two additional operating points: high-loading and near choke, Figure 4.8. The “high-loading” data (left column of Figure 4.8) arise from the operating point with the second lowest mass-flow simulated numerically. The “near choke” data (right column of Figure 4.8) are taken at the operating point with the second lowest TPR. The experimental data are presented in the first row (Figure 4.8A-B) and are indicated by the grey background shading. The results using the SST turbulence model are indicated by the maroon background shading with the baseline configuration presented in the second row (Figure 4.8C-D) and the high-fidelity configuration in the third row (Figure 4.8E-F). The results using the BSL-EARSM turbulence model are indicated by the blue background shading with the baseline configuration presented in the fourth row (Figure 4.8G-H) and the high-fidelity configuration in the last row (Figure 4.8I-J). As in the previous diffuser exit total pressure contours, 0.02 separates each contour level in the high-loading results; however, 0.05 separates each contour level in the near choke results due to the larger range of total pressure present at that operating condition. These results further support the conclusions reached previously regarding modelling decisions at the design point and regarding the general trends in overall parameters predicted by the different configurations. First, the high-fidelity configuration produces profiles that more closely align with the experimental data than the baseline configuration for both turbulence models. The one potential exception to this general conclusion is the SST

turbulence model at the near choke operating condition (Figure 4.8D and F). At this condition, it is not clear which configuration yields the best result due to the qualitative evaluation. However, the high-fidelity configuration offers tangible improvements in each of the other cases. The second general conclusion is that the BSL-EARSM model produces results closer to the experimental data in both the baseline and high-fidelity configurations. This is evident by comparing the corresponding rows for the baseline configuration (the second and fourth rows in Figure 4.8) and the high-fidelity configuration (the third and fifth rows) back to the experimental data (the first row). In both configurations the BSL-EARSM model predicts a core pressure location that is closer to the location indicated by the experimental data and a general profile that is more similar to that observed experimentally.

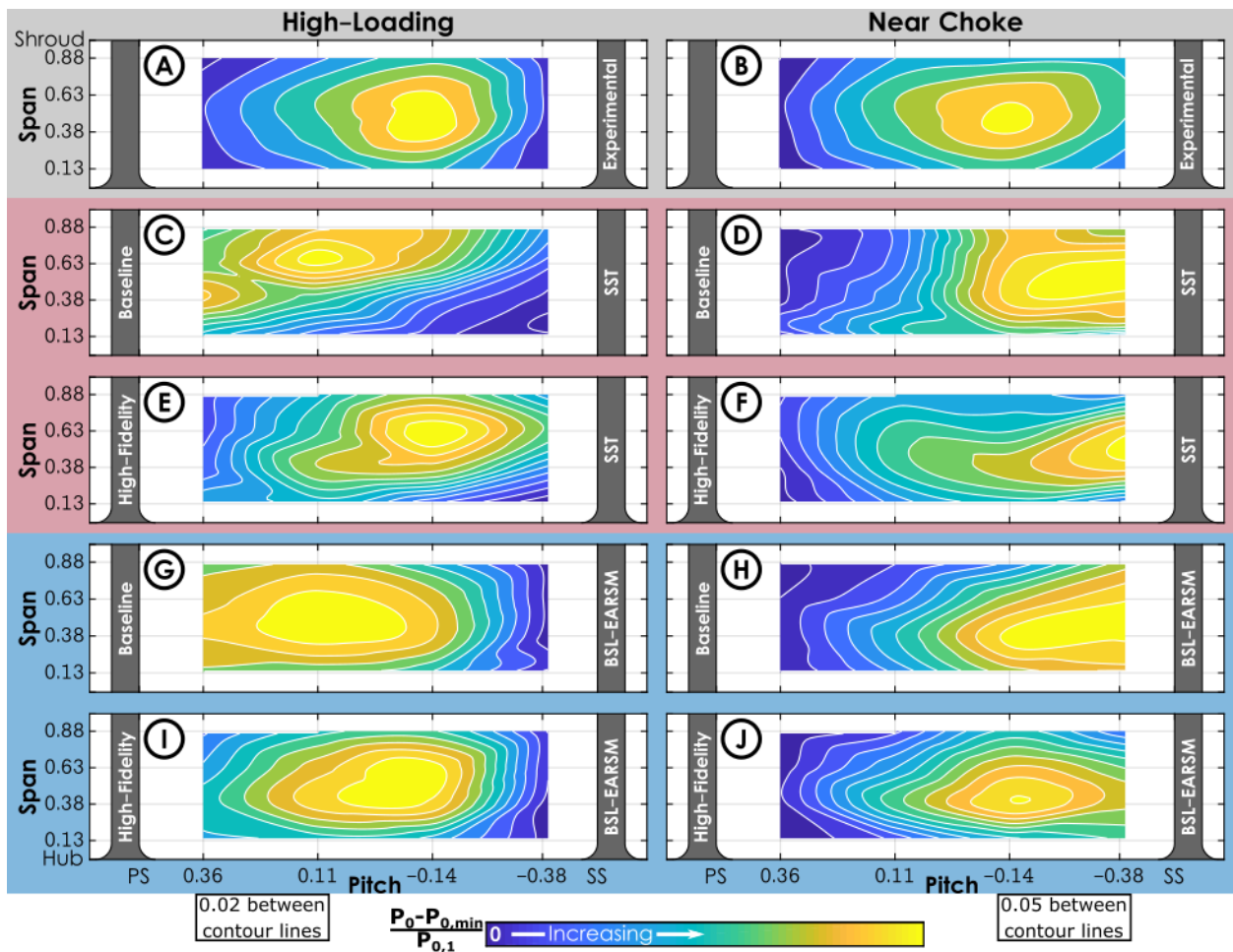


Figure 4.8: Diffuser exit total pressure contours for high-loading (left column) and near choke (right column) conditions for experimental data (A-B), SST (C-F), and BSL-EARSM (G-J)

#### 4.2.2 Modelling Recommendation for Steady-State Computations

These results lead to a recommendation for best practice in CFD modelling for centrifugal compressors in a similar design space to the one considered in this work. The approach in developing these recommendations has focused on details of the internal flow physics and overall performance trends, rather than the matching of specific overall performance parameters. To compare the conclusions reached from this approach to those that would be reached for a “traditional” evaluation of model accuracy, Figure 4.9 indicates the difference,  $\Delta$ , in the TPR (on the abscissa) and efficiency (on the ordinate) between the various modelling combinations and the experimental value. A coordinate of (0,0) would indicate a computational result that exactly matched the experimental value for both parameters. With a traditional approach, the result closest to the origin would be considered the “best.” Specifically, the Spalart-Allmaras turbulence model in the baseline configuration and the SST turbulence model with only roughness included would indicate the best performance. Both of these results predict the experimental design performance within 1% of efficiency and 0.01 in terms of TPR. However, as has been discussed, both of these results suffer from clear and obvious deficiencies when flow details are considered. The Spalart-Allmaras predicted an oversized region of separated flow and total pressure loss across the diffuser passage and a general profile that did not resemble the experimental data at the design point (Figure 4.1B and Figure 4.2A). This overprediction of loss development through the diffuser passage is correcting, in a sense, for an underlying overprediction of TPR and efficiency that occurs in the other baseline results. While this does produce a better match of overall performance metrics, it does not imply a superior predictive capability of the model.

A similar argument holds for the SST model with only roughness included. The baseline SST model tends to overpredict efficiency and TPR even with the excessive prediction of flow separation discussed previously. Adding roughness causes a decrease in these quantities, which shifts the prediction closer to the experimental values and also shifts the model closer to the physical reality in terms of drivers of flow development. However, the near-perfect matching of the computational result and experimental data is merely a coincidence. The baseline model’s shortcomings—namely, an overprediction of efficiency and TPR—are offset by the roughness effects in a way that happens to produce a result near the experimental values. If further improvements are made to the model (in terms of including more accurate physical drivers) by

including heat transfer and fillets, the results again deviate from the experimental values. This should not be interpreted as being indicative of a lower quality computational configuration.

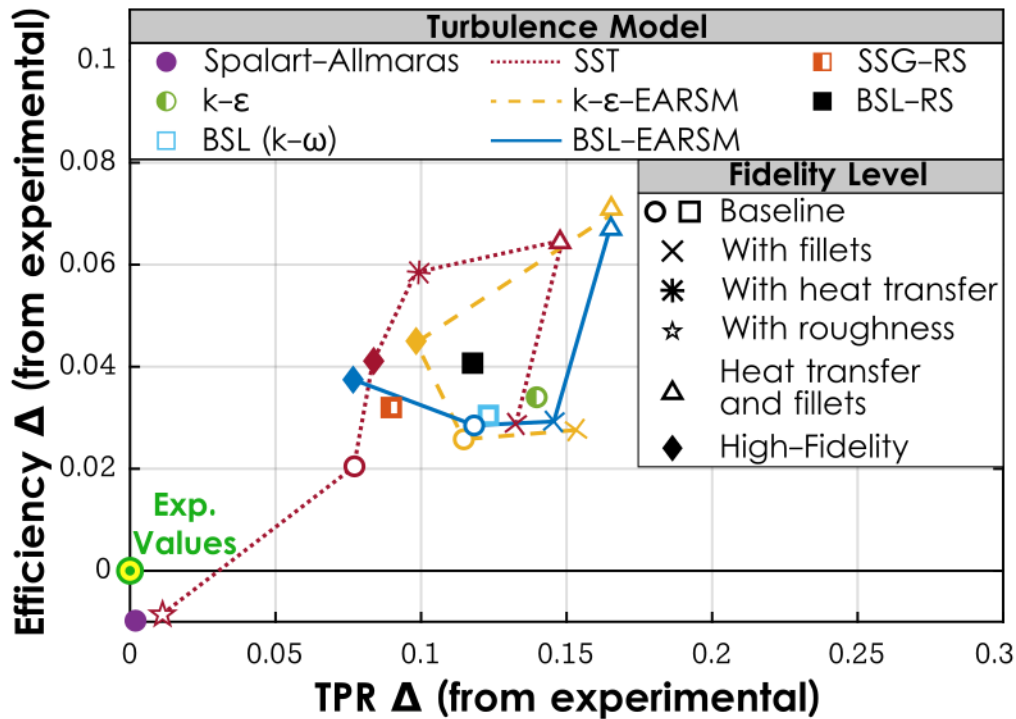


Figure 4.9: Performance difference from experimental values

Instead, the approach implemented herein leads to the selection of the BSL-EARSM turbulence model in the high-fidelity configuration as the recommended computational model. Heat transfer, surface roughness, and fillets should be included in a computational configuration as they produce a model that is closer to reality in terms of including physical flow drivers. Additionally, these phenomena impact the predicted flow field as has been illustrated. Neglecting one (or more) of these drivers to develop a performance prediction that is closer to measured one-dimensional quantities would impede the predictive capability of the simulation in new conditions. The BSL-EARSM model is recommended over the SST model because it better matches the diffuser exit total pressure profiles at multiple operating conditions and better predicts the trend in TPR and efficiency across the speedline. That being said, the SST model with the high-fidelity configuration does exhibit relatively good results and is recommended for use in applications where the BSL-EARSM model presents convergence issues or is not available in a commercial software.

### 4.3 Accuracy of the Frozen Rotor Approach in Resolving Unsteady Effects

Unsteady effects are known to be critical in the aerodynamic performance of a centrifugal compressor, and experimental measurements of the unsteady velocity field suggest that unsteadiness persists further into the diffuser passage than often assumed [54]. Specifically, the jet/wake structure at the impeller exit presents the diffuser with an unsteady inlet flow field with large variations in incidence and other flow properties, which propagate downstream. In the previous discussion, efforts were made to produce a numerical model that accurately reproduced the flow physics and drivers present in the experimental stage. Unsteadiness is one of the significant flow drivers that cannot be approximated using the mixing-plane interface. A common approach to approximating the magnitude of the influence of unsteady effects is through the implementation of frozen rotor simulations. To evaluate the ability of frozen rotor approaches to capture unsteady effects, simulations were conducted using the SST and BSL-EARSM turbulence models in the high-fidelity configuration. The angular offset between the impeller domain and the diffuser domain was adjusted between  $0^\circ$  and  $24^\circ$  (corresponding to one full blade passing event) in increments of  $2^\circ$ . The results in terms of the TPR and efficiency are presented in Figure 4.10 where the abscissa is time ( $t$ ) normalized by the full blade passing period ( $t_{BP}$ ). For the frozen rotor results,  $t$  is computed as the time required to rotate through the specified domain offset. The values from the previous mixing-plane results with each turbulence model and the experimental values are indicated by the corresponding horizontal lines. With the frozen rotor interface, the SST model predicts more pseudo-unsteady variation in both the stage TPR (0.08 compared to 0.03) and efficiency (1.8% compared to 1.3%) than the BSL-EARSM model. Both frozen rotor results present a shift toward the experimental values in both parameters.

At first glance, these results are encouraging in the ability of frozen rotor approach to accurately account for unsteady effects without the computational cost of a full transient simulation. However, the frozen rotor approach does not represent a physically realistic state or process in the actual compressor. It attempts to approximate an instantaneous “snapshot” of the flow field, yet neglects the important influence of localized unsteady events (such as periodic separation within the passage) on other parts of the flow field. To determine if the apparent improvements of the frozen rotor approach (in terms of overall performance parameters) are representative of a superior prediction of flow development, the diffuser exit total pressure contours are compared to unsteady

simulation results. The transient results utilized the time transformation method to account for the unequal pitch between the diffuser and impeller domains and will be discussed fully in Section 4.4. In the context of the frozen rotor results, the purpose of the unsteady simulation results is as a metric which the frozen rotor results should emulate.

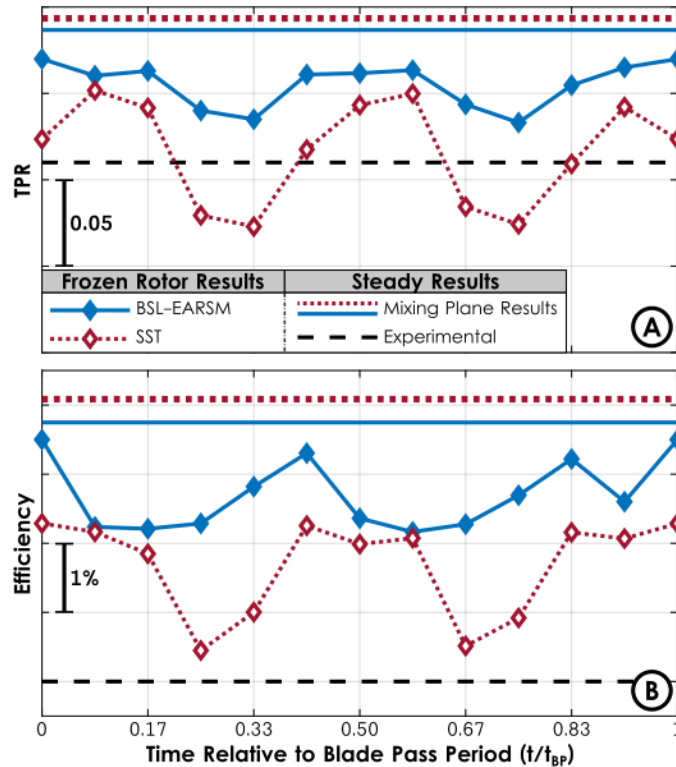


Figure 4.10: Frozen rotor variations in TPR (A) and Efficiency (B) with the high-fidelity configuration

The time-averaged diffuser exit total pressure results are presented in Figure 4.11. The experimental results are reproduced in Figure 4.11A for convenience. The frozen rotor results through the blade passing period were arithmetically averaged to produce the pseudo-time-averaged results in Figure 4.11B and D while the time-average of the unsteady results are in Figure 4.11C and E. The SST turbulence model results are in Figure 4.11B-C and the BSL-EARSM model results are in Figure 4.11D-E. These contours indicate that the frozen rotor approach predicts a diffuser exit flow profile that is less representative of the experimental values than the previous mixing plane results. The full unsteady results indicate that the accurate inclusion of unsteady effects results in a better matching of the diffuser flow development. Both turbulence models, in the full unsteady simulation, predict the peak in diffuser exit total pressure that is very

similar to the experimentally observed value. Contrarily, the frozen rotor results predict the maximum total pressure location shifted closer to the pressure surface of the passage.

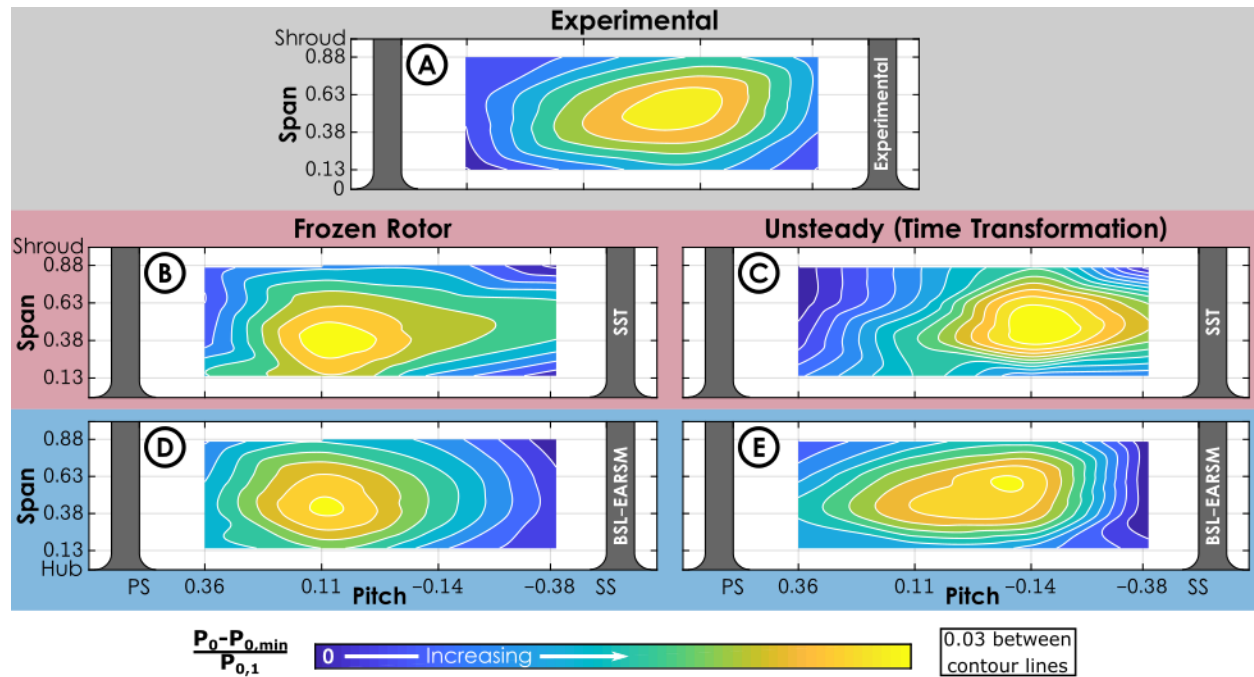


Figure 4.11: Time-averaged diffuser exit total pressure contours experimentally (A), with the SST model (B-C), and with the BSL-EARSM model (D-E)

To investigate the origin of this discrepancy, the instantaneous results of the diffuser exit total pressure contours are presented in Figure 4.12 with the SST turbulence model and in Figure 4.13 with the BSL-EARSM turbulence model. In both figures, the frozen rotor results are presented in the left column and the full unsteady results are in the right column. Time proceeds down the columns with each row equally spaced in time through the full blade passing period. The general conclusions are identical for the two turbulence models. In the unsteady simulations, the location of the peak total pressure remains relatively stable through the blade passing period; the details of the profiles fluctuate, however the general shape remains constant. On the other hand, the frozen rotor results predict drastic shifts in the flow profiles. These drastic shifts arise due to the fixed phase relationship between the impeller jet/wake profile and the diffuser vanes when the frozen rotor interface is applied. In reality, there are instances in time where the wake from the impeller passage aligns with the diffuser vane leading edge with an accompanying rise in positive incidence. With the experimental compressor (and in the full unsteady simulations) this condition is immediately followed by the propagation of the impeller passage jet with incidence closer to the

design intent and less aggressive aerodynamic loading on the vane. When this orientation is modelled in the frozen rotor simulations the wake flow condition is applied as if it were steady in time; that is, as if the large positive incidence were always present. This results in the dramatic shifts in diffuser exit total pressure profiles exhibited in Figure 4.12 and Figure 4.13 occurring due to the “freezing” of the impeller exit flow. This highlights the critical impact of unsteadiness throughout the flow field—rather than only in the diffuser inlet flow field—in impacting the flow development. In other words, it is not only the variations in the diffuser inlet flow that impacts the flow development but the propagation of those variations downstream.

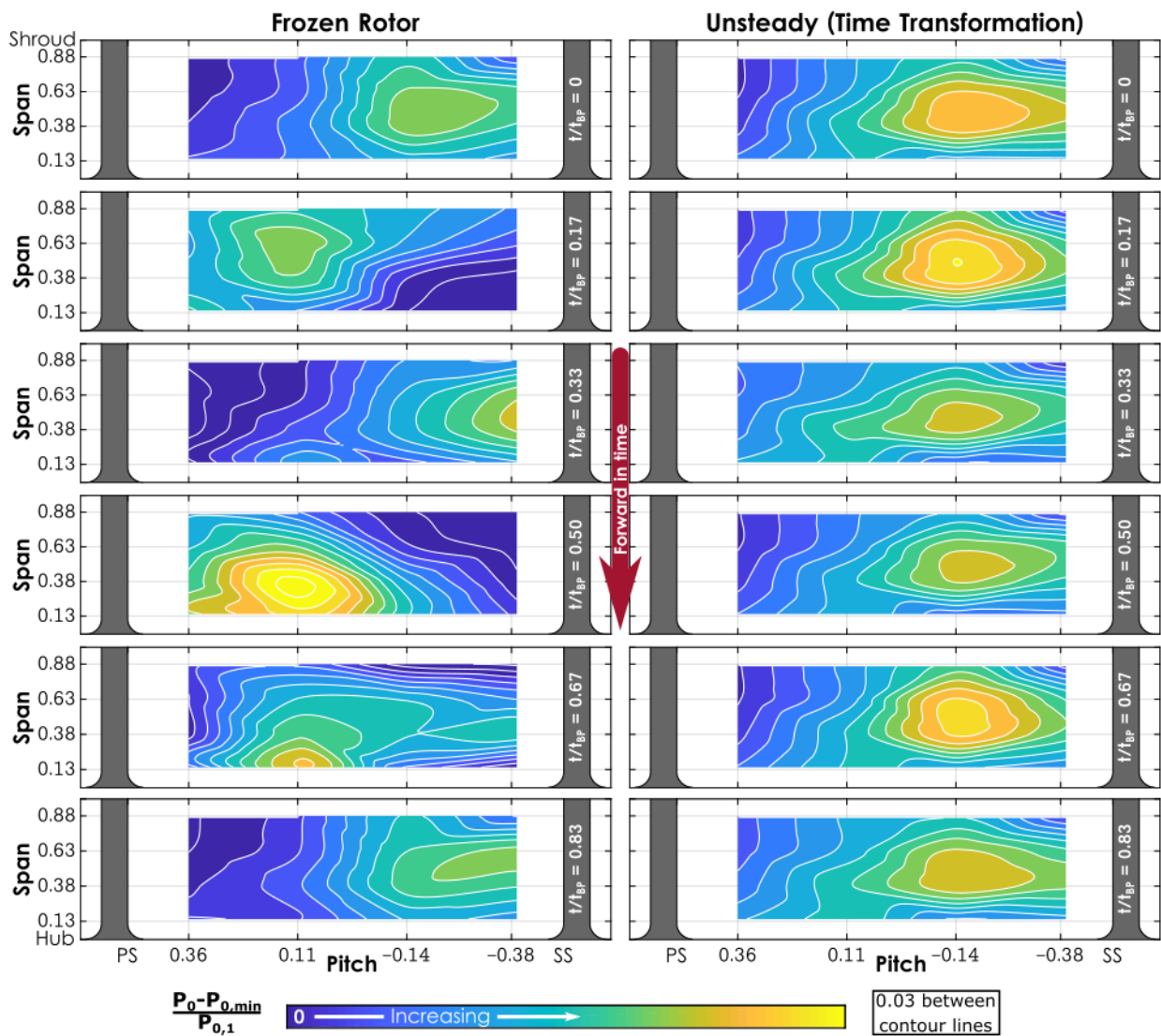


Figure 4.12: Diffuser exit total pressure with the SST turbulence model for various instances in the blade-pass period for frozen rotor (left) and unsteady (right) simulations

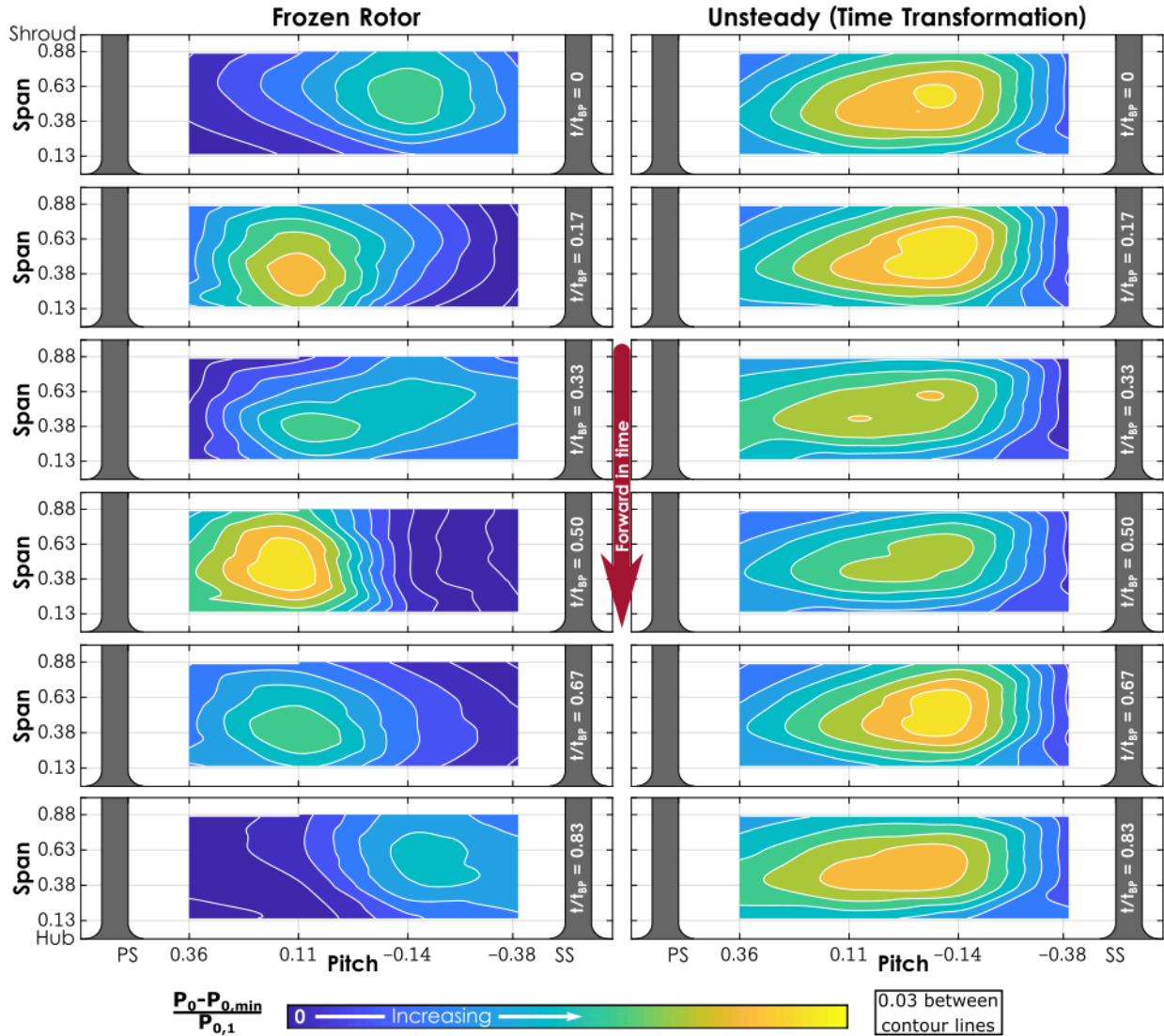


Figure 4.13: Diffuser exit total pressure with the BSL-EARSM turbulence model for various instances in the blade-pass period for frozen rotor (left) and unsteady (right) simulations

Overall, these results do not support the use of frozen rotor simulations in approximating the impact of unsteadiness on the diffuser flow development in this application. The full effect of unsteady fluctuations on the flow field cannot be captured by passing “snapshots” of the impeller exit flow field into the diffuser as is done with the frozen rotor approach. Using the pseudo-time-averaged frozen rotor results would lead to misinformed decisions if they formed the basis of a design process. In fact, the mixing plane results appear to better capture the flow development through the diffuser passage. These conclusions hold for both the SST and the BSL-EARSM turbulence models as implemented in this work.

#### 4.4 Unsteady Results

Unsteady computations were conducted in the high-fidelity configuration with both the SST and the BSL-EARSM turbulence closure models. The unsteady results discussed in this and the previous sections were conducted with the design tip clearance (approximately 2% of the exit blade height) while additional results were obtained with a larger tip clearance of approximately 4% of the exit blade height. A larger tip clearance was implemented experimentally for the LDV data acquisition for safety reasons. Therefore, the simulations conducted with the larger tip clearance will be used only for direct comparison with the LDV results in Chapter 5.

For the unsteady results, the time-averaged static pressure results (normalized by the diffuser inlet total pressure,  $P_{02}$ ) are presented in Figure 4.14. The results with the SST turbulence model are presented in the top row and the BSL-EARSM results are in the bottom row. The left column presents results near the pressure surface at a constant pitch of 37.5% (50% being the pressure surface), the center column presents results at mid-passage (MP, 0% pitch), and the right column presents results near the suction surface (-37.5% pitch, -50% being the suction surface). The abscissa is the local radius, normalized by the impeller tip radius. Data are presented at four spanwise positions and the location of the throat is indicated by the vertical dashed line. This location differs slightly between the various pitch locations because the throat is not at a constant radial location across the passage. These data describe the diffusion occurring through the diffuser as well as the aerodynamic loading on the diffuser vanes. Mach number is an alternative parameter to describe the diffusion process through the passage, and these data are presented in Figure 4.15. Diffusion is indicated by a rise in static pressure or a decrease (deceleration) in the Mach number.

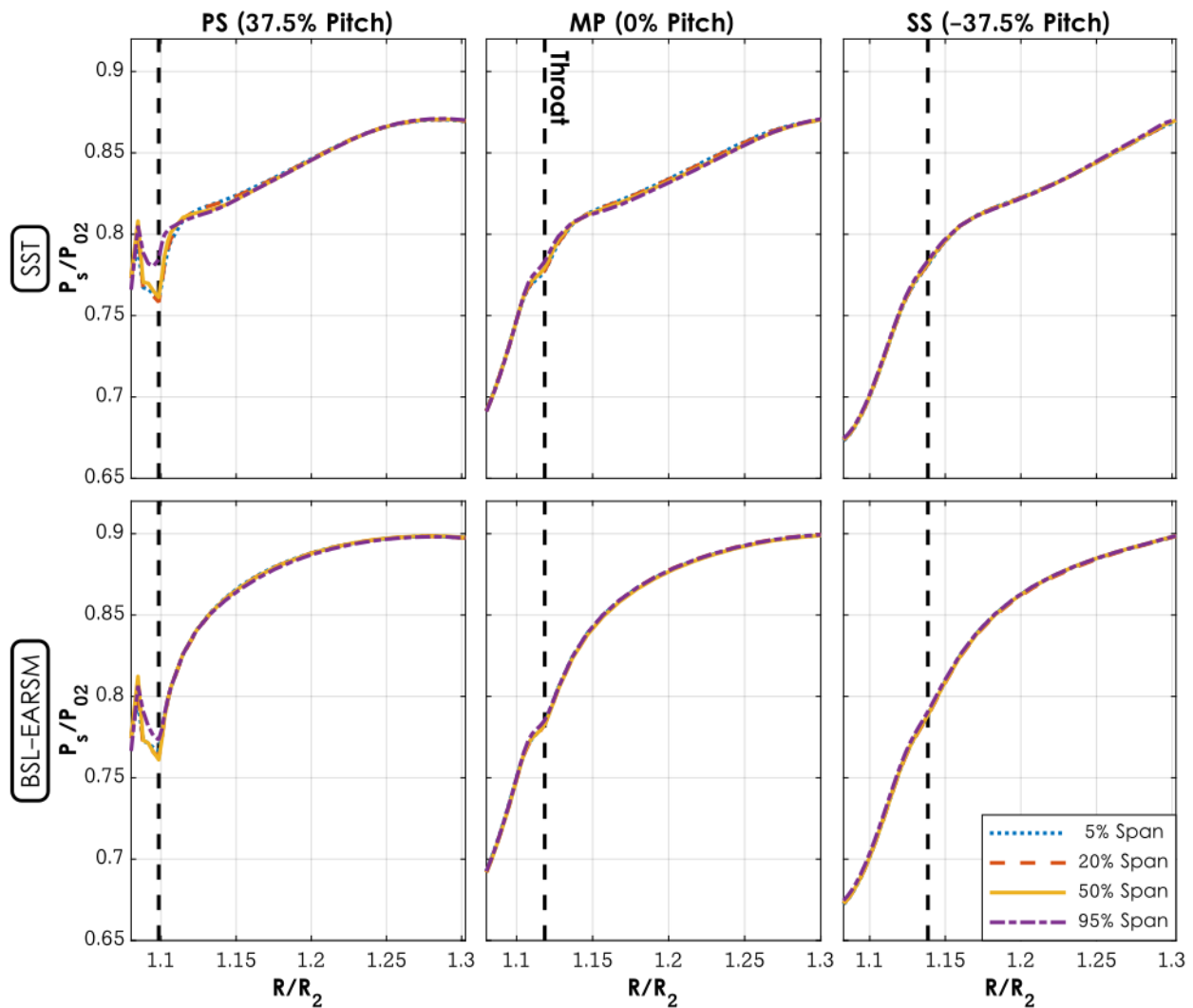


Figure 4.14: Time-averaged static pressure progression through the diffuser passage

The static pressure data predict a negligible hub-to-shroud gradient across the full passage. This result is supported by recent experimental measurements using an additive manufactured version of the diffuser with increased instrumentation capabilities [132]. The one notable exception is along the pressure surface (37.5% pitch, left column) just upstream of the throat where the near-shroud (95% span) static pressure is noticeably higher than the rest of the passage for both turbulence models. This localized spanwise difference could cause issues in experimental results when Mach number or flow angles are computed from hub-side static pressure measurements. The pressure surface data (37.5% pitch) indicate a complex diffusion-then-expansion occurring over the short portion of the vane upstream of the throat in both the Mach number and the static pressure data. This occurs due to a combination of incidence effects and the chamfer present on the vane

leading edge. This chamfer acts to limit the initial diffusion rate along the pressure surface of the vane upstream of the throat. With the SST turbulence model, the overall static pressure rise achieved downstream of the throat is similar across the passage. Along the pressure surface (37.5% pitch), the diffuser is slightly front loaded—little diffusion is achieved beyond a radius ratio of 1.25—while the other pitch locations indicate more consistent diffusion downstream of the throat with a sharper slope upstream of the throat. The BSL-EARSM results are largely similar to the SST results except in the shape of the static pressure characteristic downstream of the throat. While the SST model predicts a linear increase in static pressure with radius, the BSL-EARSM model predicts a front-loaded, parabolic increase with less diffusion occurring at larger radii. Additionally, the magnitude of the hub-to-shroud difference in static pressure just upstream of the throat is lower with the BSL-EARSM than with the SST turbulence model.

The Mach number progression (Figure 4.15) illustrates more significant differences both in terms of spanwise comparisons and between the two turbulence models. These differences are most evident along the pressure surface (37.5% pitch, left column). With the SST turbulence model, a dramatic drop in Mach number is predicted at 95% span just downstream of the throat. This is likely due to significant flow separation occurring causing a dramatic deceleration of the flow without a concomitant rise in static pressure. The flow at 50% span indicates a similar drop in Mach number further downstream and occurring over a larger radial extent. Contrarily, the hub flow at 37.5% pitch (near the pressure surface) at both 5% and 20% span show a relatively smooth and gradual decrease in Mach number through the passage. At mid-passage (center column) a relatively smooth decrease in Mach number is predicted through the passage. The only exceptions are at 50% span, where a minimum Mach number is reached at a radius ratio of 1.23 and at 95% span, where a minimum is reached relatively rapidly, and then the flow is accelerated for nearly half of the passage extent. Along the suction surface (-37.5% pitch, right column), the flow decelerates rather smoothly with the exception of a sharp deceleration at 95% span toward the trailing edge of the passage. The BSL-EARSM model, as a whole, predicts smoother Mach number distributions. The pressure surface data (37.5% pitch, left column) exhibits a significant decrease over a short radial extent at the shroud (95% span), similar to the SST prediction. However, this deceleration occurs over a much larger extent with the BSL-EARSM model, and the flow then accelerates slightly through the rest of the passage. A similar, albeit less dramatic, rapid deceleration occurs near the hub (5% span) with the flow remaining at a fairly constant Mach

number through the rest of the passage. The 20% and 50% span data indicate a gradual deceleration through the passage until a constant value is reached toward the trailing edge. The mid-passage (0% pitch, center column) flow exhibits little diffusion near the endwalls (5% and 95% span) downstream of the throat. However, the 20% and 50% span data exhibit gradual deceleration with no regions of local acceleration like were predicted with the SST model. The suction surface flow exhibits smooth deceleration across all spans.

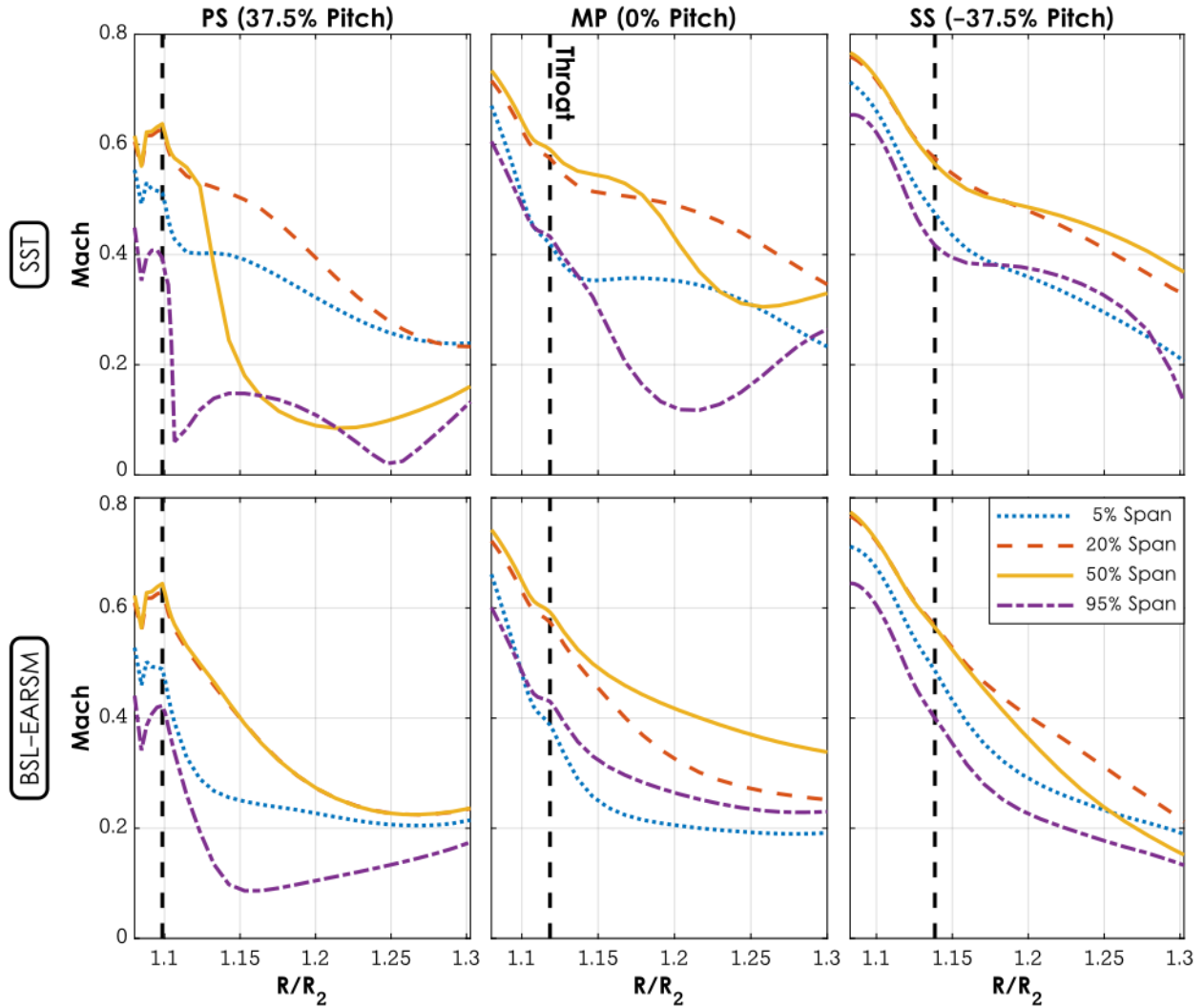


Figure 4.15: Time-averaged Mach number progression through the diffuser passage

The total pressure data, normalized by the diffuser inlet total pressure, are presented in Figure 4.16. The isentropic compressible flow relations can be used to develop an intuitive (albeit not strictly accurate) connection between the static pressure, Mach number, and total pressure data. A decrease in Mach number (indicating deceleration) without an accompanying increase in static pressure implies a decrease in the total pressure indicating the presence of irreversibilities. These data are extracted from physically convenient and recognizable regions, not from a particular streamline or streakline. As such, this relation between these three variables is meant only as a loose basis for the discussion as changes could also be caused by flow shifting around the passage. In general, the regions of sharp decreases in Mach number (for example, in the SST model, 37.5% pitch, at 95% and 50% span) are accompanied by a total pressure decrement, as would be expected from excessive flow deceleration occurring over a short length scale. Comparing the two turbulence models, the SST model predicts more chaotic total pressure progression through the passage and a lower total pressure value at the exit of the passage at the locations considered. The BSL-EARSM model predicts a general decrease in the hub-to-shroud difference in the total pressure and a convergence in the values at different pitch locations at the exit of the passage. The SST model predicts a similar general decrease, however the mid-passage and suction surface spanwise values do not converge to the same value at the passage exit. The 20% and 50% span values, especially along the suction surface, are at a higher level than the endwall (5% and 95% span) values.

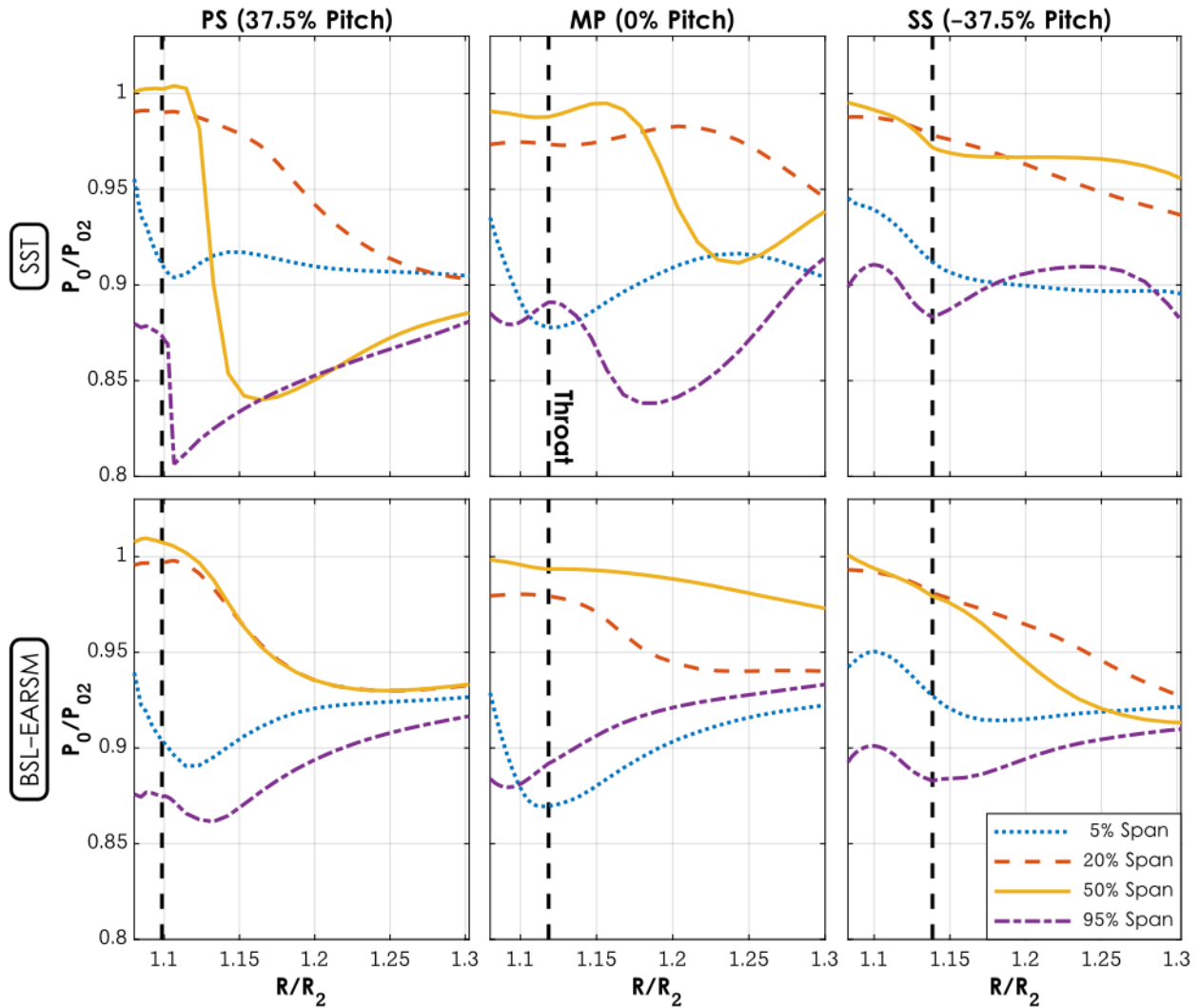


Figure 4.16: Time-averaged total pressure progression through the diffuser passage

The extent of unsteady effects through the passage can be quantified through the percent variation in quantities. In this context, the “variation” is defined at a geometric point as the maximum value present through the time period minus the minimum value, normalized by the time-averaged value. For a parameter  $X$  this can be written as:

$$\text{Variation}(X) = \frac{\max(X_i) - \min(X_i)}{\bar{X}}, \quad (25)$$

where the max, min, and average (indicated by the overbar) are taken over the full time period. The variation of the static pressure values is presented in Figure 4.17. In general, the results indicate little static pressure variation (approximately 2-3%) for the entirety of the passage with

only a slight decrease in the streamwise direction and little difference in the spanwise direction, with two exceptions. First, along the pressure surface (37.5% pitch, left column) with the SST turbulence model, the 50% and 95% span data indicate more variation than the other spanwise positions and reach a maximum downstream of the throat. Second, along the suction surface (right column, -37.5% pitch), a large peak in the variation levels, up to 5%, is present at the throat at all spans. The analogous data for the total pressure (Figure 4.18) and velocities (Chapter 5) can provide more insight into the origins of this localized peak in the variation levels. The Mach number variation through the diffuser passage is not included in this discussion because the low Mach numbers present in many locations (notably the local minimums in the SST model prediction at 37.5% pitch, 95% and 50% span, and 0% pitch, 95% span and the BSL-EARSM model predictions at 37.5% pitch, 95% span) cause surges in the variation percentage values, obfuscating meaningful conclusions.

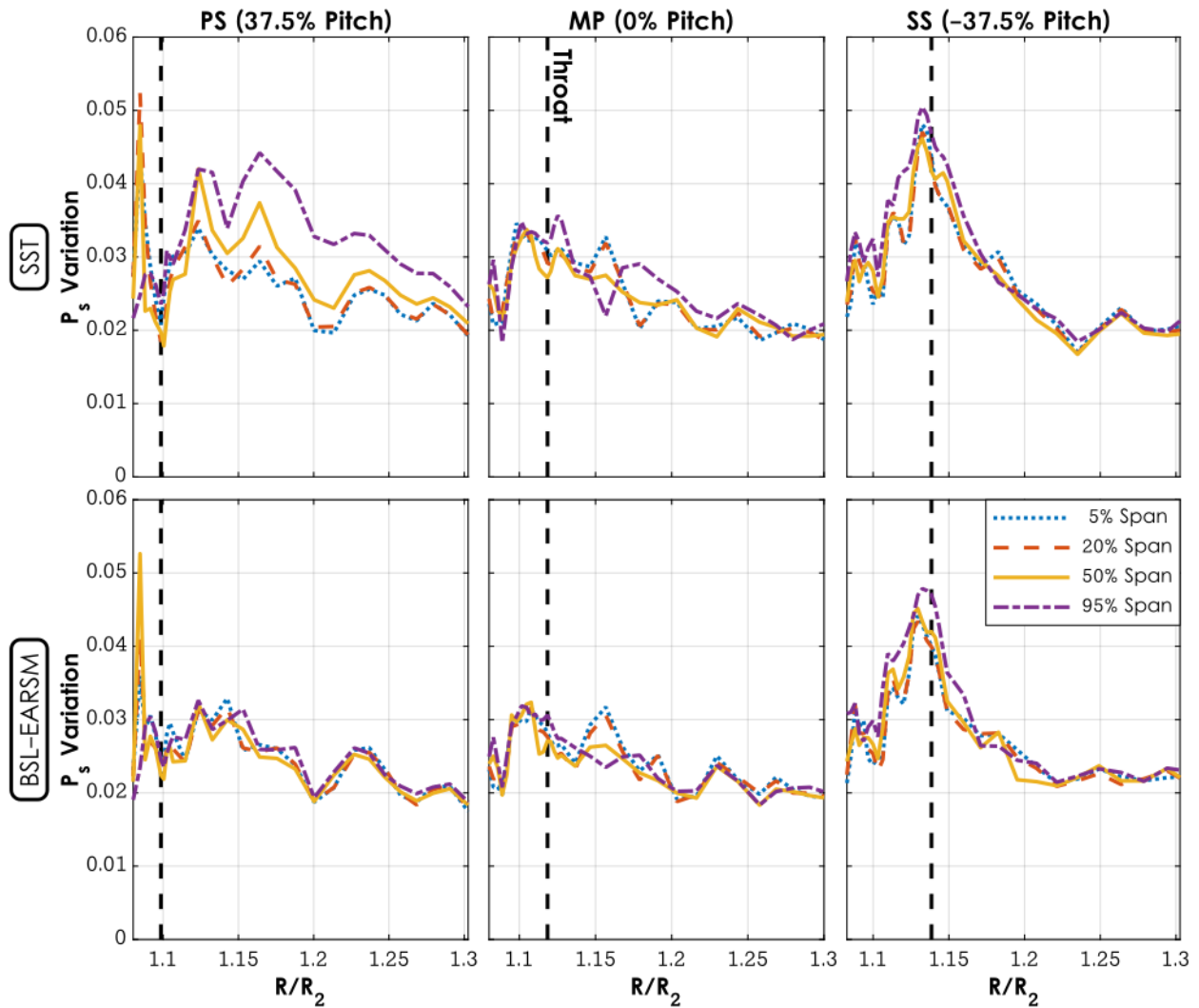


Figure 4.17: Static pressure variation through the diffuser passage

The total pressure variation data are presented in Figure 4.18. Compared to the static pressure variation, the total pressure data indicate greater variation magnitude and a larger decrease in variation levels in the downstream direction. At all pitch locations and in both turbulence models, the variation at the inlet of the diffuser passage is greatest at 50% span, at a level of 12-14%, and lowest at 95% span, at a level of 4-7%. Additionally, the variation levels at the exit of the passage are all approximately 3% with little spanwise difference. Along the pressure surface (37.5% pitch, left column) upstream of the throat, the 5% span variation level is higher than the 20% level, while in most other locations the 5% span data follow the 95% span data relatively closely. The lower levels of variation near the endwalls may lead to errors when experimental evaluations of unsteady effects are made based on hub- or shroud-based measurements. The important observation here is

that significant unsteadiness in the total pressure data is not dissipated upstream of the passage. The SST turbulence model predicts strong total pressure variations of more than 5% downstream of the throat. These variations eventually decay to stable levels of approximately 3%, however this does not occur upstream of the throat, as is often reported. The BSL-EARSM turbulence model predicts similar values with the suction surface variation data (-37.5% pitch, right column) decaying more quickly and indicating less spanwise variation than with the SST turbulence model. The details of the flow field that produce these variations will be discussed in more detail with respect to the predicted velocity field through the diffuser with direct comparison to the LDV measurements in Chapter 5.

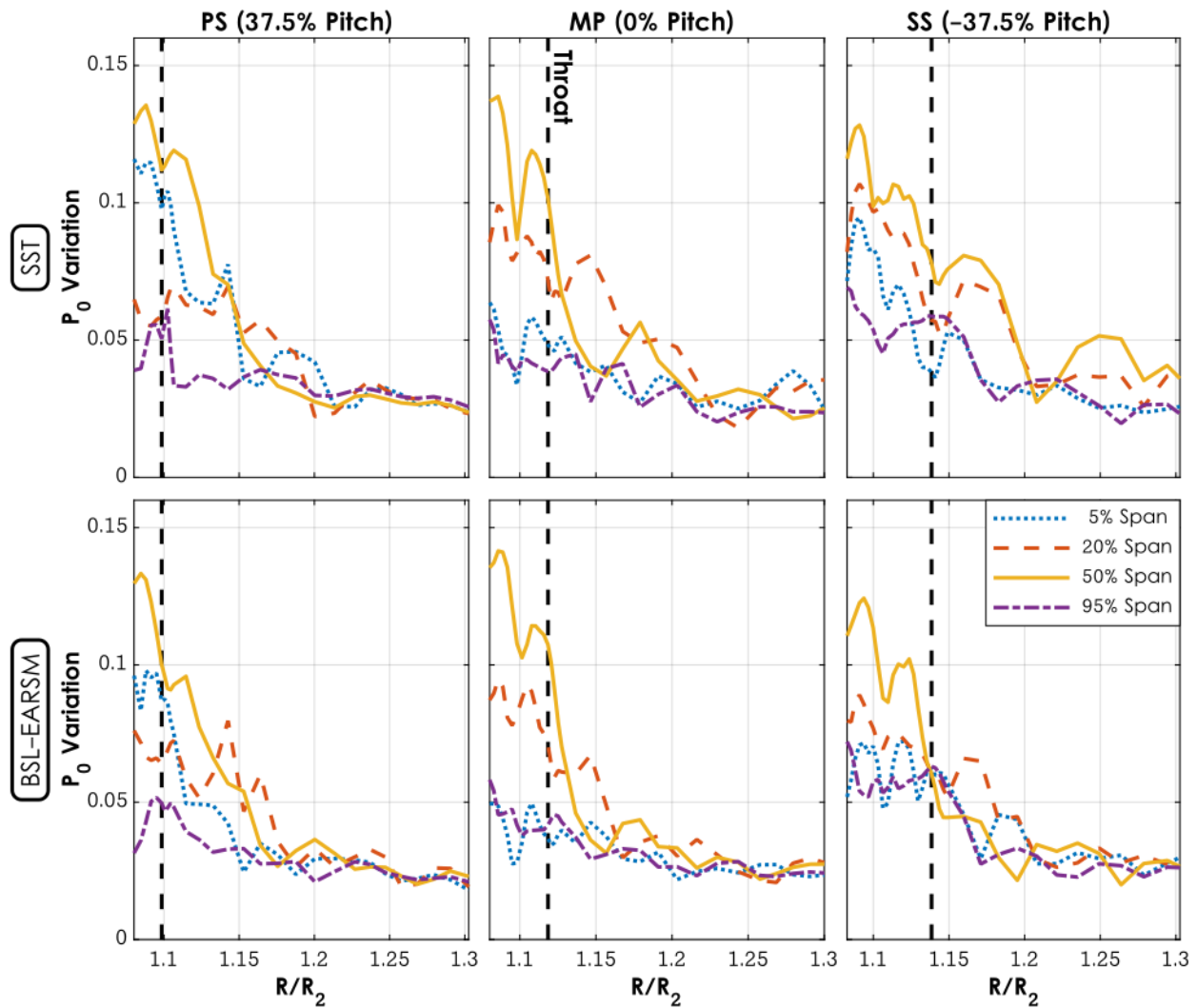


Figure 4.18: Total pressure variation through the diffuser passage

The flow field present at the diffuser throat is a significant factor in determining the overall stage performance. The total pressure field predicted at the diffuser throat for the SST turbulence model (top row) and the BSL-EARSM turbulence model (bottom row) is presented in Figure 4.19 and Figure 4.20. Figure 4.19 includes contours of total pressure, normalized by the diffuser inlet total pressure ( $P_{02}$ ), across the diffuser throat at equally spaced instances through the impeller blade passage. The vanes bounding the passage are shaded in grey with the pressure surface on the left and the suction surface on the right of each graph. The ordinate is the spanwise position. Because there is a large deficit in total pressure along the hub and shroud surfaces, the contour levels were clipped to provide a better representation of the values across most of the passage. All values below a certain level were colored with a constant color, leading to the isochromatic regions with no contour lines along the hub and shroud surfaces in Figure 4.19. Figure 4.20 gives an alternate presentation of the data. The spanwise profiles in total pressure at the throat at three pitchwise positions are presented for the same six equally spaced instances through the impeller blade passage. The abscissa is the total pressure value normalized by the diffuser inlet total pressure and the ordinate is the spanwise position across the passage. The hub and shroud endwalls are shaded in grey. In both figures,  $t/t_{BP} = 0.33$  or  $0.83$  approximately corresponds to the instance in which the wake trailing the splitter blade or the full blade convects through the throat, respectively.

As evident in Figure 4.19, the unsteady oscillations due to the impeller jet and wake are not dissipated upstream of the throat. The total pressure profile through the blade passing event varies greatly, illustrating the difficulty in capturing the nature of the flow at the diffuser throat with a single representative “picture” that would accurately describe the flow profile at all instances in time. Because a splitter blade falls between every full blade, the full blade passing event should loosely repeat every  $0.50 t_{BP}$ . While this tenet holds relatively well for these results (by comparing every third column in Figure 4.19) in terms of general profiles, the magnitudes and the details are clearly different between corresponding instances in the full and splitter blade passages. At a  $t/t_{BP}$  of 0.00 and 0.50, the corresponding instances are most similar. Both turbulence models predict a region of higher total pressure between 50% and 70% span at approximately -25% pitch (closer to the suction side of the passage). This region is at a slightly larger total pressure at  $t/t_{BP} = 0.50$ , however the general profiles are essentially the same between the two time instances. At a  $t/t_{BP}$  of 0.17 and 0.67, the instances are less similar. For  $t/t_{BP} = 0.17$ , a small region of high total pressure is present adjacent to the pressure surface. With the SST turbulence model, this region is located

between 55% and 70% span while with the BSL-EARSM it is shifted slightly down to 40-60% span. For  $t/t_{BP} = 0.67$  there is no distinct region of high total pressure along the pressure side of the vane. There is relatively little variation in total pressure (except in approaching the hub and shroud) and the overall total pressure level is lower than for  $t/t_{BP} = 0.17$ . When the wakes from the impeller blades are convecting through the throat ( $t/t_{BP} = 0.33$  and  $0.83$ ), the total pressure is higher than during the other time instances. This is because the impeller jet/wake describes a phenomenon in the *relative* frame. As illustrated in the velocity triangles in Figure 1.3, the wake's velocity deficit in the relative frame becomes a higher velocity in the stationary frame. Similarly, the total pressure in the wake is actually higher than in the jet, when the total pressure is measured relative to the stationary frame<sup>2</sup>. During the splitter blade wake convection ( $t/t_{BP} = 0.33$ ), the region of high total pressure is located between 40% and 60% span and extending from the pressure surface of the vane to approximately -25% pitch (covering approximately 75% of the passage). During the full blade wake convection, the profile is similar, although the high total pressure region is shifted in toward the pressure surface (only extending to approximately mid-passage) and covers from approximately 25% to 75% span. These results suggest that the flow developing in the full and splitter blade passages is not identical and propagates through the diffuser passage to produce distinct flow patterns.

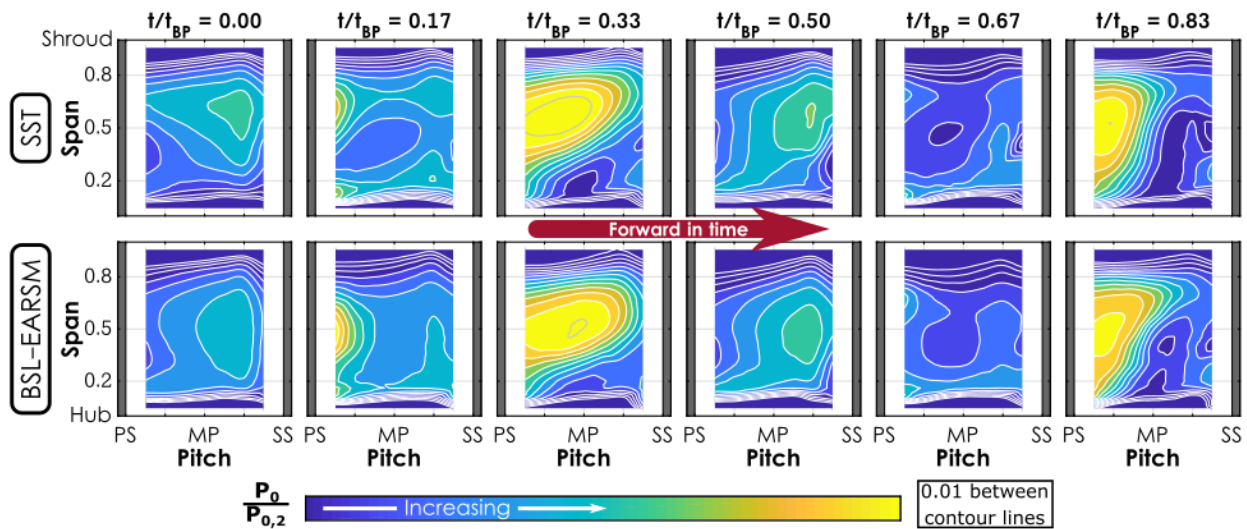


Figure 4.19: Unsteady total pressure field at the diffuser throat

<sup>2</sup> Total pressure and total temperature are frame-dependent quantities. Although it has not been explicitly stated, all total quantities discussed in this work are relative to the stationary frame, unless explicitly stated otherwise.

The spanwise profiles more explicitly show the unsteady variations at individual points. The largest unsteady fluctuations are present along the pressure surface (37.5% pitch, left column). During the wake propagations ( $t/t_{BP} = 0.33$  and  $0.83$ ), these data illustrate a total pressure profile similar to what is observed for fully developed flow in a pipe. The boundary layer deficit is asymmetrical with a larger deficit present adjacent to the shroud. During the other time instances, two peaks exist in the total pressure. One is located at approximately 15% span and the second at approximately 70% span. The lower peak has a higher total pressure except for the instance when  $t/t_{BP} = 0.17$ . At mid-passage (0% pitch, center column) all time instances indicate similar total pressure profiles with the exception of during the splitter blade wake convection ( $t/t_{BP} = 0.33$ ). At this instance, a significantly higher total pressure exists between 40% and 80% span, corresponding to the region of high total pressure growing across mid-passage (as observed in Figure 4.19, third column). The full blade wake convection ( $t/t_{BP} = 0.83$ ) presents a similar profile, however the magnitude and the extent of the total pressure peak is significantly reduced compared to the splitter blade wake data. Various observations can also be made regarding the total pressure deficit adjacent to the hub and shroud endwalls. Along the pressure side (37.5% pitch, left column), the deficit extends for a larger portion of the span along the shroud than along the hub. This is likely due to losses or incidence changes associated with tip leakage flow in the impeller. At mid-passage (0% pitch, center column) and along the suction surface (-37.5% span, right column) this observation still holds with the BSL-EARSM turbulence model for the majority of time instances, albeit the difference is less dramatic than along the pressure surface. With the SST turbulence model, the total pressure deficit is nearly identical along the hub and shroud surfaces at mid-passage and along the suction surface.

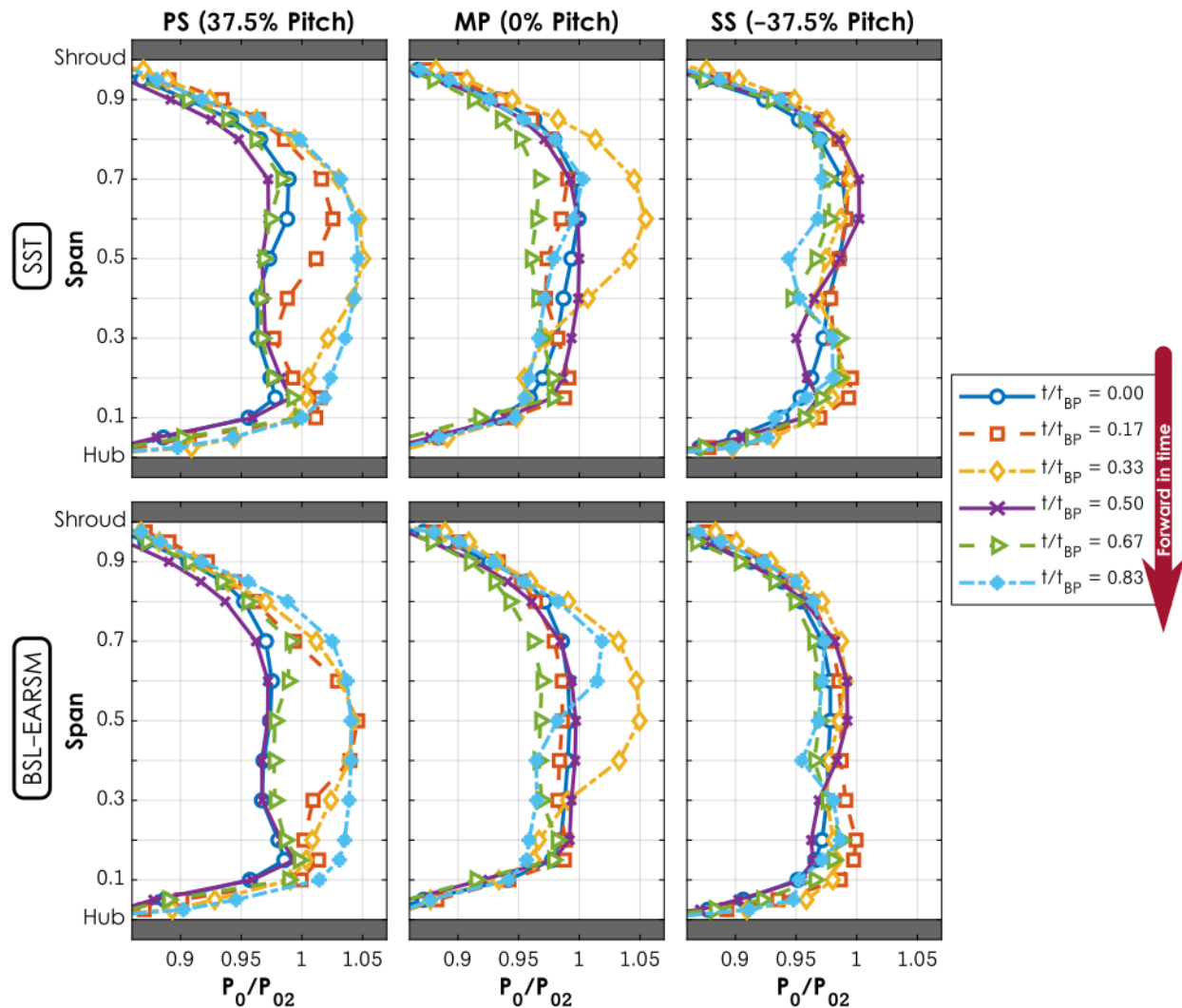


Figure 4.20: Spanwise profiles of total pressure at the diffuser throat at various pitchwise positions and instances in the blade-pass period

Altogether, these unsteady data illustrate the extraordinarily complex nature of the flow through the diffuser. Unsteady fluctuations persist downstream of the diffuser and vary in magnitude across the span and across the pitch of the diffuser passage. These fluctuations have a significant impact on the flow development through the diffuser, even when only time-averaged quantities are considered (as evident by the diffuser exit total pressure contours presented in Figure 4.5 and Figure 4.11). The two turbulence models implemented were discussed with equal weight in this section because the time-averaged diffuser exit contours were comparable between the two, and no additional unsteady data were presented to support a conclusion that one turbulence model performed better than the other in the unsteady context. However, this discussion and evaluation

will continue in Chapter 5 with a direct comparison between unsteady LDV measurements and the unsteady computational results. This comparison will provide additional data for evaluation of the SST and BSL-EARSM turbulence models in the unsteady context.

## 5. COMPARISON BETWEEN NUMERICAL AND LDV RESULTS

The detailed data acquired present a unique opportunity to compare experimental and computational results in an unsteady context throughout the diffuser flow field—rather than just along solid boundaries or in terms of overall performance parameters. The experimental data were obtained with a larger-than-design tip clearance (4% rather than 2% of the impeller exit blade height). The previous discussion of the CFD analysis involved results—both computational and experimental—with the design value of tip clearance. To facilitate the direct comparison between the LDV data and the CFD results, additional unsteady simulations were conducted with the clearance levels present during LDV collection applying both the SST and the BSL-EARSM turbulence models in the high-fidelity configuration. These results will be interrogated at the same geometric points used for LDV data acquisition and the development of the flow field from the impeller trailing edge through the diffuser will be compared at the locations detailed in Figure 5.1. Each of these locations has been discussed previously except for the DSTM A plane (5% downstream of the throat). The spatial distribution of the measurement locations for the discussion of the velocity vector field are different from that for the Reynolds stress data in order to focus on points with the greatest spanwise extent of available data.

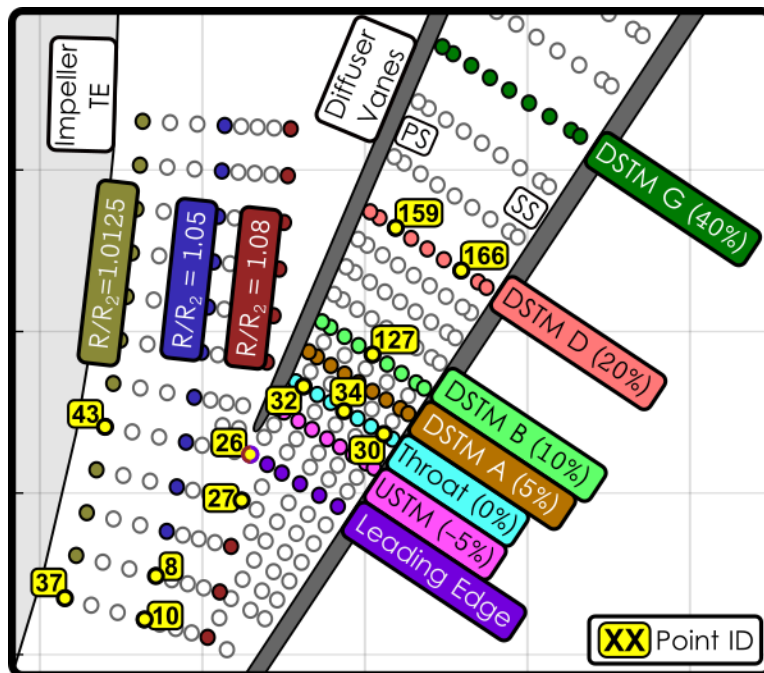


Figure 5.1: Key geometric locations for CFD-LDV comparison

## 5.1 Development of Flow Through the Vaneless Space

The impeller exit flow field is the inlet flow condition for the focus of this work. Although the development of the flow through the impeller will not be analyzed in detail, the flow present at the impeller exit is critical to the diffuser flow field. The impeller exit radial velocity profile at a radius ratio of 1.0125 (Point 37) is presented in Figure 5.2 and the axial velocity data in Figure 5.3. The abscissa is time, and the ordinate is the spanwise position. The approximate time instances of the splitter (SB) and full (FB) blades passing are indicated on the abscissa. The top row corresponds to the experimental data, the middle row corresponds to the unsteady CFD result with the SST turbulence model, and the bottom row corresponds to the result with the BSL-EARSM turbulence model. The radial velocity contours reveal a qualitative agreement between the three results in the flow structure at the impeller exit. The computational results predict a larger deficit adjacent to the shroud wall and a lower radial velocity within the wake flow. However, the general shape of the jet and the wake regions, the presence of a large deficit along the hub immediately behind each blade, and the magnitudes of the splitter and main blade wake regions relative to each other are consistent between the three results. Between the two CFD results, the SST turbulence model predicts a stronger deficit within each wake region.

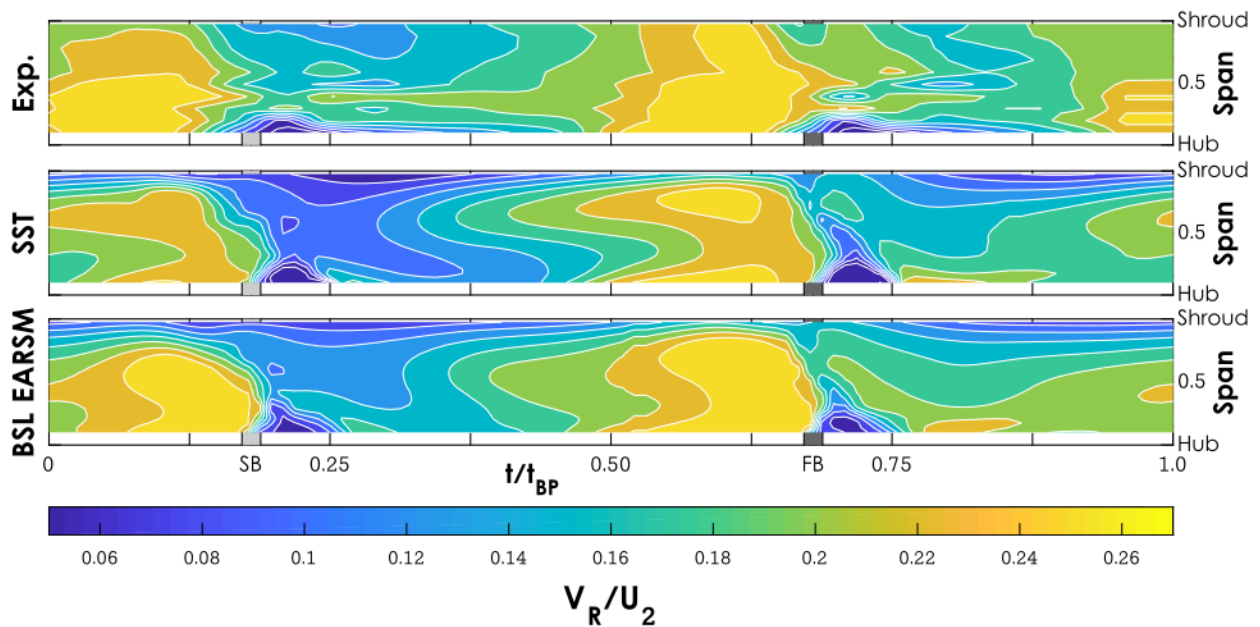


Figure 5.2: Radial velocity contour at a radius ratio of 1.0125 (Point 37) for Experimental data (top) and SST (middle) and BSL-EARSM (bottom) turbulence models

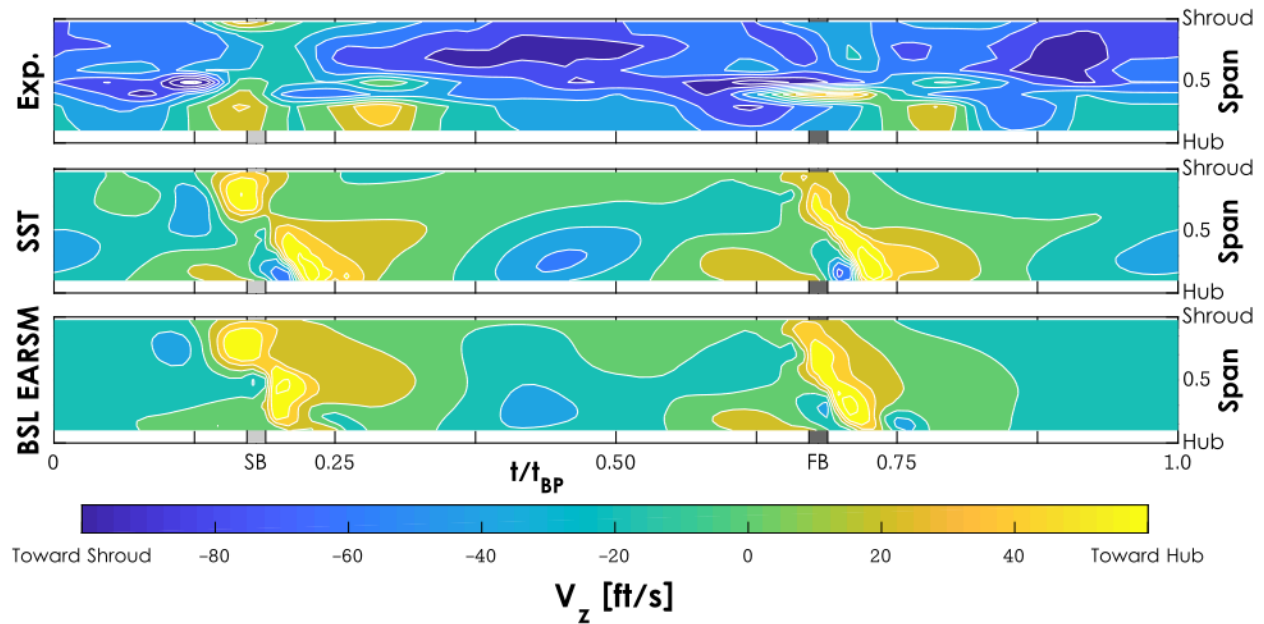


Figure 5.3: Axial velocity contour at a radius ratio of 1.0125 (Point 37) for Experimental data (top) and SST (middle) and BSL-EARSM (bottom) turbulence models

The axial velocity data indicate a difference between the experimental data and the two computational results. The computational results both indicate a large band of axial velocity toward the hub in the bluff-body wake directly behind each blade. Outside of this narrow band, the axial velocity is near-zero for the remainder of the blade-pass period for both computational results. On the other hand, the experimental data indicate a predominantly toward the shroud axial velocity above 30% span that is present through the entire blade-pass period. The difference between the experimental and numerical results is consistent through the blade-pass period meaning that the discrepancy is not connected to one particular aspect of the flow—the jet, wake, or tip leakage flow, for example—but is representative of the global flow development through the impeller. Further research is needed to determine why the computational models predict a significantly lower magnitude of axial velocity. Three potential explanations are deficiencies in the turbulence models themselves, small geometric deviations in the experimental stage (such as steps in the flow path), or discrepancies in the inlet boundary flow conditions. The observation of lower axial velocities in the computational predictions is consistent through the entire diffuser passage. Even when specific secondary flow structures develop further downstream, the magnitudes of the associated axial velocities observed experimentally are much greater than those predicted numerically, as will be discussed subsequently.

The transient turbulent kinetic energy,  $k$  (Equation (23)), at a radius ratio of 1.0125 (Point 43) is presented in Figure 5.4. Data were only acquired near the shroud; however, the general agreement between the experimental and numerical results is good. Narrow peaks are present in the experimental data that are not illustrated numerically, but the general level and the transient trend agree well.

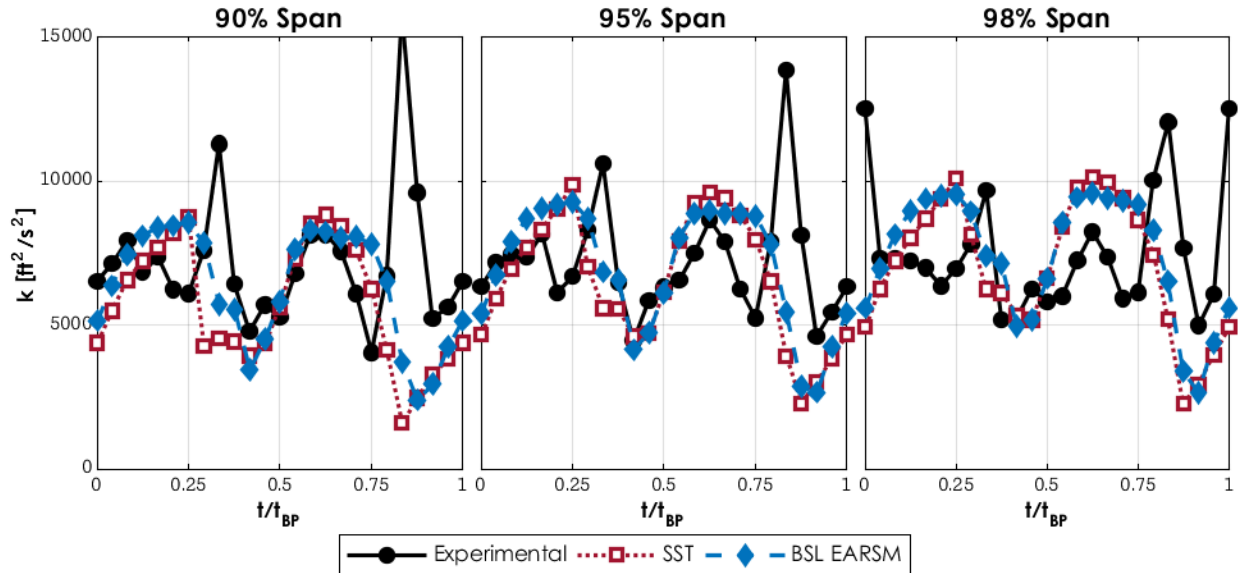


Figure 5.4: Unsteady turbulent kinetic energy,  $k$ , at a radius ratio of 1.0125 (Point 43)

Further downstream, at a radius ratio of 1.05 (Point 8), the radial velocity profiles maintain their similarity between the various datasets, Figure 5.5. The computational models predict a consistent low-velocity region adjacent to the shroud which is not observed experimentally. Additionally, the computational results indicate higher velocity levels within the jet regions. However, the relative difference between the jet and wake flow velocities is similar between all three results as the wake velocity is also higher in the computational results. The turbulent kinetic energy data at a radius ratio of 1.05 (Point 10) are presented in Figure 5.6 at 50%, 70%, and 95% span. The 50% data indicate general agreement between the computational and experimental results through most of the period. However, the experimental results indicate a short-duration doubling of the  $k$  values that is not exhibited numerically. The same is true at 70% and 95% span. The computational results also illustrate an increasing lag at 70% and 95% span between the peak  $k$  time instances (relative to the peak time instance experimentally) and a smaller fluctuation range in  $k$  values through the blade pass period.

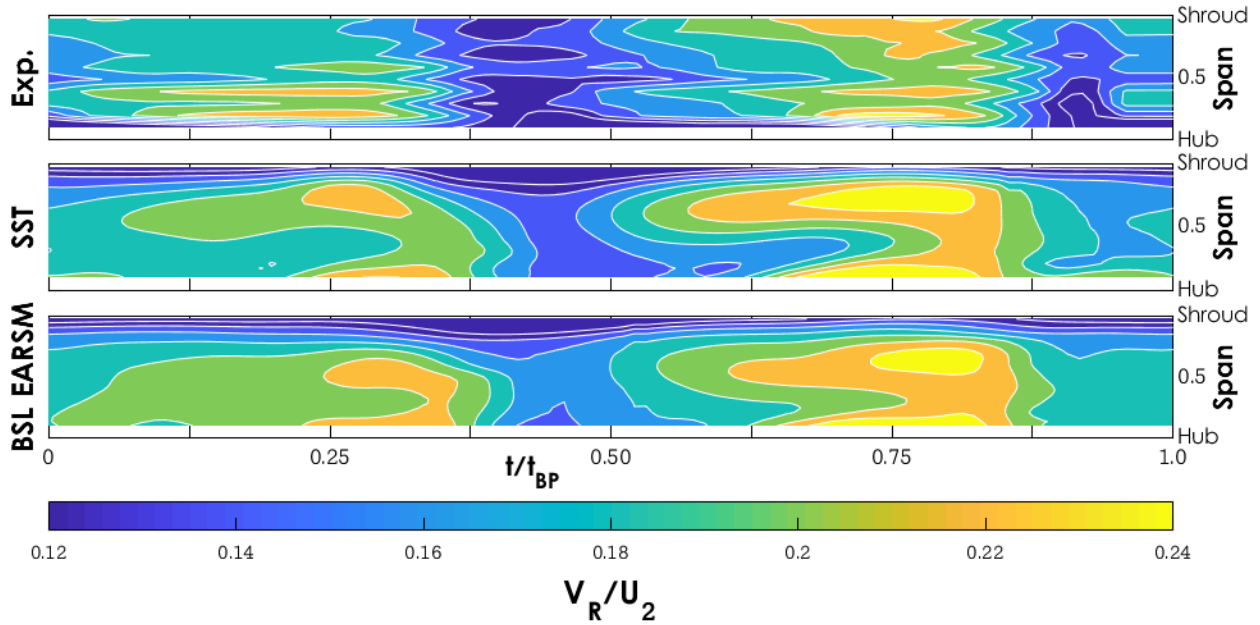


Figure 5.5: Radial velocity contour at a radius ratio of 1.05 (Point 8) for Experimental data (top) and SST (middle) and BSL-EARSM (bottom) turbulence models

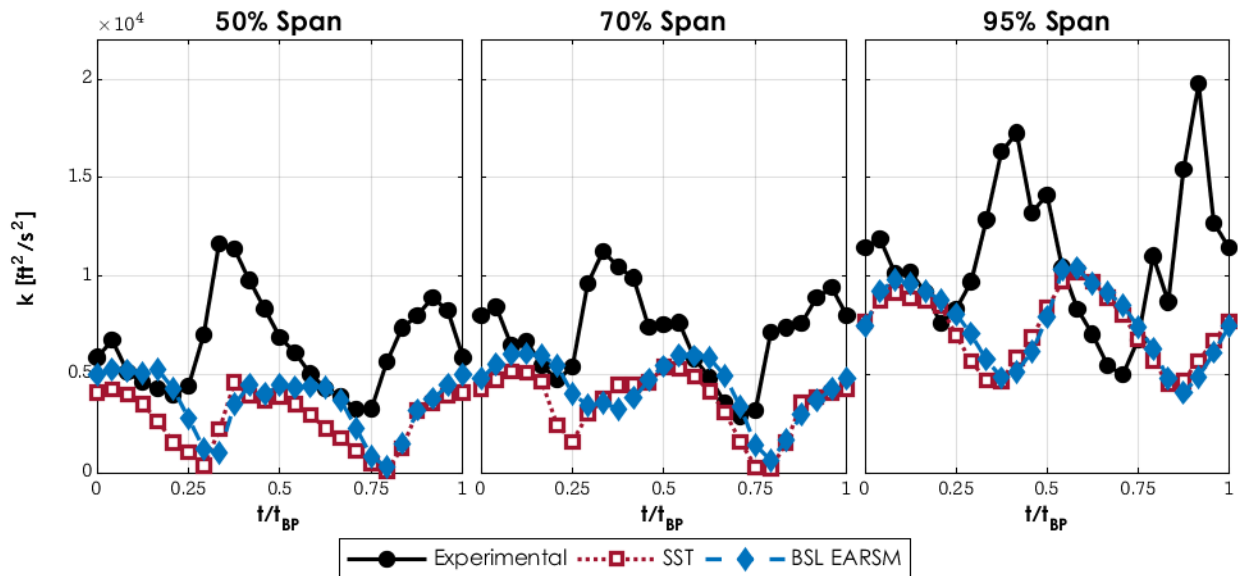


Figure 5.6: Unsteady turbulent kinetic energy,  $k$ , at a radius ratio of 1.05 (Point 10)

At the vane leading edge radius, differences are noticeable in the incidence profile between the three results, Figure 5.7. The incidence variation across the span at a radius ratio of 1.08 (Point 27) is presented within the jet flow, within the wake flow, and time-averaged. Note that positive incidence (more tangential) is toward the *left* on the abscissa to better reflect the physical direction

of the flow when viewing the vane leading edge. The experimental data indicate some scatter in the spanwise direction which is within the experimental uncertainty of  $\pm 1.5^\circ$ . Within the jet flow, the SST result indicates a profile with local maximums at 10% and 70% span with a local minimum at 30% span. The BSL-EARSM and experimental results both indicate a maximum at 15% span and then a monotonic decrease toward the shroud. Within the wake flow, the profiles differ more significantly between the experimental and computational data. Between 10% and 70% span, the experimental data have 3-5° more-positive incidence. Toward the shroud, the opposite holds, with the CFD results indicating a sharp increase in incidence in approaching the endwall. The time-averaged data contain the same relative trend between the experimental and numerical data as the data within the wake flow. The positive incidence present in the experimental wake flow between 10% and 70% span is important to the downstream flow development as outlined in Section 3.5. Adjacent to the shroud, the more-positive incidence observed numerically may lead to separation adjacent to the shroud. The difference in the incidence profiles adjacent to the shroud occurs due to the reduced axial velocity component in the CFD solutions. Axial velocity induces spanwise mixing between the shroud-adjacent fluid—dominated by tip leakage and boundary layer development—and the flow at mid-span. This reduces the gradient in flow properties in approaching the shroud and, when not present, leads to the significant gradient observed in the numerical results between 70% and 100% span.

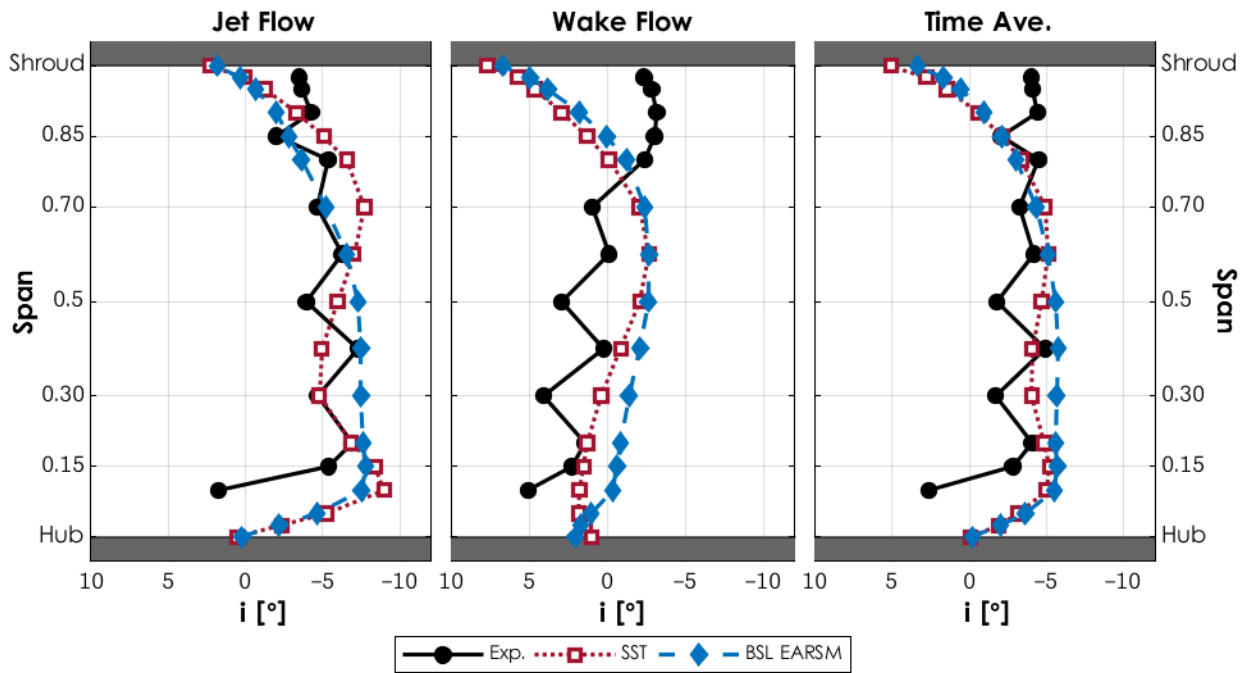


Figure 5.7: Inlet incidence field at a radius ratio of 1.08 (Point 27)

The same phenomenon is evident in the turbulent kinetic energy data at the vane leading edge radius, Figure 5.8. The experimental data indicate a consistent increase in  $k$  levels from 50% to 70% to 95% span, whereas the computational results exhibit little change from 50% to 70% span and a large increase from 70% to 95% span. This occurs due to the increased convective transport of  $k$  associated with the increased axial velocity present in the experimental stage. This conclusion is also supported based on the comparison between the relative  $k$  values in progressing from a radius ratio of 1.05 (Figure 5.6) to 1.08 (Figure 5.8). For the experimental data, the average  $k$  level at 70% span has increased while the level at 95% span has decreased. Turbulence is typically produced adjacent to the boundary layer, therefore these shifts must arise due to spanwise mixing occurring adjacent to the shroud. At 50% span, the transient trend matches well between the experimental and numerical results, with the experimental values translated toward higher  $k$  values. The 70% span data indicate higher levels experimentally while the 95% span data indicate a similar average level between all three results. The magnitude of the unsteady fluctuations is larger experimentally at both 70% and 95% span. Additionally, the same lag in the time instance associated with the peak value is present that was observed previously. Comparing between the two turbulence models. The BSL-EARSM model exhibits slightly higher  $k$  values across most of the blade-pass period. The deficit in  $k$  arising in the computational results at 70% span at  $t/t_{BP} = 0.6$  is also significantly reduced in magnitude with the BSL-EARSM model and the deficit regions generally have a shorter duration than the SST result at all other span positions.

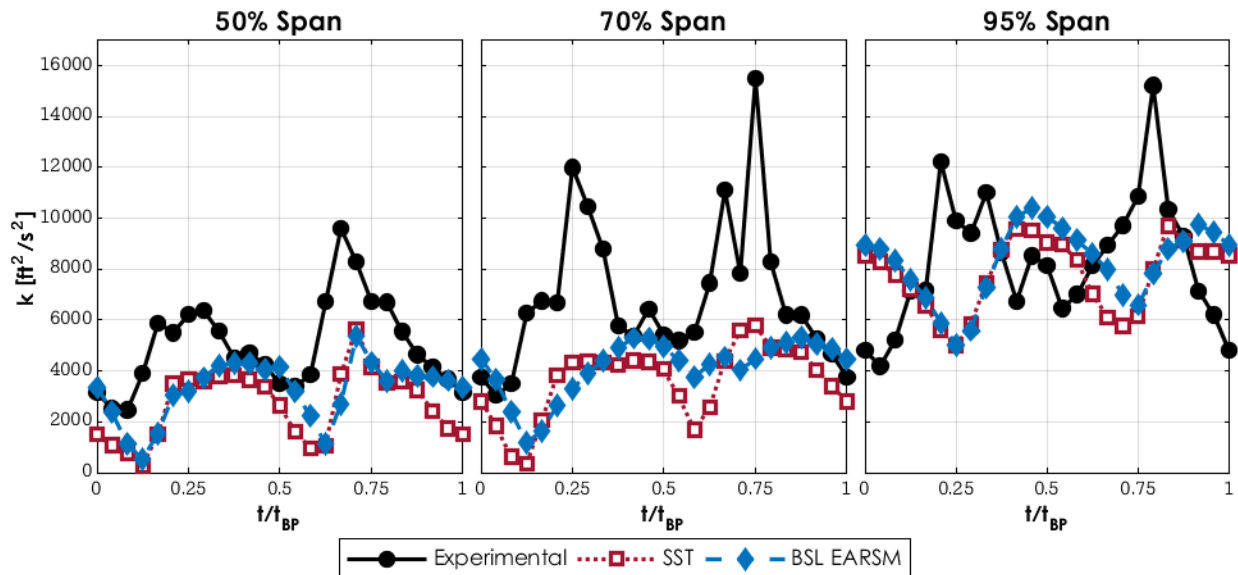


Figure 5.8: Unsteady turbulent kinetic energy,  $k$ , at a radius ratio of 1.08 (Point 26)

## 5.2 Propagation of Flow Through the Diffuser Passage

The relatively small differences in the flow fields at the diffuser leading edge radius produce large differences in the propagation of the flow through the diffuser passage. Tracking the flow downstream, as was done in Section 3.5, elucidates the streamwise development of distinct flow structures that produce the diffuser exit total pressure profiles presented in Figure 4.11.

The streamwise and axial velocity data at the Leading Edge plane are presented in Figure 5.9 and Figure 5.10, respectively. These data are presented as the difference between individual measurements ( $V_{s,i}$  or  $V_{z,i}$ ) from the mean value across the full plane at that instance in time (denoted by the overbar). The left, middle, and right columns correspond to the Experimental data, the result with the SST turbulence model, and the BSL-EARSM result, respectively. The top row corresponds to the time instance associated with jet flow, the middle row corresponds to the wake flow, and the bottom row corresponds to the time-average of the result.

The streamwise velocity results indicate good agreement between the three datasets. During jet convection, high streamwise velocity is present adjacent to the suction side of the passage with lower velocities toward the pressure side. During the wake convection, the high streamwise velocity region is centered toward the hub-PS corner of the passage. The experimental data indicate these core locations shifted toward the shroud within both the jet and the wake flow and also toward the pressure side within the wake flow. The CFD data indicate a larger boundary layer deficit adjacent to both the hub and the shroud endwalls.

The axial velocity indicates similar qualitative patterns between the various datasets: motion toward the hub in the shroud-PS corner during jet convection and shifted down toward mid-span during wake convection. However, the magnitudes of the axial velocities are significantly lower in the CFD solutions. In general, the secondary flow vectors in the CFD results indicate predominantly pitchwise motion. Within the jet flow with both turbulence models, pitchwise velocity toward the PS exists above 75% span with pitchwise velocity toward the SS present below 75% span. This is indicative of streamwise vorticity that is centered around 85% span. Altogether, these observations describe a secondary velocity field that resembles the experimental data in terms of axial velocity profiles yet differs significantly in the axial velocity magnitudes and in the pitchwise velocity profiles.

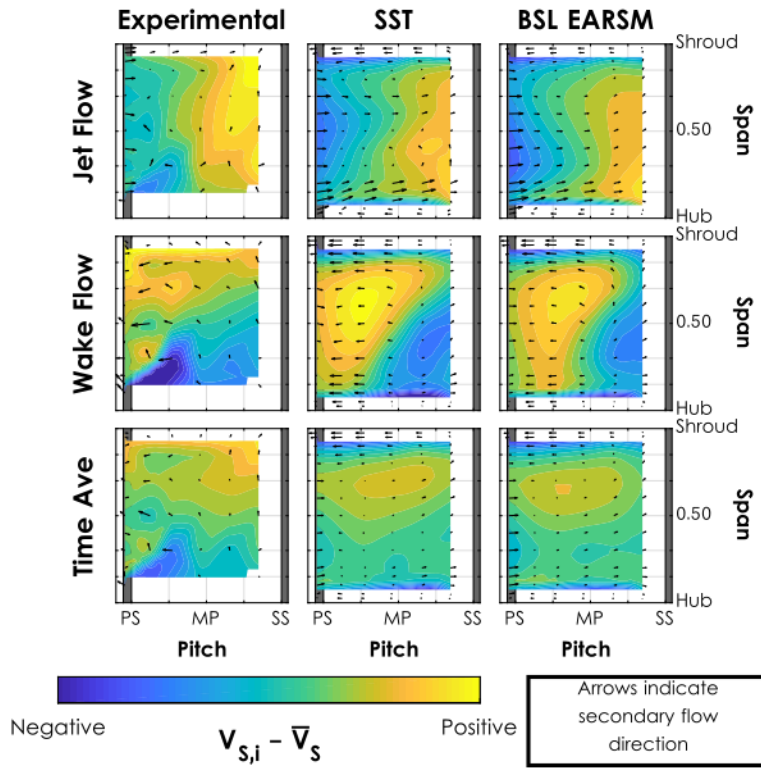


Figure 5.9: Streamwise velocity at the Leading Edge plane

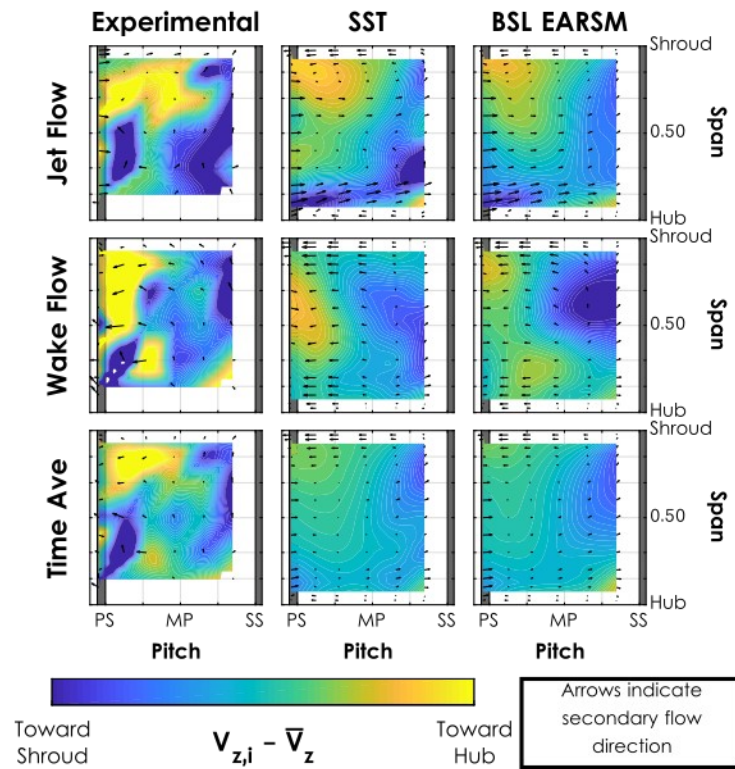


Figure 5.10: Axial velocity at the Leading Edge plane

At the throat, the computational results begin to show significant differences from the experimental results in terms of streamwise velocity, Figure 5.11. Most notably, while the experimental wake flow indicates a core region that is maintained adjacent to the shroud by the secondary flow field, the corresponding region in the computational results remains adjacent to the pressure surface of the passage. Additionally, the computational results exhibit a much larger region of low velocity adjacent to the endwalls that is not represented in the experimental data acquires near the shroud or along the suction surface of the passage. Between the two turbulence models, the streamwise velocity profiles are nearly identical. In terms of the secondary flow vectors, the SST result within the jet flow indicates a counterclockwise region of circulation occurring between 60% span and the shroud. This region is not present during the jet convection with the BSL-EARSM turbulence model. However, both models predict a narrow clockwise-oriented circulation region between the hub and 15% span during the convection of the jet through the throat.

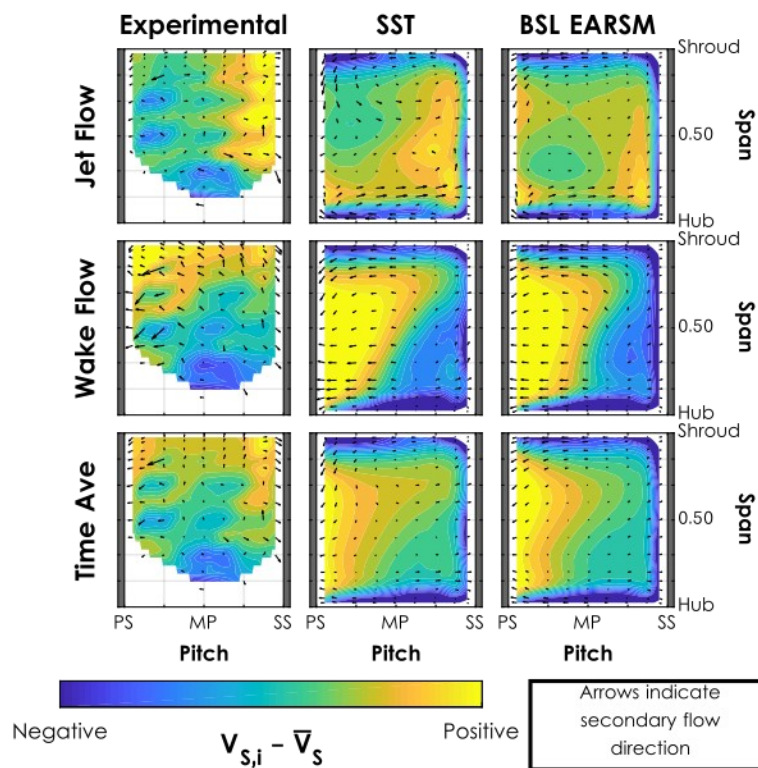


Figure 5.11: Streamwise velocity at the throat

As indicated by the vectors overlaid on Figure 5.11, the CFD results predict the development of secondary flow structures at the throat. The axial velocity data at the throat are presented in Figure 5.12. The results obtained with both turbulence models indicate a consistent region of axial velocity toward the hub in the shroud-PS corner of the passage. This region is present within both the jet and wake flows but is more pronounced within the jet flow. Within the jet flow, both numerical results also indicate a small region of axial velocity toward the shroud in the hub-PS corner of the passage. This region forms the left end of the narrow, clockwise oriented vortical motion present adjacent to the hub.

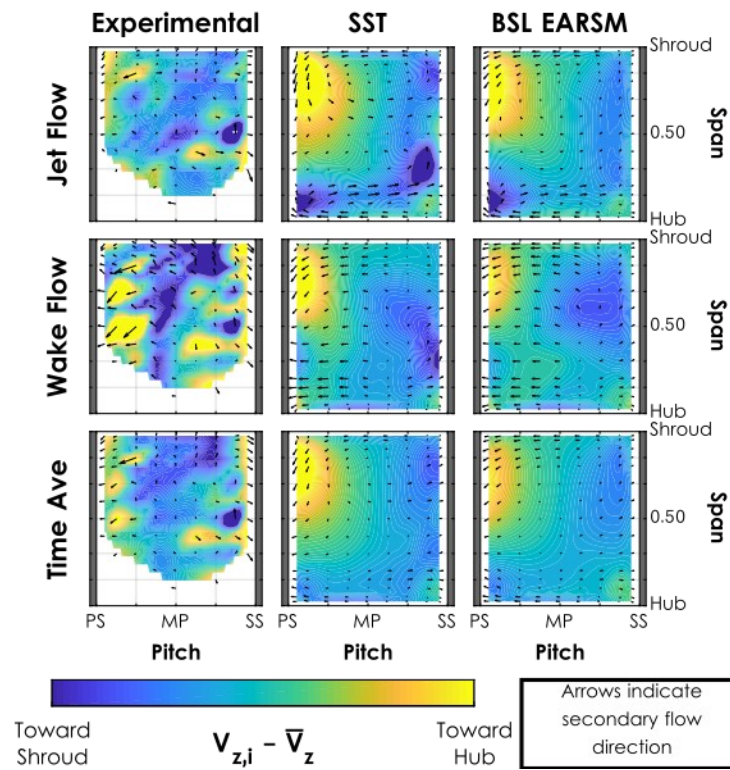


Figure 5.12: Axial velocity at the throat

Interesting patterns and discrepancies also arise in the turbulent kinetic energy data obtained at the throat. These data obtained at the throat adjacent to the pressure surface (Point 32) are presented in Figure 5.13. At this location, the comparison between the experimental and computational results is significantly different from what was observed further upstream. At 50% and 70% span, the results align well in terms of average values of  $k$ ; however, the computational results now exhibit *more* variation than the experimental data. Additionally, at 95% span, the computational

results now indicate higher  $k$  values. Comparison with upstream values indicates that this arises due to a reduction in the experimental  $k$  values and relatively little change in the values predicted by the simulations. The difference in spanwise gradient observed between the experimental and computational results at previous locations holds for these data as well. Comparing between the turbulence models, more differences are apparent between the predicted  $k$  values than were observed at upstream locations. The BSL-EARSM model predicts higher levels at 50% span and a profile that appears shifted temporally at 70% span.

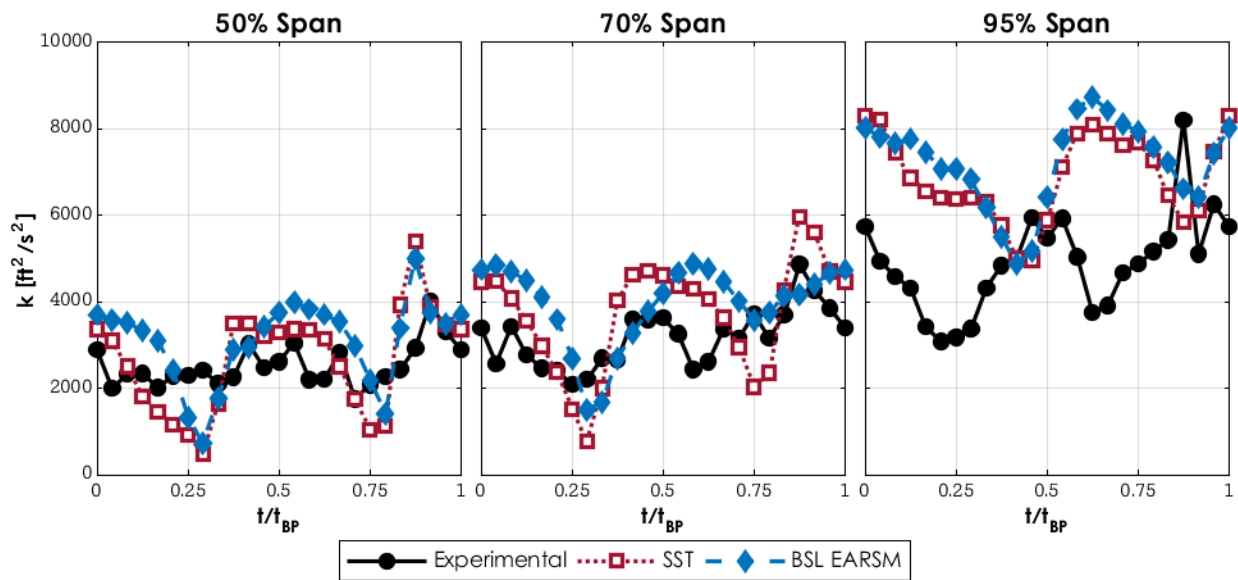


Figure 5.13: Unsteady turbulent kinetic energy,  $k$ , at the throat, pressure side (Point 32)

The corresponding data acquired at the throat at mid-passage (Point 34) are presented in Figure 5.14. Relative to the pressure side data, the  $k$  values at mid-passage measured experimentally are significantly higher: approximately double. Contrarily, both turbulence results predict nearly identical values at mid-passage and along the pressure side of the passage. Because of this, the mid-passage predictions are significantly lower than those observed experimentally.

Finally, the data at the throat adjacent to the suction surface (Point 30) are presented in Figure 5.15. Both turbulence models produce higher  $k$  predictions along the suction surface of the vane (relative to the pressure surface and mid-passage data) and, overall, close agreement with the experimental data. This change relative to other locations is primarily due to increased peak levels and a shorter time lag between the minimum and maximum values (i.e. a “sharper” peak). At 50% span the

numerical results are at slightly lower levels, especially between  $t/t_{BP} = 0.75$  and 1. However, the trend and the overall level matches remarkably well. The experimental data exhibit a larger peak in  $k$  near  $t/t_{BP} = 0.05$  at 70% span, but the levels and trends agree at both 70% and 95% span (with the exception of the temporal shift that is typical of the 95% span data). Together, these data across the passage at the throat indicate that the turbulence models are able to locally capture the correct values and trends in turbulent kinetic energy. However, there are discrepancies in the predicted cross-passage and streamwise gradients. The computational results indicate little change in the  $k$  values through the vaneless space and into the passage. The throat-SS data are the only data that indicate a significantly different trend and level—all of the other geometric locations interrogated thus far indicate consistent values, from the impeller trailing edge to the throat.

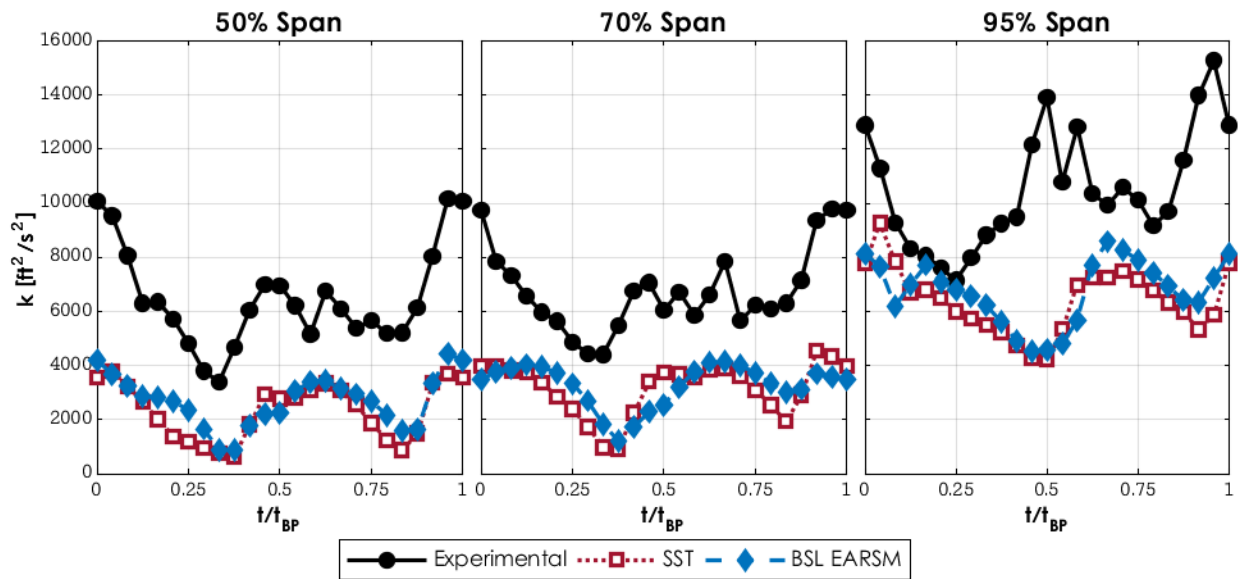


Figure 5.14: Unsteady turbulent kinetic energy,  $k$ , at the throat, mid-passage (Point 34)

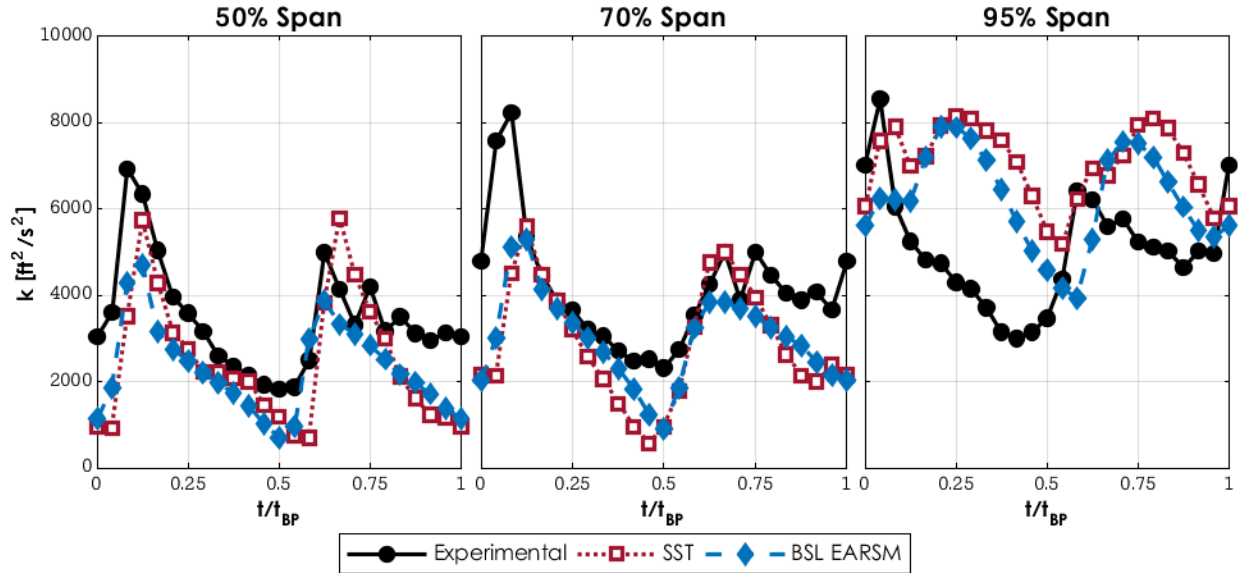


Figure 5.15: Unsteady turbulent kinetic energy,  $k$ , at the throat, suction side (Point 30)

Downstream from the throat, the flow profiles predicted in the computational models begin to deviate significantly from each other and from the experimental results. The streamwise velocity data 10% downstream of the throat (DSTM B plane) are presented in Figure 5.16. The results obtained with the SST turbulence model now indicate a region of flow separation in the shroud-PS corner of the passage. Near-zero values of the streamwise velocity are predicted that fall outside the range included in the color scale, resulting in the blank region present in the shroud-PS corner of the SST results in Figure 5.16. This separation region is present within the jet and wake flow and is also indicated in the time-averaged data. Its impact on the secondary flow structure is also apparent in an increased motion toward the hub surrounding the region of flow separation. The BSL-EARSIM turbulence model does not predict a similar region of flow separation. The velocity deficit regions adjacent to the endwalls have grown—both relative to the upstream data and the experimental data—but no separation or separation-induced-secondary-flows are observed. Instead, a pitchwise velocity toward the PS and a predominantly low-magnitude axial velocity are present across the entire passage at all time instances. Neither computational dataset resembles the primary or secondary flow field measured experimentally within the jet or wake flow or when time-averaged.

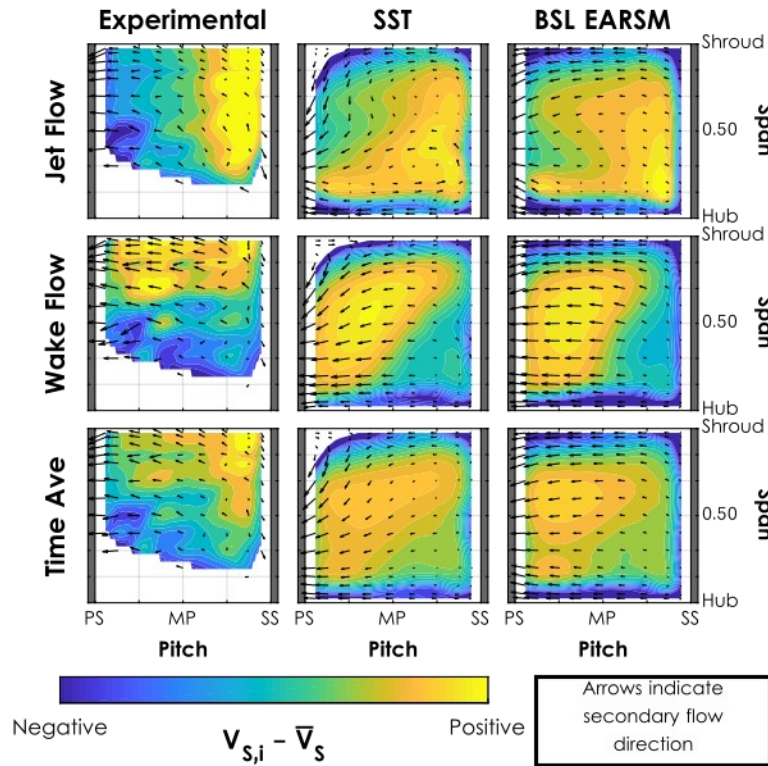


Figure 5.16: Streamwise velocity 10% downstream from the throat (DSTM B)

The flow profiles present at 10% downstream continue to grow spatially across the passage and the differences in the flow profiles dissipate slightly proceeding to 20% downstream (DSTM D). By 40% downstream, the computational and experimental results indicate that the unsteady fluctuations have largely dissipated. The streamwise velocity data at 40% downstream (DSTM G) are presented in Figure 5.17. The region of flow separation in the shroud-PS corner of the passage in the SST result has grown to extend from 60% to 97.5% span and from the pressure surface to approximately 10% pitch (close to mid-passage). This separation and the associated losses that develop lead to the diffuser exit total pressure profile that was observed in Figure 4.11C. The BSL-EARSIM data indicate a symmetric streamwise velocity profile with the core region centered in the passage. A gradual deficit in streamwise velocity is present extending approximately 15% of the span from the hub and shroud surfaces and approximately 10% of the pitch width from the pressure and suction surfaces. At this location, the deficit is approximately balanced along the pressure and suction side surfaces. However, the total pressure data (Figure 4.11E) indicate that the suction surface region grows to a greater degree further downstream. Neither computational

model reproduces the flow profile observed experimentally: high streamwise velocity adjacent to the shroud and low streamwise velocity in the hub-PS corner of the passage. The same applies to the secondary velocity fields. The axial velocity predicted in the computational results only arises as a response to the blockage predicted across the passage. This results in axial velocity toward the hub developing adjacent to the SST region of flow separation and near-zero axial velocity across the passage with the BSL-EARSM model.

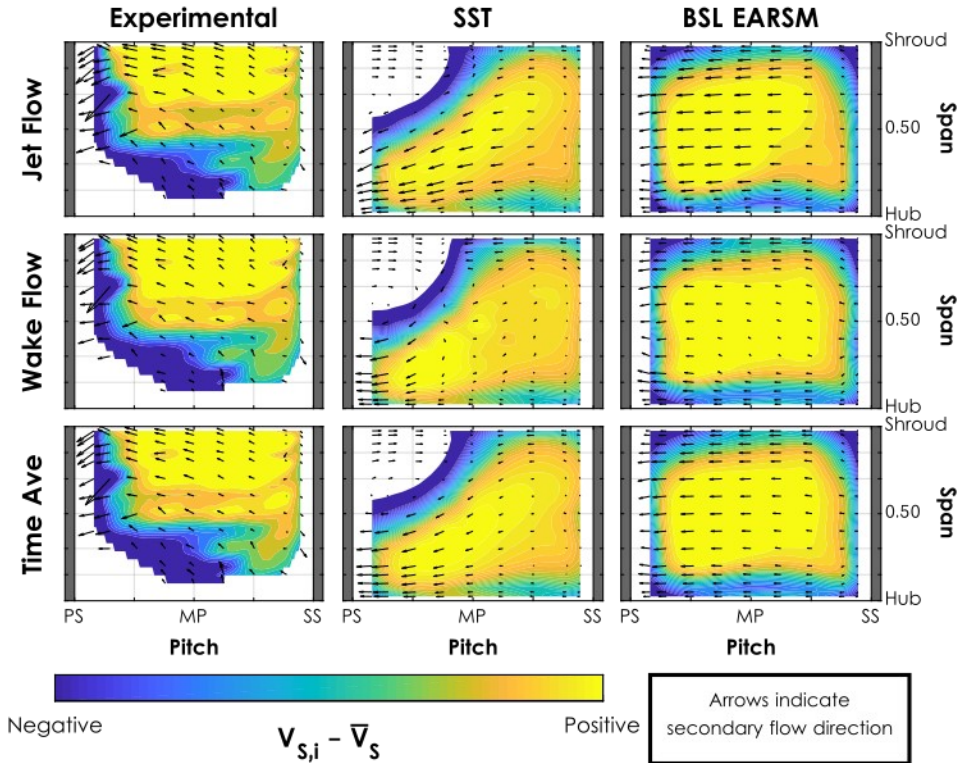


Figure 5.17: Streamwise velocity 40% downstream from the throat (DSTM G)

These differences are also clear in the streamwise propagation of the turbulent kinetic energy, Figure 5.18. The top, middle, and bottom rows present data at 37.5% pitch (near the pressure side of the passage), mid-passage, and at -37.5% pitch (near the suction surface), respectively. The columns refer to the streamwise locations detailed in Figure 5.1 and proceed downstream from left to right. The abscissa is the time-averaged turbulent kinetic energy,  $k$ , and the ordinate is the spanwise position. Experimental data are included alongside the numerical results where available. The exception to these details is the experimental data presented at the DSTM D (20%) plane.

These data were obtained at 25% and -25% pitch but are included here as turbulence data were not acquired closer to the vane surfaces. The numerical results at  $\pm 25\%$  pitch do not differ significantly from the data at  $\pm 37.5\%$  pitch, and this positional difference leads to no change in the relevant observations or discussion.

The data at the throat have been discussed previously. Near the pressure side (37.5% pitch, top row of Figure 5.18), the two turbulence models predict identical spanwise profiles in  $k$  at 5% downstream of the throat (DSTM A, second column of Figure 5.18). Local maximums are present at 95% and 5% span with a monotonic increase from 15% to 95% span. The same profile is present at mid-passage (0%, middle row of Figure 5.18) and near the suction side (-37.5% pitch, bottom row) at the same streamwise location. At 10% downstream (DSTM B, the third column of Figure 5.18) the near-pressure side profile begins to diverge with the SST turbulence model. A large increase in  $k$  between 85% and 97.5% span is present that corresponds to the region of flow separation in the shroud-PS corner of the passage indicated by the streamwise velocity data. The BSL-EARSM data do not indicate a similar increase in  $k$ . In fact, the BSL-EARSM data at all pitchwise positions develop in the streamwise direction with a consistent pattern: a broadening of the peak  $k$  regions adjacent to the endwalls (extending toward mid-span) and a slight increase across the rest of the span. The -37.5% pitch data indicate the largest streamwise increase in  $k$  and this is likely responsible for the increased total pressure deficit present adjacent to the suction surface of the passage indicated in Figure 4.11E. The experimental data available at mid-passage, 10% downstream indicate the  $k$  levels near mid-span are still higher than those predicted numerically. At 20% downstream (DSTM D, fourth column of Figure 5.18) the experimental data align well with the prediction using the BSL-EARSM turbulence model adjacent to the pressure and suction surfaces. Within the SST results, the peak  $k$  location shifts toward mid-span and to higher magnitudes in the streamwise direction. This corresponds to the growth of the region of flow separation in the spanwise direction and across the passage, as it is also observed at mid-passage beginning 40% downstream (DSTM G, fifth column of Figure 5.18).

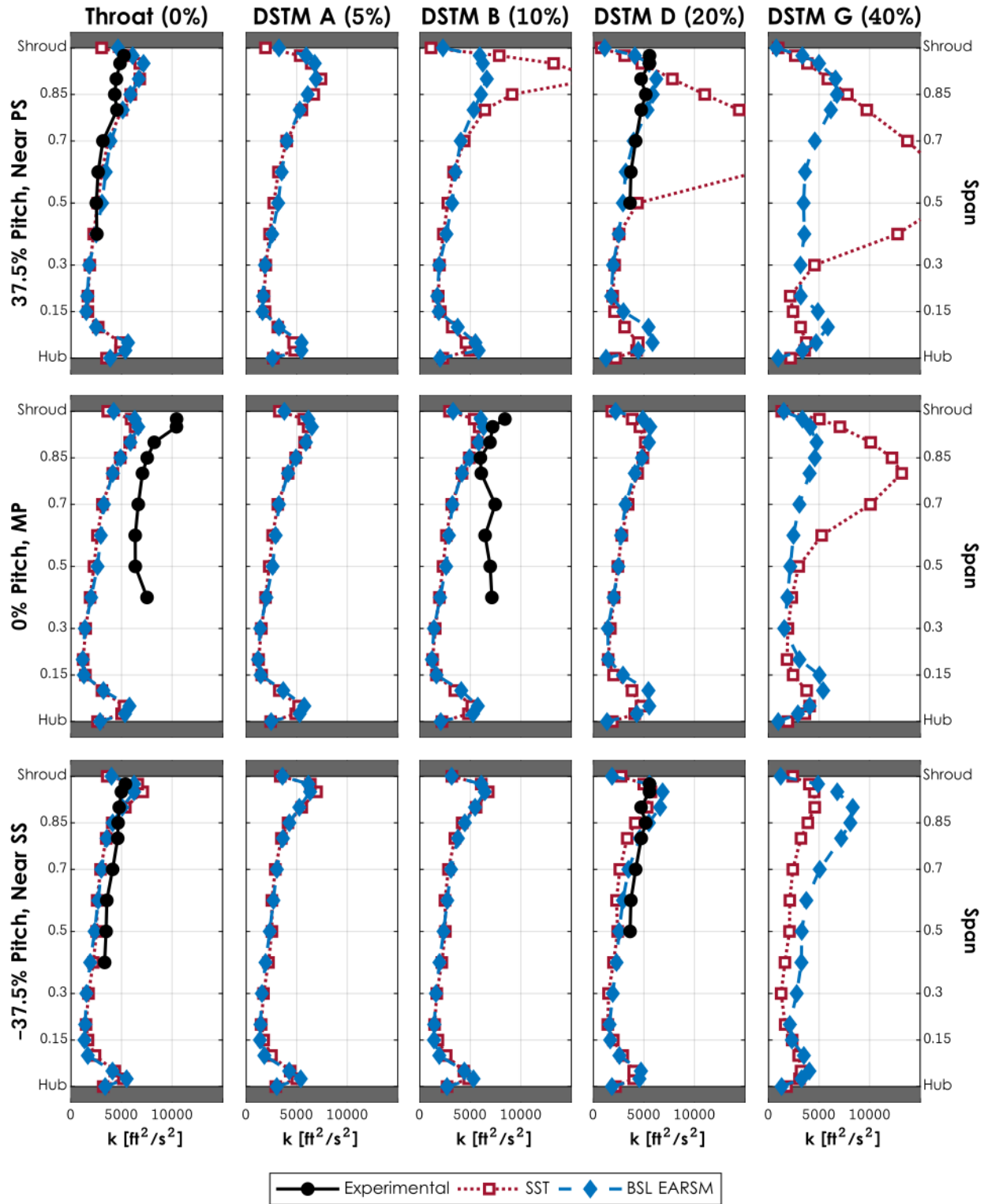


Figure 5.18: Time-averaged turbulent kinetic energy progression downstream of the throat

Overall, valuable insights arise from these observations and comparisons of the unsteady flow fields measured experimentally and predicted numerically using the SST and BSL-EARSM turbulence models. Within the vaneless space, both turbulence models accurately capture the general trend in the observed radial velocity field. However, the experimental data indicate larger axial velocities than are predicted in either numerical result. In terms of the turbulent kinetic energy, the experimental results indicate higher  $k$  values at a radius ratio of 1.05 followed by a slight decay from a radius ratio of 1.05 to 1.08 (the vane leading edge). Through the entire vaneless space, both turbulence models predict consistent  $k$  values with little change between the impeller trailing edge and the vane leading edge. Additionally, the increased axial velocities observed experimentally result in greater spanwise mixing between the shroud-adjacent flow and the freestream. This results in different incidence profiles developing at the vane leading edge, especially adjacent to the shroud.

Within the passage, the difference in incidence and the decreased spanwise mixing above 85% span result in different flow profiles developing. Neither computational model predicts significant secondary flow patterns, until the development of a region of flow separation in the shroud-PS corner of the passage 10% downstream of the throat with the SST turbulence model. This separation is also indicated in the turbulent kinetic energy data and the total pressure profiles present at the diffuser exit. This represents a significant departure from the experimentally observed flow field and leads to the conclusion that the BSL-EARSM turbulence model more accurately reproduces the unsteady flow field observed experimentally. With that being said, the BSL-EARSM has several deficiencies. It does not accurately predict the extent of flow separation in the hub-PS corner of the passage that was observed experimentally. Additionally, the velocity deficit regions due to boundary layer development along the passage boundaries are larger than observed experimentally, due to the reduced axial velocities promoting momentum transport between the boundary layer and the freestream. In general, both turbulence models predict little production or dissipation of turbulence through the vaneless space and are too diffusive of unsteady fluctuations in the turbulent kinetic energy. Additionally, the computational models underpredict axial velocity levels. The concomitant increased spanwise mixing present in the experimental has an important impact on the flow development in the streamwise direction that is missed by both turbulent models.

## 6. SUMMARY AND CONCLUSIONS

The purpose of this study was to conduct a detailed exposition of the flow field within a vaned diffuser for aeroengine application to gain a deeper understanding of the flow development and the corresponding predictive capability of computational models. The three components of the unsteady velocity vector field were studied experimentally, and these experimental data were complemented by steady and unsteady CFD results. While other studies have suggested the relative unimportance of unsteady effects, these data support a different conclusion. As designs trend toward higher pressure ratios, smaller radial gaps between the impeller and diffuser, and other novel design features, these data provide insight into the flow structure and will allow the further validation and improvement of modern computational tools. In Section 1.8, specific objectives were listed that this study sought to address. The conclusions regarding these specific objectives are summarized in the following paragraphs.

### 6.1 Observations Regarding the Research Objectives

First, the details and rate of mixing between the jet and wake through the diffuser have been directly measured. The impeller exit profile indicates a significant deficit region adjacent to the hub and shroud surfaces—not focused in the shroud-suction side corner of the passage or just along the shroud, as has been observed elsewhere. Additionally, the wake that developed along the splitter blade contained more significant deviation from the mean flow than that along the full blade. The jet flow that developed adjacent to the splitter blade wake (i.e. within the same impeller passage) also showed larger deviation from the mean than the jet adjacent to the full blade wake. Through the vaneless space, the unsteady fluctuations due to the jet and wake flows decreased only slightly. This indicated that little dissipation in the jet and wake flows occurred upstream of the passage. Quantitatively, fluctuation levels decreased from 60% of the mean radial velocity at a radius ratio of 1.0125 to 44% at the vane leading edge radius (a radius ratio of 1.08) and to 27% at the exit of the semi-vaneless space. Although this does reflect a reduction of unsteady fluctuations by half, the unsteadiness levels are still large relative to the time-averaged values at the inlet to the diffuser passage. These flow variations associated with the jet and wake propagate

through to approximately 40% downstream of the throat before agglomeration occurs in both the primary and secondary flow fields.

Second, the three-dimensional development of secondary flows was observed through the inlet region of the diffuser passage. Large axial velocities were present in the experimental data throughout the vaneless and semi-vaneless space. This had a large impact on the convective mixing between the shroud-adjacent flow and the freestream. Comparison with the unsteady computations, which predict significantly lower axial velocities, suggested the importance of this spanwise mixing process in the propagation of flow through the diffuser passage in terms of the incidence field and the turbulent kinetic energy profiles.

Third, regarding the location and temporal nature of flow separation within the diffuser passage: these measurements indicate a region of flow separation along the pressure surface of the vane, adjacent to the hub. This region was indicated in the velocity data as well as steady total pressure measurements at the diffuser exit. While this region appeared to be stable in time, its location and extent were heavily influenced by the unsteady secondary and primary flow fields present through the diffuser passage.

Fourth, the extent of unsteady fluctuations in the streamwise direction was illustrated. As mentioned previously, the unsteady fluctuations due to the jet and wake flow persisted through 40% downstream of the throat. Most of the dissipation in the unsteadiness that did occur before the throat, occurred in the upstream portion of the semi-vaneless space, also known as the “zone of rapid adjustment,” as the flow adjusted to the presence of the vanes. This dissipation likely occurred due to the potential field of the diffuser, which acted to turn the flow into the passage. This conclusion was also supported by the increased dissipation in the turbulent kinetic energy that occurred through this region along the pressure surface of the vane relative to the suction surface of the vane. This flow passed through the strongest potential field due to the short radial extent from the leading edge to the throat that existed along the pressure surface. Additionally, the unsteady fluctuations dissipated and formed a stable, coherent flow structure in terms of the secondary flow velocities prior to the streamwise velocity. This likely occurred due to the role of the axial and pitchwise velocity components in impeding mixing between the jet and wake flow within the diffuser passage.

Fifth, the unsteady and spanwise variations in the incidence at the vane leading edge were observed experimentally. These data indicated a significant variation in the incidence field at the leading edge both circumferentially and temporally. The wake flow impacted the vane leading edge with a rise in positive incidence across the majority of the span. This positive incidence decreased to negative values toward the shroud. Qualitatively, this incidence variation caused a periodic diversion of incoming flow into the adjacent passage which induced secondary flows, produced streamwise vorticity, and influenced the downstream flow development.

Sixth, the relationship and interconnectedness of the previous aspects of the flow were thoroughly discussed illustrating that these five specific flow features are intimately connected. The mixing of the jet and wake through the vaneless and semi-vaneless space influenced the development of secondary flows in that region. Those secondary flows—both in a time-averaged and an unsteady sense—influenced the nature and location of flow separation through the passage. This region of flow separation influenced the development of secondary flows through the rest of the passage which led to the unsteady fluctuations persisting further in the streamwise direction. All of these topics combined in the understanding of the unsteady formation of the passage vortex that develops due to the lack of mixing between the jet and wake, the incidence field, the secondary velocities, and the persistence of unsteadiness. These observations illustrate the innate difficulty in studying and modelling individual aspects of the flow through the centrifugal compressor diffuser. Many drivers of the flow development are deeply interconnected and no driver, in isolation, will produce the same impact on the flow development that it does as a part of the full system.

Beyond the six specific aspects of the flow that were discussed in detail, this work also presented the first direct measurements of the six components of the Reynolds stress tensor within the diffuser of a high-speed centrifugal compressor. These data were obtained at twelve positions between the impeller trailing edge and 20% downstream of the diffuser throat from 40% to 97.5% span. These data indicated that the turbulence intensity increases through the vaneless space and is not simply generated in the impeller and then convected through the diffuser. These data will provide a key dataset for the validation and further development of turbulence modelling and other CFD capabilities specifically for applications in centrifugal compressors.

In addition to the experimental results, CFD results were obtained for a wide variety of turbulence closure models and with various combinations of modelling features. A systematic analysis was conducted to develop a “best practice” recommendation for simulation methodology of similar designs. This analysis illustrated the importance of accurately including physical drivers of flow development such as fillets, surface roughness, and non-adiabatic walls. Picking and choosing which features to include in order to produce the best prediction of overall performance metrics was not advised. It is recommended to always step toward reality in terms of including physics that are present in the “real-world” case. This procedure will result in a computational model that is more robust and predictive in various operating conditions and with novel designs. Regarding turbulence closure models, the SST and the BSL-EARSM models indicated the best steady performance in terms of most accurately predicting the profile of the diffuser exit total pressure that was observed experimentally. In addition to these recommendations for “best practice” modelling of a centrifugal compressor, observations were made on four specific aspects of the numerical flow fields, as outlined in Section 1.8.

First, the experimental and computational models produced similar estimates of the dissipation of the jet and wake through the vaneless space and into the diffuser passage. Both indicated significant fluctuations in the primary and secondary flow fields present through the diffuser throat and to approximately 40% downstream. The initial magnitude of the fluctuations was larger in the experimental data and the impact on the flow development was, therefore, more significant experimentally than was predicted computationally.

Second, the turbulent kinetic energy at several key locations through the diffuser passage was compared between the computational and experimental results. Both turbulence models implemented in the unsteady simulations accurately predicted the levels of turbulent kinetic energy at the impeller trailing edge, although data were only obtained adjacent to the shroud (above 85% span). Through the vaneless space and into the diffuser passage, the computational results predicted little change in the turbulent kinetic energy in the streamwise direction. Additionally, the higher axial velocities observed experimentally produced increased spanwise mixing and acted to decrease the gradient in turbulent kinetic energy developed toward the shroud. Both models underpredicted the turbulent kinetic energy level at mid-passage within the diffuser passage.

However, the BSL-EARSM model accurately reproduced the spanwise profiles in turbulent kinetic energy adjacent to the pressure and suction surfaces at the throat and 20% downstream of the throat.

Third, regarding the prediction of flow separation within the passage, neither model accurately reproduced the significant flow separation observed experimentally in the hub-pressure-side corner of the passage. The SST model erroneously predicted a significant separation developing in the shroud-pressure-side corner of the passage, as indicated by the total pressure contours at the diffuser exit and the streamwise progression of turbulent kinetic energy and streamwise velocity. The BSL-EARSM model predicted uniform velocity deficit regions around the perimeter of the passage and a streamwise velocity core region that was centered in the passage.

Fourth, the observations of the unsteady flow field and the persistence of unsteadiness in the streamwise direction illustrated the important information that is lost across a mixing-plane interface. The unsteady simulations did not perfectly predict the flow development through the diffuser. However, these errors appear to be related to the accurate prediction of the axial velocity component and the streamwise production and dissipation of turbulence through the vaneless and semi-vaneless space. The importance and prevalence of unsteady effects through the flow field indicated that a mixing-plane approach will never be able to accurately reproduce all of the significant drivers of diffuser flow development, especially as designs are pushed toward smaller radial gaps and higher pressure ratios. Additionally, the frozen rotor approach was observed to not accurately produce a realistic characterization of a true “snapshot” of the flow field. The impact of unsteadiness on the flow field was observed to stem not only from the diffuser inlet flow condition, but also from the propagation of those unsteady variations through the passage.

Furthermore, the unsteady computations identified specific aspects of the flow development through the diffuser that need additional focus to develop more accurate computational tools for centrifugal compressor design. First, the axial velocity present at the impeller exit and through the diffuser was much larger experimentally than predicted with either turbulence model. The spanwise mixing and streamwise vorticity developed by this large axial velocity had a significant impact on the entire flow field that was neglected in the computational results. Additionally, the streamwise progression of turbulence indicated different trends of turbulence production and

dissipation between the experimental and computational results through the vaneless space, the semi-vaneless space, and in approaching the throat.

## **6.2 Recommendations for Future Study**

Several topics of future study have been mentioned throughout this work. The clearest continuation of this study would be to extend the measurements into the impeller. The resolution of the velocity development within the impeller would aid in determining the origin of the increased axial velocity observed experimentally, the more prevalent splitter blade wake, and the development of the consistent hub-to-shroud velocity deficit associated with the wake. The basic infrastructure has been acquired for this proposed study; however, significant work is needed to address beam misalignment and measurement errors induced by the window curvature. The acquisition of unsteady pressure levels would also provide a good complement to the velocity data obtained herein. Longer term, the acquisition of the static temperature field through the application of thermographic phosphor techniques would provide another dimension to the characterization of the flow field. Another extension would be to acquire a similar dataset at off-design conditions. Finally, acquisition of data closer to the hub wall could be attempted through the replacement of the hub surface with absorption glass to further reduce reflection levels.

Computationally, additional steps could be taken to model more aspects of the experimental flow field. Modelling the backface cavity would allow the determination of the impact of backface bleed flow and, with a conjugate heat transfer analysis, hub-side heat transfer on flow development. The inclusion of rakes (especially the diffuser exit rakes), the collector, and real gas effects would also yield interesting conclusions and increased model fidelity. Finally, experimental work could be leveraged to investigate the nature of the impact of hub-side fillets on flow separation along the suction surface of the vane. An alternate configuration of the experimental compressor allows the installation of additively manufactured diffusers. This technology could be used to install a diffuser without fillets and determine if the increased separation predicted with the SST turbulence model without fillets is representative of true flow physics or is a relic of numerical issues in predicting flow in a perfectly sharp corner.

## REFERENCES

- [1] W. J. Gooding, J. C. Fabian, and N. L. Key, “Numerical Analysis of Unsteady Vaned Diffuser Flow in a Centrifugal Compressor,” in *Proceedings of the 27th ISABE Conference*, 2017.
- [2] N. A. Cumpsty, *Compressor Aerodynamics*. Krieger Pub, 2004.
- [3] R. C. Pampreen, “Small Turbomachinery Compressor and Fan Aerodynamics,” *J. Eng. Power*, 1973, doi: 10.1115/1.3445730.
- [4] D. Japikse, “Turbomachinery Performance Modeling,” in *SAE World Congress*, 2009, doi: 10.4271/2009-01-0307.
- [5] D. Japikse, *Centrifugal Compressor Design and Performance*. Concepts ETI, 1996.
- [6] B. Nichelson, “Early Jet Engines and the Transition From Centrifugal to Axial Compressors: A Case Study in Technology Change,” University of Minnesota, 1988.
- [7] D. P. Kenny, “The History and Future of the Centrifugal Compressor in Aviation Gas Turbines,” 1984.
- [8] Grundfos, “Facts About Pumps and Sustainability.” [Online]. Available: <https://www.grundfos.com/water-energy/meet-the-water-and-energy-challenge-now/facts-about-pumps-and-sustainability.html>. [Accessed: 18-Dec-2019].
- [9] R. C. Pampreen, *Compressor Surge and Stall*, 1st ed. Concepts ETI, 1993.
- [10] H. Krain, “Swirling Impeller Flow,” *J. Turbomach.*, vol. 110, no. 1, pp. 122–128, 1988, doi: 10.1115/1.3262157.
- [11] J. Moore, “A Wake and an Eddy in a Rotating, Radial-Flow Passage Part 1: Experimental Observations,” *J. Eng. Power*, 1973.
- [12] R. C. Dean and Y. Senoo, “Rotating Wakes in Vaneless Diffusers,” *J. Basic Eng.*, 1960.
- [13] K. Fischer, “Investigation of Flow in a Centrifugal Pump,” NACA, TM 1089, 1931.
- [14] J. Moore, “A Wake and an Eddy in a Rotating, Radial-Flow Passage Part 2: Flow Model,” *J. Eng. Power*, 1973.
- [15] D. Eckardt, “Detailed Flow Investigations Within a High-Speed Centrifugal Compressor Impeller,” *J. Fluids Eng.*, vol. 98, no. 3, pp. 390–399, 1976, doi: 10.1115/1.3448334.
- [16] D. Eckardt, “Investigation of the Jet-Wake Flow of a Highly-Loaded Centrifugal Compressor Impeller,” NASA, TM-75232, 1978.

- [17] M. el Hajem, R. Morel, J. Champagne, and F. Spettel, “Detailed Measurements of the Internal Flow of a Backswept Centrifugal Impeller,” in *9th International Symposium on Applications of Laser Techniques to Fluid Mechanics*, 1998.
- [18] A. Marsan, I. Trébinjac, S. Coste, and G. Leroy, “Influence of Unsteadiness on the Control of a Hub-Corner Separation Within a Radial Vaned Diffuser,” *J. Turbomach.*, vol. 137, 2014, doi: 10.1115/1.4028244.
- [19] H. Krain, “A Study on Centrifugal Impeller and Diffuser Flow,” *J. Eng. Power*, vol. 103, no. 4, pp. 688–697, 1981, doi: 10.1115/1.3230791.
- [20] D. Stahlecker, E. Casartelli, and G. Gyarmathy, “Secondary Flow Field Measurements with a LDV in the Vaned Diffuser of a High-Subsonic Centrifugal Compressor,” in *9th International Symposium on Applications of Laser Techniques to Fluid Mechanics*, 1998, pp. 1–12.
- [21] D. Stahlecker and G. Gyarmathy, “Investigations of Turbulent Flow in a Centrifugal Compressor Vaned Diffuser by 3-Component Laser Velocimetry,” in *International Gas Turbine & Aeroengine Congress & Exhibition*, 1998, pp. 1–14.
- [22] G. J. Skoch, P. Prahst, M. Wernet, J. R. Wood, and A. Strazisar, “Laser Anemometer Measurements of the Flow Field in a 4:1 Pressure Ratio Centrifugal Impeller,” NASA, TM-107541, 1997.
- [23] J. Fagan and S. Fleeter, “L2F and LDV Velocity Measurement and Analysis of the 3D Flow Field in a Centrifugal Compressor,” in *Joint Propulsion Conference*, 1989, pp. 1–9, doi: 10.2514/6.1989-2572.
- [24] A. Cattanei, D. Ottolia, M. Ubaldi, and P. Zunino, “Unsteady Boundary Layers on the Diffuser Blades of a Centrifugal Stage Due to Rotor Blade Wake Interaction,” in *9th International Symposium on Applications of Laser Techniques to Fluid Mechanics*, 1998.
- [25] D. Adler and Y. Levy, “Laser-Doppler Investigation of the Flow Inside a Backswept, Closed, Centrifugal Impeller,” *J. Mech. Eng. Sci.*, vol. 21, no. 1, pp. 1–6, 1979.
- [26] H. Schlichting, *Boundary-Layer Theory*, 6th ed. New York: McGraw-Hill, 1968.
- [27] J. Johnston, “Effect of System Rotation on Turbulence Structure: A Review Relevant to Turbomachinery Flows,” *Int. J. Rotating Mach.*, vol. 4, no. 2, 1998, doi: 10.1115/S1023621X98000098.

- [28] H. Nippert, "Über den Stromungsverlust in Gekrummten Kanälen (On the Flow Losses in Bends)," *Forschungsarbeiten Auf Dem Gebiete Des Ingenieurwesens*, 1929.
- [29] A. Anderson, "Fluid Flow Diversion: A Summary and Bibliography of Literature," 1947.
- [30] M. Clauser and F. Clauser, "The Effect of Curvature on the Transition from Laminar to Turbulent Boundary Layer," NACA, TN: 613, 1937.
- [31] R. C. Dean, D. Wright, and P. Runstadler, "Fluid Mechanics Analysis of High-Pressure-Ratio Centrifugal Compressor Data," USAAVLABS, 1970.
- [32] Y. Senoo and M. Ishida, "Deterioration of Compressor Performance Due to Tip Clearance of Centrifugal Impellers," *J. Turbomach.*, 1987, doi: 10.1299/kikaib.52.386.
- [33] J. Moore, J. G. Moore, and P. H. Timmis, "Performance Evaluation of Centrifugal Compressor Impellers Using Three-Dimensional Viscous Flow Calculations," *J. Gas Turbines Power*, vol. 106, 1984.
- [34] R. Kunte, P. Schwarz, B. Wilkosz, P. Jeschke, and C. Smythe, "Experimental and Numerical Investigation of Tip Clearance and Bleed Effects in a Centrifugal Compressor Stage With Pipe Diffuser," *J. Turbomach.*, vol. 135, no. 1, 2013, doi: 10.1115/1.4006318.
- [35] C. Hah and H. Krain, "Analysis of Transonic Flow Fields inside a High Pressure Ratio Centrifugal Compressor at Design and Off Design Conditions," in *Proc. of ASME Turbo Expo*, 1999.
- [36] M. Marconcini, F. Rubecchini, A. Arnone, and S. Ibaraki, "Numerical Investigation of a Transonic Centrifugal Compressor," *J. Turbomach.*, vol. 130, no. 1, 2008, doi: 10.1115/1.2752186.
- [37] R. C. Dean, "On the Unresolved Fluid Dynamics of the Centrifugal Compressor," in *Advanced Centrifugal Compressors*, New York: ASME Gas Turbine Division, 1971.
- [38] C. Rodgers, "Impeller Stalling as Influenced by Diffusion Limitations," *J. Fluids Eng.*, 1977, doi: 10.1115/1.3448569.
- [39] D. P. Kenny, "Novel Low-Cost Diffuser for High-Performance Centrifugal Compressors," *J. Eng. Power*, 1969.
- [40] D. P. Kenny, "Supersonic Radial Diffusers," in *AGARD Lecture Series No. 39: Advanced Compressors*, 1970.
- [41] J. P. Johnston and R. C. Dean, "Losses in Vaneless Diffusers of Centrifugal Compressors and Pumps," *J. Eng. Power*, 1966.

- [42] Y. Senoo and Y. Kinoshita, "Influence of Inlet Flow Conditions and Geometries of Centrifugal Vaneless Diffusers on Critical Flow Angle for Reverse Flow," *J. Fluids Eng.*, 1977, doi: 10.1115/1.3448577.
- [43] Y. Yoshinaga, I. Gyobu, H. Mishina, F. Koseki, and H. Nishida, "Aerodynamic Performance of a Centrifugal Compressor with Vaned Diffuser," *J. Fluids Eng.*, vol. 102, 1980, doi: 10.1115/1.3240730.
- [44] M. Inoue and N. A. Cumpsty, "Experimental Study of Centrifugal Impeller Discharge Flow in Vaneless and Vaned Diffusers," *J. Eng. Gas Turbines Power*, vol. 106, 1984, doi: 10.1115/1.3239588.
- [45] N. Bulot *et al.*, "Experimental and Numerical Investigation of the Flow Field in a High-Pressure Centrifugal Compressor Impeller Near Surge," *J. Power Energy*, vol. 223, 2009, doi: 10.1243/09576509JPE817.
- [46] D. P. Kenny, "A Comparison of the Predicted and Measured Performance of High Pressure Ratio Centrifugal Compressor Diffusers," in *Gas Turbine and Fluids Engineering Conference*, 1972.
- [47] C. Rodgers, "The Performance of Centrifugal Compressor Channel Diffusers," in *Gas Turbine Conference*, 1982, doi: 10.1115/82-GT-10.
- [48] R. C. Dean, "Fluid Dynamic Design of Advanced Centrifugal Compressors." Von Karman Institute, Brussels, Belgium, 1974.
- [49] R. L. Elder and M. Gill, "A Discussion of the Factors Affecting Surge in Centrifugal Compressors," *J. Eng. Gas Turbines Power*, vol. 107, no. 2, 1985, doi: 10.1115/1.3239759.
- [50] P. M. Came and M. V. Herbert, "Design and Experimental Performance of Some High Pressure Ratio Centrifugal Compressors," in *AGARD Centrifugal Compressors, Flow Phenomena, and Performance*, 1980.
- [51] F. Kano, N. Tazawa, and Y. Fukao, "Study of Flow Distribution and Aerodynamic Performance of Centrifugal Compressor," Technical Paper 830328, 1982.
- [52] A. Jaatinen, "Performance Improvement of Centrifugal Compressor Stage with Pinched Geometry or Vaned Diffuser," Lappeenranta University of Technology, 2009.
- [53] E. Morishita, "Centrifugal Compressor Diffusers," University of Cambridge, 1982.

- [54] W. J. Gooding, J. C. Fabian, and N. L. Key, “LDV Characterization of Unsteady Vaned Diffuser Flow in a Centrifugal Compressor,” in *Proc. of ASME Turbo Expo*, 2019, pp. 1–10.
- [55] V. Pothuri, R. Govindaraju, V. Ganapathiraju, N. Palati, and S. Badisa, “CFD Analysis of Effect of Diffuser Vane Setting Angle and Shape on the Performance of a Centrifugal Compressor Stage,” in *Proc. ASME Gas Turbine India Conference*, 2015.
- [56] T. Reddy, G. Murty, P. Mukkavilli, and D. Reddy, “Effect of the Setting Angle of a Low-Solidity Vaned Diffuser on the Performance of a Centrifugal Compressor Stage,” *J. Power Energy*, vol. 218, 2004, doi: 10.1115/GTINDIA2015-1369.
- [57] A. Marsan, I. Trébinjac, S. Coste, and G. Leroy, “Temporal Behaviour of a Corner Separation in a Radial Vaned Diffuser of a Centrifugal Compressor Operating Near Surge,” *J. Therm. Sci.*, vol. 22, no. 6, 2013, doi: 10.1007/s11630-013-0662-6.
- [58] K. Ziegler, H. Gallus, and R. Niehuis, “A Study on Impeller-Diffuser Interaction: Part II - Detailed Flow Analysis,” in *Proc. of ASME Turbo Expo*, 2002.
- [59] S. Baghdadi and A. T. McDonald, “Performance of Three Vaned Radial Diffusers With Swirling Transonic Flow,” *J. Fluids Eng.*, 1975, doi: 10.1115/1.3447238.
- [60] S. Baghdadi, “The Effect of Rotor Blade Wakes on Centrifugal Compressor Diffuser Performance—A Comparative Experiment,” *J. Fluids Eng.*, 1977, doi: 10.1115/1.3448548.
- [61] M. Peeters and M. Sleiman, “A Numerical Investigation of the Unsteady Flow in Centrifugal Stages,” in *Proc. of ASME Turbo Expo*, 2000.
- [62] C. J. Robinson, M. Casey, B. Hutchinson, and R. Steed, “Impeller-Diffuser Interaction in Centrifugal Compressors,” in *Proc. of ASME Turbo Expo*, 2012.
- [63] Y. Bousquet, X. Carbonneau, and I. Trébinjac, “Assessment of Steady and Unsteady Model Predictions for a Subsonic Centrifugal Compressor Stage,” in *Proc. of ASME Turbo Expo*, 2012.
- [64] F. Justen, K. U. Ziegler, and H. E. Gallus, “Experimental Investigations of Unsteady Flow Phenomena in a Centrifugal Compressor Vaned Diffuser of Variable Geometry,” in *International Gas Turbine & Aeroengine Congress & Exhibition*, 1998.
- [65] J. Bourgeois, R. Martinuzzi, E. Savory, C. Zhang, and D. Roberts, “Experimental and Numerical Investigation of an Aero-Engine Centrifugal Compressor,” in *ASME Turbo Expo*, 2009, pp. 1–10, doi: 10.1115/GT2009-59808.

- [66] R. Gao, Z. S. Spakovszky, D. Rusch, and R. Hunziker, “Area-Schedule Based Design of High Pressure Recovery Radia,” in *Proc. of ASME Turbo Expo*, 2016.
- [67] ASME, “PTC 22-2005: Gas Turbines,” 2005.
- [68] ASME, “PTC 19.2-2010: Pressure Measurement Instruments and Apparatus Supplement,” 2010.
- [69] R. Abernethy and J. Thompson, “Handbook Uncertainty in Gas Turbine Measurements,” 1973.
- [70] D. Japikse, *Advanced Experimental Techniques in Turbomachinery*. Concepts ETI, 1986.
- [71] D. Eckardt, “Advanced Experimental Techniques for Turbomachinery Development,” in *Advanced Experimental Techniques in Turbomachinery*, D. Japikse, Ed. Norwich, Vermont: Concepts ETI, 1986, pp. 1–52.
- [72] R. Rayle, “An Investigation of the Influence of Orifice Geometry on Static Pressure Measurements,” Massachusetts Institute of Technology, 1949.
- [73] R. Moffat, “Thermocouple Theory and Practice,” in *Advanced Experimental Techniques in Turbomachinery*, D. Japikse, Ed. Norwich, Vermont: Concepts ETI, 1986.
- [74] W. Alwang, “State-of-the-Art Gas Turbine Measurement Techniques,” in *Advanced Experimental Techniques in Turbomachinery*, D. Japikse, Ed. Norwich, Vermont: Concepts ETI, 1986.
- [75] M. Lucia, C. Mengoni, and P. Boncinelli, “Synchronized LDV Measurement in Centrifugal Impeller: Seeding Insemination Set Up and CFD Comparison,” in *ASME Turbo Expo*, 2000, pp. 1–7.
- [76] W. Heisenberg, “Über den Anschaulichen Inhalt der Quantentheoretischen Kinematik und Mechanik (On the descriptive content of quantum kinematics and mechanics),” *Zeitschrift für Phys.*, vol. 43, no. 3–4, Mar. 1927, doi: 10.1007/BF01397280.
- [77] A. Steiner, “Techniques for Blade Tip Clearance Measurements with Capacitive Probes,” *Meas. Sci. Technol.*, vol. 11, no. 7, 2000, doi: 10.1088/0957-0233/11/7/303.
- [78] C. Abram, B. Fond, A. Heyes, and F. Beyrau, “High-speed Planar Thermometry and Velocimetry Using Thermographic Phosphor Particles,” *Appl. Phys. B Lasers Opt.*, vol. 111, 2013, doi: 10.1007/s00340-013-5411-8.
- [79] M. Raffel, C. Willert, F. Scarano, C. Kähler, S. Wereley, and J. Kompenhans, *Particle Image Velocimetry: a Practical Guide*. Springer, 1998.

- [80] M. Wernet, "Digital PIV Measurements in the Diffuser of a High Speed Centrifugal Compressor," *AIAA J.*, 1998, doi: 10.2514/6.1998-2777.
- [81] M. P. Wernet, "A Flow Field Investigation in the Diffuser of a High-Speed Centrifugal Compressor Using Digital Particle Imaging Velocimetry," *Meas. Sci. Technol.*, vol. 11, 2000, doi: 10.1088/0957-0233/11/7/316.
- [82] R. Schodl, W. Förster, G. Karpinsky, H. Krain, and I. Röhle, "3-Component-Doppler-Laser-Two-Focus Velocimetry Applied to a Transonic Centrifugal Compressor," in *10th International Symp. on Application of Laser Techniques to Fluid Mechanics*, 2002.
- [83] H. Z. Cummins, N. Knable, and Y. Yeh, "Observation of Diffusion Broadening of Rayleigh Scattered Light," *Phys. Rev. Lett.*, vol. 12, no. 6, 1964, doi: 10.1103/PhysRevLett.12.150.
- [84] F. Durst, A. Melling, and J. Whitelaw, *Principles and Practice of Laser-Doppler anemometry*. New York: Academic Press, 1976.
- [85] K. Jensen, "Flow Measurements," *J. Brazilian Soc. Mech. Sci. Eng.*, vol. 26, no. 4, pp. 400–419, 2004, doi: 10.1590/S1678-58782004000400006.
- [86] H. Albrecht, M. Borys, N. Damaschke, and C. Tropea, *Laser Doppler and Phase Doppler Measurement Techniques*. Berlin: Springer Berlin Heidelberg, 2003.
- [87] W. J. Gooding and N. L. Key, "Leveraging LDV Techniques for the Investigation of Unsteady Turbomachinery Flows," *Aeronaut. J.*, vol. 123, no. 1270, pp. 1919–1937, 2019.
- [88] W. George and J. Lumley, "The Laser Doppler Velocimeter and its Application to the Measurement of Turbulence," *J. Fluid Mech.*, vol. 60, no. 2, 1973.
- [89] R. G. Seasholtz, "Laser Doppler Velocimeter Measurements in a Turbine Stator Cascade Facility," NASA, West Lafayette, TM X-71524, 1974.
- [90] W. George, "Processing of Random Signals," in *Proc. of the Dynamic Flow Conference*, 1978.
- [91] K. Orloff and P. Snyder, "Laser Doppler Anemometer Measurements Using Nonorthogonal Velocity Components: Error Estimates," *Appl. Opt.*, vol. 21, no. 2, pp. 339–344, 1982, doi: 10.1364/AO.21.000339.
- [92] J. Agarwal, "Generating Aerosols for Laser Velocimeter Seedings," NASA, N86-11455, 1986.

- [93] M. Wernet, G. J. Skoch, and J. Wernet, “Demonstration of a Stabilized Alumina/Ethanol Colloidal Dispersion Technique for Seeding High Temperature Air Flows,” NASA, TM 106945, 1995.
- [94] J. Fagan and S. Fleeter, “An Investigation of the Three-Dimensional Flow Field in a Centrifugal Compressor,” NASA, TR-90-C-004, 1990.
- [95] M. Hathaway, R. Chriss, J. R. Wood, and A. Strazisar, “Experimental and Computational Investigation of the NASA Low-Speed Centrifugal Compressor Flow Field,” *J. Turbomach.*, vol. 115, no. 3, pp. 527–541, 1993, doi: 10.1115/1.2929285.
- [96] W. Gizzi, C. Roduner, D. Stahlecker, P. Koppel, and G. Gyarmathy, “Time-Resolved Measurements with Fast-Response Probes and Laser Doppler Velocimetry at the Impeller Exit of a Centrifugal Compressor: A Comparison of Two Measurement Techniques,” in *Proceeding of the Institution of Mechanical Engineers*, 1999, vol. 213, doi: 10.1115/98-GT-241.
- [97] S. Ibaraki, T. Matsuo, H. Kuma, K. Sumida, and T. Suita, “Aerodynamics of a Transonic Centrifugal Compressor Impeller,” *J. Turbomach.*, vol. 125, no. 2, pp. 346–351, 2003, doi: 10.1115/1.1540117.
- [98] N. Buffaz and I. Trébinjac, “Detailed Analysis of the Flow in the Inducer of a Transonic Centrifugal Compressor,” *J. Therm. Sci.*, vol. 21, no. 1, pp. 1–12, 2012, doi: 10.1007/s11630-012-0513-x.
- [99] J. Moore and J. G. Moore, “Calculations of Three-Dimensional, Viscous Flow and Wake Development in a Centrifugal Impeller,” *J. Eng. Power*, vol. 103, pp. 367–372, 1981, doi: 10.1115/1.3230730.
- [100] D. Wilcox, *Turbulence Modeling for CFD*, 3rd ed. La Canada, California: DCW Industries, Inc, 2006.
- [101] J. Boussinesq, “Theorie de l’Ecoulement Tourbillant,” in *Mem. Presentes par Divers Savants Acad. Sci. Inst. Fr. Vol. 23*, 1877.
- [102] L. Prandtl, “Uber die Ausgebildete Turbulenz,” *ZAMM*, vol. 5, 1925.
- [103] A. Smith and T. Cebeci, “Numerical Solution of the Turbulent Boundary Layer Equations,” Douglas Aircraft Company, 33735, 1967.
- [104] B. Baldwin and H. Lomax, “Thin-Layer Approximation and Algebraic Model for Separated Turbulent Flows,” in *16th Aerospace Sciences Meeting*, 1978, doi: 10.2514/6.1978-257.

- [105] W. Jones and B. Launder, “The Prediction of Laminarization with a Two-Equation Model of Turbulence,” *Int. J. Heat Mass Transf.*, vol. 15, pp. 301–314, 1972.
- [106] F. R. Menter, “Two-Equation Eddy-Viscosity Turbulence Models for Engineering Applications,” *AIAA J.*, vol. 32, no. 8, 1994, doi: 10.2514/3.12149.
- [107] G. Blaisdell, “Class Notes: AAE 626 Turbulence and Turbulence Modeling.” Purdue University.
- [108] D. C. Wilcox, “Formulation of the  $k$ - $\omega$  Turbulence Model Revisited,” *AIAA J.*, vol. 46, no. 11, pp. 2823–2838, 2008, doi: 10.2514/1.36541.
- [109] C. Morsbach, “Reynolds Stress Modelling for Turbomachinery Flow Applications,” Technischen Universität Darmstadt, 2016.
- [110] P. Smirnov and F. R. Menter, “Sensitization of the SST Turbulence Model to Rotation and Curvature by Applying the Spalart–Shur Correction Term,” *J. Turbomach.*, vol. 131, 2009, doi: 10.1115/1.3070573.
- [111] P. R. Spalart and M. Shur, “On the Sensitization of Turbulence Models to Rotation and Curvature,” *Aerosp. Sci. Technol.*, vol. 1, no. 5, pp. 297–302, 1997, doi: 10.1016/S1270-9638(97)90051-1.
- [112] S. Wallin and A. V. Johansson, “An Explicit Algebraic Reynolds Stress Model for Incompressible and Compressible Turbulent Flows,” *J. Fluid Mech.*, vol. 403, pp. 89–132, 2000, doi: 10.1017/S0022112099007004.
- [113] W. J. Gooding, M. A. Meier, and N. L. Key, “The Impact of Various Modelling Decisions on Flow Field Predictions in a Centrifugal Compressor,” in *Submitted to IGTI 2020*, 2020, pp. 1–11.
- [114] J. Oh, “The Effects of Blade Fillets on Aerodynamic Performance of a High Pressure Ratio Centrifugal Compressor,” in *23rd International Compressor Engineering Conference*, 2016.
- [115] J. D. Denton, “The Calculation of Three-Dimensional Viscous Flow Through Multistage Turbomachines,” in *Proc. of ASME Turbo Expo*, 1990, doi: 10.1115/1.2927983.
- [116] N. He, A. Turlidakis, and R. L. Elder, “Predictions for Impeller - Diffuser Interactions in a Centrifugal Compressor Stage,” in *Proc. of ASME Turbo Expo*, 2007.
- [117] S. Connell, M. Braaten, L. Zori, R. Steed, B. Hutchinson, and G. Cox, “A Comparison of Advanced Numerical Techniques to Model Transient Flow in Turbomachinery Blade Rows,” in *Proc. of ASME Turbo Expo*, 2011, doi: 10.1115/GT2011-45820.

- [118] M. Giles, "Calculation of Unsteady Wake/Rotor Interaction," *J. Propuls. Power*, vol. 4, no. 4, 1988, doi: 10.2514/3.23074.
- [119] J. Erdos and E. Alzner, "Computation of Unsteady Transonic Flows Through Rotating and Stationary Cascades," NASA, CR 2900, 1977.
- [120] L. He, "An Euler Solution for Unsteady Flows Around Oscillating Blades," *J. Turbomach.*, vol. 112, 1990, doi: 10.1115/1.2927714.
- [121] M. Dolan, "Establishing Repeatable Operation of a Centrifugal Compressor Research Facility for Aerodynamic Investigations," Purdue University, 2015.
- [122] W. J. Gooding, M. A. Meier, E. J. Gunter, and N. L. Key, "Nonlinear Response and Stability of an Experimental Overhung Compressor Mounted with a Squeeze Film Damper," in *Submitted to IGTI 2020*, 2020, pp. 1–10.
- [123] B. Heckaman, "Design of Optical Access for the Application of Laser Doppler Velocimetry in a Low Specific Speed Centrifugal Compressor," Purdue University, 2014.
- [124] Dantec Dynamics, "Principles," in *Dantec 57N10 BSA Manual*, .
- [125] D. Robinson, "Understanding Mixture Models and Expectation-Maximization (Using Baseball Statistics)," *Variance Explained*, 2017. [Online]. Available: <http://varianceexplained.org/r/mixture-models-baseball/>. [Accessed: 22-Jul-2018].
- [126] J. P. Bons, "A Review of Surface Roughness Effects in Gas Turbines," *J. Turbomach.*, vol. 132, no. 2, pp. 1–16, 2010, doi: 10.1115/1.3066315.
- [127] C. C. Koch and L. H. Smith, "Loss Sources and Magnitudes in Axial-Flow Compressors.," *J. Eng. Power*, no. July, pp. 411–424, 1976.
- [128] A. Shabbir and M. G. Turner, "A Wall Function for Calculating the Skin Friction with Surface Roughness," *Proc. ASME Turbo Expo*, pp. 1–11, 2004.
- [129] R. S. Bunker, "The Effect of Thermal Barrier Coating Roughness Magnitude on Heat Transfer with and Without Flowpath Surface Steps," *Proc. of IMECE2003*, pp. 1–10, 2003.
- [130] N. Ahmed and R. L. Elder, "Flow Behaviour in a High Speed Centrifugal Impeller Passage Under 'Design' and 'Off Design' Operating Conditions," *JSME Int. J.*, vol. 43, no. 1, pp. 22–28, 2000, doi: 10.1093/jxb/erl177.
- [131] L. H. Benedict and R. D. Gould, "Towards Better Uncertainty Estimates for Turbulence Statistics," *Exp. Fluids*, vol. 22, no. 2, pp. 129–136, 1996, doi: 10.1007/s003480050030.

[132] R. Adkins-Rieck, “Additive Manufacturing for Aerodynamic Diffuser Designs in a Centrifugal Compressor,” Purdue University, 2018.

## APPENDIX A: MAXWELL'S EQUATIONS

Light propagation is governed by the theory of electromagnetic fields, based on Maxwell's Equations, describing the relationship between electric field strength,  $\mathbf{E}$ , magnetic field strength,  $\mathbf{H}$ , and spatial charge distribution,  $\rho$ , given by:

$$\begin{aligned} \nabla \times \mathbf{H} &= \mathbf{S} + \frac{\partial \mathbf{D}}{\partial t}, & \nabla \times \mathbf{E} &= -\frac{\partial \mathbf{B}}{\partial t}, \\ \nabla \cdot \mathbf{D} &= \rho, & \nabla \cdot \mathbf{B} &= 0, \\ \mathbf{D} &= \varepsilon \mathbf{E}, & \mathbf{S} &= \kappa \mathbf{E}, \quad \text{and} \quad \mathbf{B} = \mu \mathbf{H}. \end{aligned} \tag{A-1}$$

These fields are related to the electric displacement,  $\mathbf{D}$ , current density,  $\mathbf{S}$ , and the magnetic induction,  $\mathbf{B}$ , through the material properties  $\kappa$ ,  $\varepsilon$ , and  $\mu$ , the electric conductivity, permittivity, and magnetic permeability of the medium [86]. Expressing these relations in complex form (denoted by an underbar) and solving for the case of charge-free space yields the wave equations of the electromagnetic field:

$$\nabla^2 \underline{\mathbf{E}} + \underline{k}^2 \underline{\mathbf{E}} = 0 \quad \text{and} \quad \nabla^2 \underline{\mathbf{H}} + \underline{k}^2 \underline{\mathbf{H}} = 0, \tag{A-2}$$

where  $k$  represents the wavenumber dependent upon the wave frequency and the medium. Laser (Light Amplification by Stimulated Emission of Radiation) beams form a solution of the wave equation which are highly monochromatic, have high power densities, and have a long coherence length. The physical boundary conditions for the particular solution to the wave equations are dictated by the construction of the laser. The distribution of intensity across the beam is given by a Gaussian distribution and the propagating wave has spherical wave fronts. At the focal point of the beam lies the beam waist, corresponding to the measurement volume of an LDV system, with diameter  $d_w$ , where the wave fronts are planar, Figure A-1. The beam propagates in the  $z$  direction and has a maximum intensity (with respect to the radial direction) along the propagation axis which itself reaches a maximum (with respect to the  $z$  direction) at the beam waist. In an LDV system, Gaussian beams of a known diameter are focused to the measurement volume through a focusing lens with focal length  $f$ . This creates a second beam waist at the measurement volume with a focused diameter given by:

$$d_f = \frac{4 \lambda f}{\pi d_w}. \tag{A-3}$$

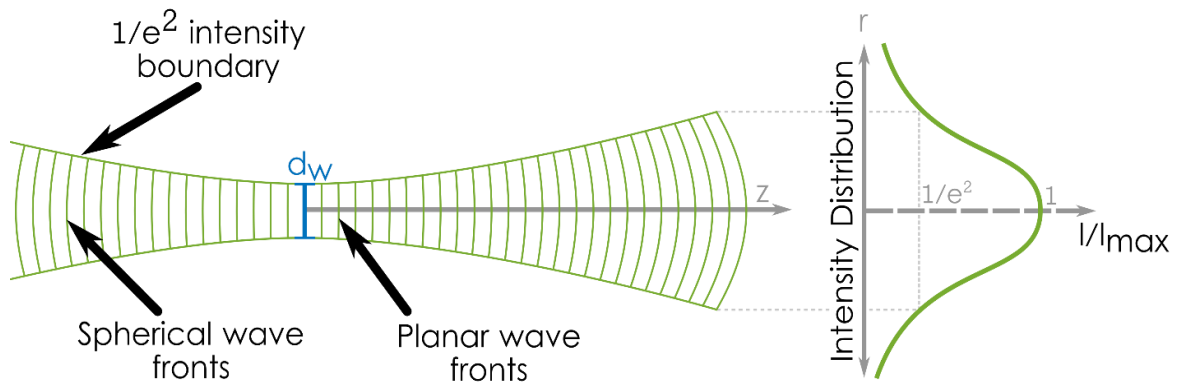


Figure A-1: Gaussian beam parameters

## APPENDIX B: ADDITIONAL REYNOLDS STRESS DATA

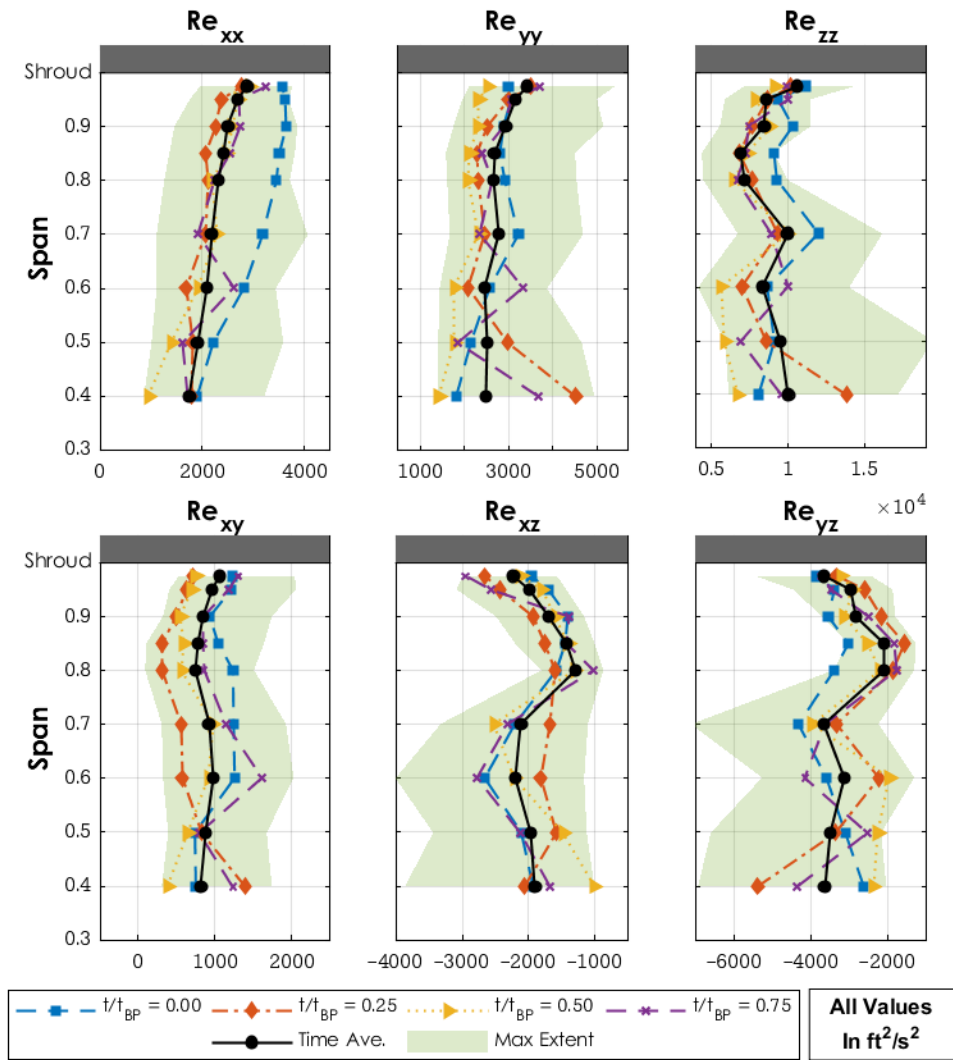


Figure B-1: Reynolds stress components 10% downstream from throat, at mid-passage (Point 127)

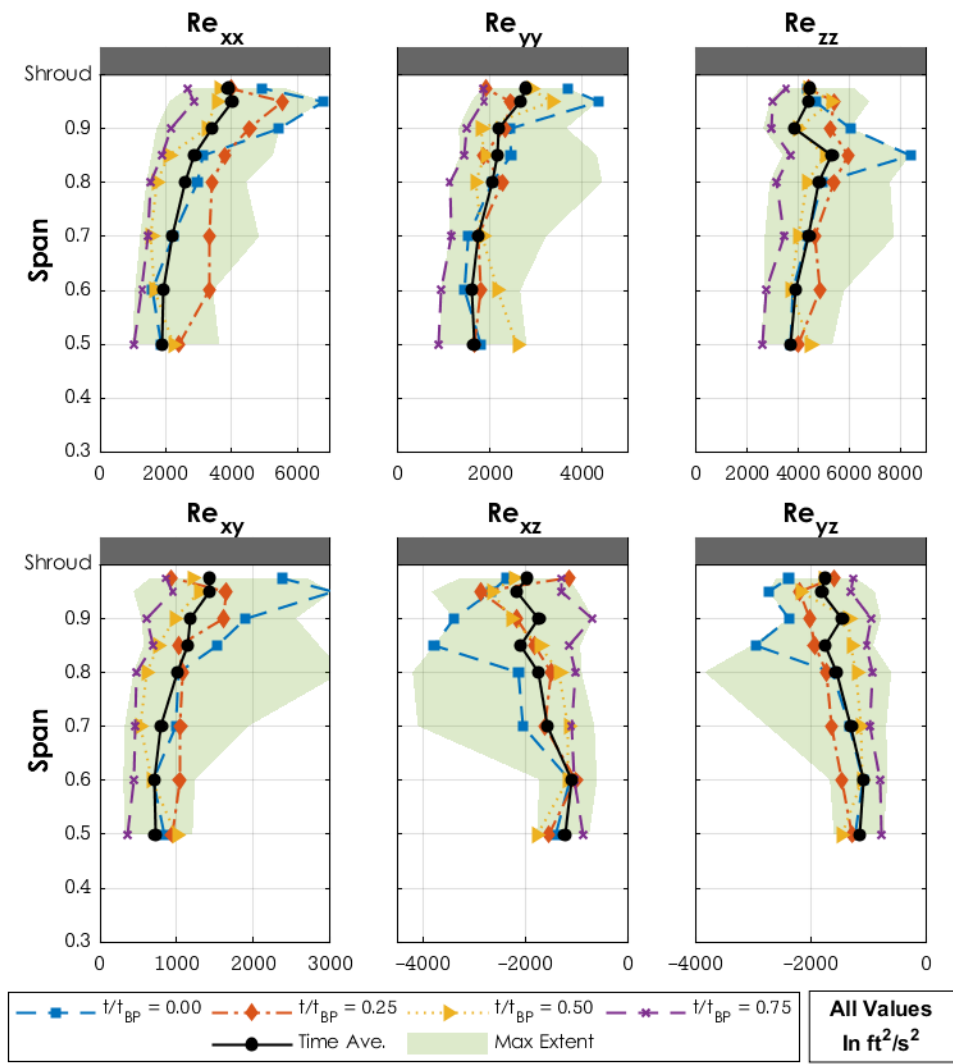


Figure B-2: Reynolds stress components 20% downstream from the throat, along the pressure side (Point 159)

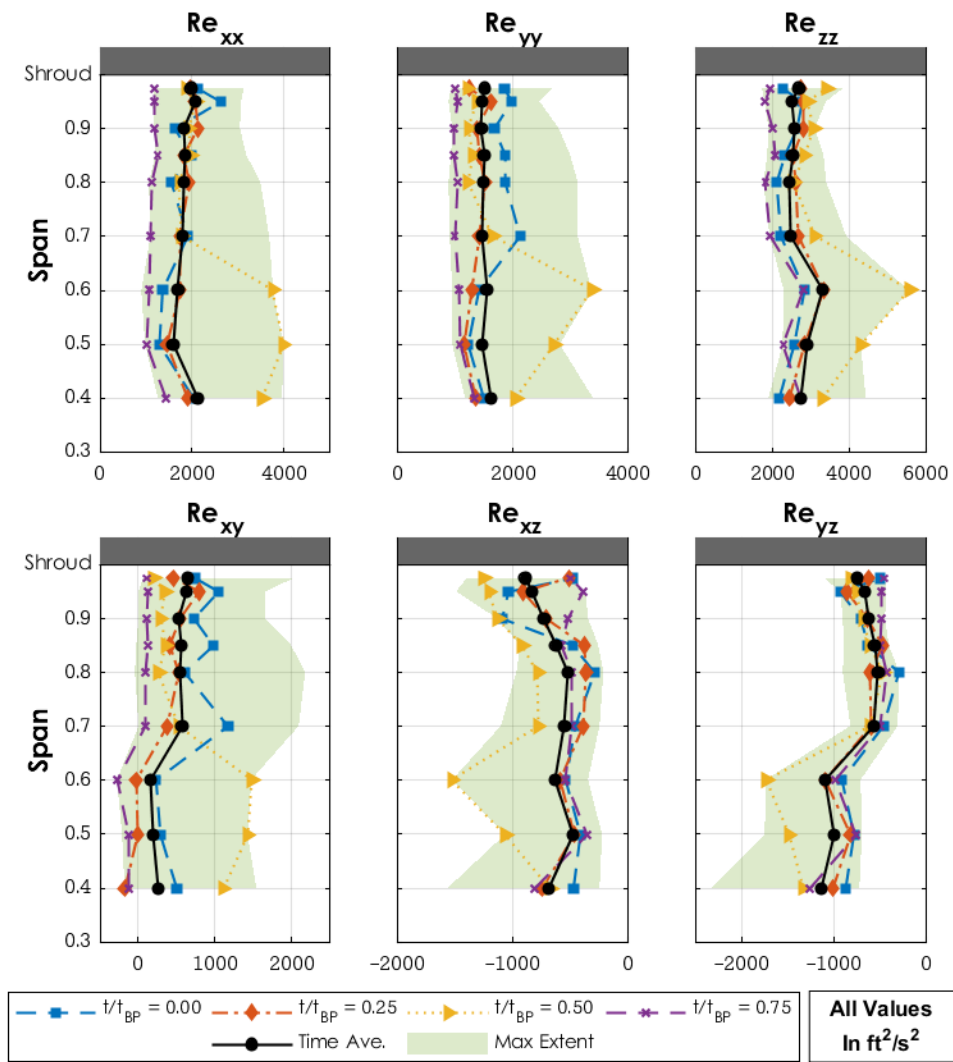


Figure B-3: Reynolds stress components 20% downstream from the throat, along the suction side (Point 166)

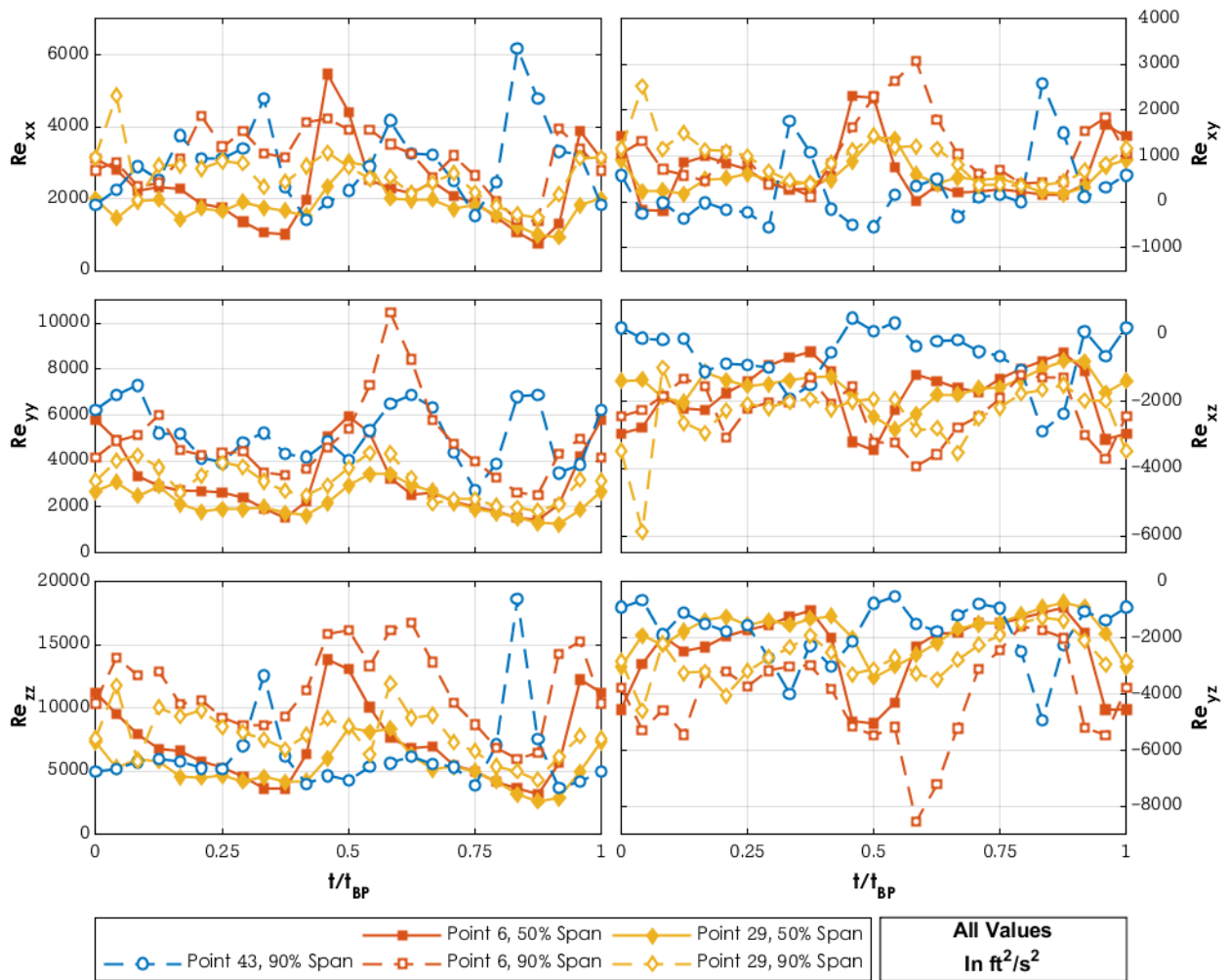


Figure B-4: Unsteady variation in Reynolds stress components within the vaneless space

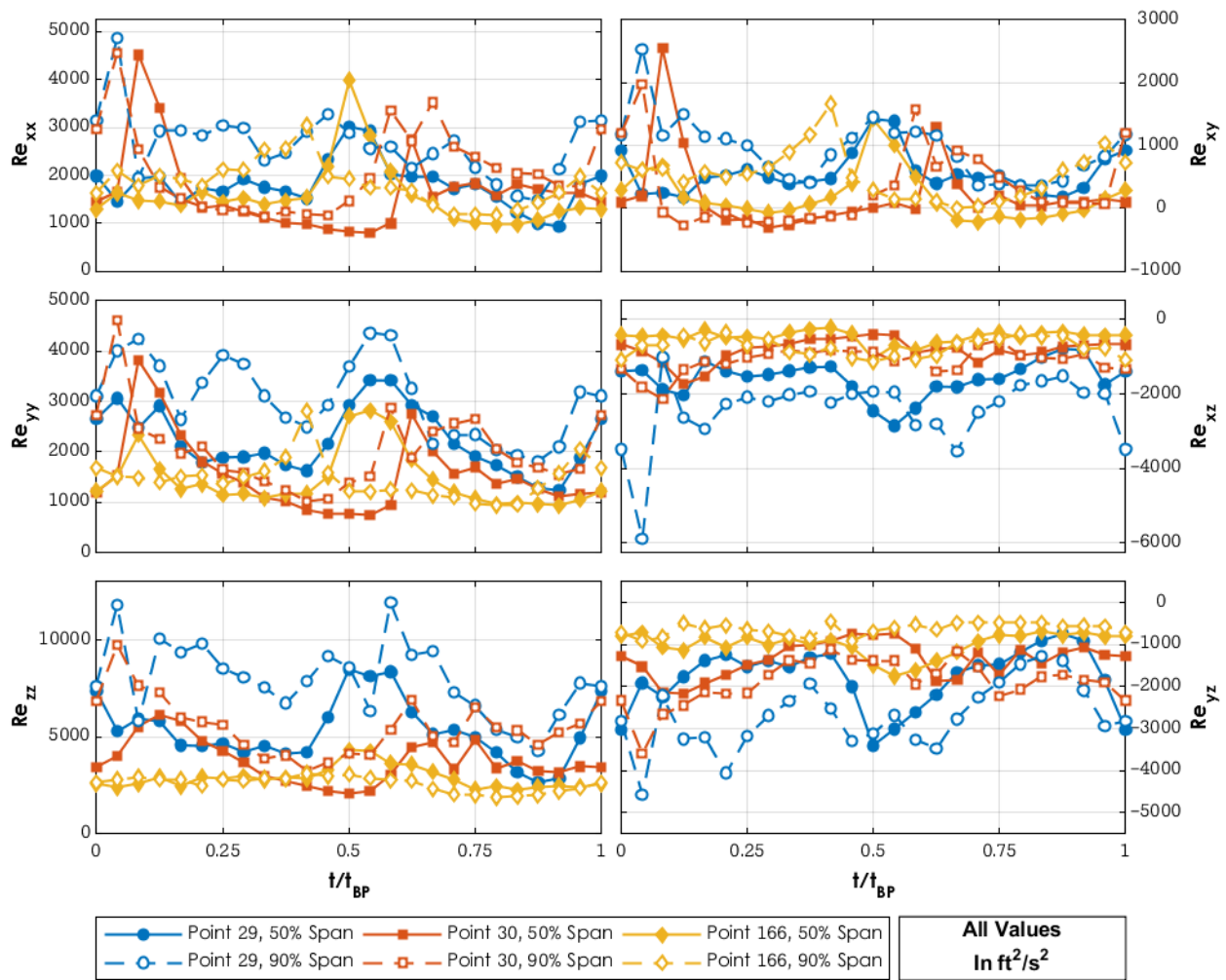


Figure B-5: Unsteady variation in Reynolds stress components along the suction surface of the passage

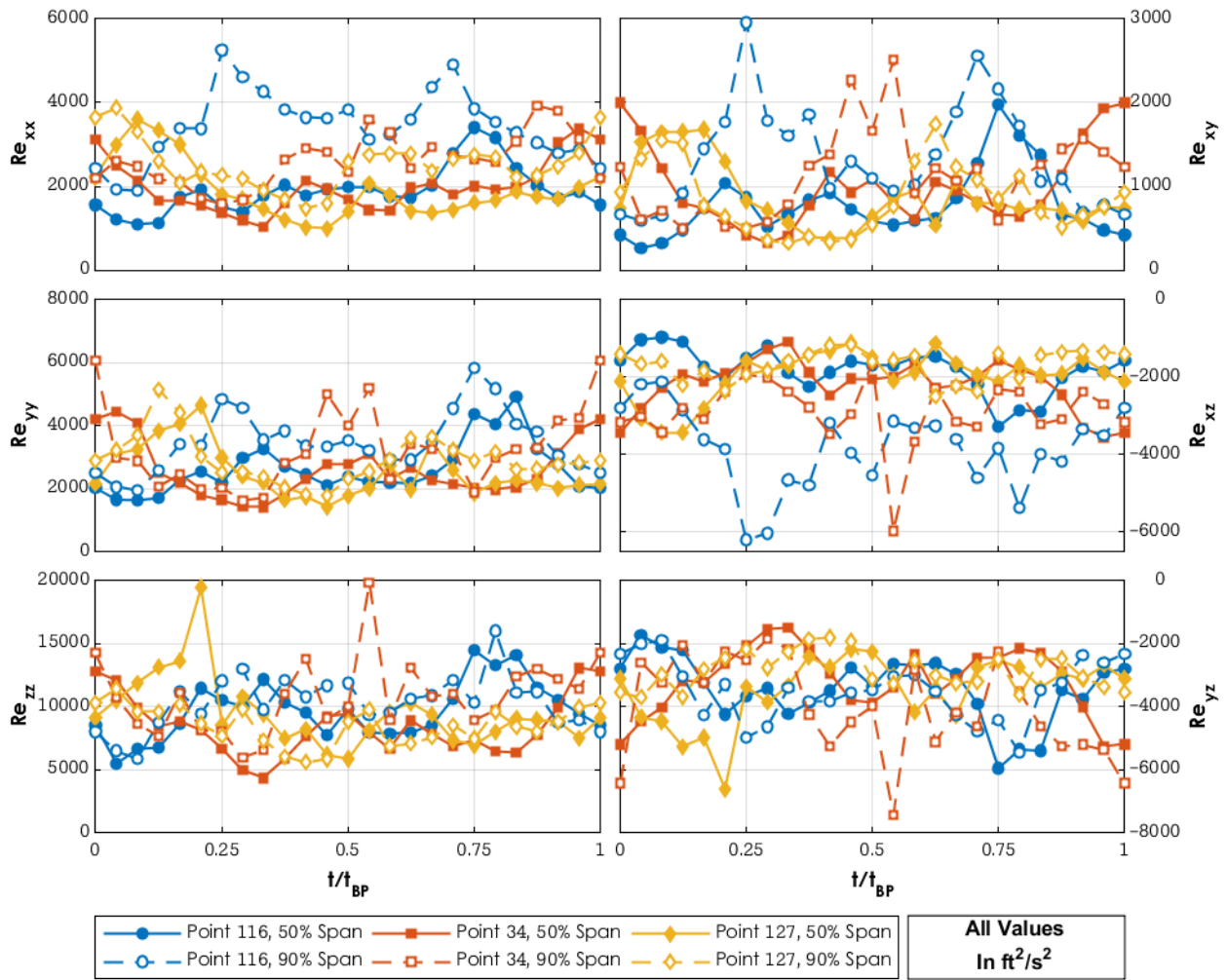


Figure B-6: Unsteady variation in Reynolds stress components along mid-passage

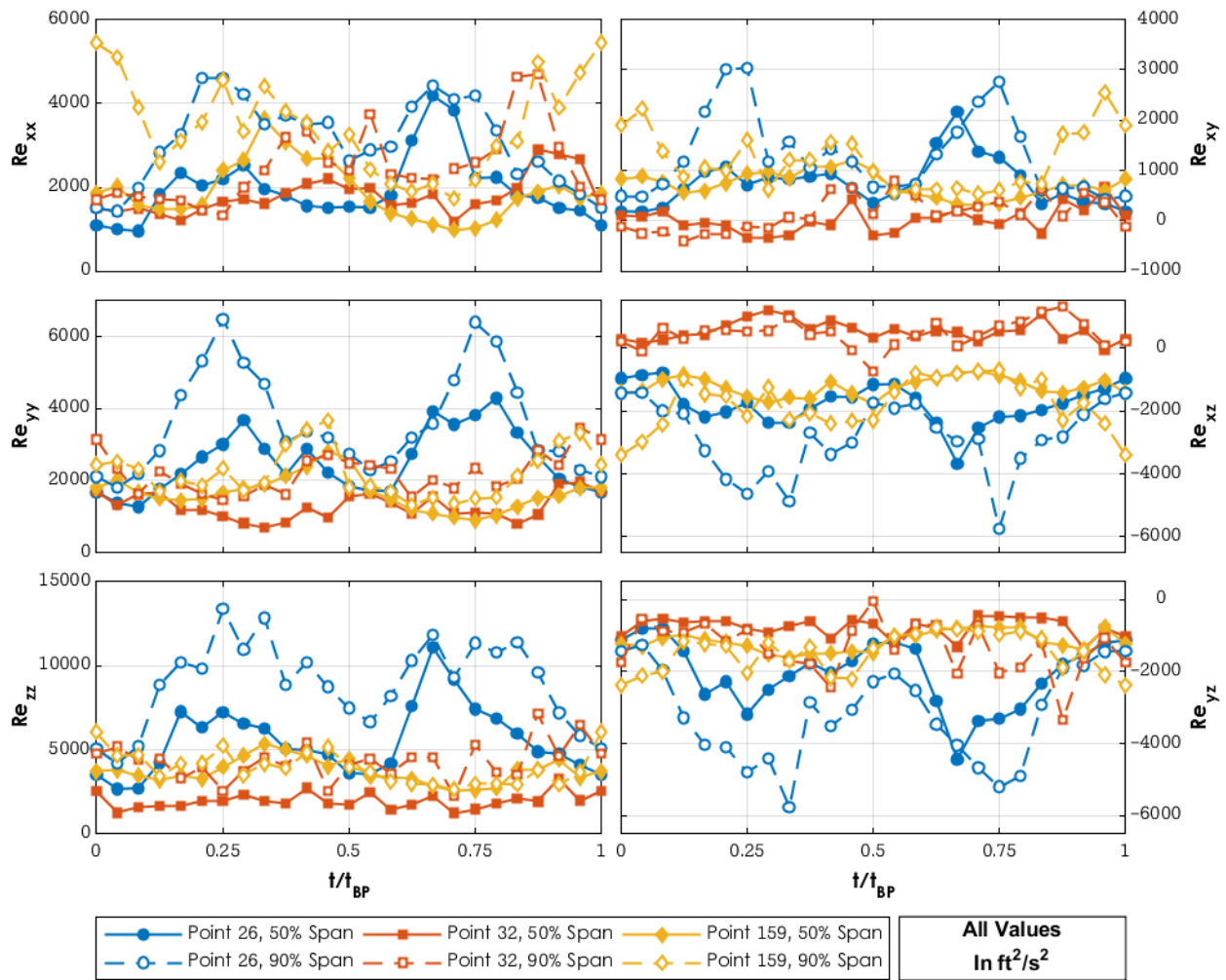


Figure B-7: Unsteady variation in Reynolds stress components along the pressure surface of the passage

## VITA

William James Gooding was born to parents James and Linda Gooding on July 15, 1993 in Roanoke, Virginia. He has a brother, Andrew Gooding, a sister, Emily Gooding, and a wife, Hannah (née Gould) Gooding, whom he married in 2017. He graduated from Hidden Valley High School in 2011 and began pursuing a bachelor's degree in Mechanical Engineering and Mathematics at Washington University in St. Louis. During his undergraduate studies, William received the Undergraduate Award in Technical Writing and conducted research on harmonic analysis under Professor Guido Weiss. William graduated from Washington University in St. Louis with a Bachelor of Science in 2015 and began his graduate studies at Purdue University in August 2015. Under the guidance of Professor Nicole Key, he studied the detailed aerodynamics of a centrifugal compressor at the Centrifugal Stage for Aerodynamic Research (CSTAR) facility. This work focused on the unsteady flow field through the diffuser of a low-specific speed centrifugal compressor for aeroengine application using experimental and numerical techniques. He was named an Honorable Mention for the National Science Foundation Graduate Research Fellowship Program in 2016 before completing the degree requirements for a Master of Science in Mechanical Engineering in 2017. He will receive his Ph.D. from the School of Mechanical Engineering in May 2020.

## PUBLICATIONS

**Gooding, W. J.**, Meier, M. A., and Key, N. L., 2020, "The Impact of Various Modeling Decisions on Flow Field Predictions in a Centrifugal Compressor," *Accepted Manuscript: ASME Turbo Expo 2020*, GT2020-14516.

**Gooding, W. J.**, Meier, M. A., Gunter, E. J., and Key, N. L., 2020, "Nonlinear Response and Stability of an Experimental Overhung Compressor Mounted with a Squeeze Film Damper," *Accepted Manuscript: ASME Turbo Expo 2020*, GT2020-15212.

**Gooding, W. J.**, Fabian, J. C., and Key, N. L., 2020, "LDV Characterization of Unsteady Vaned Diffuser Flow in a Centrifugal Compressor," *Journal of Turbomachinery*, vol. 142(4), pp. 041001.

Meier, M. A., **Gooding W. J.**, Fabian J. C., and Key, N. L., 2020, "Considerations for Using Additive Manufacturing Technology in Centrifugal Compressor Research," *Journal of Engineering for Gas Turbines and Power*, vol. 142(3), pp. 031018.

**Gooding, W. J.** and Key, N. L., 2019, "Leveraging LDV Techniques for the Investigation of Unsteady Turbomachinery Flows," *The Aeronautical Journal*, vol. 123(270).

**Gooding, W. J.**, Fabian, J. C., and Key, N. L., 2017, "Numerical Analysis of Unsteady Vaned Diffuser Flow in a Centrifugal Compressor," *Presented at ISABE 2017*, Manchester, United Kingdom, ISABE-2017-21417.

Methel, J., **Gooding, W. J.**, Fabian, J. C., Key, N. L., and Whitlock, M., 2016, "The Development of a Low Specific Speed Centrifugal Compressor Research Facility," *Presented at ASME Turbo Expo 2016*, Seoul, South Korea, GT2016-56683.